

A STUDY OF THE WIND-DRIVEN OCEAN CIRCULATION
IN AN EQUATORIAL BASIN

by

Mark A. Cane

B.A., Harvard College, 1965

M.S., Harvard University, 1968

SUBMITTED IN PARTIAL FULFILLMENT OF THE
REQUIREMENTS FOR THE DEGREE OF DOCTOR OF PHILOSOPHY
at the

MASSACHUSETTS INSTITUTE OF TECHNOLOGY

August 1975

(i.e. February 1976)

Signature of Author: _____

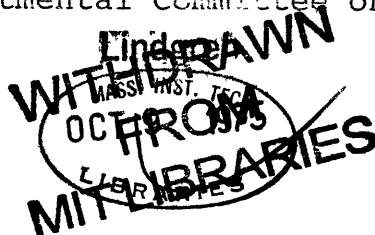
Department of Meteorology, August 1975

Certified by _____

Thesis Supervisor

Accepted by _____

Chairman, Departmental Committee on Graduate Students



A STUDY OF THE WIND-DRIVEN OCEAN CIRCULATION
IN AN EQUATORIAL BASIN

by

Mark A. Cane

Submitted to the Department of Meteorology on
18 August, 1975 in partial fulfillment of the
requirements for the degree of Doctor of Philosophy

ABSTRACT

A simple model has been developed to study the wind-driven equatorial ocean circulation. It is a time dependent, primitive equation, beta plane model that is two-dimensional in the horizontal. The vertical structure consists of two layers above the thermocline with the same constant density. The ocean below the thermocline is taken to be of a higher constant density and to be approximately at rest. The surface layer is of constant depth and is acted upon directly by the wind. The depth of the lower active layer is dynamically determined. This is the simplest vertical structure which allows an undercurrent.

The linear response of the model has been investigated thoroughly by analytic methods, as well as numerically. The nonlinear response has been studied numerically with the aid of some simple analytic arguments. The numerical scheme employs a variable mesh spacing, is fourth order in space and energy conserving (except for boundary effects). Small-scale noise is suppressed by a special treatment of the gravity wave terms.

The linear responses to uniform southerly and easterly wind stress and the nonlinear responses to uniform wind stresses from the south, the east, the west, and the southeast have been studied numerically. The linear results are in agreement with analytic theory. In all cases, the surface flow is established within twenty days, a timescale determined by friction. There is also a timescale for the establishment of large-scale pressure gradients and mass transports. Linear theory shows that this "setup time" varies linearly with the time it takes for planetary waves to cross the ocean in the zonal direction. The nonlinear setup time can be either longer or shorter than the corresponding linear time, depending on the case, but in all cases would be six months or more for the world's oceans. Since this is at least as long as the timescale of the monsoonal wind systems, steady state theories should be applied to

equatorial oceans with caution.

Flows become nonlinear within two weeks. A substantial amount of the energy put in at the surface by the wind stress is advected downwards by the strong vertical motions that arise near the equator. In the presence of meridional motions, exchanges of relative and planetary vorticity are dynamically significant.

The nonlinear response to an easterly wind includes an eastward equatorial undercurrent in qualitative agreement with observations in many respects. In the linear response, the vertically integrated mass transport is westward at the equator. The flow that returns the undercurrent transport to the west takes place in the lower layer within 5° of the equator. The response to a west wind has eastward currents in both layers at the equator with a maximum at the surface. Both zonal wind cases exhibit variations in the zonal direction. It is argued that such variations are required by the dynamics in the absence of large frictional forces.

The zonal mean state in response to a southerly wind has a narrow eastward jet at about 3°N and a broad area of westward flow at the equator. This state is barotropically unstable and after about 100 days westward propagating waves appear. With a southeast wind there is an eastward jet at 4°N and the mean position of the undercurrent shifts south of the equator. The undercurrent meanders with longitude but is steady in time. In this and the south wind case, the waves appear first at the western side of the basin and then spread eastward across the basin. There are no meanders in the zonal wind responses, suggesting that observed undercurrent meanders are instabilities of the equatorial current system as a whole and not of the undercurrent itself.

Thesis Supervisor: Jule G. Charney
Title: Sloan Professor of Meteorology

In memory of my mother

ACKNOWLEDGEMENTS

I am grateful to my advisor, Professor Jule G. Charney, for his guidance and encouragement, and, most of all, for teaching me how to think about geophysical phenomena.

Several valuable conversations with Professor Henry Stommel are gratefully acknowledged. My special thanks to Dr. Edward Sarachik, who originally brought the subject area of this thesis to my attention and has provided invaluable criticisms throughout the course of this work. It is a pleasure to acknowledge Professor Eugenia Rivas for many hours of useful discussion about numerical methods. I am grateful to my fellow denizens of the fourteenth floor for their general camaraderie, as well as for a number of valuable conversations on various aspects of this work. Dr. Antonio Moura, Dr. Li-or Merkine and Mr. John Willett have been especially helpful.

My thanks to Professor Dennis Moore for sharing his knowledge about equatorial waves. I am grateful to Dr. George Philander, Professor Walter Düing and Dr. Robert Knox for allowing me to see preliminary versions of their work.

The computations were carried out at the Goddard Institute for Space Studies and I am grateful to Dr. Robert Jastrow and Dr. Milton Halem for making this possible.

Many others at GISS provided needed assistance during the course of this work; special thanks to Ms. Ilene Shifrin, Mr. Leonard Keegan and Mr. Kenneth Woods. My thanks, too, to Ms. Sandy Congleton, Ms. Sylvia Wong and Ms. Helena Dinerman, who typed various drafts of this thesis.

Some of the work reported in Chapter 4 was done in the summer of 1974, while I was a fellow in the Geophysical Fluid Dynamics program at the Woods Hole Oceanographic Institution, financially supported by NSF Grant GA-37116X. The larger part of my financial support was provided under NASA Grant NGR 22-009-727.

I am happy to express my gratitude to my father for his unflinching faith and encouragement through the years. Most of all, I am grateful to my wife, Barbara, and my children, Laura and Jacob, for their patience and understanding, love and support, throughout the course of this work. I owe them more than I can ever say.

Finally, I would like to acknowledge my grandmother, Rebecca Cohen, an inspiration, always.

TABLE OF CONTENTS

	<u>page</u>
Abstract	2
Dedication	4
Acknowledgements	5
Table of Contents	7
List of Tables	9
List of Illustrations	10
1. Introduction	19
2. Formulation of the Physical Model	27
2.1 The Model Equations	27
2.2 Choice of Parameter Values	37
3. Linear Analytic Solutions	49
3.1 Formulation of the Mathematical Problem	49
3.2 Solution of the Steady State Interior Problem	53
3.3 Sidewall Boundary Layers	59
3.4 Solution of the Time Dependent Interior Problem	63
4. Time Dependent Forced Shallow Water Equations in an Equatorial Basin	69
4.1 Introduction	69
4.2 Free Solutions	71
4.3 Forced Response in an Unbounded Basin	76
4.4 Forced Response in a Bounded Basin	94
5. Model Response to Simple Wind Stress Patterns	106
5.1 Introduction	106
5.2 Linear Response to a Uniform South Wind	108
5.3 Nonlinear Response to a Uniform South Wind	138
5.4 Linear Response to a Uniform East Wind	180
5.5 Nonlinear Response to a Uniform East Wind	214

	<u>page</u>
5.6 Nonlinear Response to a Uniform West Wind	250
5.7 Nonlinear Response to a Uniform Southeast Wind	275
6. Summary and Conclusions	301
References	320
Appendix A Eddy Viscosity	326
Appendix B Numerical Methods	329
B.1 Variable Grid	329
B.2 Time Differencing	330
B.3 Spatial Differencing: Finite Difference Approximations	332
B.4 Spatial Differencing: Conservation Form	335
B.5 Gravity Wave Terms	344
B.6 Summary	351
Appendix C Finite Difference Equations on a Beta Plane	353
Appendix D Computational Stability (Linear Analysis)	359
Appendix E Computational Formulas for Chapter 4	363
E.1 Properties of the Hermite Functions	363
E.2 The Projections of the Forcing Functions	364
E.3 Boundary Response Terms	365
Appendix F Orthogonality and Completeness of the Eigenfunctions for the Shallow Water Equations	369
Biographical Note	372

LIST OF TABLES

	<u>page</u>
Table 1 Non-dimensionalization of Variables	38
Table 2 Position of Points in the Standard Grid	48

LIST OF ILLUSTRATIONS¹

<u>Figure</u>		<u>Page</u>
2.1	Multi-layer model.	28
2.2	Model with two active layers.	28
4.1	Dispersion relation for waves on an equatorial beta plane.	74
4.2	Response to $F=1$, $G=Q=0$ in an unbounded basin; see Equation (4.19).	83
4.3	Response to $F=0$, $G=1$, $Q=0$ in an unbounded basin.	85
5.1	Schematic view of linear adjustment to a south wind.	114
5.2	Energies from 15°S to 15°N . Linear. South wind.	117
5.3	Energies from 5.6°S to 5.6°N . Linear. South wind.	118
5.4a	\tilde{u}^{S} vectors at 8 days. Linear. South wind.	120
5.4b	\tilde{u}^{I} vectors at 8 days. Linear. South wind.	121
5.5	\bar{u} vectors at 16 days. Linear. South wind.	124
5.6a	\tilde{u}^{S} vectors at 40 days. Linear. South wind.	126
5.6b	\tilde{u}^{I} vectors at 40 days. Linear. South wind.	127
5.6c	h contours at 40 days. Linear. South wind.	128

¹Some explanatory material related to the computer-produced figures may be found in Section 5.1.

	<u>page</u>
5.7a Meridional sections of h to day 398 at $x=25.4^\circ$. Linear. South wind.	129
5.7b Meridional sections of h to day 398 at $x=14.3^\circ$. Linear. South wind.	130
5.7c Meridional sections of h to day 398 at $x=3.2^\circ$. Linear. South wind.	131
5.8 Meridional sections of \bar{u} to day 398 at $x=14.3^\circ$. Linear. South wind.	132
5.9a \tilde{u}^S vectors at 398 days. Linear. South wind.	134
5.9b \tilde{u}^1 vectors at 398 days. Linear. South wind.	135
5.9c h contours at 398 days. Linear. South wind.	136
5.10 $\tilde{\bar{u}}$ vectors at 398 days. Linear. South wind.	137
5.11 Energies from $15^\circ S$ to $15^\circ N$. Nonlinear. South wind.	140
5.12 Energies from $5.6^\circ S$ to $5.6^\circ N$. Non- linear. South wind.	141
5.13 u^1 contours at the equator to day 398. Nonlinear. South wind.	143
5.14 h contours at 8 days. Nonlinear. South wind.	145
5.15 \bar{u} contours at 8 days. Nonlinear. South wind.	146
5.16a \tilde{u}^S vectors at 16 days. Nonlinear. South wind.	148
5.16b \tilde{u}^1 vectors at 16 days. Nonlinear. South wind.	149
5.17 $\tilde{\bar{u}}$ vectors at 16 days. Nonlinear. South wind.	150

		<u>page</u>
5.18a	\tilde{u}^S vectors at 40 days. Nonlinear. South wind.	151
5.18b	\tilde{u}^1 vectors at 40 days. Nonlinear. South wind.	152
5.18c	h contours at 40 days. Nonlinear. South wind.	153
5.19	h contours at 119 days. Nonlinear. South wind.	164
5.20a	\tilde{u}^S vectors at 159 days. Nonlinear. South wind.	165
5.20b	\tilde{u}^1 vectors at 159 days. Nonlinear. South wind.	166
5.20c	h contours at 159 days. Nonlinear. South wind.	167
5.21a	\tilde{u}^S vectors at 398 days. Nonlinear. South wind.	169
5.21b	\tilde{u}^1 vectors at 398 days. Nonlinear. South wind.	170
5.21c	h contours at 398 days. Nonlinear. South wind.	171
5.22a	\bar{u} contours at 398 days. Nonlinear. South wind.	172
5.22b	\bar{v} contours at 398 days. Nonlinear. South wind.	173
5.23a	Meridional sections of h to day 398 at $x=25.4^\circ$. Nonlinear. South wind.	176
5.23b	Meridional sections of h to day 398 at $x=14.3^\circ$. Nonlinear. South wind.	177
5.23c	Meridional sections of h to day 398 at $x=3.2^\circ$. Nonlinear. South wind.	178
5.24	Meridional sections of \bar{u} to day 398 at $x=14.3^\circ$. Nonlinear. South wind.	179

	<u>page</u>
5.25 Energies from 15°S to 15°N. Linear. East wind.	186
5.26 Energies from 5.6°S to 5.6°N. Linear. East wind.	187
5.27 Sections of h along the equator to day 38. Linear. East wind.	189
5.28 Sections of h along the equator to day 398. Linear. East wind.	190
5.29 Sections of \bar{u} along the equator to day 38. Linear. East wind.	191
5.30 Sections of \bar{u} along the equator to day 398. Linear. East wind.	192
5.31a Meridional sections of h to day 397 at x=25.4°. Linear. East wind.	195
5.31b Meridional sections of h to day 397 at x=14.3°. Linear. East wind.	196
5.31c Meridional sections of h to day 397 at x=3.2°. Linear. East wind.	197
5.32a \tilde{u}^S vectors at 16 days. Linear. East wind.	199
5.32b \tilde{u}^1 vectors at 16 days. Linear. East wind.	200
5.32c h contours at 16 days. Linear. East wind.	201
5.33a \tilde{u}^S vectors at 40 days. Linear. East wind.	202
5.33b \tilde{u}^1 vectors at 40 days. Linear. East wind.	203
5.33c h contours at 40 days. Linear. East wind.	204
5.33d \tilde{u} vectors at 40 days. Linear. East wind.	205

	<u>page</u>
5.34a h contours at 200 days. Linear. East wind.	206
5.34b \bar{u} vectors at 200 days. Linear. \sim East wind.	207
5.35a u^S vectors at 397 days. Linear. \sim East wind.	208
5.35b u^1 vectors at 397 days. Linear. \sim East wind.	209
5.35c h contours at 397 days. Linear. East wind.	210
5.35d \bar{u} vectors at 397 days. Linear. \sim East wind.	211
5.36 Energies from 15°S to 15°N. Nonlinear. East wind.	216
5.37 Energies from 5.6°S to 5.6°N. Nonlinear. East wind.	217
5.38 Sections of h along the equator to day 40. Nonlinear. East wind.	219
5.39 Sections of h along the equator to day 398. Nonlinear. East wind.	220
5.40 Sections of \bar{u} along the equator to day 40. Nonlinear. East wind.	222
5.41 Sections of \bar{u} along the equator to day 398. Nonlinear. East wind.	223
5.42a Meridional sections of h to day 398 at $x=25.4^\circ$. Nonlinear. East wind.	225
5.42b Meridional sections of h to day 398 at $x=14.3^\circ$. Nonlinear. East wind.	226
5.42c Meridional sections of h to day 398 at $x=3.2^\circ$. Nonlinear. East wind.	227
5.43 Meridional sections of \bar{u} to day 40 at $x=14.3^\circ$. Nonlinear. East wind.	229

	<u>page</u>
5.44 Meridional sections of \bar{u} to day 398 at $x=14.3^\circ$. Nonlinear. East wind.	230
5.45a \tilde{u}^S vectors at 16 days. Nonlinear. East wind.	231
5.45b \tilde{u}^1 vectors at 16 days. Nonlinear. East wind.	232
5.45c h contours at 16 days. Nonlinear. East wind.	233
5.46a \tilde{u}^S vectors at 40 days. Nonlinear. East wind.	235
5.46b \tilde{u}^1 vectors at 40 days. Nonlinear. East wind.	236
5.46c h contours at 40 days. Nonlinear. East wind.	237
5.46d \tilde{u} vectors at 40 days. Nonlinear. East wind.	238
5.47a \tilde{u}^S vectors at 400 days. Nonlinear. East wind.	239
5.47b \tilde{u}^1 vectors at 400 days. Nonlinear. East wind.	240
5.47c h contours at 400 days. Nonlinear. East wind.	241
5.47d \tilde{u} vectors at 400 days. Nonlinear. East wind.	242
5.48 Energies from 15°S to 15°N . Nonlinear. West wind.	252
5.49 Energies from 5.6°S to 5.6°N . Nonlinear. West wind.	253
5.50 Sections of h along the equator to day 40. Nonlinear. West wind.	255
5.51 Sections of h along the equator to day 398. Nonlinear. West wind.	256

	<u>page</u>
5.52 Sections of \bar{u} along the equator to day 40. Nonlinear. West wind.	257
5.53 Sections of \bar{u} along the equator to day 398. Nonlinear. West wind.	258
5.54a Meridional sections of h to day 398 at $x=25.4^\circ$. Nonlinear. West wind.	260
5.54b Meridional sections of h to day 398 at $x=14.3^\circ$. Nonlinear. West wind.	261
5.54c Meridional sections of h to day 398 at $x=3.2^\circ$. Nonlinear. West wind.	262
5.55 Meridional sections of \bar{u} to day 40 at $x=14.3^\circ$. Nonlinear. West wind.	263
5.56 Meridional sections of \bar{u} to day 398 at $x=14.3^\circ$. Nonlinear. West wind.	264
5.57a \tilde{u}^S vectors at 16 days. Nonlinear. West wind.	266
5.57b \tilde{u}^1 vectors at 16 days. Nonlinear. West wind.	267
5.57c h contours at 16 days. Nonlinear. West wind.	268
5.58 \tilde{u} vectors at 40 days. Nonlinear. West wind.	270
5.59a \tilde{u}^S vectors at 398 days. Nonlinear. West wind.	271
5.59b \tilde{u}^1 vectors at 398 days. Nonlinear. West wind.	272
5.59c h contours at 398 days. Nonlinear. West wind.	273
5.59d \tilde{u} vectors at 398 days. Nonlinear. West wind.	274
5.60 Energies from $15^\circ S$ to $15^\circ N$. Nonlinear. Southeast wind.	277

	<u>page</u>
5.61 Energies from 5.6°S to 5.6°N. Nonlinear. Southeast wind.	278
5.62 u^1 contours at the equator to day 398. Nonlinear. Southeast wind.	279
5.63a u^S vectors at 16 days. Nonlinear. \sim Southeast wind.	281
5.63b u^1 vectors at 16 days. Nonlinear. \sim Southeast wind.	282
5.63c \bar{u} vectors at 16 days. Nonlinear. Southeast wind.	283
5.64a u^S vectors at 40 days. Nonlinear. \sim Southeast wind.	284
5.64b u^1 vectors at 40 days. Nonlinear. \sim Southeast wind.	285
5.64c h contours at 40 days. Nonlinear. Southeast wind.	286
5.65a u^S vectors at 398 days. Nonlinear. \sim Southeast wind.	288
5.65b u^1 vectors at 398 days. Nonlinear. \sim Southeast wind.	289
5.65c h contours at 398 days. Nonlinear. Southeast wind.	290
5.66a \bar{u} contours at 398 days. Nonlinear. Southeast wind.	291
5.66b \bar{v} contours at 398 days. Nonlinear. Southeast wind.	292
5.67 Meridional sections of \bar{u} to day 398 at $x=14.3^\circ$. Nonlinear. Southeast wind.	295
5.68a Meridional sections of h to day 398 at $x=25.4^\circ$. Nonlinear. Southeast wind.	296

page

- 5.68b Meridional sections of h to day 398
at $x=14.3^\circ$. Nonlinear. Southeast
wind.
- 5.68c Meridional sections of h to day 398
at $x=3.2^\circ$. Nonlinear. Southeast
wind.

297

298

1. Introduction

Since the vertical component of the Coriolis force vanishes at the equator, the geostrophic balances which dominate the dynamics of the extra-equatorial oceans must break down. The most striking physical manifestation of this singularly is the Equatorial Undercurrent, a narrow (half width of 1°), fast (speeds up to 170 cm/ sec), eastward flowing subsurface current in the thermocline of all the world's oceans. (While it is a permanent feature in the Atlantic and Pacific at most longitudes, it has been observed only intermittently in the Indian Ocean.) Many of the characteristics of the undercurrent are highly variable: e.g., the downstream velocities and transports may vary by a factor of two or more at different longitudes or at different times. Available observational data allows many of these variations to be related systematically to variations in the winds over the equatorial ocean. However, the evidence is, in general, too spotty to allow such correlations to be conclusive. Philander (1973b) presents a thorough review of the measurements of the undercurrent made up to 1973. An important series of measurements of the undercurrents in the Atlantic was made during the GATE experiment in the summer of 1974. (Preliminary results are available in Düing et.al., 1975). The most important finding was a meandering of the undercurrent core between 1°S and 1°N at all observed longitudes between July 26 and August 19. The period of these meanders was about 18 days.

A second important consequence of the vanishing of the

Coriolis term is that equatorial motions have time scales which are very much shorter than those of midlatitude motions: the baroclinic time scale is weeks at the equator, as against years at mid-latitudes. The most impressive instance of this short time scale is the reversal in direction of the Somali Current within a month of the onset of the Southwest Monsoon (e.g., Leetmaa 1973). In general, time dependent oceanic motions with time scales longer than a few days have received relatively little attention. Equatorial regions are rewarding areas for the study of such time variations because of the rapidity of the ocean's response to atmospheric forcings. The Indian Ocean is particularly favorable because, while the wind systems over the Atlantic and Pacific Oceans have monsoonal components, the monsoon regime is predominant over the Indian Ocean. The winds there reverse direction completely twice a year and the currents are known to vary greatly. Nevertheless, there have been few theoretical studies of time dependent phenomena in equatorial oceans. Cox (1970) and Lighthill (1969) investigated the setup of the Somali Current in response to the onset of the Southwest Monsoon. On the basis of a numerical simulation, Cox concluded that the Somali Current began to flow northward in response to the local winds along the African coast. Lighthill's analytic model suggested that the propagation of signals from the interior of the ocean could be the causal mechanism. Gill (1972) applied a Lighthill-like model to the undercurrent in the western Pacific. He associated the undercurrent with the second baroclinic mode

Kelvin wave which propagates in from the western boundary. It is not clear how such a model explains the presence of the undercurrent as a more permanent feature.

In contrast to the situation for time varying equatorial currents, numerous theoretical models for the steady state undercurrent appear in the literature. These have recently been reviewed by both Gill (1972) and Philander (1973b). For this reason we shall forego a detailed review here; rather, we shall discuss them only to the extent needed to establish a theoretical context for the present work. On the basis of his observations in the Pacific, Knauss (1966) estimated that the only negligible terms in the momentum equation were those giving the time rate of change of momentum and the horizontal component of the Coriolis force due to vertical motion. (He did not consider horizontal eddy diffusion processes.) The upshot is that a great variety of processes are available to be used as explanations for the undercurrent. Since there is a certain amount of freedom in the choice of eddy coefficients, all of these can be expected to give agreement with at least some of the observed scales. In what follows, we seek to isolate those processes which are most significant.

We shall immediately restrict ourselves to those models which idealize the thermocline as a discontinuity between a shallow upper homogeneous layer and a deeper lower homogeneous layer of greater density. The lower layer is assumed to be so deep that its horizontal pressure forces and velocities vanish. As shown by Charney (1955) the upper layer of such a model is

equivalent to a single layer homogeneous ocean with the force of gravity reduced by a factor $\Delta\rho/\rho$, the relative density difference between the two layers. Models with thermohaline components (Robinson 1960, Philander 1972, 1973a) are required to explain certain effects at depth; for example, the double celled structure often observed in the Pacific (see Philander 1973b). Homogeneous models appear to be sufficient for explaining observed features above the thermocline.

The most basic physical notion about the undercurrent is the idea of flow down a pressure gradient (Charney 1960). The prevailing easterly winds pile up water at the western side of the ocean basin, thus establishing an eastward pressure gradient. Stommel (1960) exploited this idea to obtain an eastward flowing subsurface current in a linear model with vertical friction. He assumed free slip boundary condition at the bottom and that the vertically integrated transport vanishes at the equator. In a similar model without the latter two assumptions, Charney (1960) and Philander (1971) found that the current at the equator did not reverse with depth. In any case, one would wish any theory to account for the substantial eastward transports observed at the equator. In the linear theory of Gill (1971), the pressure gradient force is balanced by the horizontal mixing of momentum. By using an unrealistically large value for the coefficient of horizontal eddy viscosity ($10^8 \text{ cm}^2 \text{ sec}^{-1}$), Gill obtains the observed latitudinal scale for the undercurrent, but the transport is too low by a factor of at least four.

Nonlinear theories have ignored the downstream inertial terms. The (suspect) assumption is made that the zonal and meridional velocities have the same scale. Then, since the meridional length scale (an equatorial boundary layer scale) is so much shorter than the zonal one (the length of the basin), it follows that in the momentum equation the downstream inertial term is negligible relative to the cross-stream inertial term. Attention is then directed to the meridional circulation. For an easterly wind, the Ekman drift in the surface layers will be poleward. Continuity then requires a compensatory equatorward mass flux at depth, producing an upwelling region at the equator to complete the fluid circuit. Fofonoff and Montgomery (1955) considered the subsurface flow in the light of the barotropic vorticity equation. If it is assumed that a parcel approximately conserves the vertical component of its absolute vorticity, it must change its relative vorticity to make up for the loss of planetary vorticity as it moves equatorward. This results in an eastward flow at the equator. It may also be shown that the meridional circulation near the equator enhances the eastward transport at the equator regardless of whether the wind is easterly or westerly. (See Robinson (1966) for an analytic demonstration; Gill (1972) gives a more physical argument.)

The models of Charney (1960), Charney and Spiegel (1971), Robinson (1966), and McKee (1973) all incorporate the nonlinear effects due to the circulation in the meridional plane. The first three include momentum mixing in only the

vertical direction. McKee's model is an extension of Gill's (1971) model into the non-linear regime; horizontal eddy viscosity is the important frictional force here. A more realistic value for the zonal velocity is obtained, compared to the linear model, but an unreasonably large value for the eddy coefficient is again used ($10^8 \text{ cm}^2 \text{ sec}^{-1}$) to obtain the observed undercurrent width. The models of Charney (1960) and Charney and Spiegel (1971) (the first calculates the flow only at the equator by assuming it is an axis of symmetry; the second paper extends the first model to a meridional plane) give the observed undercurrent velocity and width using a value for the vertical eddy viscosity coefficient ($15 \text{ cm}^2 \text{ sec}^{-1}$) in agreement with existing observational evidence (see Section 2.2). This model also gives good agreement with the observed vertical profile of the undercurrent. Vertical viscosity must be of some importance at depth in order to obtain a non-constant profile below the boundary layer. Most importantly, a mechanism for the vertical exchange of momentum is needed to introduce the wind stress into the water. There is no similar logical necessity for introducing a significant amount of horizontal mixing. Further, there is no evidence that modeling such mixing gives better agreement with observations.

Previous work thus shows that it is necessary to consider vertical eddy viscosity and inertial effects but not lateral eddy viscosity in order to model the undercurrent effectively. As noted above, all of these models neglect any variation in the zonal direction (except that the zonal

pressure gradient is taken as constant). This makes it impossible to ask a number of interesting questions; for example, one cannot investigate the undercurrent meanders observed during GATE. More generally, the issue of the relation of the undercurrent to the entire equatorial current system cannot be explored without considering the whole ocean basin. Since there is a substantial eastward transport at the equator, there must be compensating westward flow elsewhere in the ocean basin. Further, many time varying effects are inseparable from zonal variations. For example, the length of time it takes for the sea surface to set up from rest in response to a wind stress is determined by the speed of waves which propagate in from the boundaries of the basin.

In order to investigate questions of this sort, our model will be time dependent and two dimensional in the horizontal. Since the phenomena of interest are confined to an area near the equator, the basin need not have a great latitudinal extent; 15°S to 15°N has proven to be sufficient. The model equations are solved numerically because it is imperative that they be fully nonlinear. A stretched coordinate system is used so as to give greater resolution near the equator where smaller scales of motion demand higher resolution.

In order to make it practical to perform many numerical integrations, the vertical structure is drastically simplified. It consists of two layers above the thermocline with the same constant density. The ocean below the thermocline is taken to

be of a higher constant density and to be approximately at rest. The upper of the two active layers is a constant depth surface layer which is acted upon directly by the wind stress. The lower active layer is not directly affected by the wind. Its depth is variable, with the variations being dynamically determined. The two layers communicated via the vertical velocity at their interface as well as being frictionally coupled. This is the simplest vertical structure which will give an undercurrent.

Of course, this simplification prevents the simulation of the detailed vertical structure of the undercurrent. It is not our intention to do such numerical simulations. Previous work (especially Charney and Spiegel 1971) provides a bridge for relating the results of our simple model to the real world. Our philosophy is to treat the numerical experiments reported here in the manner of laboratory experiments. We do not seek to simulate the real world; we seek merely to preserve enough analogy to the real world for the results to give insight into natural phenomena.

There are a large number of phenomena which may be investigated with such a model. In the present study we impose very simple wind stress patterns and study the evolution from a state of rest and eventual steady state configuration of the model ocean. To aid in the interpretation of the numerical experiments, some analytic models are developed. These provide a descriptive vocabulary as well as checks on the numerical results.

2. Formulation of the Physical Model

In this section the equations for the simplest vertical structure which will give an undercurrent are derived, and in the following section the values of the parameters to be used in the numerical experiments are chosen.

2.1 Model Equations

Since we are concerned with the inertial and viscous dynamics of a wind-driven ocean, thermohaline effects will be ignored. We divide the ocean vertically into N stable material layers which are assumed to be non-mixing (Fig. 2.1). For any quantity q the average over the j th layer is defined as:

$$\bar{q}^j(x, y) = \frac{1}{h_j(x, y)} \int_{z_j(x, y)}^{z_{j-1}(x, y)} q dz \quad ; \quad h_j = z_{j-1} - z_j$$

Then the equations of motion become, in standard notation,

$$\begin{aligned} \frac{\partial (h_j \bar{u}^j)}{\partial t} + \nabla \cdot (h_j \bar{u} \bar{u}^j) + f \hat{k} \times h_j \bar{u}^j &= -h_j \nabla P_j + \bar{z}_{j-1} - \bar{z}_j + h_j \nu \nabla^2 \bar{u}^j \\ \frac{\partial h_j}{\partial t} + \nabla \cdot (h_j \bar{u}^j) &= 0 \end{aligned} \quad (2.1)$$

The horizontal component of the Coriolis force due to the vertical motion has been omitted; it may be shown negligible a posteriori (sufficient conditions are given by a scaling argument). The vertical component due to horizontal motion is also ignored; the pressure is then given hydrostatically. Assuming a constant surface pressure and a flat bottom (as is

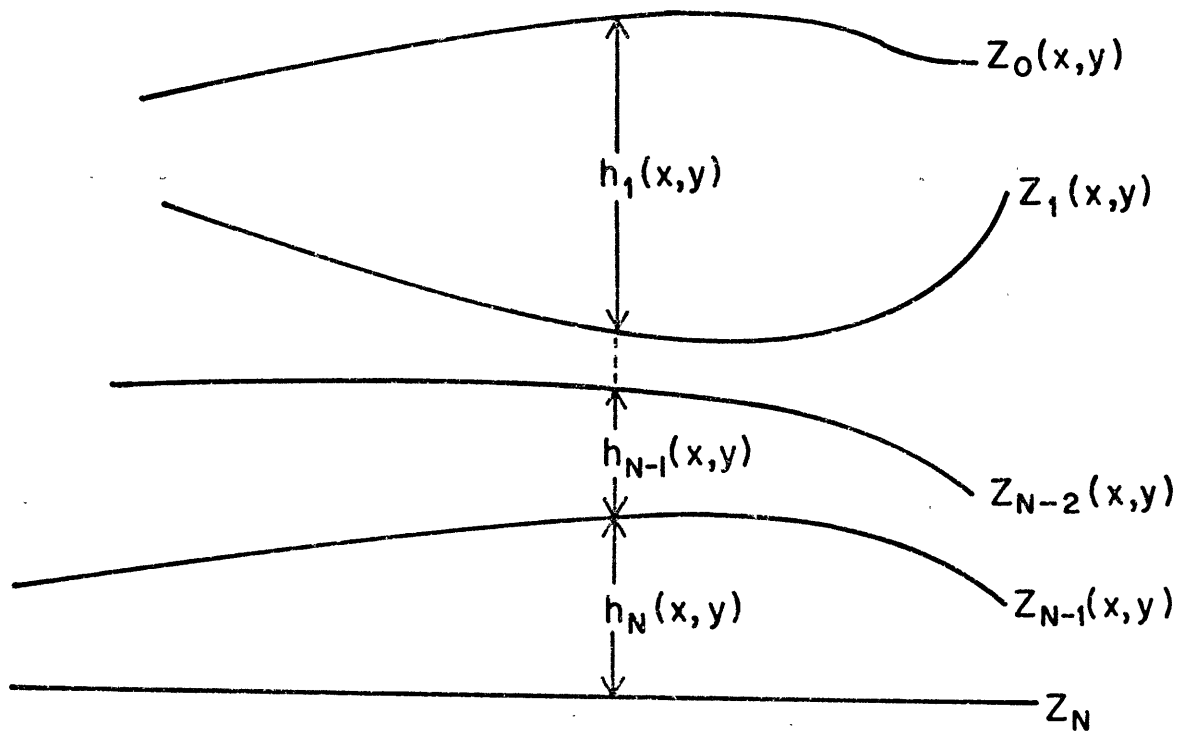


Fig. 2.1 Multi-layer model

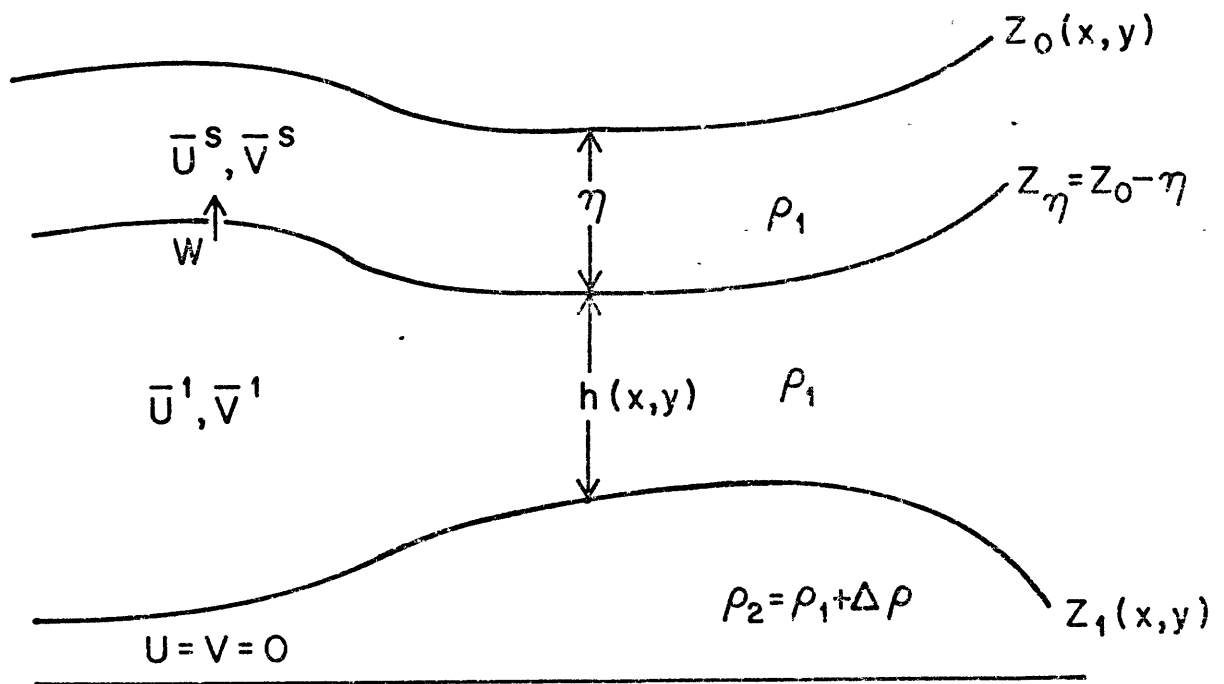


Fig. 2.2 Model with two active layers.

sufficient for our purposes) we may write:

$$P_j = g/\rho_j \sum_{i=1}^N \rho_{min(i,j)} h_i \quad (2.2)$$

The viscosity in the model is considered to be due to turbulent eddy processes, with different horizontal and vertical structure but isotropic in the horizontal. Following Kamenkovich (1967) and Kirwan (1969) the operator F_H , which gives the horizontal eddy viscous terms is written in a vector invariant form. Details may be found in Appendix A. The horizontal stress term at the surface, τ_0 is taken to match the wind stress; otherwise τ_j is the frictional stress at the interface between layers. It is modelled in the form:

$$\tau_j = K (\bar{u}^j - \bar{u}^{j+1})$$

Since $\tau_j \equiv (v \cdot u)_{z=z_j}$, a heuristic argument suggests that $K \approx v_v/H^*$, where H^* is a characteristic layer depth.

The usual finite-difference assumptions that the layers may be treated as homogeneous are made:

$$\nabla \cdot (h_j \bar{u}^j) \approx \nabla \cdot (h_j \bar{u}^j \bar{u}^j); \quad \overline{F_H(u)} \approx F_H(\bar{u}^j) \quad (2.3)$$

We now identify the bottom layer with the water mass below the thermocline and regard it as being sufficiently deep so that its velocity vanishes. Equatorial regions are a favorable environment for this approximation: the thermocline is shallow (150 - 200 m), the wind stress projects about twenty times more strongly on the first baroclinic mode than it does on the barotropic mode (Lighthill, 1969), and, unlike midlatitudes

(Veronis and Stommel, 1956), the baroclinic signals are only about one order of magnitude slower than the barotropic. Observational evidence also tends to support the validity of this approximation (see Philander, 1973 for a summary).

Since the velocities in the lowest layer vanish, the pressure gradient must vanish there as well¹. This allows h_N to be eliminated in (2.2). For a single layer the equations become:

$$\frac{\partial \underline{u}}{\partial t} + (\underline{u} \cdot \nabla) \underline{u} + f \hat{k} \times \underline{u} = -g' \nabla h + \frac{\hat{\tau}_0 - K \underline{u}}{h} + \nu_H \nabla^2 (\underline{u})$$

$$\frac{\partial h}{\partial t} + \nabla \cdot (h \underline{u}) = 0 \quad (2.4)$$

where

$$g' = g \left(\frac{\rho_2 - \rho_1}{\rho_2} \right)$$

In (2.4) the wind stress appears as a body force. This is a commonly used modelling procedure in oceanography; for many purposes it can be rigorously justified (e.g. Charney 1955). For some purposes, such as modelling the undercurrent, a difficulty is created by introducing the wind stress as a body force averaged over the uppermost layer. Consider a curl-free wind stress vector introduced in this manner. It may be

¹ In order to deduce that $\nabla \cdot P_N = 0$ from the lowest layer momentum equation ((2.1) for $j = N$), we must neglect the stress term $\tau_{N-1} = K u^{N-1}$ that appears there. This term is quite small. If it were not neglected and h_N is eliminated, it would appear in the momentum equation for each layer. We feel that our modelling of the stress due to turbulent mixing is too crude to justify complicating the equations by retaining this small term.

balanced by the gradient of the height field, allowing the velocities to be identically zero (as is consistent with the Sverdup relation). Note that such a solution is a solution to the full non-linear equations. Similar no-motion solutions can easily be found for a multi-layer model whether or not the bottom layer is constrained to be motionless: the layer depths may always adjust to reduce the pressure gradient to zero in each subsurface layer.

For example, consider a constant easterly wind stress (of magnitude τ per unit mass) applied to a model ocean with one active layer. The steady state solution to (2.4) is

$$\underline{u} \equiv 0 ; \quad h = [h_0^2 + \chi \tau / g']^{1/2} \quad (2.5)$$

The wind stress is balanced by the zonal pressure gradient. In reality this pressure gradient is sufficient to drive the equatorial undercurrent because the fluid at depth feels the pressure force but not the wind stress (Charney 1960; Gill 1971). Obviously the layered models miss this effect.

We wish to emphasize that such models are not wrong in some simple sense. In fact, the profile of the thermocline depth specified by (2.5) is very close to what is observed at the equator (cf. Gill 1972, Fig. 3). The difficulty is that the feature of interest is missed by the layered models because they consider only the depth averaged currents within each layer. A correct treatment of the wind stress would introduce it as a boundary condition e.g. $\nu \frac{\partial u}{\partial z} = \tau_{\text{wind}}$ at the surface. This guarantees that with a non-zero wind stress there is no

solution where the velocities vanish at all depths. The vertically averaged velocities may vanish. For the example discussed above, this could come about at the equator if the surface flow driven westward by the wind stress were just compensated by the flow at depth driven eastward by the pressure force. (In reality, inertial effects give a net eastward transport at the equator.) This is precisely the mechanism for generating an undercurrent referred to above. To capture this essential mechanism we modify the model with a single active layer. This upper layer is divided into two parts: a surface layer of constant depth η and a lower layer of variable depth h (Fig. 2.2). There is no density difference between these two layers and transfer of mass and momentum between the two is permitted. The wind stress is felt directly only by the surface layer. This is the simplest vertical structure which will give a steady state undercurrent.

Denoting the average of a quantity q over the upper layer by \bar{q}^s and over the lower by \bar{q}^l define:

$$\bar{w} = \kappa \nabla \cdot \bar{u}^s$$

then

$$\bar{w} = w(z_\eta) - \frac{dz_\eta}{dt}$$

where z_η is the height of the interface between the two active layers (Fig. 2.2). This says that the suction into (or pumping out of) the surface layer is the vertical velocity at the interface less the change in the interface height. Making

assumptions (2.3) about the averages of nonlinear terms we obtain:

$$\begin{aligned} \frac{\partial \bar{u}^s}{\partial t} + (\bar{u}^s \cdot \nabla) \bar{u}^s + \frac{\bar{w}}{\eta} (\bar{u}^s - \underline{u}(z_\eta)) + f \hat{k} \times \bar{u}^s = \\ - g' \nabla h + \frac{\bar{\tau}_0}{\eta} + \frac{K}{\eta} (\bar{u}^L - \bar{u}^s) + \nu_H \bar{E}_H(\bar{u}^s) \\ \frac{\partial \bar{u}^L}{\partial t} + (\bar{u}^L \cdot \nabla) \bar{u}^L + \frac{\bar{w}}{h} (\underline{u}(z_\eta) - \bar{u}^L) + f \hat{k} \times \bar{u}^L = \\ - g' \nabla h - \frac{K_B}{h} \bar{u}^L - \frac{K}{h} (\bar{u}^L - \bar{u}^s) + \nu_H \bar{E}_H(\bar{u}^L) \\ \frac{\partial h}{\partial t} + \nabla \cdot (h \bar{u}^L) + \bar{w} = 0 \end{aligned} \quad (2.6)$$

(K_B is a bottom friction parameter usually taken equal to K).

To avoid spurious sources or sinks of energy $\underline{u}(z_\eta)$ must be given by:

$$\underline{u}(z_\eta) = \frac{1}{2} (\bar{u}^s + \bar{u}^L)$$

which is consistent with the notion that \underline{u} varies more rapidly within the boundary layer. The energy equation for this system is then:

$$\begin{aligned} \frac{\partial}{\partial t} (KE_s + KE_L + PE) = \iint dA \{ \bar{u}^s \cdot \bar{\tau}_0 - K (\bar{u}^s - \bar{u}^L)^2 \\ - K_B \bar{u}^L \cdot \bar{u}^L + \nu_H [\eta \bar{u}^s \cdot \bar{E}_H(\bar{u}^s) + h \bar{u}^L \cdot \bar{E}_H(\bar{u}^L)] \} \end{aligned}$$

$$KE_1 = \iint h \bar{u}^2 \cdot \bar{u}^2 dA \quad KE_3 = \iint \eta \bar{u}^3 \cdot \bar{u}^3 dA$$

$$PE = \iint \frac{1}{2} g' (h - \bar{H}_k)^2 dA \quad \bar{H}_1 = \iint h dA / \iint dA$$

Next, Eqs. (2.6) are non-dimensionalized. Since a variety of phenomena with different scales will occur within the model basin there is no single consistent scaling. The non-dimensionalization used is given in Table 1, together with the dimensionless parameters it introduces and the numerical values used in the model runs.

One final consideration brings the equations into their final form. In order to facilitate the introduction of variable mesh spacing, general orthogonal coordinates are introduced. Let the coordinates in physical space be (x^*, y^*) and the grid coordinates in the "computational space" be (x, y) . That is, there will be equally spaced intervals $(\Delta x, \Delta y)$ in (x, y) .

Define:

$$m_x = \frac{\partial x^*}{\partial x}, \quad m_y = \frac{\partial y^*}{\partial y} \quad (2.7)$$

$$m_{xy} = \frac{1}{m_x m_y} \frac{\partial m_x}{\partial y} \quad m_{yx} = \frac{1}{m_x m_y} \frac{\partial m_y}{\partial x}$$

then with some obvious changes in notation and with:

$$\underline{u} \equiv (u, v)$$

$$(\underline{u} \cdot \nabla) \equiv \frac{u}{m_x} \frac{\partial}{\partial x} + \frac{v}{m_y} \frac{\partial}{\partial y}$$

$$\nabla \cdot \underline{u} \equiv \frac{1}{m_x} \frac{\partial u}{\partial x} + \frac{1}{m_y} \frac{\partial v}{\partial y} + m_{yx} u + m_{xy} v$$

and f_{nd} as the non-dimensional Coriolis parameter, the equations are:

$$w = \eta \nabla \cdot \underline{u}$$

$$\begin{aligned} \frac{\partial u^s}{\partial t} = & -R_o (\underline{u}^s \cdot \nabla) u^s + v^s [f_{nd} + R_o (m_{yx} v^s - m_{xy} u^s)] \\ & - \frac{w}{2\eta} (u^s - u^t) - F_r^{-1} \frac{R_o}{m_x} \frac{\partial h}{\partial x} + \frac{T \hat{c}^{(s)}}{\eta} - \frac{B}{\eta} (u^s - u^t) + E_H F_H^{(s)}(u^s) \end{aligned}$$

$$\begin{aligned} \frac{\partial v^s}{\partial t} = & -R_o (\underline{u}^s \cdot \nabla) v^s - u^s [f_{nd} + R_o (m_{yx} v^s - m_{xy} u^s)] \\ & - \frac{w}{2\eta} (u^s - u^t) - F_r^{-1} \frac{R_o}{m_y} \frac{\partial h}{\partial y} + \frac{T \hat{c}^{(s)}}{\eta} - \frac{B}{\eta} (v^s - v^t) + E_H F_H^{(s)}(u^s) \end{aligned}$$

(2.8)

$$\begin{aligned} \frac{\partial u^t}{\partial t} = & -R_o (\underline{u}^t \cdot \nabla) u^t + v^t [f_{nd} + R_o (m_{yx} v^t - m_{xy} u^t)] \\ & - \frac{w}{2h} (u^s - u^t) - F_r^{-1} \frac{R_o}{m_x} \frac{\partial h}{\partial x} + \frac{B}{h} (u^s - u^t) - \frac{B_B}{h} u^t + E_H F_H^{(t)}(u^t) \end{aligned}$$

$$\begin{aligned} \frac{\partial v^t}{\partial t} = & -R_o (\underline{u}^t \cdot \nabla) v^t - u^t [f_{nd} + R_o (m_{yx} v^t - m_{xy} u^t)] \\ & - \frac{w}{2h} (v^s - v^t) - F_r^{-1} \frac{R_o}{m_y} \frac{\partial h}{\partial y} + \frac{B}{h} (v^s - v^t) - \frac{B_B}{h} v^t + E_H F_H^{(t)}(u^t) \end{aligned}$$

$$\frac{\partial h}{\partial t} = -R_o \nabla \cdot (h \underline{u}^t) - w$$

We consider three possible sets of boundary conditions for this set of equations:

$$u = v = 0 \quad \text{at all lateral boundaries} \quad (2.9a)$$

$$\begin{aligned} u = v = 0 & \quad \text{at meridional boundaries;} \\ v = \frac{\partial u}{\partial y} = 0 & \quad \text{at zonal boundaries} \end{aligned} \quad (2.9b)$$

$$\begin{aligned} u = 0 & \quad \text{at meridional boundaries} \\ v = 0 & \quad \text{at zonal boundaries} \end{aligned} \quad (2.9c)$$

We generally use (2.9a). Eq. (2.9b) is based on the notion that the northern and southern boundaries are artificial; (2.9c) is consistent with taking the horizontal eddy viscosity to be zero. In all cases, there is no special boundary treatment of the layer depth; the boundary is computed from the last of Eqs. (2.8).

Written in this way the equations allow treatment of a variety of geometries. It would be straightforward to treat spherical coordinates or a basin whose boundaries are not perpendicular to the equator. In the present investigation, however, we restrict ourselves to a rectangular basin on an equatorial beta plane (e.g., Veronis 1963a, b). Since the meridional extent of the basin will generally be 15° of latitude on either side of the equator, the beta plane is an excellent approximation. As noted in Appendix A, with this

coordinate system we may approximate the horizontal viscosity F_H by the usual horizontal Laplacian of the velocity components. The coordinate stretching is independent of the perpendicular direction: i.e.,

$$f_{nd} = y^*, \quad \frac{\partial x^*}{\partial y} = \frac{\partial y^*}{\partial x} = 0$$

In this case, $m_{xy} = m_{yx} = 0$ which simplifies the equations considerably.

2.2 Choice of Parameter Values

The values for the model parameters given in Table 1 are intended to be a "standard" set for all the model runs. Deviation from these values will be noted where appropriate. The standard value for the wind stress ($.47 \text{ gm cm}^{-1} \text{ sec}^{-2}$) is approximately the mean value over the equatorial oceans. The relative density step $\Delta\rho/\rho$ between the active layer and the layer of no motion below it is taken as .002. This is a representative value for the density step across the thermocline in equatorial waters.

Vertical eddy viscosity is to be the principal dissipative mechanism in the model. The argument which follows (2.3) related the coefficient of interfacial friction K to the vertical eddy viscosity ν_v by

$$K = \nu_v / H^*$$

where H^* is a characteristic vertical distance between fluid elements in the active layer. H^* is taken to be 100 m. -- one

Table 1 Non-dimensionalization (primes on dimensional quantities)

$$t' = (2\Omega)^{-1} t$$

$$(2\Omega)^{-1} = (4\pi)^{-1} \text{days} \approx 1.9 \text{ hrs.}$$

$$u' = U u$$

$$U = 1 \text{ m sec}^{-1}$$

$$(h', n') = H(h, n)$$

$$H = 100 \text{ m}$$

$$(x', y') = L(x, y)$$

$$L = 6367 \text{ Km} = \text{radius of the earth}$$

$$\tilde{\tau}' = \tilde{J} \tilde{\tau}$$

$$\tilde{J} = .465 \text{ dyn cm}^{-2} / (\text{gm cm}^{-3})$$

$$w' = (2\Omega H) w$$

$$= U(H/L) R_0^{-1} w = 1.46 \text{ cm sec}^{-1} w$$

Dimensionless numbers:

$$R_0 = U / (2\Omega L)$$

$$= 1.077 \cdot 10^{-3}$$

$$F_r^{-1} = g \frac{\rho_2 - \rho_1}{\rho_2} H / U^2$$

$$= 1.724 \quad \text{for } \frac{\Delta\rho}{\rho} = 1.86 \cdot 10^{-2}$$

$$T = \tilde{J} / (2\Omega H U)$$

$$= 3.095 \cdot 10^{-3}$$

$$B = K / (2\Omega H)$$

$$= 10^{-3} \left. \begin{array}{l} \text{for } K = K_B = \nu_v / H^* \text{ with} \\ \nu_v = 15 \text{ cm}^2 \text{ sec}^{-1} \quad H^* = 100 \text{ m} \end{array} \right\}$$

$$B_B = K_B / (2\Omega H)$$

$$= 10^{-3} \left. \begin{array}{l} \nu_v = 15 \text{ cm}^2 \text{ sec}^{-1} \quad H^* = 100 \text{ m} \end{array} \right\}$$

$$E_H = \nu_H / (2\Omega L^2)$$

$$= 10^{-8} \quad \text{for } \nu_H = 5.86 \cdot 10^5 \text{ cm}^2 \text{ sec}^{-1}$$

Other parameters: (dimensional values in parentheses)

$$\Delta t = .5 \text{ (.95 hrs)}$$

timestep

$$n = .25 \text{ (25 m)}$$

depth of the surface layer

$$\bar{H}_1 = 1.75 \text{ (175 m)}$$

depth of the lower active layer

$$\Theta_T = -\Theta_B = 15^\circ$$

basin walls are at 15°S and 15°N

$$X_L = 28.6^\circ \text{ (3184 Km)}$$

zonal extent of the basin

half the depth of the active layer.

The same value of H^* is used to determine the bottom friction parameter K_B . This is at once the most reasonable and the simplest choice. It remains to choose the coefficient of vertical eddy viscosity ν_v . In the interest of simplicity, we take our standard value to be independent of depth; hence $K_B = K$. Robinson (1966) used a value of $10^4 \text{ cm}^2/\text{sec}$, which he found by identifying the Ekman depth with the extra-equatorial mixed layer depth. This identification is surely incorrect and the value much too large. Knauss (1966) calculated a value of $5 \text{ cm}^2 \text{ sec}^{-1}$ by fitting a parabola to the velocity profile of the undercurrent observed in the Pacific. Williams and Gibson (1974) applied universal similarity and local isotropy assumptions to measurements of small scale temperature fluctuation at 150°W and a depth of 100 m. They found values of ν_v of 25 cm sec^{-1} at the equator and 12 cm sec^{-1} at 1°N . Charney (1960) and Charney and Spiegel (1971) found that their models best fit the observed undercurrent for a value of the eddy viscosity in the range $14\text{-}17 \text{ cm}^2 \text{ sec}^{-1}$. These models give eastward flow at the surface in the face of an east wind but this may, in fact, be a realistic feature. Not only has such a situation been observed (at 150°W by Taft, et. al., 1974), but our calculations indicate that the addition of a northward component to the wind stress (as is generally present in the real oceans) gives eastward surface flow at the equator in conformity with more typical observations. In the light of all of this evidence, we use $15 \text{ cm}^2 \text{ sec}^{-1}$ as a

standard value for ν_v , feeling some confidence in (at least) the order of magnitude of the choice.

It is essential to postulate some vertical mixing in order to have a physical mechanism by which the wind drives the ocean circulation. There is no similar necessity for including a horizontal mixing of momentum. Further, there is very little basis for assigning a numerical value to the coefficient of horizontal eddy viscosity. (Even the form that we use for the functional is justified primarily by simplicity and tradition.) For these reasons we wish to use a value of the horizontal eddy coefficient that is small enough to have no significant effect on the equatorial dynamics. Two considerations prevent us from simply taking this coefficient to be zero, the first numerical and the second physical.

It is well known that numerical calculations of geophysical flows often exhibit spurious short wavelength computational modes (e.g., two grid point waves or "checkerboard" patterns; see, for example, Messinger, 1972). These not only destroy the accuracy of the calculation but may contribute to so-called nonlinear computational instabilities. Some mechanism is required to suppress their growth: either a smoothing operation of some kind which redistributes their energy to longer wavelength components, or a dissipative operator which acts to damp them. Energy conserving difference schemes (e.g., Arakawa, 1966), as well as the special treatment of the gravity wave terms used in our model (see Section B.5) are examples of smoothing devices, albeit implicit ones. Our "momentum

waves" (Section B.5) are a more explicit smoothing device. Dissipative mechanisms have a physical basis: a horizontal eddy viscosity is a parameterization of processes at scales too small to be resolved by the grid point computation. As a matter of taste, we prefer to rely on the well studied, physically motivated, viscous damping rather than computational devices whose effects are less well known. For this form of viscosity the amount of damping of the shortest waves the grid will resolve depends on a Reynolds number based on the physical distance between grid points. For an unequally spaced grid the largest grid spacing will determine the viscosity needed. For the grid that is used sole reliance on such a mechanism demands a viscosity large enough to have a significant effect on the flow near the equator, the region of primary interest in this work. However, the local grid spacing there allows a viscosity an order of magnitude smaller. It was determined by experimentation that the value in Table 1 is large enough to dominate the effects of "computational viscosity" near the equator where the grid is closely spaced though the latter may be the more important mechanism where the grid is coarse.

A more stringent lower bound on the value of v_H arises from a physical consideration. As will be shown in Section 3.3, no-slip boundary conditions cannot be applied to all velocity components in the absence of lateral friction. (Only the normal transport may be specified this case.) We therefore expect sidewall boundary layers whose thickness will

depend on (a power of) the coefficient of lateral eddy viscosity. If A is the Ekman number based on this coefficient, then there will be $A^{1/3}$ layers at the meridional walls and $A^{1/4}$ layers at the latitudinal walls to reduce the vertically integrated mass transports to zero. Interior to these layers there will be $A^{1/2}$ layers to reduce the wall velocities in each vertical layer to zero. (See Section 3.3; also Pedlosky, 1968.) For the values of v_H in Table 1 this implies thicknesses of 30, 14, and 3 km for the three types of layers.

Resolving such small scales would be extremely costly in computer time. Fortunately, it is not necessary to do so in order to calculate the interior flow correctly because the internal dynamics of the sidewall boundary layers have a negligible effect on the interior flow. Rather, it is overall properties of these boundary layers which are important for the interior. The boundary layers have the role of reducing certain interior velocity components (or integrated mass fluxes) to zero. The interior flow cannot be correct unless this is done, but the details of how it is done within the boundary layer have little influence on the interior solution. An analogous example is the replacement of an Ekman layer with a boundary condition on the mass flux. (Also see Orzsag and Israeli, 1974.)

As a further example, consider the $A^{1/2}$ layers. The wider layers reduce the vertically integrated mass flux to zero at the walls but they do not make the velocity zero at all depths. In our model the $A^{1/2}$ layer provides the necessary

upwelling (or downwelling) to bring the velocity within each of the two active vertical layers to zero at the walls. The grid spacing is too coarse to resolve any structure within the very narrow $A^{1/2}$ layer, but the necessary vertical mass exchange takes place in the model calculation. (Virtually all of it occurs at the grid point on the boundary.) We performed a number of numerical computations in which the grid spacings near the boundaries were varied. These experiments verified that increasing the resolution beyond a certain point (i.e., the grid configuration given in Table 2) changed the interior solution by less than 3%, although it did make a significant difference in the magnitude of the currents near the sidewall boundaries. Further experiments showed that the value of v_H given in Table 1 ($5.86 \times 10^5 \text{ cm}^2 \text{ sec}^{-1}$) is sufficiently large so that horizontal eddy viscosity rather than the "computational viscosity" of Section B.5, is the principal viscous mechanism entering into the momentum balance at the walls.

The size of the basin plays a role in determining the flow. Since our interest is in equatorial regions it would be wasteful of computer time to extend the basin too far toward the poles. On the other hand, the northern and southern walls of the basin should be sufficiently far from the equator so that their presence has negligible influence on the dynamics in the region of interest. The possibility of separating the effects of zonal walls from the equatorial dynamics depends on these dynamics being locally determined; i.e., "trapped" to the equator. That this is the case is borne out by our subsequent

analytic investigations (Chapter 3); it is also evident from the flow field pictures obtained from the numerical calculations (Chapter 5). We performed two numerical experiments which differed only in that the zonal walls were 15° and 20° from the equator, respectively. (A uniform easterly wind was used; all other parameters were as given in Table 1.) The flow in the vicinity of the equator (8°S to 8°N) was the same in both cases. We have therefore taken the meridional extent of the basin to be from 15°S to 15°N . The zonal width of the basin (28.6° of longitude) is smaller than that of the world's oceans, but is large enough to have a broad interior region where the dynamics may be clearly separated from the dynamics of the meridional boundary layers.

There are two possible choices for the mean depth of the whole active layer: the observed depth of the thermocline or the equivalent depth of the first baroclinic mode (cf., Lighthill, 1969). Both give approximately the same value: 150 to 200 m. We choose the higher value because it reduces the chance that the layer depth will go to zero at some point. If this happened, the numerical model would be unable to continue the calculation.

The presence of the surface layer introduces another parameter, the layer depth η . The numerical value we attach to η will determine how the vertically integrated transport is divided between the two active layers. For example, if $\eta=25$ m and \bar{H} , the total depth of the layer, is 200m, then u^S is the average zonal velocity in the top 25 m and u^1 is the average

zonal velocity in the next 175 m. Their depth-weighted sum $25 u^S + 175 u^1$ is the zonal transport. The choice of the surface layer depth has two effects on the model physics, as may be seen by considering its effect on the transport equations. First, the bottom drag is proportional to the lower layer velocity, whose value will depend on the value of η . This is true even in a linear model (cf. Section 3.1). The second effect is nonlinear, and comes about because we make the modelling assumptions (2.3) that the velocities are independent of depth within each layer. This means that the way we choose to divide up the average velocity affects the size of the nonlinear terms.

Because the choice of the surface layer depth does affect the model physics, we seek a physical bases for determining its value. Unfortunately, the available observational evidence from the world's oceans is not sufficient to help us choose this parameter. We make the choice on theoretical grounds. Consider a shallow homogeneous ocean driven by an imposed wind stress. The ocean is specified to be shallow so that the horizontal component of the Coriolis force may be ignored everywhere. Extra-equatorially, the wind stress is felt in an Ekman layer of depth $D_E = [2\nu_V/f]^{1/2}$. Below this boundary layer (and away from the bottom) the dynamics are inviscid and geostrophic. The influence of the wind stress is indirect: it is transmitted via the boundary layer pumping of the Ekman layer. (See, for example, Charney 1955, Pedlosky 1968, or Robinson 1970 for a detailed account.) As the

equator is approached, the Ekman depth D_E increases, becoming infinite at the equator in the absence of additional dynamical balances. We are, however, interested in modelling a parameter range when the wind stress is sufficiently strong and the value of the vertical viscosity sufficiently small so that inertial effects become important in the vicinity of the equator. A measure of these effects in the boundary layer is a Rossby number based on the boundary layer velocity, the local Coriolis parameter and a length scale set by the distance from the equator. For a wind stress per unit mass of magnitude τ the velocity scale in the Ekman layer is given by

$$u = \tau / D_E f = \tau [2\nu_v \beta y]^{-1/2}$$

Then

$$R_o = u / f y = [\tau^2 / 2\nu_v \beta^3 y^5]^{1/2}$$

or

$$y = R_o^{2/5} [\tau^2 / 2\nu_v \beta^3]^{1/5} \quad (2.10)$$

Now the inertial terms will enter into the boundary layer momentum balance (along with the Coriolis and vertical friction terms) when the Rossby number is order one. As the equator is approached, the Rossby number increases. We expect that equatorward of some latitude Y_c the inertial effects will prevent the boundary layer from deepening any further. In fact, if the velocities increase toward the equator, we may expect that the boundary layer will get shallower. These expectations are

borne out by the numerical calculation of Charney and Spiegel (1971). If we assume that the boundary layer stops deepening when $R_0 = .5$ and use the values in Table 1 (i.e., $\tau = .5 \text{ cm}^2 \text{ sec}^{-2}$, $v_v = 15 \text{ cm}^2 \text{ sec}^{-1}$), we obtain $Y_c \approx 2^\circ$. The Ekman depth D_E is approximately 25 m at this latitude. (Note that neither of these is very sensitive to the precise value of R_0 for $R_0 = 0$ (1)). These values agree well with Charney and Spiegel's calculation for the same parameter values (see their Fig. 1). On the basis of this argument we choose the value $\eta = 25 \text{ m}$ so that our surface layer will contain the boundary layer to be expected from a continuous model.

It remains to make a few remarks about the grid spacing we employ. Because our spacial differencing scheme is fourth order, it requires fewer points than a second order scheme to obtain a given accuracy. The position of the points in the grid we generally employ is given in Table 2. In the latitudinal direction the narrowest spacing occurs near the equator, where the grid interval is 30 km. The widest grid spacing (140 km) occurs at about 9° north and south. The grid spacing narrows to 33 km at the zonal boundaries. The intent is to put more points where the features of greatest interest (and/or of smallest scale) occur and not waste points elsewhere: more than one-third of the points lie between 2.5°S and 2.5°N . In the longitudinal direction the narrowest spacings (33 km) occur at the eastern and western walls where the boundary layers occur; the widest spacing (176 km) occurs at the center of the basin.

Table 2 Positions of the Points in the Standard Grid

Values are given in degrees of latitude or longitude ($1^\circ = 111 \text{ km}$)

(i) Longitude

0.00	0.30	0.61	0.96	1.36	1.85	2.45	3.21	4.15	5.28
6.58	8.00	9.52	11.09	12.70	14.32	15.95	17.56	19.13	20.65
22.07	23.37	24.50	25.44	26.20	26.80	27.29	27.69	28.04	28.35
28.65									

(ii) Latitude

-15.00	-14.70	-14.36	-13.94	-13.38	-12.61	-11.60	-10.42	-9.16	-7.89
-6.68	-5.57	-4.59	-3.75	-3.05	-2.46	-1.97	-1.55	-1.19	-0.86
-0.56	-0.28	0.00	0.28	0.56	0.86	1.19	1.55	1.97	2.46
3.05	3.76	4.59	5.57	6.68	7.89	9.16	10.42	11.60	12.61
13.38	13.94	14.36	14.70	15.00					

3. Linear Analytic Solutions

3.1 Formulation of the Mathematical Problem

We now consider Eqs. (2.6) on an equatorial beta plane with no-slip boundary conditions (2.9a). Let \bar{H}_1 = the mean depth of the lower active layer and $\bar{H} = \bar{H}_1 + \eta$. To facilitate analytic treatment we scale the variables as follows:

$$\begin{aligned} (x, y) &= L(x', y') ; \quad \eta = \bar{H}\alpha ; \quad t = Tt' ; \quad \tau = \tau_0 \tau' ; \\ (u^x, u^y) &= \mathcal{U}(u^{x'}, u^{y'}) ; \quad w = \mathcal{U}\bar{H}/Lw' ; \quad h = \bar{H}_1 + [\mathcal{U}\beta L^2/g]h' \end{aligned}$$

We take the length and time scales as the baroclinic equatorial ones (e.g., Matsuno, 1966; Blandford, 1966):

$$\begin{aligned} L &= (c/\beta)^{1/2} ; \quad T = (c\beta)^{-1/2} = (\beta L)^{-1} \quad \text{where} \\ c &= (g'\bar{H})^{1/2} , \quad \beta = 2\Omega/R \end{aligned}$$

These lengths and time scales are internal scales, picked out by the dynamics of the fluid motions. We assume that the wind stress is a smooth function at these scales and that the dimensions of the basin are large compared with L . (For the values in Table 1, $L = 296$ km, $T = 42.6$ hours and $c = 1.92 \text{ sec}^{-1}$.)

Velocities are related to the wind stress by $\mathcal{U} = \tilde{\tau}_0 / (H\beta L)$.

Dropping the primes the scaled equations are:

$$W = \alpha \nabla \cdot \underline{u}^s$$

$$\begin{aligned}
\underline{u}_t^s + \epsilon \left\{ (\underline{u}^s \cdot \nabla) \underline{u}^s + \frac{w}{2\alpha} (\underline{u}^s - \underline{u}^l) \right\} + \gamma \hat{K} \times \underline{u}^s + \nabla h &= \underline{z}/\alpha \\
&+ A \nabla^2 \underline{u}^s - (1-\alpha) \gamma_I (\underline{u}^s - \underline{u}^l) \\
\underline{u}_t^l + \epsilon \left\{ (\underline{u}^l \cdot \nabla) \underline{u}^l + \frac{w}{2(1-\alpha+\epsilon h)} (\underline{u}^s - \underline{u}^l) \right\} + \gamma \hat{K} \times \underline{u}^l + \nabla h &= \quad (3.1) \\
A \nabla^2 \underline{u}^l + \alpha \gamma_I (\underline{u}^s - \underline{u}^l) \left[\frac{1-\alpha}{1-\alpha+\epsilon h} \right] - \frac{\gamma}{1-\alpha+\epsilon h} \underline{u}^l \\
h_t + (1-\alpha) \nabla \cdot \underline{u}^l + \alpha \nabla \cdot \underline{u}^s + \epsilon \nabla \cdot (h \underline{u}^l) &= 0
\end{aligned}$$

where the following non-dimensional numbers have been introduced:

$$\begin{aligned}
\text{Rossby number} & \quad \epsilon = \mathcal{U}/(\beta L^2) \\
\text{Horizontal Ekman number} & \quad A = \nu_H/(\beta L^3) \\
\text{Interfacial Ekman number} & \quad \gamma_I = K/(\beta L \bar{H} \alpha [1-\alpha]) \quad (3.2) \\
\text{Bottom Ekman number} & \quad \gamma = K_B/(\beta L \bar{H}) \\
\text{Non-dimensional boundary layer depth} & \quad \alpha = \eta/\bar{H}
\end{aligned}$$

The three numbers γ_I , γ and α are logically independent parameters as the model is formulated. However, since they are all related to vertical friction, there is a physical basis for ordering them relative to one another. First, we expect that K and K_B are approximately equal so that $\gamma_I = O(\alpha^{-1} \gamma)$. From the arguments of Section 2.2 we expect η to be on the order of the Ekman depth, η_E , at the edge of the equatorial boundary layer $y = L$. Now

$$\eta_E = (2\nu_v/f)_{y=L} = (2\nu_v/(\beta L))^{1/2} = [2KH^*/(\beta L)]^{1/2}$$

where H^* is a characteristic layer depth (cf (2.2) ff). As before we take, $H^* = \bar{H}/2$, so

$$\alpha \equiv \eta / \bar{H} = O(\eta_E / \bar{H}) = O(\gamma^{1/2})$$

so that

$$\gamma_I = O(\gamma^{1/2})$$

and we may write

$$\alpha = a \gamma^{1/2}, \quad \gamma_I = b \gamma^{1/2} \quad (3.3)$$

where a and b are order one constants. (If we take $a = b = 1$ then this scaling is comparable to that of Philander (1971), except that our velocity scale is $\gamma^{1/2}$ times his--but see (3.7) below.)

Since it is the linear dynamics of the model which are to be investigated analytically, we linearize (3.1) by assuming $\varepsilon \equiv 0$.

The equations become

$$\underline{u}_t^s + \gamma \hat{k} \times \underline{u}^s + \nabla h = A \nabla^2 \underline{u}^s + \tau / \alpha - (1-\alpha) \gamma_I (\underline{u}^s - \underline{u}^t) \quad (3.4)$$

$$\underline{u}_t^t + \gamma \hat{k} \times \underline{u}^t + \nabla h = A \nabla^2 \underline{u}^t - \frac{\gamma}{1-\alpha} \underline{u}^t + \alpha \gamma_I (\underline{u}^s - \underline{u}^t) \quad (3.5)$$

$$h_t + (1-\alpha) \nabla \cdot \underline{u}^t + \alpha \nabla \cdot \underline{u}^s = 0 \quad (3.6)$$

Define $\bar{\underline{u}} = (1-\alpha) \underline{u}^t + \alpha \underline{u}^s$; $\tilde{\underline{u}} = \alpha (\underline{u}^s - \underline{u}^t)$ (3.7)

then $\underline{u}^1 = \underline{\bar{u}} - \underline{\tilde{u}}$ and $\underline{u}^s = \underline{\bar{u}} + \left(\frac{1-\alpha}{\alpha}\right) \underline{\tilde{u}}$

The quantity $\underline{\bar{u}}$ is the (scaled) vertically integrated mass transport. In order to elucidate the physical meaning of $\underline{\tilde{u}}$ consider the following relations derivable from (3.7):

$$\underline{\bar{u}} = \underline{u}^1 + \underline{\tilde{u}} \quad ; \quad \underline{u}^s = \underline{u}^1 + \frac{1}{\alpha} \underline{\tilde{u}} \quad (3.8)$$

We now interpret $\underline{\tilde{u}}$ as a boundary layer correction to the interior velocity \underline{u}^1 . The first of Eqs. (3.8) says that the vertically integrated velocity is the sum of the interior velocity and the boundary layer velocity; the second equation says that the velocity in the surface layer is composed of a component independent of depth and a correction for the surface boundary layer. Extra-equatorially \underline{u}^1 is the geostrophic interior velocity while $\underline{\tilde{u}}$ is the Ekman layer transport. Henceforth we will refer to $\underline{\tilde{u}}$ as the boundary layer velocity.

By taking appropriate combinations of (3.4) and (3.5) one obtains

$$\underline{\tilde{u}}_t + \gamma \hat{K} \times \underline{\tilde{u}} + E \underline{\tilde{u}} = \underline{\zeta} + A \nabla^2 \underline{\tilde{u}} + \frac{\alpha}{1-\alpha} \gamma \underline{\bar{u}} \quad (3.9)$$

$$\underline{\bar{u}}_t + \gamma \hat{K} \times \underline{\bar{u}} + \nabla h' = \underline{\zeta} + A \nabla^2 \underline{\bar{u}} - \gamma (\underline{\bar{u}} - \underline{\tilde{u}}) \quad (3.10a)$$

$$h'_t + \nabla \cdot \underline{\bar{u}} = 0 \quad (3.10b)$$

where
$$E = \gamma_I + \frac{\alpha}{1-\alpha} \gamma \approx \gamma_I \quad (3.11)$$

We are interested in parameter ranges for which vertical friction is more important than horizontal friction: $A \ll \gamma$,

γ_I . We also assume that $\gamma, \gamma_I < O(1)$. For the values of the parameters given in Table 1.

$$\alpha = .125, \quad A = 10^{-4}, \quad \gamma = 1.1 \times 10^{-2}, \quad \gamma_I = 10^{-1}$$

and this is the case. Horizontal friction will be neglected in the interior of the basin, including the equator¹. Boundary conditions and sidewall boundary layers will be discussed in Section 3.3, where it will be shown that A must be non-zero to allow the governing equations to satisfy the no-slip conditions (2.9a). It will also be shown that with A = 0 the appropriate boundary conditions are only that the normal component of \bar{u} vanish at the walls.

3.2 Solution of the Steady State Interior Problem

We now consider the system which results from assuming that all time derivatives are identically zero. It is convenient to work from Eqs. (3.9) and (3.10). We neglect horizontal friction and impose the condition that the normal component of the mass transport vanish at the boundaries. Eq. (3.9) is solved for the components of the boundary layer velocity:

¹ Strictly, this neglect is justified in the equation for \tilde{u} (3.9) if $A \ll \gamma_I^3$; with the values given above γ_I^3 is an order of magnitude larger than A. Similar neglect in the equations for \tilde{u} requires $A \ll \gamma\gamma_I^2$ whereas with the values we are using $\gamma\gamma_I^2$ is only slightly larger than A. Nevertheless, the qualitative results of this analytic treatment should be in agreement with the linear numerical computations.

$$\bar{u} = [E^2 + Y^2]^{-1} \{ Y \tau^{(y)} + E \tau^{(x)} + \gamma_* (E \bar{u} + Y \bar{v}) \} \quad (3.12a)$$

$$\bar{v} = [E^2 + Y^2]^{-1} \{ -Y \tau^{(x)} + E \tau^{(y)} + \gamma_* (-Y \bar{u} + E \bar{v}) \} \quad (3.12b)$$

with

$$E = \gamma_E + \gamma_* \quad \text{and} \quad \gamma_* = \frac{\alpha}{1-\alpha} \gamma = O(E^3)$$

The steady state form of the continuity equation allows us to introduce a mass transport stream function Ψ with

$$\bar{u} = -\Psi_y, \quad \bar{v} = \Psi_x \quad (3.13)$$

The boundary condition now becomes $\Psi = 0$ at the boundaries. A vorticity equation in Ψ may then be derived from (3.10):

$$\gamma \nabla^2 \Psi + \Psi_x - [\tau_x^{(y)} - \tau_y^{(x)}] = \gamma (\bar{v}_x - \bar{u}_y) \quad (3.14)$$

Extra-equatorially ($y > O(E)$) it is clear what to expect. To highest order the boundary layer velocity \bar{u} , is directed 90° to the right of the wind stress with magnitude $|\tau|/\gamma$. It is the "Ekman layer" transport. To highest order we may set the right hand side of (3.14) to zero, reducing it to the Stommel (1948) model for the mass transport stream function. As is well known, this equation admits boundary layers at the zonal boundaries and at the western side of the basin, but not at the eastern side. The appropriate boundary condition for the interior problem is $\Psi = 0$ at $x = X_E$, the eastern boundary. The solution is

$$\begin{aligned} \Psi &= -\int_x^{X_E} \hat{K} \cdot \text{curl} \hat{z} dx' + O(\gamma) \\ h &= -\int_x^{X_E} y^2 \hat{K} \cdot \text{curl} (\hat{z}/\gamma) + \int_0^y \tau^{(y)}(x=X_E) dy + K + O(\gamma) \end{aligned} \quad (3.15)$$

(K is a constant determined by the condition that the integral of h over the basin be zero.)

For $|y| \leq 0(E)$ \bar{u}_y becomes $O(E^{-2})$ so that the right hand side of the vorticity equation (3.14) becomes $O(1)$. Hence, there is a region at the equator in which the circulation controlled by the interfacial friction, which itself has no net transport, induces a mean circulation via bottom friction. Note that if the bottom friction parameter, γ , is zero, the flow in the interior of the basin (including the equator) is completely described by (3.12) and (3.15). In order to investigate this bottom frictional circulation, we proceed more formally.

First, make use of the relations (3.3) to write

$$\gamma_* = cE^3 \quad \gamma = dE^2 \quad c, d = O(1)$$

To simplify the exposition, we will take $c = d = 1$. Now re-scale y : $y = E\zeta$. Then, using (3.12) when $y \leq 0(E)$ we may write

$$\begin{aligned} \bar{u}(x, \zeta) &= E^{-1} \bar{u}^{(0)}(x, \zeta) + E \bar{u}^{(1)}(x, \zeta) + \dots \\ (\bar{u}^{(0)}, \bar{v}^{(0)}) &= (1 + \zeta^2)^{-1} \left\{ \int \hat{z}^{(y)}(x, y) + \hat{z}^{(x)}(x, y), \right. \\ &\quad \left. - \int \hat{z}^{(x)}(x, y) + \hat{z}^{(y)} \right\} \end{aligned}$$

Now write

$$\psi = \psi^{(1)}(x, y) + \pi^{(1)}(x, \zeta) + E \pi^{(2)}(x, \zeta) + E^2 (\psi^{(2)}(x, y) + \pi^{(3)}(x, \zeta)) + \dots$$

with $\bar{u}^{(1)}(x, \zeta) = -E^{-1} \pi_s^{(1)}$, $\bar{v}^{(1)}(x, \zeta) = \pi_x^{(1)}$, etc.

and where $\psi^{(1)}$ is the solution to (3.5). At the equator $\psi^{(1)}$ determines the part of the transport which is due to non-local conditions; $\Pi^{(1)}$ and $\Pi^{(2)}$ depend only on the local winds. The equations for these equatorial boundary layer transports are

$$\Pi_{ss}^{(1)} + \Pi_x^{(1)} = -\tilde{u}_s^{(0)}(x, \xi) \quad (3.16)$$

$$\Pi_{ss}^{(2)} + \Pi_x^{(2)} = \tilde{v}_x^{(0)} - (1 + \xi^2)^{-1} [\xi \tau_y^{(y)} + \tau_y^{(x)}]$$

We will pursue the solution only for the higher order stream function $\Pi^{(1)}$. (Since the equations have the same form, the mathematical problem is the same for each.) It may be shown that, as with (3.14), the equation for $\Pi^{(1)}$ admits a boundary layer only at the western side. The boundary conditions for (3.16) are then

$$\Pi^{(1)} \rightarrow 0 \text{ as } \xi \rightarrow \pm\infty \text{ and } \Pi^{(1)} = 0 \text{ at } x = x_E$$

It is convenient to change variables by defining $\sigma = x_E - x$; (3.16) may then be written

$$\Pi_{ss}^{(1)} - \Pi_\sigma^{(1)} = -\tilde{u}_s^{(0)} \quad (3.17)$$

with $\Pi^{(1)} = 0$ at $\sigma = 0$

this is a diffusion-like equation with σ the time-like variable. To solve it, the Laplace Transform in the σ direction is first taken, the resulting ordinary differential equation in ζ is solved subject to the boundary conditions at infinity, and then the inverse transform taken. After some manipulation, the result

is

$$\pi^{(1)}(x, \xi) = \frac{1}{2} \int_0^\infty d\nu \int_0^\sigma d\sigma' \frac{e^{-\nu^2/4\sigma'}}{(\pi\sigma')^{1/2}} [\tilde{u}^{(0)}(\sigma-\sigma', \xi+\nu) + \tilde{u}^{(0)}(\sigma-\sigma', \xi-\nu)] \quad (3.18)$$

In particular, if the winds at the equator are independent of x

$$\pi^{(1)} = \frac{1}{2} \sigma^{1/2} \int_0^\infty \text{erfc} \left(\frac{\nu}{2\sigma^{1/2}} \right) [\tilde{u}^{(0)}(\xi+\nu) + \tilde{u}^{(0)}(\xi-\nu)] d\nu$$

or

$$\pi^{(1)} = \frac{1}{2} \int_0^\infty \text{erfc} \left(\frac{\nu}{2\sigma^{1/2}} \right) [\tilde{u}^{(0)}(\xi+\nu) - \tilde{u}^{(0)}(\xi-\nu)] d\nu \quad (3.19)$$

At the equator

$$\begin{aligned} \bar{u}^{(1)}(\sigma, 0) &= -E^{-1} \pi^{(1)} = \\ &= E^{-1} \left\{ \tilde{u}^{(0)}(\xi=0) - \frac{1}{2} (\pi\sigma)^{-1/2} \int_0^\infty e^{-\nu^2/4\sigma} [\tilde{u}^{(0)}(\nu) + \tilde{u}^{(0)}(-\nu)] d\nu \right\} \\ &= E^{-1} \hat{\tau}^{(x)}(y=0) \left\{ 1 - (\pi\sigma)^{-1/2} \int_0^\infty \frac{e^{-\nu^2/4\sigma}}{1+\nu^2} d\nu \right\} \\ \bar{u}^{(1)} &= E^{-1} \hat{\tau}^{(x)}(y=0) \left\{ 1 - \frac{1}{2} (\pi/\sigma)^{1/2} \text{erfc} \left(\frac{1}{2\sigma^{1/2}} \right) e^{1/4\sigma} \right\} \quad (3.20) \end{aligned}$$

For small σ , asymptotic analysis gives

$$\bar{u}^{(1)} \sim E^{-1} \hat{\tau}^{(x)}(y=0) \cdot 2\sigma.$$

Also

$$\begin{aligned} \bar{v}^{(1)}(\sigma, 0) &= -\pi_\sigma = -\frac{1}{4} (\pi\sigma^3)^{-1/2} \int_0^\infty \nu e^{-\nu^2/4\sigma} [\tilde{u}^{(0)}(\nu) - \tilde{u}^{(0)}(-\nu)] d\nu \\ &= -\frac{1}{2} \hat{\tau}^{(y)}(y=0) (\pi\sigma^3)^{-1/2} \int_0^\infty e^{-\nu^2/4\sigma} \frac{\nu^2}{1+\nu^2} d\nu \end{aligned}$$

$$\bar{v}^{(1)} = - \hat{\tau}^{(y)}(y=0) \sigma^{-1} e^{\frac{1}{2}\sigma} D_2 [(2\sigma)^{-1/2}] \quad (3.21)$$

We are now in a position to describe the non-zero transport circulation induced by bottom friction (at least for an x independent wind stress). The most important conclusion to be drawn from the above formulas is that for a zonal wind stress the net transport at the equator is in the direction of the wind. This is, of course, contrary to what is observed for the undercurrents. It says that we must look to other (i.e. nonlinear) effects to explain the undercurrent. For any wind stress pattern the flow will be predominantly zonal ($\bar{u}^{(1)} = O(E^{-1} \bar{v}^{(1)})$), since flow along the equator is favored. For a meridional wind it may be shown from (3.17) and (3.19) that the transport will be in the direction of the wind drift current in both hemispheres. The fluid circuit will be closed by a weak interior transport directed opposite to the wind and a downwind flow in the western boundary layer. For any wind stress pattern the diffusion-like nature of (3.17) means that the region of frictionally induced transport will broaden from east to west. This description will be compared with the steady state linear numerical results in Chapter 5.

To summarize, we have found that the steady state interior circulation consists of two parts. The first part, described by (3.12) and (3.14) has a Sverdrup balance everywhere for the transport and essentially a wind drift solution for the

boundary layer. The second part, described by (3.18) is important in a region extending about 300 km on either side of the equator. (Note that although $\zeta = 1$ corresponds to only $y = 30$ km, variables fall off slowly--like ζ^{-1} in some cases.) There is a net transport at the equator in the direction of the zonal wind. Return flow also takes place within this frictional region. These results may be compared with those of Philander (1971) for a homogeneous ocean continuous in the vertical. For that model, the frictional layer deepens toward the equator and extends throughout the ocean at the equator. The boundary layer in which this happens is embedded in a more diffuse boundary layer in which bottom friction is important. There is a net transport in the direction of the zonal wind in the first of these layers, which is returned in the broader layer. It appears that our modelling assumption, which fixes the boundary layer depth, has the effect of combining these two layers.

3.3 Sidewall Boundary Layers

It is clear from (3.4)-(3.6) or (3.9) and (3.10) that some lateral friction is necessary to reduce the tangential velocities to zero at the walls. From the latter set it may also be seen that the normal velocities may be nonzero in the absence of lateral friction. Consider for example, (3.9), (3.10) with all friction terms set to zero. Eqs. (3.10) are simply the inviscid shallow water equations which permit us to impose the value of the normal component of the transport, $\bar{u} \cdot \hat{n}$ at the boundary. (This is well-known; the solution for

this form of (3.10) given in the next chapter may be taken as a constructive proof.) Eq. (3.9) with $A = 0$ contains no horizontal derivatives, so it is not possible to impose any boundary conditions at the side walls. Restoring the vertical friction couples the equations but does not increase the number of horizontal derivatives in the set of equations (3.9), (3.10). It may then be possible to impose a different boundary condition on some combination of \bar{u} and \bar{v} but the number of side wall boundary conditions is unchanged. In any case, the most natural condition to impose is that the transport normal to the boundary should vanish at the sidewalls, since we do not wish to consider mass sources or sinks at the boundaries. Since in the inviscid solution the normal velocities in the two layers need not be zero, one may anticipate that vertical exchanges of mass (upwelling or downwelling) between the friction layer and the layer below may be required to make the velocities in each layer vanish at the boundaries.

These results are similar to those of previous investigators who have considered a homogeneous model with a vertical frictional layer (e.g., Pedlosky, 1968; Robinson, 1970). The supposition that the fluid is homogeneous and hydrostatic means that the pressure gradient is independent of depth. Since the normal velocity in the interior will generally be different from that in the frictional layer it is not possible for the pressure gradient to adjust the velocity to zero at all depths.

We now consider the sidewall boundary layers required to close the steady state circulation described in the previous section, beginning with the upwelling layers needed to bring the individual velocity component to zero at the walls. Let $\tilde{u}_B = (\tilde{u}_B, \tilde{v}_B)$ be the boundary layer velocity in such a layer and let $\phi_B = \tilde{u}_B + i\tilde{v}_B$. The relevant equation is derivable from the steady state homogeneous form of (3.9). To highest order in E this is

$$(E+i\gamma)\phi_B - A\left[\frac{\partial^2}{\partial x^2} + \frac{\partial^2}{\partial y^2}\right]\phi_B = 0 \quad (3.22)$$

with the boundary condition that at the walls

$$\phi_B = -(\tilde{u} + i\tilde{v}) \equiv -\phi_0$$

where \tilde{u}, \tilde{v} are given by (3.12). At the eastern and western boundaries the $\partial^2/\partial y^2$ term may be neglected; this is true even at the equator provided $A \ll E^3$ (cf Eq. (3.12)). At the western wall, for example the solution is approximately

$$\phi_B \approx -\phi_0(x=0, y) \exp\left\{-[(E+i\gamma)/A]^{1/2} x\right\}$$

At the northern wall $y = y_N$, the term $\partial^2/\partial x^2$ in (3.22) is negligible and

$$\phi_B \approx -\phi_0(x, y=y_N) \exp\left\{-[(E+i\gamma_N)/A]^{1/2} (y-y_N)\right\}$$

The solution at the eastern side is similar to that at the west; that at the southern boundary is similar to that at the north. There are no east-west or north-south asymmetries among these

layers. From the equations above we may readily determine the boundary layer scales δ :

$$\delta \approx (2A/\gamma)^{1/2} \text{ for } \gamma \gg E \text{ and } \delta \approx (A/E)^{1/2} \text{ for } \gamma \approx 0$$

Dimensionally $\delta \approx 10$ km, 4 km and 1 km for $\gamma = 0^\circ$, 3° and 15° , respectively.

The boundary layers required to satisfy the boundary conditions on the vertically integrated mass transports are familiar in the oceanographic literature and we will treat them only briefly here. (See, for example, Pedlosky 1968 or Robinson 1970 for a more complete description). The boundary layer correction for the interior solution Ψ given by (3.15) must satisfy the homogeneous form of the vorticity equation (3.14) with $A \neq 0$; i.e.

$$\frac{\partial}{\partial x} \Psi_B + \gamma \nabla^2 \Psi_B - A \nabla^4 \Psi_B = 0 \quad (3.23)$$

with the boundary conditions that $\Psi + \Psi_B = 0$ and its normal derivative $\partial/\partial n(\Psi + \Psi_B) = 0$ at the walls. The first of these conditions requires corrections to Ψ at the western, northern and southern boundaries. In the western boundary layer the term representing the advection of planetary vorticity may be balanced either by bottom friction (Stommel, 1948) or horizontal eddy friction (Munk, 1950). The former will be true if $A \ll \gamma^3$ and the latter if $\gamma \ll A^{1/3}$. If neither of these ine-

qualities hold neither kind of friction will be negligible. The bottom frictional layer has thickness $A^{1/3}$ and the horizontal frictional layer thickness $A^{1/3}$. At the zonal boundaries there will be either a bottom frictional $\gamma^{1/2}$ layer or a horizontal frictional $A^{1/4}$ layer depending on which of γ or $A^{1/2}$ is the larger. It is not possible to satisfy the normal derivative condition on Ψ_B with bottom friction alone; $A^{1/4}$ layers at all the walls may be required to accomplish this. (Such a layer is needed at the eastern side; the tangential transports in it are only order $A^{1/2}$. See Pedlosky 1968).

Finally, the equatorial boundary layer transport $\Pi^{(1)}$ given by (3.18) requires a corner layer correction at the western side. This correction must also satisfy (3.23). For the corrections Ψ_B it was possible to neglect the derivatives in the tangential direction; in this case the meridional derivative will be negligible only if $A \ll \gamma E^2 \approx E^4$.

With the exception of the inviscid western boundary layer that forms in order to make the normal component of the vertically integrated transport zero at the walls we will not consider time dependent boundary layers in this work. These layers could be calculated by taking the Laplace Transform of the time dependent version of (3.22) and the time dependent potential vorticity equation (instead of (3.23)).

3.4 Solution of the Time Dependent Interior Problem

We consider here the initial value problem with $\underline{u}^S = \underline{u}^1 = h = 0$ at $t = 0$. A is taken to be zero and we impose the condi-

tion that the normal component of the vertically integrated mass transport vanish at the walls.

We again work with the equations in the form (3.9), (3.10), beginning with the first of these. To the highest order this is an equation in \tilde{u} alone since $\bar{u} < 0(E^{-2})$ for all time. Eq. (3.9) is now readily solved. First, rewrite it in the form

$$\left[\frac{\partial}{\partial t} + i\gamma + E \right] (\tilde{u} + i\tilde{v}) = \tilde{\tau}^{(x)} + i\tilde{\tau}^{(y)}$$

which is first order in time with only a parametric dependence on x and y . The solution is

$$\tilde{u} + i\tilde{v} = \int_0^t \left[\tilde{\tau}^{(x)}(x, y, s) + i\tilde{\tau}^{(y)}(x, y, s) \right] \exp[(E + i\gamma)(t-s)] ds \quad (3.24)$$

It is sufficient for our purposes to consider a wind stress which is a step function in time turned on at $t = 0$. In this case

$$\begin{aligned} \tilde{u} + i\tilde{v} = & (E^2 + \gamma^2)^{-1/2} \left\{ (\gamma\tilde{\tau}^{(y)} + E\tilde{\tau}^{(x)}) + i(-\gamma\tilde{\tau}^{(x)} + E\tilde{\tau}^{(y)}) \right\} \\ & \times \left\{ 1 - \exp[-(E + i\gamma)t] \right\} \end{aligned} \quad (3.25)$$

The timescale for the buildup of this component of the current system is clearly E^{-1} - 20 days for the values in Table 1. For times long compared to this the solution approaches the Ekman wind drift solution extra-equatorially. At the equator it is a current in the direction of the wind whose magnitude is limited by friction (cf. (3.12)).

For short times ($t \ll O(E^{-1})$) and points sufficiently near the equator ($|y| \ll O(t^{-1})$) (3.25) simplifies to $\tilde{u} = t\tau$; i.e. the solution is in the direction of the wind and grows linearly with time. Right at the equator the solution valid for all time is simply $\tilde{u} = \tau E^{-1} [1 - e^{-Et}]$ so that the \tilde{u} at the equator is always in the direction of the wind with magnitude approaching $E^{-1} |\tau|$.

Eqs. (3.10) with the bottom friction term neglected are just the inviscid shallow water equations. The term $\gamma(\tilde{u} - \bar{u})$ in (3.10a) is less than $O(E)$ for all time and so it might seem that such neglect is justified. This is indeed the case away from the equator ($|y| \gg E$), but it is clear from the steady state solution (Eq. (3.15)ff) that the bottom friction term will eventually become a non-negligible part of the vorticity balance at the equator. The inviscid equations will hold for all time away from the equator and for some initial time period even at the equator. Since it is the small time linear behavior that provides the most insight into the non-linear case and since the inviscid equations are easier to treat analytically, we will confine our analysis to these equations. (Actually, the term $\gamma\tilde{u}$ may be treated as a forcing term in addition to the wind stress and readily included in the analysis to be described below. The term $-\gamma\bar{u}$ is the one which causes serious complications.)

The method of solution for (3.10) in a bounded equatorial

ocean is of great interest in its own right as well as being rather involved. We have therefore found it advisable to devote the entire next chapter to these inviscid shallow water equations. For the reader who is not concerned with the methodology or the details of the results we provide here a brief summary of the principal results of that analysis as they apply to an x -independent wind stress turned on at $t=0$ and steady thereafter. A more detailed account of the response for the special cases $\tau=(-1,0)$ and $\tau=(0,1)$ will be given in Sections 5.2 and 5.4, respectively.

There are four types of waves that are free solutions the inviscid form of (3.10): inertia-gravity waves, Rossby waves, the mixed mode or Yanai wave and the Kelvin wave (see Fig. 4.1). All of these are essentially standing waves in the north-south direction. Inertia-gravity waves play only a minor role in the adjustment problems of interest to us. The Rossby waves have westward group velocity for long wavelengths and (slow) eastward group velocity for short wave-lengths. The smaller the meridional index n , the more equatorially confined the Rossby wave and the faster its group velocity. Hence disturbances propagate more quickly at the equator. The Kelvin wave and mixed mode have eastward group velocity at all wave-lengths; for small wavelengths the mixed mode behaves like a Rossby wave.

The solution to the forced problem in an unbounded equa-

torial ocean is obtained as an eigenmode expansion. There is a one-to-correspondence between these eigenmodes and the free wave solutions to the unforced problem. The response to an x -independent zonal wind stress consists of inertia-gravity waves needed to satisfy the initial conditions, a steady \bar{v} component, and secularly growing \bar{u} and h components. The secularly growing part of the solution tends to be equatorially confined; extra-equatorially \bar{v} tends to the wind drift solution. The response to an x -independent meridional wind stress consists of inertia-gravity waves and steady \bar{u} and h fields. There is no steady \bar{v} component. Extra-equatorially \bar{u} tends to the wind drift solution; at the equator the sea surface sets up so that its slope balances the wind stress.

To complete our description we must consider the effects of meridional boundaries. (The zonal boundaries are taken sufficiently far from the equator so as to have negligible effect on the flow there.) We take account of the boundaries by adding to the unbounded forced response those free wave solutions of (3.10) which will make the total solution satisfy the boundary conditions. A mode incident on a western boundary excites a response which is as equatorially confined as it, itself, is. Most of this response remains near the boundary forming a strong boundary current. Unlike the mid-latitude situation, a mixed mode or Kelvin wave will be part of the response. The latter propagates away from the boundary quick-

ly; the former remains near the western side, though it shows some effects extending into the basin. A mode incident on an eastern boundary excites a response which is less equatorially confined than itself. The more equatorially confined parts of the response propagate away from the boundary the most rapidly. Extra-equatorially, this response asymptotes to a coastal Kelvin wave.

4. Time Dependent Forced Shallow Water Equations in an Equatorial Basin

4.1 Introduction

In Section 3.4 it was shown that finding the time dependent vertically integrated transport of the linear model amounted to solving the inviscid shallow water equations on an equatorial beta plane. The linear shallow water theory is of great interest in its own right. For example, it has been used for an unbounded ocean (O'Brien and Hurlbut, 1974) to explain the equatorial jet which forms when the southwest monsoon begins to blow over the Indian Ocean (Wyrтки, 1973). The effects of boundaries must be taken into account to obtain a complete description of the ocean's response. Once the solution to this problem has been obtained, the linear baroclinic response of an ocean with arbitrary stratification may be constructed as a synthesis of the response of individual vertical modes (e.g., Lighthill, 1969). Associated with each mode there is a different equivalent depth (see below) which enters the scaling, but the scaled mathematical problem is the same for each baroclinic mode. (The barotropic response has a qualitatively different behavior because it is not equatorially confined. It is more like the mid-latitude case (See Lindzen, 1967.)

The equations are the inviscid form of (3.10) and (3.11). We rewrite them here in the form

$$\begin{aligned}
 u_t - yv + h_x &= F \\
 v_t + yu + hy &= G \\
 h_t + u_x + vy &= Q
 \end{aligned}
 \tag{4.1}$$

The scaling for these equations is as given in Section 3.1. F and G are the wind stress components $\tau(x)$ and $\tau(y)$. The equations have been generalized to include a heat (or buoyancy) source Q .

In the parlance of tidal theory, these are the equations for the vertical mode of equivalent depth $H^* = (\Delta\rho/\rho)\bar{H}$. For the numbers we are using (Table 1) $H^* = .4$ m. The quantity which effects the length and time scales is $c = (g'\bar{H})^{1/2} = (gH^*)^{1/2}$; this is the same whether defined in terms of "reduced gravity" or "equivalent depth". In tidal theory, F and G are the projections of the momentum forcing terms (e.g., wind stress) onto this baroclinic mode; Q is the projection of a mass or buoyancy source. We note that for an ocean with such a small equivalent depth, the beta plane is an excellent approximation to the spherical geometry in the sense that the solutions to the unforced version of (4.1) are close to the eigenfunctions on a sphere (Lindzen, 1967, Lonquet-Higgins, 1968).

Since the solution of the entire problem is rather complicated, it would be well to outline our method of attack. In the next section the free wave solutions of (4.1) are reviewed. These provide a useful vocabulary as well as themselves entering into the solution of the forced problem. The following

section considers the forced response in an unbounded basin. Useful solutions are obtained by taking a forcing that is a step function in time (i.e., the forcing is turned on at $t=0$; the response is initially zero). The zonal spatial structure is simplified by considering only two cases: an x -independent forcing and one which is a step function in x . (With such solutions in hand, the response to a delta function (in time and/or space) may be found simply by differentiating; the response to an arbitrary function may be found by a convolution.) In the final section of this chapter we present a method for calculating the effects of the boundaries on the unbounded solutions.

4.2 Free Wave Solutions

The free solutions ($F=G=Q=0$) to (4.1) for an infinite ocean with the boundary conditions

$$u, v, h \rightarrow 0 \text{ as } |y| \rightarrow \infty$$

may be written (Matsuno, 1966; Blandford, 1966).

$$(u, v, h) = \exp i(kx - \omega_{n,j}(k)t) \phi_{n,j}(k, y) \quad (4.2)$$

As a rule, n indexes the meridional structure (it is analogous to the meridional wave number) and j , the wave type (inertia-gravity or Rossby). The subscript pairs (n, j) range over the set

$$I = \{(-1,1), (0,1), (0,2)\} \cup \{(n,j) | n>0, j=1,2,3\} \quad (4.3)$$

For $n>0$, the $\omega_{n,j}(k)$'s satisfy the dispersion relation

$$\omega_{n,j}^2 - k^2 - \frac{k}{\omega_{n,j}} = 2n + 1 \quad (4.4)$$

For a given n and k there are three real roots to this equation, indexed by $j=1,2$, or 3 . For definiteness we distinguish among these by their values as $k \rightarrow 0$

$$\omega_{n,1} \rightarrow (2n+1)^{1/2}, \quad \omega_{n,2} \rightarrow -(2n+1)^{1/2}, \quad \omega_{n,3} \rightarrow -k/(2n+1)$$

Then $j=1$ and $j=2$ label inertia-gravity waves with phase speeds to the east and west, respectively, while $j=3$ labels the Rossby waves. When $n=0$ the root $\omega=-k$ of (4.4) must be rejected because the corresponding u and h functions become unbounded at infinity. The acceptable $n=0$ mode is referred to as the mixed mode or Yanai wave. The dispersion relation (4.4) simplifies to

$$\omega_{0,j} - \omega_{0,j}^{-1} = k \quad (4.5)$$

For definiteness take $\omega_{01} > 0$; then $\omega_{02} < 0$. We have labelled the equatorial Kelvin wave by $n=-1$. Its dispersion relation is simply

$$\omega_{-1} = k \quad (4.6)$$

(We drop the redundant second subscript.) The dispersion relations (4.4), (4.5), (4.6) are displayed in Fig. 4.1 for $\omega > 0$; since $\omega(-k) = -\omega(k)$, the values for negative ω may be obtained by reflecting the graph through the origin.

The vector functions $\phi_{n,j}(k,y)$ specify the meridional structure of u , v , and h for each wave. First define three

vector functions of y only:

$$\begin{aligned} \underline{P}_1^n(y) &= (y \Psi_n(y), 0, -d\Psi_n(y)/dy) \\ \underline{P}_2^n(y) &= (0, \Psi_n(y), 0) \\ \underline{P}_3^n(y) &= (-d\Psi_n(y)/dy, 0, y \Psi_n(y)) \end{aligned} \quad (4.7)$$

where Ψ_n is the n th (normalized) Hermite function. (The Hermite functions are described in Appendix E.1.) For $n \geq 0$

$$\underline{\phi}_{n,j}(k, y) = N_{n,j}^{-1} \left\{ \omega_{n,j}(k) \underline{P}_1^n + k \underline{P}_3^n - i(\omega_{n,j}^2 - k^2) \underline{P}_2^n \right\} \quad (4.8a)$$

For the Kelvin wave, $n=-1$,

$$\underline{\phi}_{-1}(k, y) = \underline{P}_1^{-1}(y) \equiv 2^{-1/2} (\Psi_0(y), 0, \Psi_0(y)) \quad (4.8b)$$

Finally, the N 's are normalization factors defined in Appendix E (E6).

Having established our notation, we wish to describe some of the characteristics of these solutions with the aid of Fig. 4.1. The higher frequency branches in Fig. 4.1 are the dispersion curves for $j=1$ and 2 ; i.e., the inertia-gravity waves. The lower frequency curves for $n > 0$ are Rossby waves. The nomenclature is carried over from the mid-latitude case: for the first set, the restoring forces are primarily inertial-gravitational while for the latter, they are primarily the gradient of planetary vorticity. The difference in frequencies and phase speeds between the two classes of waves is much less than for mid-latitude baroclinic waves; an equatorial ocean responds much faster than a mid-latitude one. The Rossby waves all have a westward phase velocity. The dotted line $2 k\omega = -1$

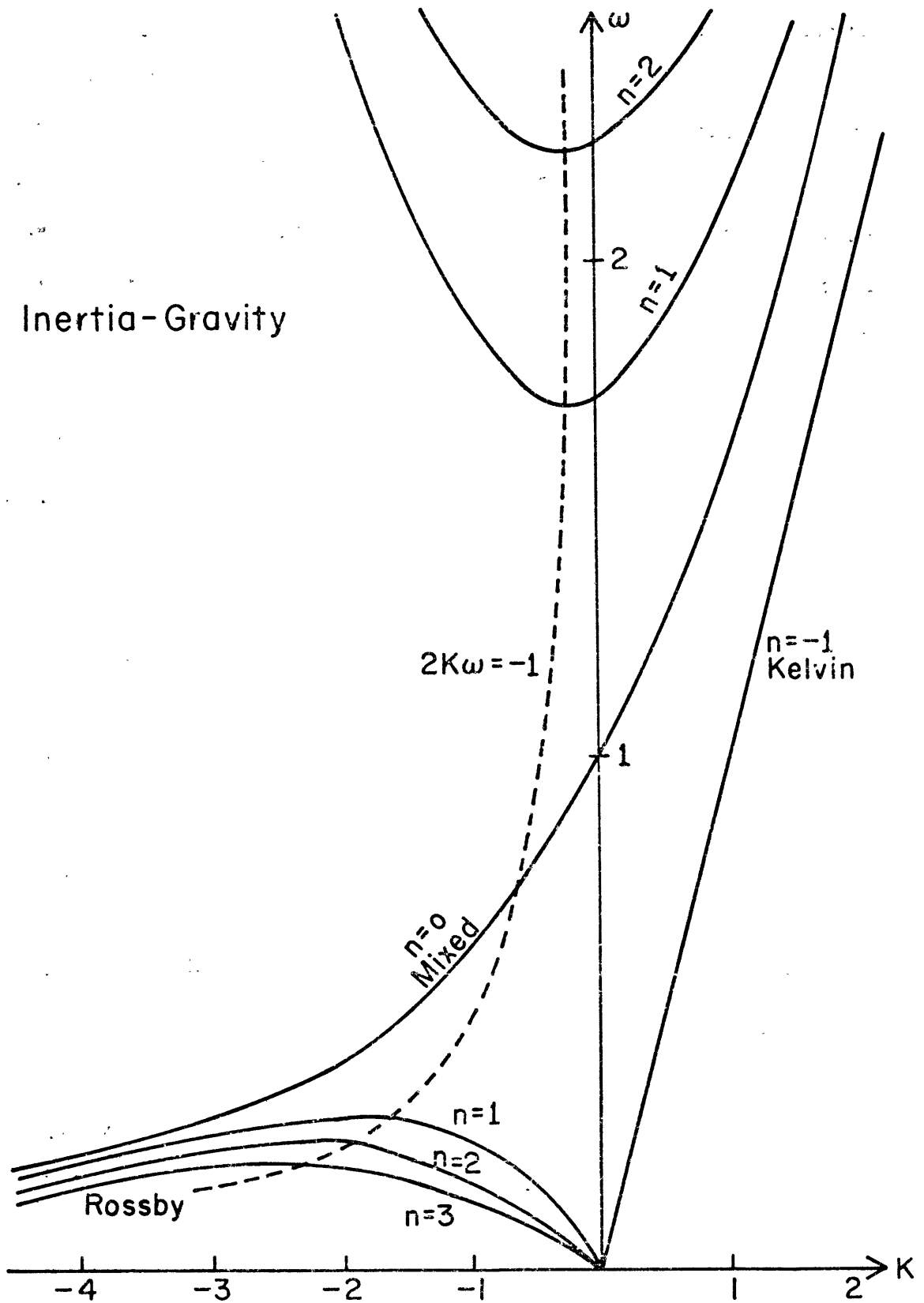


Fig. 4.1 Dispersion relation for waves on an equatorial beta plane.

divides those waves with eastward group velocity from those with westward group velocity. For the Rossby modes v and h are in approximate geostrophic balance for large k , while as $k \rightarrow 0$, u and h approach geostrophic balance. (Recall that differentiation by x multiplies by ik and that for the Rossby modes, $\omega \rightarrow 0$ as $k \rightarrow \infty$. Then the large k limit follows immediately from the definitions (4.7) and (4.8). The small k limit may be obtained by judicious use of (E3).) It will prove useful to define a special multiple of the Rossby modes for $k=0$ (cf., (E7)):

$$\tilde{P}_R^n \equiv \tilde{P}_3^n - (2n+1)^{-1} \tilde{P}_1^n \quad (4.9)$$

\tilde{P}_R^n has u and h in geostrophic balance and $v=0$.

The Yanai wave or mixed mode ($n=0$) behaves like a Rossby wave for small wavelength waves with westward phase speed; it behaves like a gravity wave for $k > 0$. The equatorial Kelvin wave has behavior analogous to coastal Kelvin waves with the equator acting like a boundary: the meridional velocity is zero and the zonal velocity is geostrophically balanced by the cross-stream pressure gradient; the downstream momentum balance is like that for a gravity wave. Both the Kelvin wave and the mixed mode have eastward group velocity for all wavelengths.

From the symmetries of the Hermite functions and the relations (E4), it follows that the eigenfunctions indexed by even n have u and h components which are anti-symmetric and v components which are symmetric about the equator; those indexed

by odd n have the opposite symmetries. It also follows that the smaller n is the more equatorially confined the mode is.

Note that all of the modes have ψ_{n+1} and ψ_{n-1} coupled in their u and h field, except for $n=0$ and $n=-1$. Finally, we note that for a given zonal wave number the larger n is the smaller the group velocity. As we shall see, all of the properties mentioned in this paragraph have important consequences for the response of a meridional boundary to an incoming mode.

4.3 Forced Response in an Unbounded Basin

The shallow water equations (4.1) may be written in the compact form

$$\frac{\partial \underline{u}^T}{\partial t} + \underline{\Omega} \underline{u}^T = \underline{F}^T \quad \text{where } \underline{u} \equiv (u, v, h) \text{ and } \underline{F} = (F, G, Q) \quad (4.10)$$

Superscript T indicates transpose and $\underline{\Omega}$ is an operator depending only on the spacial variables x and y . Fourier transform \underline{u} and \underline{F} from (x, y, t) space to (k, y, t) space by applying the operator $\int_{-\infty}^{\infty} e^{-ikx} dx$ to each component. Then

$$\frac{\partial \underline{u}^T(k, y, t)}{\partial t} + \underline{\Omega}(k, y) \underline{u}^T(k, y, t) = \underline{F}^T(k, y, t)$$

where

$$\underline{\Omega}(k, y) = \begin{bmatrix} 0 & -y & ik \\ y & 0 & \partial/\partial y \\ ik & \partial/\partial y & 0 \end{bmatrix}$$

It now follows immediately that the free wave solutions (4.2) ff. to (4.1) yield the vector eigenfunctions of $\underline{\Omega}(k, y)$; i.e.,

$$\underline{\Omega}(k, y) \underline{\phi}_{n,j}^T(k, y) = i\omega_{n,j}(k) \underline{\phi}_{n,j}^T(k, y) \quad (4.11)$$

where the eigenvalues $i^{\omega_{n,j}}$ are given by the free wave dispersion relation (4.4) - (4.6). In Appendix F it is shown that these eigenfunctions are orthogonal and complete. This means that any vector forcing may be expanded in the $\phi_{n,j}$'s if its components may be expanded in Hermite functions. As a general rule, a function may be represented as a convergent series of Hermite functions if it is square integrable in the interval $(-\infty, +\infty)$. Questions of convergence make for some nice mathematical problems, but in view of our purpose such questions may be circumvented. We are concerned with ocean basins in equatorial regions of limited latitudinal extent. The form of the forcing function (or the response) beyond the limits of the basin should make no difference to the basin response so the forcing may always be taken to go to zero sufficiently rapidly as $|y| \rightarrow \infty$. For example, any physically reasonable forcing may be multiplied by $\exp(-by^2)$, $b \ll 1$ to guarantee convergence without changing its value near the equator. The projection of this forcing onto the modes with n small will be unchanged (since these modes have small amplitude away from the equator). The fact that modes with n large might be affected by this alteration is an indication of the fact that these infinite beta plane modes are not the eigenfunctions for a bounded basin. (The correct modes involve the parabolic cylinder functions which give $v=0$ at the zonal walls.) Those modes which have their turning latitudes equatorward of the latitudes

bounding the basin will be essentially unaffected by the walls. For an ocean bounded at $\pm 15^\circ$ with a baroclinic radius of deformation of 300 km this means those modes with $n \leq 12$. Higher modes must be corrected by considering the effects of walls at a finite distance from the equator. Such changes will make little difference near the equator where the amplitudes of these modes is small. Furthermore, we feel that it is generally preferable not to calculate the extra equatorial flow by correcting the infinite beta plane modes, but rather to use a more local approximation (e.g., a "mid-latitude" beta plane, cf., Lindzen, 1967). In summary, since our problem is to calculate the equatorial response we needn't concern ourselves much with questions of convergence or the influence of northern and southern boundaries. The chief exception to this statement is the possibility of fast moving boundary trapped modes which may turn the corners at the bounding meridians and propagate into the equatorial region (e.g., coastal Kelvin waves; see Moore, 1968).

The completeness of the eigenfunctions means that for any (physically interesting) forcing function we may write

$$F(k, y, t) = \sum_{(n,j) \in \mathbf{I}} b_{n,j}(k, t) \phi_{n,j}(k, y) \quad (4.12)$$

where \mathbf{I} is the set of permissible subscripts, (4.3). Formulas for computing the $b_{n,j}$'s are given in Appendix E.2. Once the $b_{n,j}$'s--the projections of the forcing onto the eigenfunctions--are obtained, one proceeds in the manner usual for

eigenfunction expansions:

$$\text{Let } \underline{u} = \sum_{(n,j)} a_{n,j}(k,t) \phi_{n,j}(k,y) \quad (4.13)$$

then

$$\frac{\partial a_{n,j}}{\partial t} + i\omega_{n,j} a_{n,j} = b_{n,j} \quad \text{for all } (n,j) \in I$$

an equation familiar from the linear oscillator problem. If the initial conditions are that $\underline{u}=0$ at $t=0$ and the forcing is at a single frequency σ so that $b_{n,j}(k,t) = B_{n,j}(k) e^{-i\sigma t}$, then

$$a_{n,j}(k,t) = \frac{B_{n,j}(k)}{i(\omega_{n,j} - \sigma)} \left[e^{-i\sigma t} - e^{-i\omega_{n,j} t} \right]$$

As with the linear oscillator, the first term has the same time behavior as the forcing, while the second is the free wave response needed to satisfy the initial conditions.

Clearly, the closer the forcing frequency is to the natural frequency the larger the response. At resonance $\sigma = \omega_{n,j}$ and $a_{n,j} = t B_{n,j}(k)$ -- secular growth. For a steady forcing $\sigma=0$ so that

$$a_{n,j}(k,t) = \frac{b_{n,j}(k)}{i\omega_{n,j}} \left[1 - e^{-i\omega_{n,j} t} \right] \quad (4.14)$$

In a formal sense the problem of finding the ocean's response to an arbitrary forcing is now solved--one need only invert each Fourier transform $a_{n,j}(k,t) \phi_{n,j}(k,y)$. This is, in general, extremely difficult: such expressions have a very complicated dependence on k . Some simplifications are clearly in order. To begin with, we consider only the case where \underline{F} is

steady and the initial conditions are $u=v=h=0$ so that (4.14) applies. This amounts to seeking the response to a step function in time; the response to other time structures may be found by a convolution.

One possible strategy is to restrict oneself to long-wave forcings (Lighthill, 1969; Cane, 1974). With the long-wave approximation, the inertia-gravity mode $\omega_{n,j}$'s are independent of k while the Rossby modes are nondispersive ($\omega_{n,3} = -k(2n+1)^{-1}$); the necessary inverse transforms are not difficult to calculate.¹ Here we employ a different strategy. We solve the problem for a step function in x .

First we find the response to an x -independent forcing $F = F(y)$ everywhere, and then modify it to account for the forcing "turning off" for $x < X$. The first part is simpler than the long wave approximation but qualitatively similar. The step function case is directly applicable to some physically interesting situations (e.g., the Somali jet), as well as allowing the response to an arbitrary zonal structure to be calculated by convolutions.

The response to an x -independent forcing $F(y)$ is a sum

$$u_k + \sum_{n=0}^{\infty} u_{n,G} + \sum_{n=1}^{\infty} u_{n,R} \quad \text{where}$$

¹We exploit the one-to-one correspondence between the eigenfunctions $\phi_{n,j}$ and the free waves $\exp i(kx - \omega_j t)$ $\phi_{n,j}$ as well as between the eigenvalues and free wave frequencies to carry over the free wave nomenclature.

$$\begin{aligned} \underline{u}_{n,G} = & \left[d_n (2n+1)^{-3/2} \sin(2n+1)^{1/2} t + \right. \\ & \left. g_n (2n+1)^{-1} (1 - \cos(2n+1)^{1/2} t) \right] \underline{P}_1^n \\ & + \left[d_n (2n+1)^{-1} (\cos(2n+1)^{1/2} t - 1) + g_n (2n+1)^{1/2} \sin(2n+1)^{1/2} t \right] \underline{P}_2^n \end{aligned} \quad (4.15)$$

$$\underline{u}_{n,R} = t \underline{v}_n \underline{P}_R^n \quad (4.16)$$

$$\underline{u}_K = t d_1 \underline{P}^{-1} \quad (4.17)$$

The d_n 's, etc. are defined in Appendix E.2 and the subscripts G, R, and K denote inertia-gravity, Rossby and Kelvin modes, respectively. To see how the secularly growing terms arise, consider (4.14) for the n th Rossby mode. After making the long wave approximation $\omega_{n,3} \approx -k/(2n+1)$, the Fourier synthesis of (4.14) yields

$$a_{n,3}(x,t) = -(2n+1) \left\{ \int_{-\infty}^x b_{n,3}(x') dx' - \int_{-\infty}^{x+t/(2n+1)} b_{n,3}(x') dx' \right\} = (2n+1) \int_x^{x+t/(2n+1)} b_{n,3}(x') dx'$$

For an x -independent forcing this is just

$$a_{n,3}(t) = (2n+1) b_{n,3} \left\{ (x+t/(2n+1)) - x \right\} = b_{n,3} t \quad (4.18)$$

This shows that the secularly growing part of the solution may be viewed as the sum of a locally forced part which goes like $-x$, and a propagating part (required by the initial conditions) which goes like $x + t (2n + 1)^{-1}$.

We now wish to describe the response in words. Suppose first that the forcing consists solely of an east-west wind stress (i.e., $F = F(y)$; $G = Q = 0$). The response consists of secularly growing u and h fields, plus a steady v component:

$$(u, v, h) = (t U(y), V(y), t H(y)) \quad (4.19)$$

In addition, there is a series of inertia-gravity waves which are required to satisfy the initial condition $v = 0$. The steady v field asymptotes to the wind drift value $-F(y)/y$ as $y \rightarrow \infty$ and the Coriolis balance becomes dominant. At the equator the Coriolis term is absent and the wind stress causes a steady acceleration in the direction of the wind: $u = t F(0)$. As a general rule, the time growing part of the response will be equatorially confined. From a mathematical point of view the solution is best explained in terms of the dispersion diagram (Fig. 4.1) and Eq. (4.14). The forcing function has zero frequency and zonal wavenumber so it lies at the origin of the dispersion diagram. This is a point of resonance for the Rossby and Kelvin waves resulting in a secularly growing solution. The steady part $v = V(y)$ is the forced response of the inertia-gravity modes at $k = 0$ (not on resonance), while the oscillating

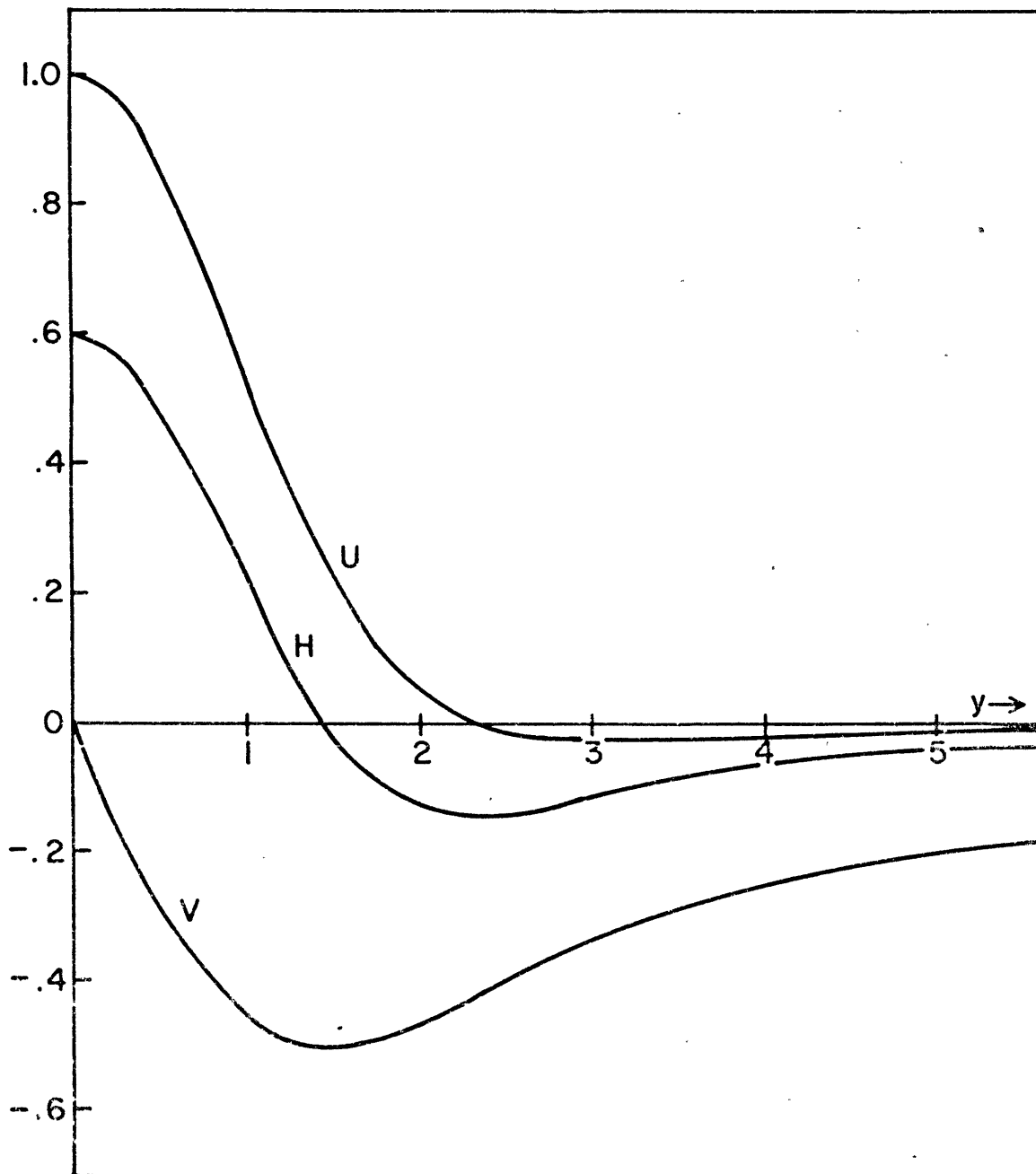


Fig. 4.2 Response to $F=1$, $G=Q=0$ in an unbounded basin.
See Equation (4.19).

part is made up of inertia gravity waves with $k = 0$. Figure 4.2 shows the functions $U(y)$, $H(y)$, $V(y)$ of (4.19) for the case $F \equiv 1$. (This solution was first obtained by Yoshida, 1958.) This solution has the symmetry associated with n odd: u and h are symmetric about the equator and v anti-symmetric. U and H are equatorially confined while V asymptotes to $-1/y$.

The response to a purely meridional wind stress ($G = G(y)$, $F = Q = 0$) is very different, consisting of steady u and h components and a series of inertia-gravity waves of zero zonal wavenumber which are required to satisfy $u = h = 0$ at $t = 0$. There is no steady (or other non-oscillating) v component. Extra-equatorially, the steady part of the solution $U^*(y)$, $H^*(y)$ approaches the wind drift:

$$\text{as } |y| \rightarrow \infty, U^*(y) \rightarrow G(y)/y, H^*(y) \rightarrow 0 \quad .$$

At the equator the Coriolis term vanishes and the wind stress is balanced by the "sea-surface setup" -- that is, by dH^*/dy . Mathematically speaking, the response comes from the inertia-gravity modes at the points on the axes $k = 0$ of Figure 4.1. While the forcing is again at $k = 0$, $\omega = 0$, there is no resonant response in the Rossby and Kelvin modes because these modes have no meridional component at $k = 0$. Figure 4.3 shows $U^*(y)$ and $H^*(y)$ for the case $G = 1$. This solution has the symmetry associated with n even. $U^* = 0$ at the equator and asymptotes to $1/y$ as $y \rightarrow \infty$; these constraints determine its general shape.

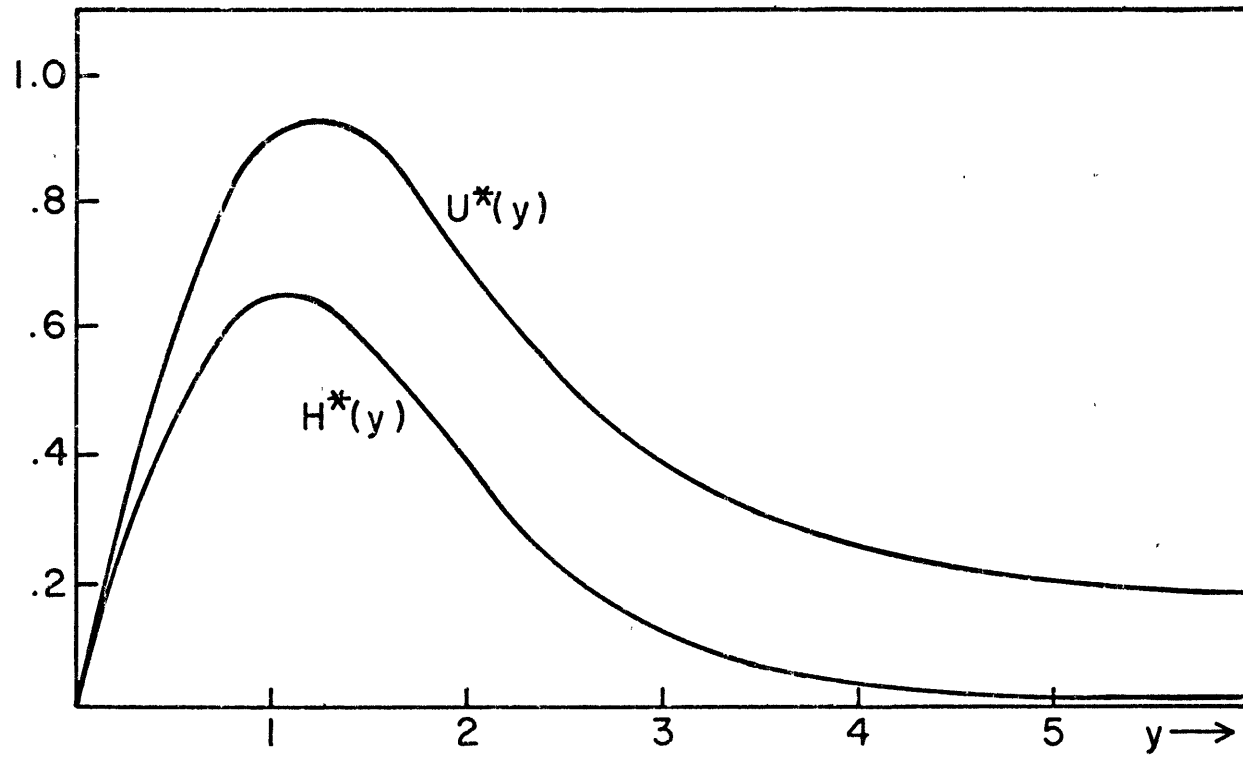


Fig. 4.3 Response to $F=0$, $G=1$, $Q=0$ in an unbounded basin.

Finally, we remark that the response to only a heating function forcing ($F = G = 0$, $Q = Q(y)$) has the same general components as the case of a zonal wind stress; that is, a form like (4.19) plus inertia-gravity waves. Of course, on a less superficial level of description, it is very different. For example, the response to $Q = 1$ is simply $u = v = 0$ and $h = t$; no gravity waves are excited. (Such a large-scale heating sets up no gradients and hence creates no motions.)

With the x -independent solution in hand, we may proceed to the step function response. Let the forcing be given by $\underline{F}(x, y) = \underline{F}(y) S(x - X)$, where S is the Heaviside step function ($S(x) = 0$ for $x < 0$; $S(x) = 1$ for $x > 0$). Without loss of generality we may take $X = 0$. If the solution for the x -independent case is applied for $x \geq 0$ with $u = v = h = 0$, then the forced response is accounted for, except that the jumps in u , v and h at $x = 0$ are not consistent with the original equations. Call this part of the solution $\underline{U}^{(1)}$. The problem is thus changed to one of adding free solutions which make the total solution satisfy the appropriate jump conditions. For our method of solution it is sufficient to note that the jumps in u and h must be zero. If we find free solutions which "match" the values of $u^{(1)}$ and $h^{(1)}$ at $x = 0$, the total solution must have a v component which satisfies the correct jump condition. These free solutions consist of a part $\underline{U}^{(2)}$, which is needed if F or $Q \neq 0$, and a part $\underline{U}^{(3)}$, needed if $G \neq 0$. The solution is a sum

$$\begin{aligned} & \underline{u}_K^{(1)} + \underline{u}_K^{(2)} + \sum_{n=0}^{\infty} \left\{ \underline{u}_{n,G}^{(1)} + \underline{u}_{n,G}^{(2)} + \underline{u}_{n,G}^{(3)} \right\} \\ & + \underline{u}_{0,R}^{(3^+)} + \sum_{n=1}^{\infty} \left\{ \underline{u}_{n,R}^{(1)} + \underline{u}_{n,R}^{(2)} + \underline{u}_{n,R}^{(3^+)} + \underline{u}_{n,R}^{(3^-)} \right\} \end{aligned}$$

where

$$\underline{u}_K^{(1)} = \underline{u}_K, \quad \underline{u}_{n,G}^{(1)} = \underline{u}_{n,G}, \quad \underline{u}_{n,R}^{(1)} = \underline{u}_{n,R} \quad \text{for } x > 0 \quad (4.20)$$

$$\begin{aligned} \underline{u}_{n,G}^{(2)} = & -d_n (2n+1)^{-3/2} \sin(2n+1)^{1/2} t \underline{P}_1^n \\ & - d_n (2n+1)^{-1} \cos(2n+1)^{1/2} t \underline{P}_2^n \quad \text{for } 0 \leq x < \frac{1}{2}t/(2n+1) \end{aligned} \quad (4.21)$$

$$\begin{aligned} \underline{u}_{n,R}^{(2)} = & r_n \left\{ [t + (2n+1)x] \underline{P}_R^n + \left[\frac{4n(n+1)}{2n+1} \right] \right\} \\ & \text{for } 0 < -x < t/(2n+1) \end{aligned} \quad (4.22)$$

$$\underline{u}_K^{(2)} = (x-t) d_{-1} \underline{P}^{-1} \quad \text{for } 0 < x \leq t \quad (4.23)$$

$$\begin{aligned} \underline{u}_{n,G}^{(3)} = & g_n \left\{ (2n+1)^{-1} \cos(2n+1)^{1/2} t \underline{P}_1^n - (2n+1)^{-1/2} \sin(2n+1)^{1/2} t \underline{P}_2^n \right\} \\ & \text{for } 0 \leq x < \frac{1}{2}t/(2n+1) \end{aligned} \quad (4.24)$$

$$\underline{u}_{n,R}^{(3^-)} = -g_n \underline{P}_R^n \quad \text{for } 0 < -x < t/(2n+1) \quad (4.25)$$

$$\begin{aligned} \underline{u}_{n,R}^{(3^+)} \approx & -g_n J_0(2\sqrt{xz_n}) \underline{P}_3^n + g_n \left[\frac{z_n}{x} \right]^{1/2} J_1(2\sqrt{xz_n}) \underline{P}_2^n \\ & \text{for } n > 0, \quad 0 \leq x \leq t/(2(2n+1)) \\ & \text{with } z_n = t - (2n+1)x \end{aligned} \quad (4.26)$$

$$\underline{u}_{n,R}^{(3+)} = -g_0 P_3^0 J_0(2\sqrt{x(t-x)}) + g_0 P_2^0 \left[\frac{t-x}{x}\right]^{1/2} J_1(2\sqrt{x(t-x)})$$

for $0 \leq x \leq t$ (4.27)

Here, \underline{u}_K , $\underline{u}_{n,G}$ and $\underline{u}_{n,R}$ are given by (4.15) - (4.17), J_n is the Bessel function of order n and the terms are non-zero only for the ranges of x and t shown.

We now wish to show how the solution shown in (4.20) - (4.27) is obtained. Consider first the non-gravity wave part of $\underline{u}^{(2)}$. As remarked above (see 4.18) each Rossby and Kelvin mode piece of the solution $\underline{u}^{(1)}$ may be viewed as consisting of a locally forced part varying like $C_n x$ and a propagating part, which goes like $t - C_n x$. Only the latter violate the jump conditions. But since each such propagating part is a free solution of (4.1), the jump conditions can be matched by considering how these modes propagate through $x = 0$. The n th Rossby mode may be thought of as a synthesis of Rossby waves with amplitude $\delta(k)$, where δ is the Dirac delta function. It has a group velocity of magnitude $1/(2n + 1)$ to the west. Each such mode continues to propagate westward beyond $x = 0$, so we must add these propagating solutions for $x < 0$ (4.22). The Kelvin mode propagates eastward with group velocity 1. At time t the propagating mode arriving at a point x must have originated at a point $x_0 = x - t$. If $x_0 < 0$, there was no forcing at x_0 and no such mode was generated. Hence, for points

$x < t$, we must subtract off the propagating part of the Kelvin mode which was included in the response to the x -independent forcing, (4.24).

The inertia-gravity wave parts of the forced response were all waves with zero wavenumber; the n th such mode propagates to the east with group velocity $(2(2n+1))^{-1}$. Since the forcing extended only as far to the west as $x = 0$ at time t , the n th inertia-gravity mode will be present only for $x < t/(2(2n+1))$, (4.21). The same result holds for the inertia-gravity waves forced when the north-south wind stress G is non-zero, (4.24).

It remains to calculate the free solutions needed to correct for the jump in u and h which results from the steady part of the response to G . Our technique for doing this is less intuitive than what was done above; it is as readily described for an arbitrary time dependence for u and h as for the special case where these are independent of time. Suppose then that the u and h components arising from the x -independent problem are a sum of terms, each of which has the form

$$(u, o, h)_n = a^*(t) p_1^n + b^*(t) p_3^n \quad (4.28)$$

at $x = 0$. Let us begin with the special case where

$$a^*(t) = ae^{-i\omega t}, \quad b^*(t) = be^{-i\omega t} \quad (4.29)$$

The free wave solutions needed to satisfy the jump conditions at $x = 0$ must have the same time dependence -- they must have frequency ω . To be free solutions with meridional index n , their zonal wavenumber K must satisfy the dispersion relation (4.4). There are two possible values of K , $K = K_n^+(\omega)$ or $K_n^-(\omega)$, where

$$K_n^\pm(\omega) = -\frac{1}{2\omega} \pm \left\{ \omega^2 + \frac{1}{4\omega^2} - (2n+1) \right\}^{1/2} \quad (4.30)$$

Note that K^\pm may be complex, in which case the modes are trapped at $x = 0$. If K^\pm are real, then one mode has group velocity to the west and the other group velocity to the east (see Fig. 4). (We ignore the special case $K^+ = K^-$ when the group velocity is zero.) This is which depends on whether we are in the inertia-gravity wave frequency range or the Rossby wave frequency range. For the Rossby waves (ω small) the propagating mode associated with K^- is the one with eastward group velocity.

Let us call the K corresponding to eastward group velocity (or eastward trapping) $K_{n,e}(\omega)$ and the westward propagating (or trapped) one $K_{n,w}(\omega)$. The corresponding free waves $\underline{U}_{n,e}$ and $\underline{U}_{n,w}$ have the respective forms

$$\begin{aligned} \underline{U}_{n,e}(\omega) &= \exp i(K_{n,e}(\omega)x - \omega t) \phi_{n,e}(\omega) \\ \underline{U}_{n,w}(\omega) &= \exp i(K_{n,w}(\omega)x - \omega t) \phi_{n,w}(\omega) \end{aligned} \quad (4.31)$$

with

$$\phi_{n,e}(\omega) = \omega P_{n-1}^n(\gamma) + K_{n,e} P_{n-3}^n(\gamma) - i(\omega^2 - K_{n,e}^2) P_{n-2}^n(\gamma)$$

(cf., (4.8)). If such waves are generated at $x = 0$, the one labelled with an e will exist only to the east and the one labelled with a w only to the west of $x = 0$. The condition that u and h have no jump at $x = 0$ will be satisfied if amplitudes A_e and A_w can be calculated for the modes (4.31) to cancel the jump caused by the original u and h (i.e., those specified by (4.29)). That is, $A_e(\omega)$ and $A_w(\omega)$ must be found to satisfy

$$a P_{\sim 1}^n + b P_{\sim 3}^n = A_e (\omega P_{\sim 1}^n + K_{n,e} P_{\sim 3}^n) + A_w (\omega P_{\sim 1}^n + K_{n,w} P_{\sim 3}^n)$$

for all y . This is equivalent to the pair of equations

$$a = \omega (A_e + A_w); \quad b = A_e K_{n,e} + A_w K_{n,w} \quad (4.32)$$

which has a solution. (We again ignore the point of zero group velocity where $K_{n,e}(\omega) = K_{n,w}(\omega)$.)

We now have in hand a solution for the response to a step function forcing in the special case (4.29) when the forcing is at a single frequency ω . This may be used to solve the general case, (4.28). First transform from the time domain to the frequency domain:

$$a(\omega) = \int_0^{\infty} a^*(t) e^{i\omega t} dt \quad b(\omega) = \int_0^{\infty} b^*(t) e^{i\omega t} dt$$

Then

$$a^*(t) = \frac{1}{2\pi} \int_0^{\infty} a(\omega) e^{-i\omega t} d\omega \quad b^*(t) = \frac{1}{2\pi} \int_0^{\infty} b(\omega) e^{-i\omega t} d\omega$$

showing a^* and b^* as a synthesis of waves. (Note that $a(ip)$ is just the Laplace transform of $a^*(t)$ with $p = -i\omega$, the transform variable.) Eqs. (4.30) and (4.32) are then solved as before, except that a and b are now functions of ω . The final step is to synthesize the waves by integrating the expressions $A_e(\omega) \underline{U}_{n,e}(\omega)$ and $A_w(\omega) \underline{U}_{n,w}(\omega)$ over all ω . That is, the transform is inverted to return to the time domain from the ω domain.

For some time dependences this transform may be impossibly difficult to invert, but we need only concern ourselves with the steady part of the response to a north-south wind stress. In this case, (4.28) takes the form given by (4.15), i.e.,

$$(u, o, h)_n = g_n (2n+1)^{-1} P_1^n(\gamma)$$

Since this is steady in time, we expect the waves needed to synthesize the jump correction to have low frequencies. By assuming

$$\omega^2 \ll (2n+1)^{-1} \quad (4.33)$$

we may write

$$\begin{aligned} K_{n,e}(\omega) &= -\omega^{-1} + (2n+1)\omega + O(\omega^3) \\ K_{n,w}(\omega) &= - (2n+1)\omega + O(\omega^3) \end{aligned} \quad (4.34)$$

If we retain only the highest order terms, the transforms are readily inverted and Eqs. (4.25), (4.26) and (4.27) are obtained. (To get (4.26) we also retain the term $(2n + 1)\omega$ in the approximation to $K_{n,e}$ when it appears in the exponent in (4.31). Then the solution is a uniform approximation for $x \leq 0(\omega^{-2})$; cf., Lighthill, 1969.) The expressions (4.25) obtained for the "long wave" westward propagating modes are exact; they are just the free Rossby modes which lie at the origin of the dispersion curve with steady u and h components and v identically zero. The mixed mode solution (4.27) is also exact, because the approximate relation (4.34) for $K_{n,e}$ is exact for $n = 0$. From Laplace transform theory the small ω approximation made for the $n \geq 1$ eastward propagating modes is known to be an asymptotic solution for large t . It is an excellent approximation to the exact solution. (The exact solution is a series of terms of the form $(x/z)^{n/2} J_n(2\sqrt{xz})$ where $z = t - (2n + 1)x$ and J_n is the n th Bessel function. See Cane and Sarachik, 1975 for a further discussion.)

The distance these modes propagate; i.e., the limit $x < t \{8(2n + 1)\}$ in (4.26) was found by calculating the maximum eastward group velocity for the Rossby waves using the approximate dispersion relation,

$$\omega \approx \frac{k}{2n + 1 + k^2},$$

which is valid for small ω , i.e., when (4.33) holds.

All of the eastward propagating modes are essentially trapped to the discontinuity at $x = 0$. Due to the form of the argument of the Bessel functions which appear in (4.26) and (4.27), the region where they have substantial amplitude grows thinner as time increases. In synthesizing these forms most of the amplitude was in the waves which lie at the lower left hand portion of the dispersion diagram (i.e., $\omega \ll 1$, $-k \gg 1$). These waves have very low group velocity so the "disturbance" moves away from $x = 0$ very slowly. This is true for the mixed mode as well, although its leading edge propagates away quite quickly.

4.4 Forced Response in a Bounded Basin

As indicated in the introduction to this chapter, the forced response of the equatorial ocean in a bounded basin will be calculated by first finding the motions that would be forced in an unbounded ocean. This was done in the preceding section. We now turn to the task of finding the free solutions of (4.1) needed to reduce the normal velocities to zero at the walls. That is, we seek the boundary response to the motions forced in an unbounded basin (e.g., the reflections of waves at the walls). As discussed in Section 4.2, only the effects of meridional boundaries will be considered in this section. We assume the latitudes of the zonal boundaries are sufficiently high so that they have negligible effect on the equatorial region. The basin

is taken to be rectangular with boundaries at $x = 0$, $x = X_E$ and $y = \pm \infty$.

The problem of finding the free modes needed to satisfy the boundary conditions is similar to the problem of finding the free modes needed to satisfy the jump conditions at a discontinuity that was treated in the preceding section. There were two constraints operative in that case: the jump in u and the jump in h both had to be reduced to zero for all time and all y . Here there are also two constraints. First, $u = 0$ at the boundary for all time and all y . Second, the free modes which are needed to satisfy this condition must also be ones which propagate energy away from the boundary into the interior of the basin. For example, the free modes generated by the boundary response at the western side must have eastward group velocity.

Our technique for calculating the boundary response is similar to that employed in the step function case. We will explain how to do it for the case when the motion incident at the boundary is at a single frequency ω . The case of an arbitrary time dependence is then calculated by transforming from the time to the frequency domain, obtaining the response for each frequency, and then transforming back into the time domain.

Let us assume that the incident motion has a u component at the boundary of the form

$$u = a_J \psi_{J+1}(y) e^{-i\omega t} \quad (4.35)$$

where ψ_{J+1} is, as before, the $J + 1^{\text{th}}$ Hermite function, so that an arbitrary function in y is a sum of such terms. Moore (1974) has shown how to calculate the boundary response to such a form. We review the method here. At a western boundary we seek a sum of eastward propagating (or trapped) solutions of (4.1), i.e., the $\psi_{n,e}$ of (4.31), which will cancel u at the boundary. That is, we wish to calculate the amplitude factors $a_{J,n}$ so that the sum

$$(a_J \psi_{J+1}, 0, 0) + \sum_{n=1}^{\infty} a_{J,n} \phi_{n,e} + a_{J,0} \phi_0 + a_{J,-1} \phi_{-1} \quad (4.36)$$

has a zero u component. Recall that the mixed mode and Kelvin waves have eastward group velocity for all k and ω . Since for a given ω there is only a single k which satisfies their dispersion relations they are unambiguously specified as functions of ω . The additional subscript "e" is redundant. As mentioned in Section 4.2, the u component of each $\phi_{n,e}$ with $n > 0$ may be written as a linear combination of ψ_{n+1} and ψ_{n-1} , i.e.,

$$u_{n,e} = \left[\frac{n+1}{2} \right]^{1/2} (\omega + K_{n,e}) \psi_{n+1} + \left[\frac{n}{2} \right]^{1/2} (\omega - K_{n,e}) \psi_{n-1}$$

Since $\omega \neq \pm K_{n,e}$, the coefficients are always non-zero for $n > 0$. Also, it is clear that if J is even then only those modes with n even have a u component with the same symmetry as ψ_{J+1} . Similarly, if J is odd, only the odd n modes have the same symmetry. Hence, only those modes with the same odd-even parity as J need appear in the sum (4.36).

With these facts in mind, we may construct an algorithm for calculating the coefficients $a_{J,n}$. Only modes with $n \leq J$ and $n \equiv J \pmod{2}$ are needed. First, find $a_{J,J}$ to eliminate ψ_{J+1} in the sum (4.36). This leaves ψ_{J-1} with a non-zero coefficient. Calculate $a_{J,J-2}$ to eliminate it. Continue in this way, choosing $a_{J,n}$ to eliminate ψ_{n+1} for $n = J-2, J-4, \dots$, until $n = 1$ or 2 . Which value one arrives at will depend on whether J was odd or even. Let us assume J was odd, so $n = 1$. At this point, (4.36) has only a non-zero coefficient for ψ_0 . We still have the Kelvin mode ($n = -1$) available. Its u component has only the single Hermite function ψ_0 . Therefore, when its coefficient is chosen to eliminate ψ_0 , (4.36) will have its u component identically zero. If J had been even, we would have gotten to $N = 2$ with only the coefficient of ψ_1 non-zero. The mixed mode ($n=0$) can then be used to eliminate ψ_1 and leave the u component of (4.36) identically zero. This procedure is, precisely,

$$(1) \text{ Let } a_{J,n} = 0 \text{ if } n > J \text{ or } n \not\equiv J \pmod{2}$$

$$(2) \quad a_{J,J} = -a_J \left\{ \left[\frac{J+1}{2} \right]^{1/2} (\omega + K_{J,e}) \right\}^{-1} \quad (4.37)$$

$$(3) \quad a_{J,n} = a_{J,n+2} \left[\frac{n+2}{n+1} \right]^{1/2} \left[\frac{K_{n+2,e} - \omega}{K_{n,e} + \omega} \right]$$

$$(4) \quad a_{J,-1} = a_{J,1} [K_{1,e} - \omega]$$

A mode incident on a western boundary thus stimulates a boundary response consisting of modes with the same symmetry and equal or lower meridional index n . The crucial property that allowed the procedure for calculating the $a_{J,n}$'s to terminate is that for all frequencies there is an eastward propagating wave whose u component consists of a single Hermite function. There is no similar simply structured wave propagating westward -- the Kelvin wave and mixed mode have eastward group velocity at all frequencies. Because of this, an eastern boundary cannot respond to an arbitrary incident u component with a series of modes with lower meridional index. Instead, the eastern boundary response is an infinite series of modes with higher meridional index. Formally, the eastern boundary response to the form (4.35) is a sum

$$\sum_{n=1}^{\infty} a_{J,n} \underbrace{\phi(\omega)}_{\sim n,w} \quad (4.38)$$

The coefficient $a_{J,n}$ is calculated according to the rules:

$$(1) a_{J,n} = 0 \quad \text{if } n \leq J \text{ or } n \neq J \pmod{2}$$

$$(2) a_{J,J+2} = a_J \left\{ \left[\frac{J+2}{2} \right]^{1/2} [K_{J+2,w} - \omega] \right\}^{-1} \quad (4.39)$$

$$(3) a_{J,n+2} = a_{J,n} \left[\frac{n+1}{n+2} \right]^{1/2} \left[\frac{K_{n,w} + \omega}{K_{n+2,w} - \omega} \right]$$

We now have a procedure for calculating the boundary response at the west or east for motions with an arbitrary spacial structure but with time dependence being an oscillation at a single frequency. As indicated above, these results may be extended to a motion with arbitrary time structure. To do this, analyze this time dependence into its frequency spectrum, calculate the boundary response as a function of frequency, and then synthesize overall frequencies to obtain the time dependence of this response.

We need only evaluate this final transform for the case where the original forcing is a step function in x and t . This includes the case where the forcing is independent of x , that is, the step is outside the basin. It is not difficult to do this if we make use of our previous results. In particular, the transforms that must be evaluated are similar to those that arose in finding the unbounded response to a step function forcing, if we again make the approximation (4.33) that ω is small. The complete solutions are rather lengthy and will not be given here; see Cane (1974) and Cane and Sarachik (1975) for

further details. Here we will only discuss some of the qualitative features of the boundary effects for the case of an x -independent forcing. Some supporting computational details are given in Appendix E.3. In Chapter 5, we will describe the complete basin response to the forcings $F = 1, G = Q = 0$ and $G = 1, F = Q = 0$.

We now consider the boundary corrections to the unbounded response to an x -independent wind stress, Eqs. (4.15) - (4.17). The inertia-gravity waves (4.15) all have eastward group velocity and $k = 0$. At a western boundary, the response to each such wave is a similar wave with equal amplitude but exactly out of phase. The effect is a cancellation of the original wave which propagates away from the boundary with the group velocity of the wave. This response is exactly like the step function case, Eqs. (4.21) and (4.24). These $k = 0$ inertia-gravity waves are carrying energy into an eastern boundary. The response must be motions which carry this energy away from the boundary. The largest fraction of this incoming energy goes into a long ($k = -\omega^{-1}$) westward propagating wave with the same frequency. This fraction is approximately $1 - \frac{2}{2n + 1}$ for the wave with meridional index n . The remaining energy goes into an infinite series of boundary trapped modes with the same frequency and meridional index $m > n$ and $m \equiv n \pmod{2}$ (see Appendix E.3).

The Kelvin mode part of the unbounded solution (4.17) which grows like t , may be cancelled at a western boundary by a

free Kelvin mode with the same amplitude and t, x structure like $x - t$. This is precisely like the step function response, (4.23). As was remarked in that connection, we may say that the original response is the sum of a locally forced part that goes like x and another eastward propagating part that goes like $t - x$. The western boundary has the effect of cutting off the forcing to the west of $x = 0$. This results in the propagating part of the original solution being absent for $x < t$, leaving only the locally forced part. The secularly growing Rossby modes (4.16) have qualitatively similar behavior at the eastern boundary. These modes propagate energy westward; the effect of the boundary is to cut off the source of these modes; it turns the forcing into a step function forcing which is non-zero only for $x \leq X_E$. The eastern boundary response to these modes is like the step function solution, (4.22), except that the origin is shifted from $x = 0$ to $x = X_E$ and the amplitudes have opposite sign.

The boundary response is of two different types. The first is due to the effect of converting the forcing function into a step function at the boundary, thus cutting off the energy source for motions which would otherwise propagate into the basin from beyond the boundaries. The $k = 0$ inertia-gravity waves and Kelvin mode at the western boundary and the "long wave" Rossby modes at the eastern boundary are examples of this type

of response. The other type of response is a reflection: a motion incident on the boundary carries energy from the interior toward the boundary. Since this energy cannot propagate through the boundary, the presence of the boundary excites motions which reflect this energy back toward the interior. These motions may freely propagate into the interior or they may be trapped to the boundary, thus allowing energy to accumulate there. The eastern boundary response to inertia-gravity waves discussed above is an example of a reflection. In this case, the motions generated at the boundary consisted of both boundary trapped modes and propagating waves.

The reflection of Kelvin waves at an eastern boundary is another example of this type. For an incoming wave with a frequency $\omega > 1 + \sqrt{2}/2$ the reflection is a series of inertia-gravity waves with odd meridional index n . Some of these (i.e., those for which n is high enough to make the expression under the radical sign in (4.30) negative) will be boundary trapped. For $1 - \sqrt{2}/2 < \omega < 1 + \sqrt{2}/2$ all the reflecting modes are boundary trapped since there are no westward propagating waves at this frequency. At lower frequencies the response will be in Rossby waves; again, some of these will be boundary trapped. It can be shown (Moore, 1968) that the response to an incoming Kelvin wave asymptotes to a coastal Kelvin wave as y becomes large. In our case, (4.17), the Kelvin waves present synthesize to have a linear time dependence. The reflection consists of an

infinite series of Rossby modes with odd index n . (These are given by (E13).) They are similar to the free modes, (4.22), that arose in the step function case. The mode with index n has a t, x -dependence like $t + (2n + 1) (x - X_E)$ and propagates away from the boundary with group velocity $(2n + 1)^{-1}$. Since the lower n modes propagate faster, at a given time t , this response extends further into the basin near the equator and becomes narrower with increasing y . As noted above, this response asymptotes to a coastal Kelvin wave with increasing y . Because of the beta effect, this coastal Kelvin wave has a non-zero component of group and phase velocity in the direction normal to the coast so it can propagate away from the coast, albeit slowly (Moore, 1968).

The Rossby mode, (4.16), which is part of the unbounded response to a zonal wind stress, carries energy into the western boundary. The reflection, (Appendix E.3) must have an equal energy flux to the east. It consists of modes with meridional index lower than or equal to that of the incoming mode. Most of these modes are a synthesis of short wavelength Rossby waves with low group velocity so that these modes stay near the western boundary. Most of their energy is in the v component, which is in geostrophic balance. Since their group velocity is so low, their energy density must be high in order for their energy flux to balance that of the incident motion. These features are qualitatively similar to the mid-latitude case.

This asymmetry in the character of the eastward and westward propagating Rossby waves helps to explain why currents intensify on the western side of the ocean (Pedlosky, 1965). In addition, this reflection has features which are distinctly equatorial. Specifically, each incoming wave reflects as a whole series of waves, including the mixed mode or the Kelvin wave. The mixed mode's behavior is similar to the Rossby modes. It shares the Bessel function behavior of the Rossby modes which results in the boundary current becoming thinner and more intense with time. Most of its amplitude remains near the boundary, though its leading edge propagates away with group velocity one. The Kelvin mode has a very different behavior. Kelvin waves have group velocity 1 at all frequencies. They carry energy away from the western boundary quickly, so that less of the incoming energy flux remains in the western boundary current than is the case for mid-latitudes.

The boundary response to the steady current which results from a north-south wind stress will not be discussed here (see Section 5.2). We only remark that it is qualitatively similar to the step function response. The eastern boundary response is a series of Rossby modes like those of (4.25) which have $v \equiv 0$ and u and h independent of x and t . The western boundary response is a series of boundary trapped modes like those of (4.26); they result in an intense, narrow current along the

western boundary. The amplitudes of these modes may be computed by the algorithms (4.37) and (4.39).

The most prominent effects of the boundaries were summarized in Section 3.4.

5. MODEL RESPONSE TO SIMPLE WIND STRESS PATTERNS

5.1 Introduction

In this chapter we consider the model response to some simple wind stress patterns. The results presented were obtained from the numerical integration of the model described in Chapter 2. The analytic results of Chapters 3 and 4 will be used to elucidate the model's behavior. Using the parameter values in Table 1, a timestep of .95 hours, and the grid of Table 2, it takes one hour of IBM 360/95 time to compute the nonlinear response for 400 days. The linear response can be calculated about 20 per cent faster.

The linear response is of some interest in its own right, particularly in view of recent work on equatorial waves. We are also interested in it here because of the light it sheds on the more realistic nonlinear response. Consideration of certain symmetries make the results presented below applicable to other wind stress patterns. The linear response to a uniform westerly wind may be obtained from that to the easterly wind by reversing the sign of all velocity components (u , v , w) and the layer depth, h . That is, the pattern of the response is the same but the amplitude has opposite sign. A similar rule holds for obtaining the linear response to a northerly wind from that to a southerly wind. The nonlinear response to a uniform northerly wind may be obtained from the south wind response by reflecting the latter solution about the equator

and changing the sign of v . Formally, if $u(y)$, $v(y)$, $h(y)$ is a solution for a uniform south wind, then $u(-y)$, $v(-y)$, $h(y)$ is a solution for a uniform north wind. There is no simple relation between the nonlinear responses to an east and west wind stress. A helpful way to orient oneself through all of this is to begin by considering what the wind drift part of the solution is.

Although the figures presented below are largely self-explanatory, a few preliminary comments may prove helpful. Values of quantities are generally in the scaling given in Table 1. Energy integrals are in units of $10^2 \text{ m}^3 \text{ sec}^{-1} \text{ a}^2$, where a is the radius of the earth. Values of horizontal velocities shown on the graphs are in units of $10^{-2} \text{ msec}^{-1}$ ($= 1 \text{ cm sec}^{-1}$). The values of the contour interval or scaling given below the graph reflect the original scaling of 1 msec^{-1} (see, e.g., Fig. 5.4). The values for vertically integrated transports were originally scaled in units of $10^2 \text{ m}^2 \text{ sec}^{-1}$, while the labels on the graph are in units of $\text{m}^2 \text{ sec}^{-1}$ (e.g., Fig. 5.5). The graphs labelled "layer depth" are, strictly speaking, the deviation of the layer depth from its mean value. The values below the graph are in units of 100 m., while the contour lines are labelled in units of m. Recall that for this model, h_s , the deviation of the surface height from the mean, is related to the deviation of the layer depth by $h_s = \Delta\rho/\rho = 2 \times 10^{-3} h$.

Most of the graphs are plotted in the "computational" (stretched) coordinates. This allows the graphs more area in the regions of greatest interest. Note that the arrows (e.g., Fig. 5.4) are all the same length; the magnitude of the velocity is given at the tail of the arrow and its direction is the direction of the flow without regard to stretching. That is, an arrow oriented 45 degrees from the horizontal has equal u and v components even though the stretching may be such that moving 1 cm along the page in the x direction represents 5 times the physical distance of a 1 cm space in the y direction.

5.2 Linear Response to a Uniform South Wind

We are concerned here with the linearized equations (i.e., (2.8) with $R_0 \equiv 0$ except $F_r^{-1} R_0$ finite and $h = H_1 =$ mean depth of the lower level everywhere except in the pressure gradient terms; cf., Section 3.1). The wind stress is taken as a step function turned on at $t = 0$; the wind is uniform over the basin from the south with a stress of $.465 \text{ dynes/cm}^2$. Other parameters are given in Table 1; the grid is described by Table 2. In chapters 3 and 4 the analytic tools were developed to solve for the model response to such a forcing. We now make use of those results to interpret the numerical computation, beginning with a review of the qualitative features of the initial time dependent behavior.

The method of Chapter 3 was to divide the flow into a vertically integrated transport \bar{u} and a boundary layer velocity

\tilde{u} . Extra-equatorially \tilde{u} is the Ekman transport. Extra-equatorially it quickly [0 - (20 days)] becomes a wind drift so that $\tilde{v} = 0$ and \tilde{u} is eastward in the northern hemisphere and westward in the southern hemisphere. Within about 3° of the equator (cf., (3.25)) there is a boundary layer in which interfacial friction is important; at the equator $\tilde{u} = 0$ and $\tilde{v} = \tau(y) E^{-1} \{1 - e^{-Et}\}$; this boundary layer effects the transition between the flow at the equator and the extra-equatorial wind drift solution.

The response of the transport has even symmetry about the equator (that is, \bar{u} and h are anti-symmetric and \bar{v} is symmetric about $y = 0$). The response exclusive of boundary effects consists of: a steady forced component with \bar{v} identically zero; and a time varying component composed of inertia-gravity waves (including a mixed mode) with zonal wave number k equal to zero (4.15). The steady component is depicted in Fig. 4.3. It has $\bar{u} \approx \tau(y)/y$ for large y and $\bar{u} = 0$ at the equator so $|\bar{u}|$ has maxima near the equator. At the equator the wind stress is balanced by the height gradient.

We now describe the boundary response to this flow field. At the western side the boundary response to the steady current is a synthesis of free Rossby modes with low frequency and high wavenumber; i.e., the lower left hand corner of the dispersion diagram, Fig. 4.1. This response is boundary trapped; that is, it has such a low group velocity that it can't escape from the

boundary region (except for the mixed mode; cf., Section 4.4). It transports water from south to north, but only at the western side of the basin. The inertia-gravity waves (including the $k = 0$ mixed mode) initially generated all have eastward group velocity. Therefore, as discussed in Section 4.4, the western boundary response to the n th such wave is a wave of equal and opposite amplitude propagating away at group velocity $(4n + 2)^{-1}$. The effect is to just cancel the original wave.

At the eastern side the response is more varied. There are no propagating waves at the frequency of the mixed mode; hence, the response to it is a series of boundary trapped modes. When an inertia-gravity wave with its meridional structure indexed by $n > 0$ impinges on the boundary the response is a series of boundary trapped modes together with a propagating inertia-gravity wave of index n with westward group velocity and wave number $k = -(2n + 1)^{-\frac{1}{2}}$; a long wave. Most of the energy goes into this propagating mode. When this reaches the western side, most of its energy will go into a reflected eastward propagating wave of index n and $k = 0$; that is, a wave like the original gravity wave. Propagating modes with lower meridional indexes will also be excited, but with much smaller amplitude.

The part of the boundary response described so far thus consists of boundary trapped modes plus some gravity waves

which bounce back and forth across the basin. We anticipate a final state in which the wind stress is balanced by the tilt of the sea surface in the interior (cf., (3.15)). Using the scaling and notation of Chapter 3,

$$h_y = \tau^{(y)} \text{ or } h = \int \tau^{(y)} dy = y \tau^{(y)} \quad (5.1)$$

The last equality holds when the wind stress is constant; the first as long as $\tau^{(y)}$ is a function of y only. In such a case, the wind stress has no vorticity so the Sverdrup balance requires that the transport in the interior vanish. It is possible that the state described by (5.1) would never be reached in the absence of friction. Nevertheless, one would expect the inviscid motions to adjust toward it or oscillate around it. Since the boundary trapped motions cannot effect this adjustment, it must be done by the part of the solution which has not yet been discussed; that is, the eastern boundary response to the steady part of the unbounded solution.

Denote the incoming steady velocity and height fields by $U^I(y)$ and $H^I(y)$ respectively. These satisfy

$$yU^I + H_y^I = \tau^{(y)}. \quad (5.2)$$

It follows from Section 4.4 that the eastern boundary response to this, which we will denote with superscript E , must consist of wave packets which propagate energy westward and synthesize to a form which is independent of time and has U^E and $-U^I$ at

the eastern boundary $x = X_E$. The response solution may be found by the methods of Section 4.4 or one may simply recognize from the results presented there that the answer must be of the form

$$(U^E, v^E, h^E) = \sum_{n=1}^{\infty} C_n P_R^{2n}. \quad (5.3)$$

This is a sum of Rossby modes of zero frequency and zero zonal wave number. They fall at the origin of the dispersion curve, Fig. 4.1. Each mode has $V = 0$ and U and h in geostrophic balance so that

$$v^E \equiv 0; \quad yU^E + h_y^E = 0. \quad (5.4)$$

A mode indexed by $2n$ has westward group velocity of magnitude $(4n + 1)^{-1}$; hence, for a given x and t

$$(U^E(x, t), 0, h^E(x, t)) = \sum_{n=1}^N C_n P_R^{2n} \quad (5.5)$$

where $N = N(x, t)$ is the largest integer such that

$$X_E - x \leq \frac{t}{(4N + 1)}.$$

This simply says that the solution at a point (x, t) consists only of those modes which propagate energy fast enough to have reached x from the eastern boundary. Since the group velocity decreases with increasing n , and since the modes with smaller n are more equatorially confined, for a given distance from the eastern boundary the response is felt more quickly the closer

one is to the equator. This is shown schematically in Fig. 5.1. There is no effect for points with $x < X_E - t/5$. Right at the eastern wall all modes are present; adding (5.2) and (5.4)

$$y (U^E + U^I) + (h^I + h^E)_y = \tau(y).$$

Since $U^E + U^I = 0$

$$(h^I + h^E)_y = \tau(y) \text{ or } (h^I + h^E) = \int \tau(y) dy$$

which is the balance described by (5.1). For a point away from the wall

$$(U^I + U^E, v^I + v^E, h^I + h^E) = (0, 0, \int \tau(y) dy)$$

$$- \sum_{n=N+1}^{\infty} C_n P_R^n$$

so that the last sum gives the deviation from a state of no motion with the wind stress balanced by the tilt of the height field. For a fixed x , N increases as time passes -- more and more modes arrive at the longitude x -- so the balanced state is approached more closely.¹

There may be some initial puzzlement when one first considers the mass fluxes that go with the solution outlined

¹We have obviously finessed the question of the convergence of the series (5.5). See the remarks in Section 4.2.

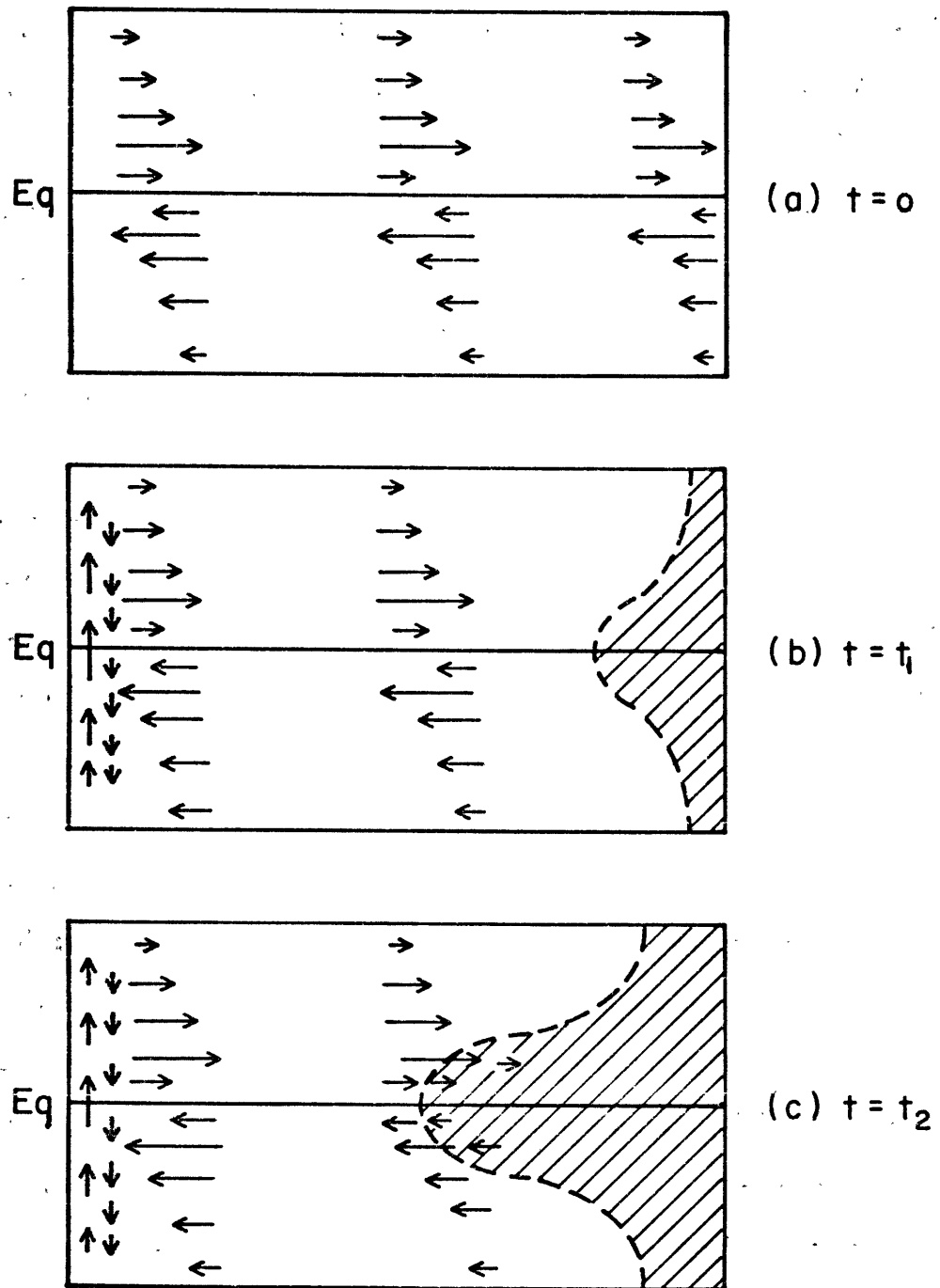


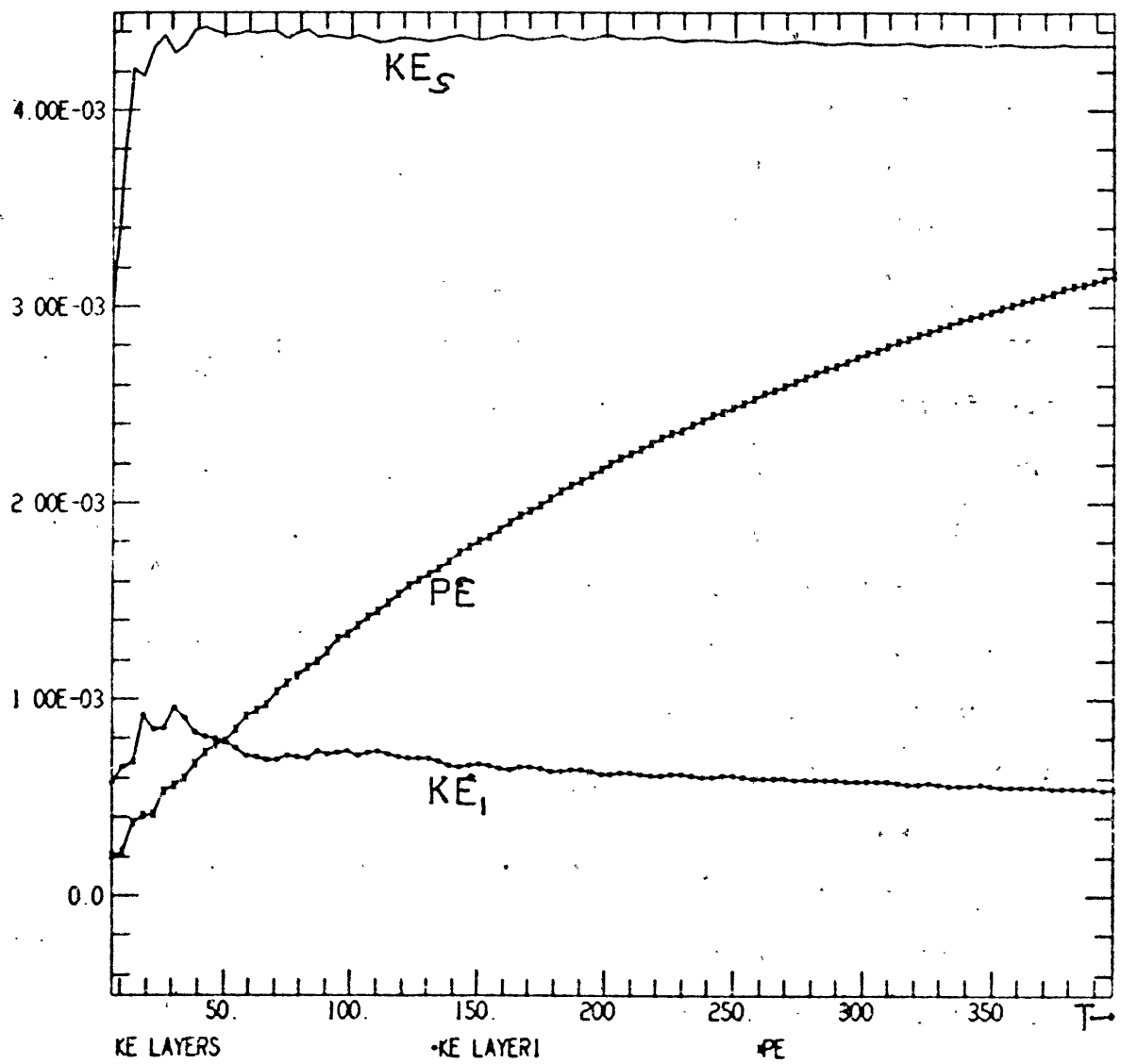
Fig. 5.1 Schematic view of linear adjustment to a South wind.

above. The adjustment which is to be reached requires that mass be moved from the southern to the northern hemisphere, yet the modes which apparently do the adjusting have no north-south velocities associated with them. The mass flow may be described as follows: When the inertia-gravity waves which are initially excited are cleared away, there remains a steady flow toward the eastern wall north of the equator and away from the eastern wall south of it. As the front which marks the edge of the eastern boundary response (the dotted line of Fig. 5.1) moves away from the wall it leaves behind a region where the zonal velocity is reduced in magnitude. Hence, there is a convergence of mass into this region north of the equator and a divergence out of it south of the equator. If there were no western boundary, this process would simply roll on toward $x = -\infty$. The presence of a western boundary makes it necessary for the mass flowing westward in the southern hemisphere to be carried northward across the equator in a western boundary current. It then flows eastward to pile up behind the front advancing from the east (Fig. 5.1). Finally, we note that there is some recirculation associated with the western boundary current. This is required to give conservation of potential vorticity in the boundary current.

We now turn to the numerical calculation of the linear response to a uniform south wind. The wind stress is turned on

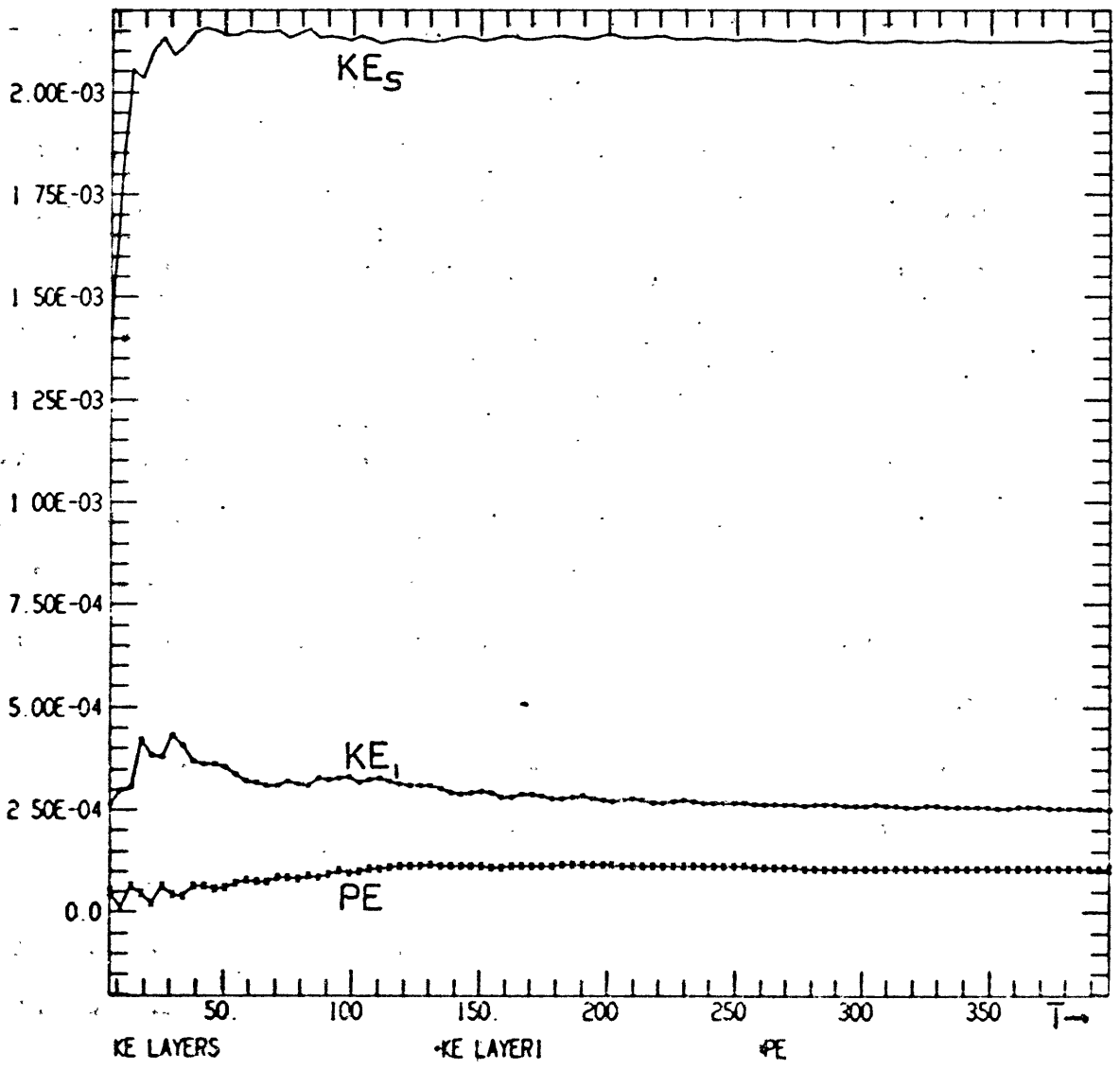
suddenly at $t = 0$; as with the analytic model, it is a step function in time.

Some of the gross characteristics of the evolution are implicit in Fig. 5.2, which gives the kinetic energies of the surface and lower layers and the potential energy in the basin. (These are defined after Eq. 2.6.) In sixteen days, the surface layer kinetic energy has attained 98 per cent of its final value, a value which changes little after this time. The lower layer kinetic energy rises to about its final value in only eight days, reaches a peak at 32 days and then diminishes until about day 60, at which point it remains approximately constant. The potential energy continues to rise as the sea surface tilts to balance the wind stress. Even after 400 days, it has not reached a final value. However, Fig. 5.3, which gives the energies in the region between 5.6° S and 5.6° N, shows that in the vicinity of the equator, the potential energy has attained its approximate final value within 100 days and is within $1/e$ of this value within 60 days. All of these time scales are consistent with analytic theory. The boundary layer velocity \bar{u} is expected to spin up with a time scale of 20 days (Eq. (3.25) ff.). Disregarding the boundaries, the transports are initially due to the generation of gravity waves with frequencies on the order of a few days. The discussion above suggests that the height field and transports (and hence, the PE and lower layer KE) in the equatorial region



ENERGIES FOR X= 0.0 TO 28.6 Y=-15.0 TO 15.0 T= 5.68 TO 396.61 DAYS
 L2E3 N4CH3 30X44STR DELT= 5 E-1. E=8.88-BI-.001 WIND= 5 SOUTH EVERYWHERE 07/23/15

Fig. 5.2 Energies from 15°S to 15°N . Linear. South wind.

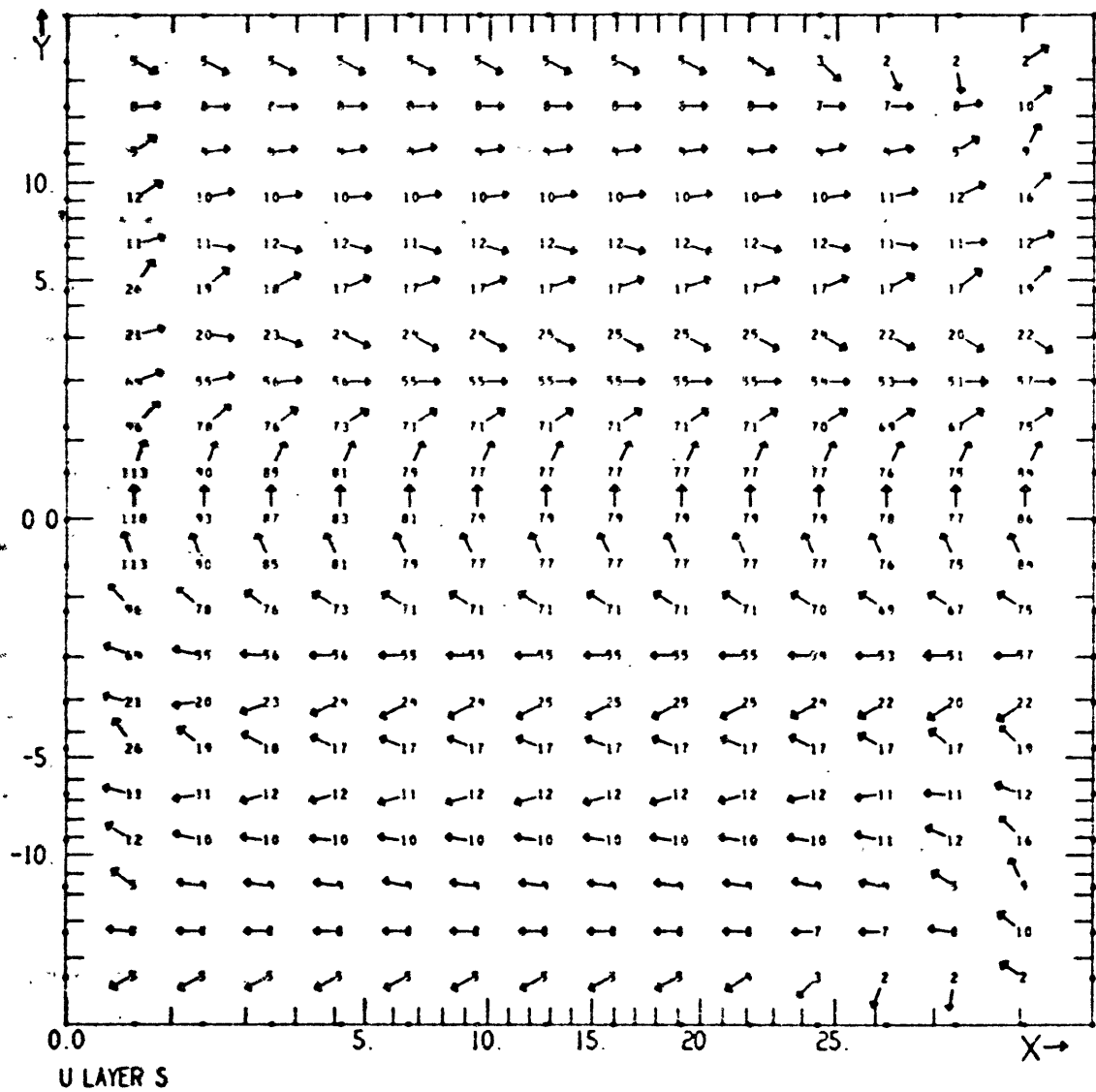


ENERGIES FOR X= 0.0 TO 28.6 Y= -5.6 TO 5.6 T= 6.68 TO 396.61 DAYS
 L2E3 N4CH3 30X44STR DELT= 5 E-1 E-8 BB-BI= 001 WIND= 5 SOUTH EVERYWHERE 07/23/15

Fig. 5.3 Energies from 5.6°S. to 5.6°N. Linear. South wind.

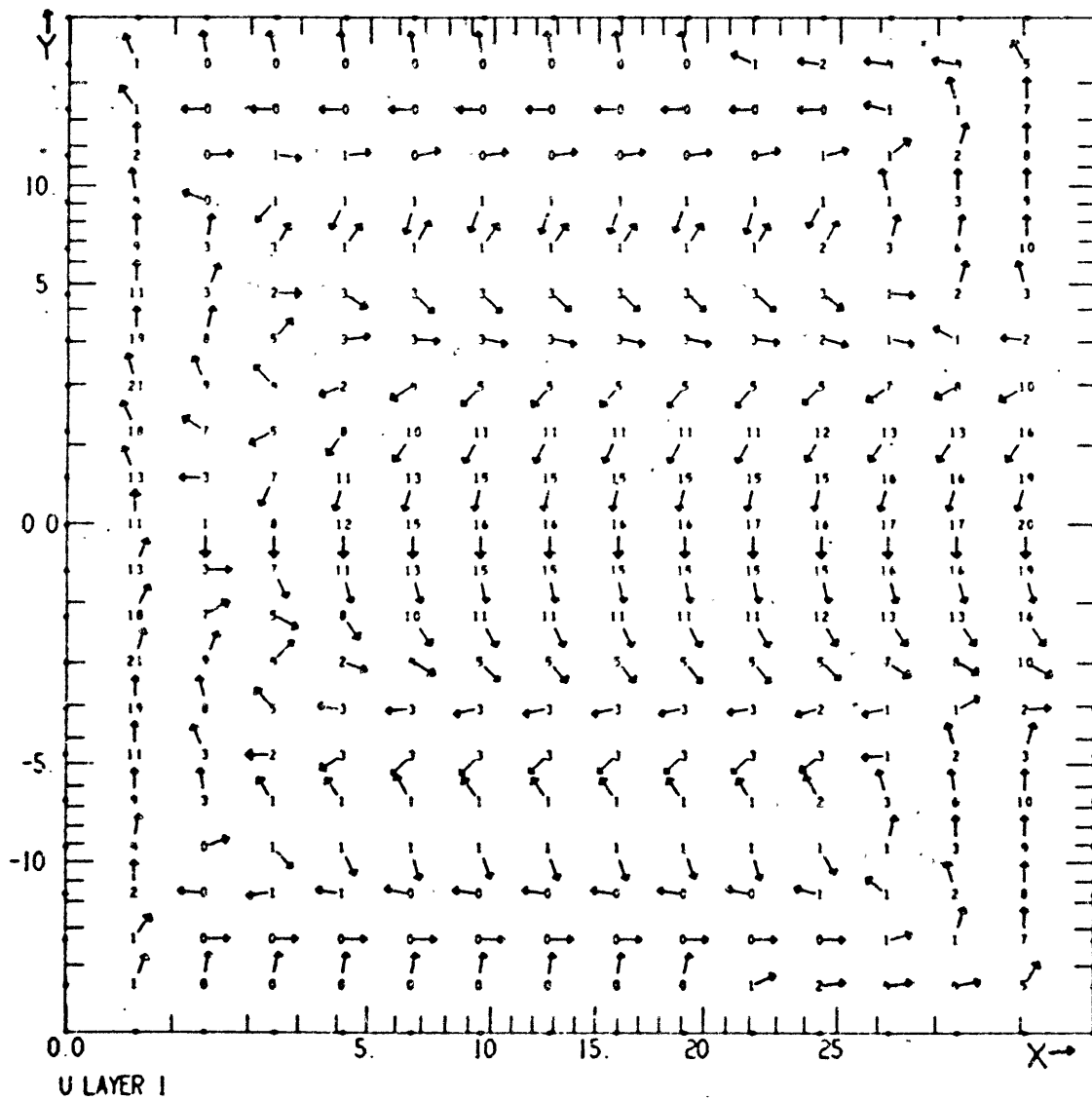
should be close to their final value when the first Rossby mode which originated at the eastern boundary has reached the western side. For the present model, this time is 96 days. In extra-equatorial regions, adjustment is via the much slower modes with a higher index n (for example, the mode $n = 10$, which has its turning point at about 13° , would take 400 days to cross the basin). In summary, the wind stress is felt directly by the upper layer which is quickly spun up to approximately its final value. The lower layer is set in motion by pressure gradient forces and by friction, but not, in this linear case, by advection of momentum from the surface layer. The lower layer KE never exceeds $1/5$ of that of the upper layer. As the height field sets up to balance the wind stress, the potential energy continues to increase, though it adjusts quickly in the vicinity of the equator.

We now consider the flow fields in some detail. At all times the model response exhibits the expected symmetries: meridional velocities are symmetric about the equator; zonal and vertical velocities and the height field are all anti-symmetric about the equator. Figs. 5.4 a and b show the velocities in the two layers after eight days. Since this is too short a time for the boundary effects to propagate far into the basin, the interior flow is uniform in x . The only substantial interior meridional velocity in the surface layer occurs in the region from 1.5° S to 1.5° N, with a maximum of



DAY 7.96 (T= 100.00 MODEL STEP 200) X= 0.0 TO 28.6 Y=-15.0 TO 15.0
 L2E3 N4CH3 30X44STR DELT= 5 E=1.E-8,B8=B1= .001 WIND= 5 SOUTH EVERYWHERE 07/23/1!

Fig. 5.4a u^S vectors at 8 days. Linear. South wind.



DAY 7.96 IT= 100.00 MODEL STEP 2001 X= 0.0 TO 28.6 Y=-15.0 TO 15.0
 L2E3 N4CH3 30X44STR DELT= 5 E=1 E=8,B8=81= 001 WIND= 5 SOUTH EVERYWHERE 07/23/15

Fig. 5.4b u^1 vectors at 8 days. Linear. South wind.

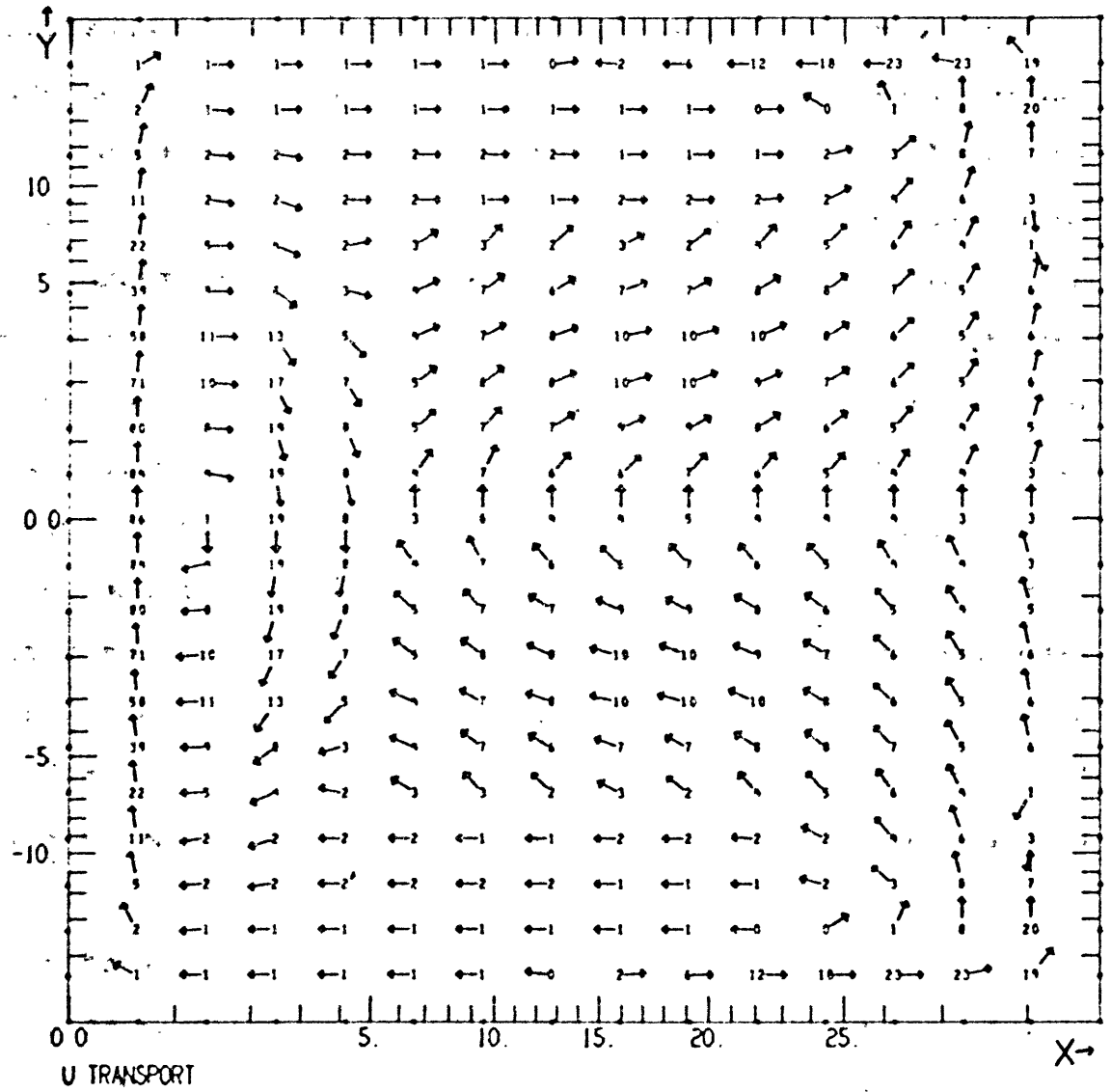
.8m sec⁻¹ at the equator. This is clearly a product of the frictionally induced component \tilde{v} ; there is an opposite and (approximately) equal meridional transport in the lower layer. This roll circulation is completed by a narrow region of strong downwelling centered at 1.2° N and a corresponding upwelling region south of the equator. The zonal component of the interior flow is essentially given by the Ekman wind drift -- to the right of the wind in the northern hemisphere and to the left of it in the southern hemisphere. The magnitude of this component increases toward the equator until the effect of the interfacial friction becomes significant, reducing it to zero at the equator. Poleward of about 2.5° the lower layer zonal flow is in the same direction as that in the upper layer, being driven that way by both frictional and pressure forces. Equatorward of this point the lower layer flow is opposite to that above. Thus, vertically integrated transport is everywhere eastward in the northern hemisphere and westward in the southern, with extrema at 3° (cf., Fig. 4.3). The interior surface height is consistent with this transport: it tilts upward from 3° S to 3° N and returns rapidly to zero poleward of these latitudes.

The boundary responses are already discernable by 8 days. The strongest meridional velocities in both layers occur at the western boundary. The maximum transport is at the equator, though the subsurface extrema are at 3°. At the eastern side,

the boundary effect is seen most clearly in h , and U^1 . At this time, the fastest moving symmetric mode ($n = 2$) should have its leading edge 2.5° from the eastern boundary. Only at the eastern side does the layer depth slope upward to the north poleward of 3° .

At 16 days the pattern of the adjustment process may be seen from the vertically integrated transport, Fig. 5.5. The meridional transport shows an intense, narrow, northward jet along the western boundary. Adjacent to this is a broader, weaker southward jet. This is due to the Bessel function behavior of the boundary response described in Chapter 4. The northward jet is stronger and narrower than it was at 8 days, at which time the southward flow was not apparent. The zonal component shows a wavelike pattern with the wavelength increasing and the amplitude diminishing to the east (note that by this time the leading edge of the mixed mode would have propagated 24° of longitude from the western boundary). This pattern merges into the westward moving region of lower transport near the eastern wall.

The evolution of the model circulation proceeds as we have outlined above. Significant meridional transports take place only near the western boundary. These northward currents continue to narrow, reaching a width of less than 1° in 30 days; thereafter, frictional forces prevent a further narrowing (Lighthill, 1969). The zonal flow also shows the wavelike

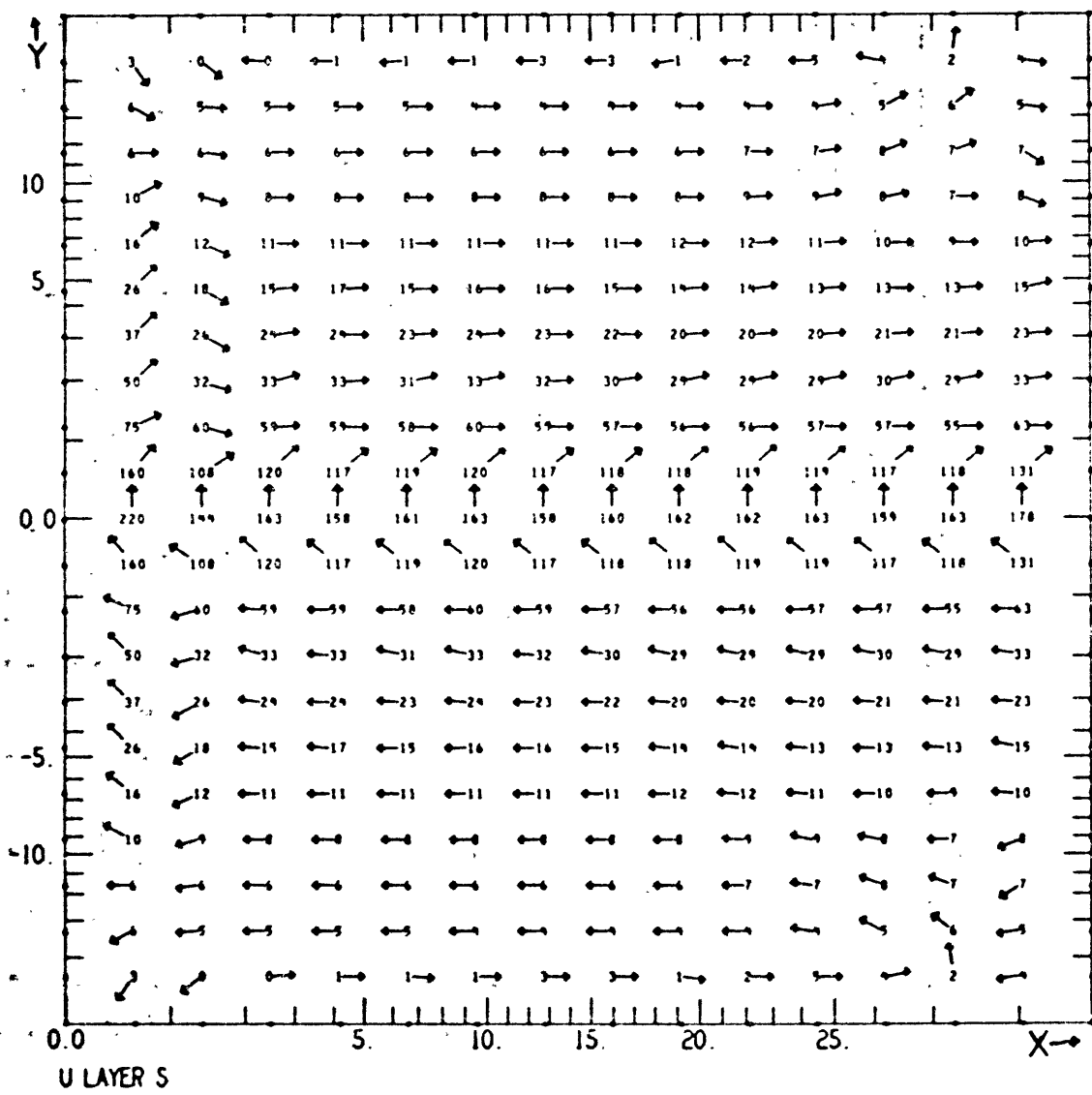


U TRANSPORT
DAY 15.92 (T= 200.00 MODEL STEP 400) X= 0.0 TO 28.6 Y=-15.0 TO 15.0
L2E3 N4CH3 30X44STR DELT=.5 E-1.E-8,BB-BI=.001 WIND=.5 SOUTH EVERYWHERE 08/05/21 (

Fig. 5.5 \bar{u} vectors at 16 days. Linear. South wind.

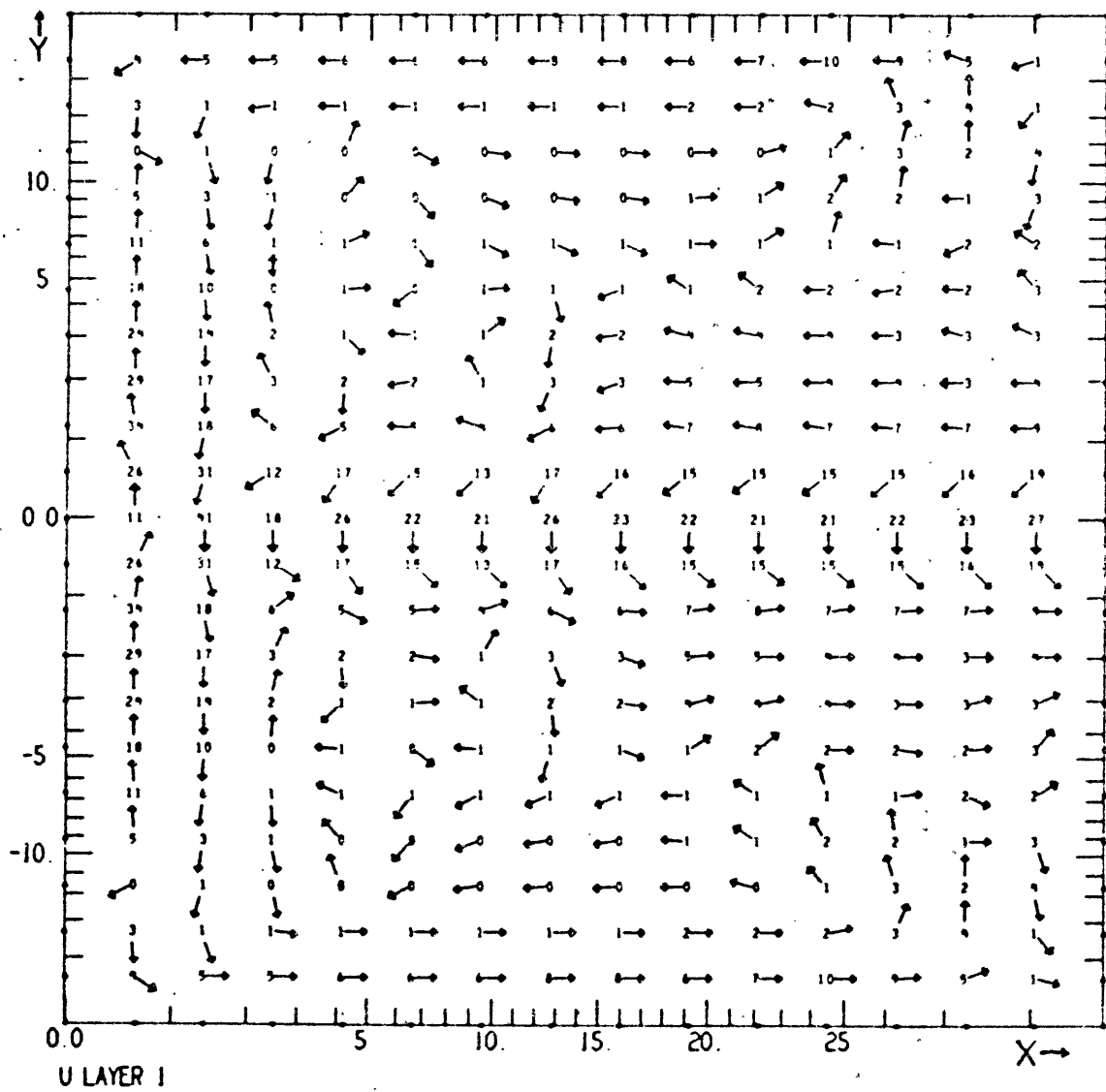
Bessel function pattern squeezing toward the western boundary. The only other sizeable meridional velocities are equatorially confined: by day 16, these frictionally controlled currents are within $1/e$ of their final values. The main adjustment proceeds from east to west, leaving a region where the height slopes upward to the north and the zonal velocities are reduced. Indeed, in some places the transports are opposite to the wind drift velocity (e.g., they are westward north of the equator). We note also that the boundary trapped modes generated along the eastern wall turn the corner and proceed westward along the northern and southern boundaries. As is the case for the western boundary current, the layer depth tilts to geostrophically balance these boundary currents. Figs. 5.6 a, b and c depict the velocity fields and layer depth contours at 40 days. At this time, the leading edge of the eastern boundary response is at $x = 16^\circ$.

Figs. 5.7 a, b and c afford a different view of the adjustment process. They show north-south sections of the layer depth at positions 3.2° from the eastern boundary, at the center of the basin, and 3.2° from the western boundary. These figures clearly support the claim that the adjustment process proceeds from east to west with the equatorial region reaching its final configuration most rapidly. After 20 days, the $n = 2$ and $n = 4$ modes will have passed the point 3.2° from the eastern boundary and the layer depth in the equatorial region



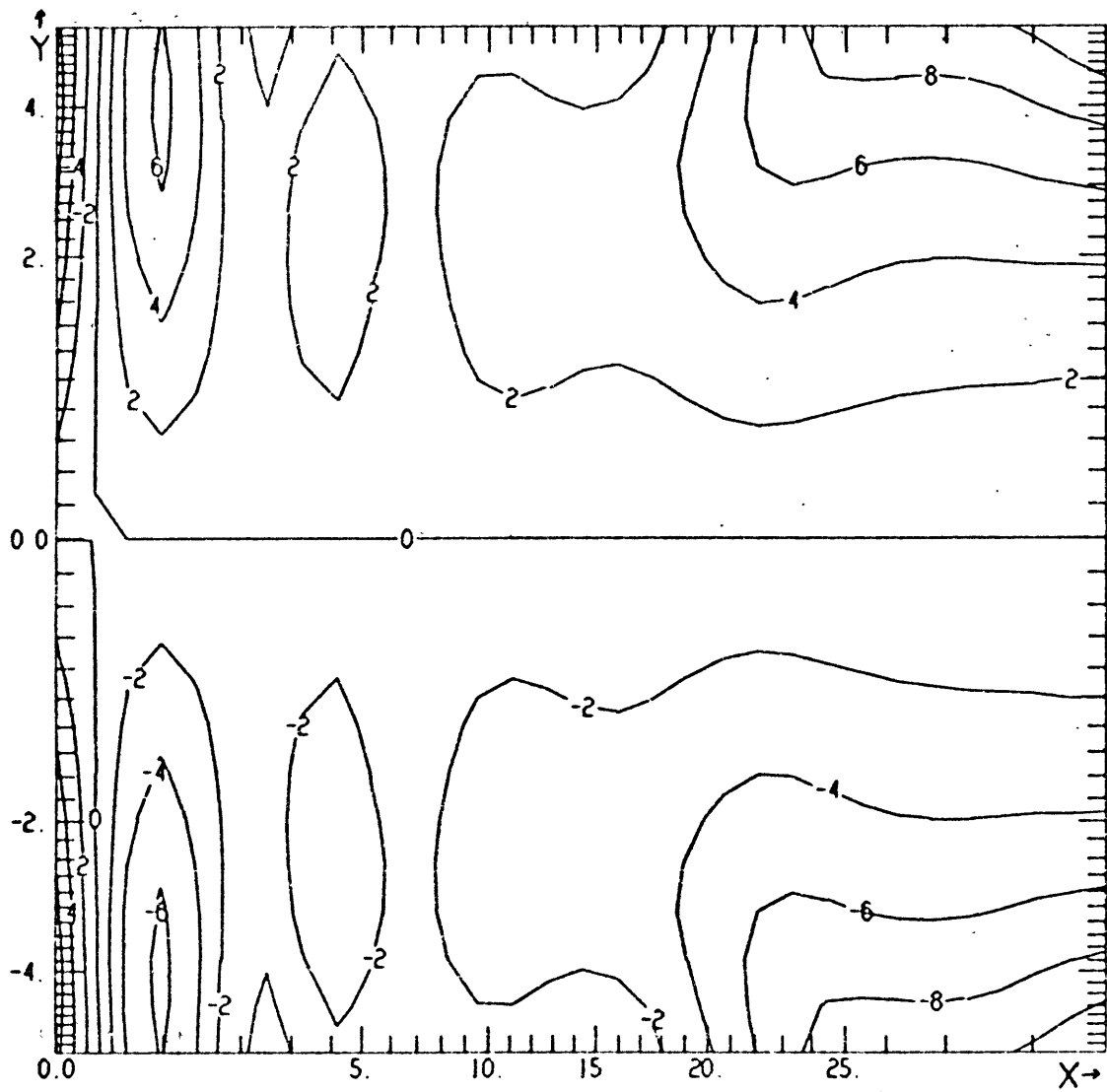
U LAYER S
 DAY 39.79 (T= 500.00 MODEL STEP 1000) X= 0.0 TO 28.6 Y=-15.0 TO 15.0
 L2E3 N4CH3 30X44STR DELT= .5 E-1 E-8 BB=BI=.001 WIND= 5 SOUTH EVERYWHERE 07/23/15

Fig. 5.6a \vec{u}^s vectors at 40 days. Linear. South wind.



DAY 39 79 (T= 500 00 MODEL STEP 1000) X= 0 0 TO 28 6 Y=-15 0 TO 15 0
 L2E3 N4CH3 30X44STR DELT= 5 E-1 E-8.BB-BI= 001 WIND= 5 SOUTH EVERYWHERE 07/23/15

Fig. 5.6b u^1 vectors at 40 days. Linear. South wind.



LAYER DEPTH LOW--1.20E-01 HIGH+ 1.20E-01 CI- 2 * 1 E-02

DAY 39.79 IT- 500.00 MODEL STEP 1000) X- 0.0 TO 28.6 Y- -5.6 TO 5.6
 L2E3 N4CH3 30X44STR DELT- 5 E-1 E-8, BB-BI- .001 WIND- .5 SOUTH EVERYWHERE 08/05/21

Fig. 5.6c h contours at 40 days. Linear. South wind.

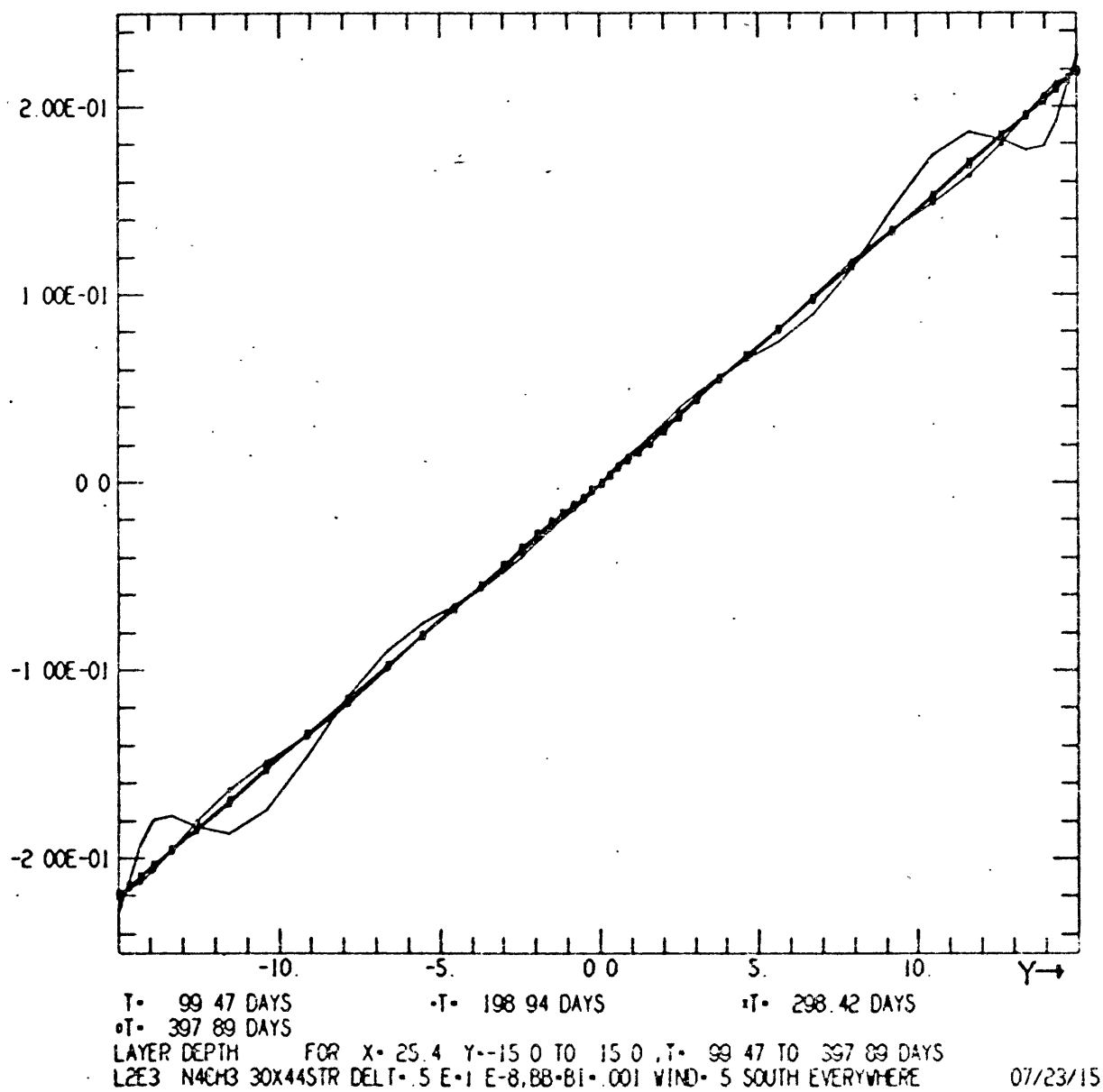
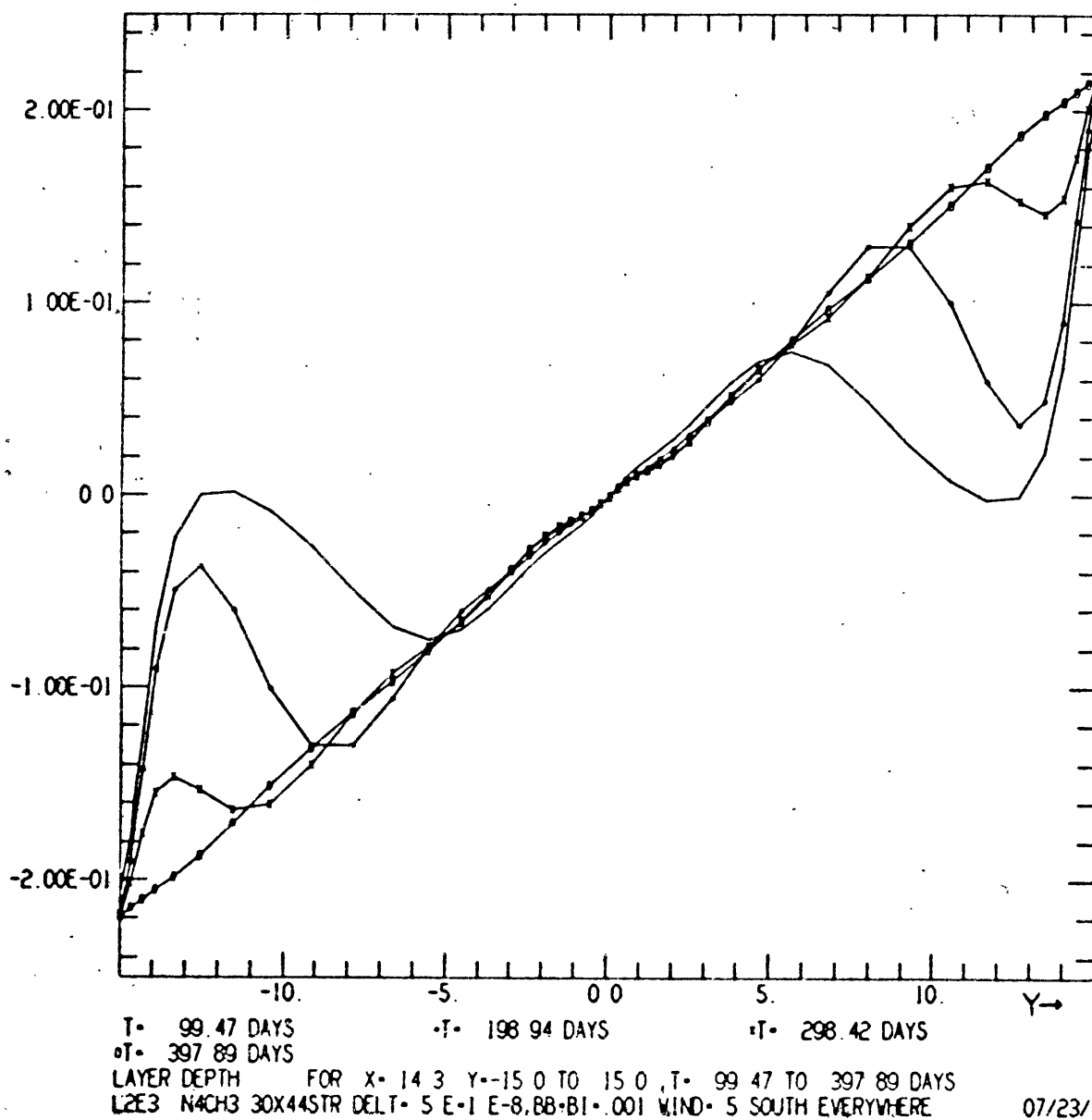


Fig. 5.7a Meridional sections of h to day 398 at $x=25.4^\circ$. Linear. South wind.



07/23/15

Fig. 5.7b Meridional sections of h to day 398 at $x=14.3^\circ$. Linear. South wind.

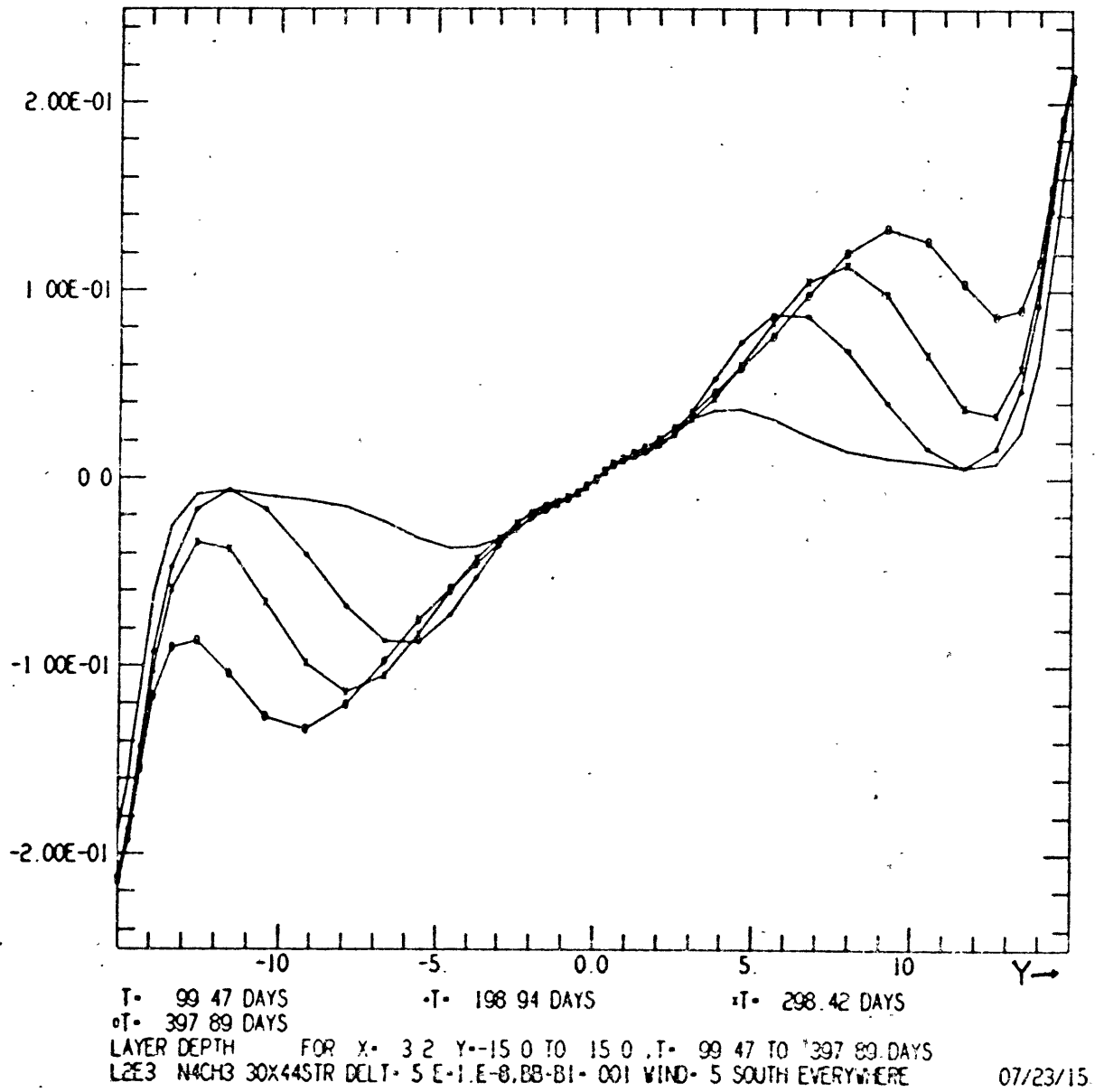


Fig. 5.7c Meridional sections of h to day 398 at $x=3.2^\circ$. Linear. South wind.

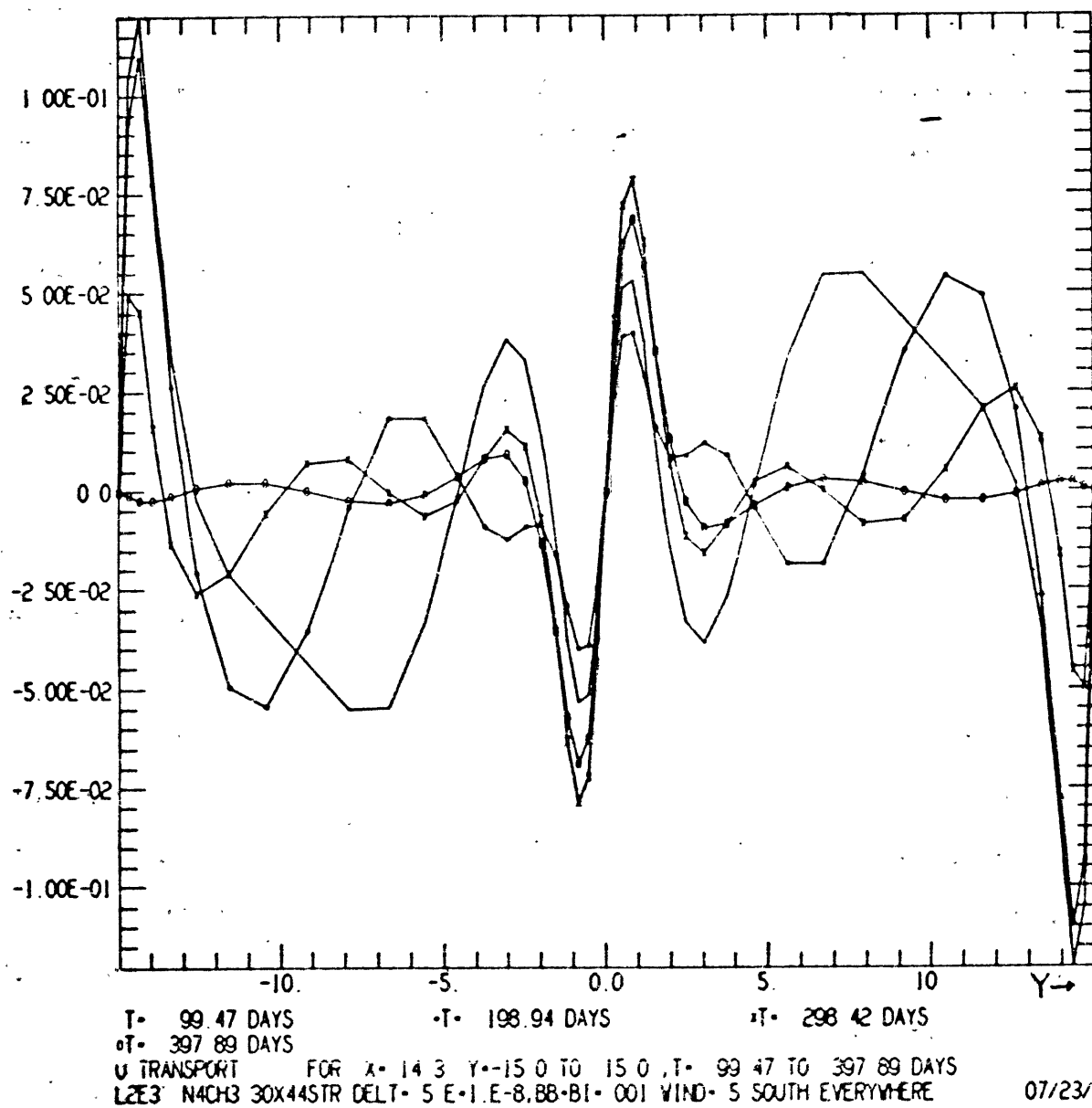
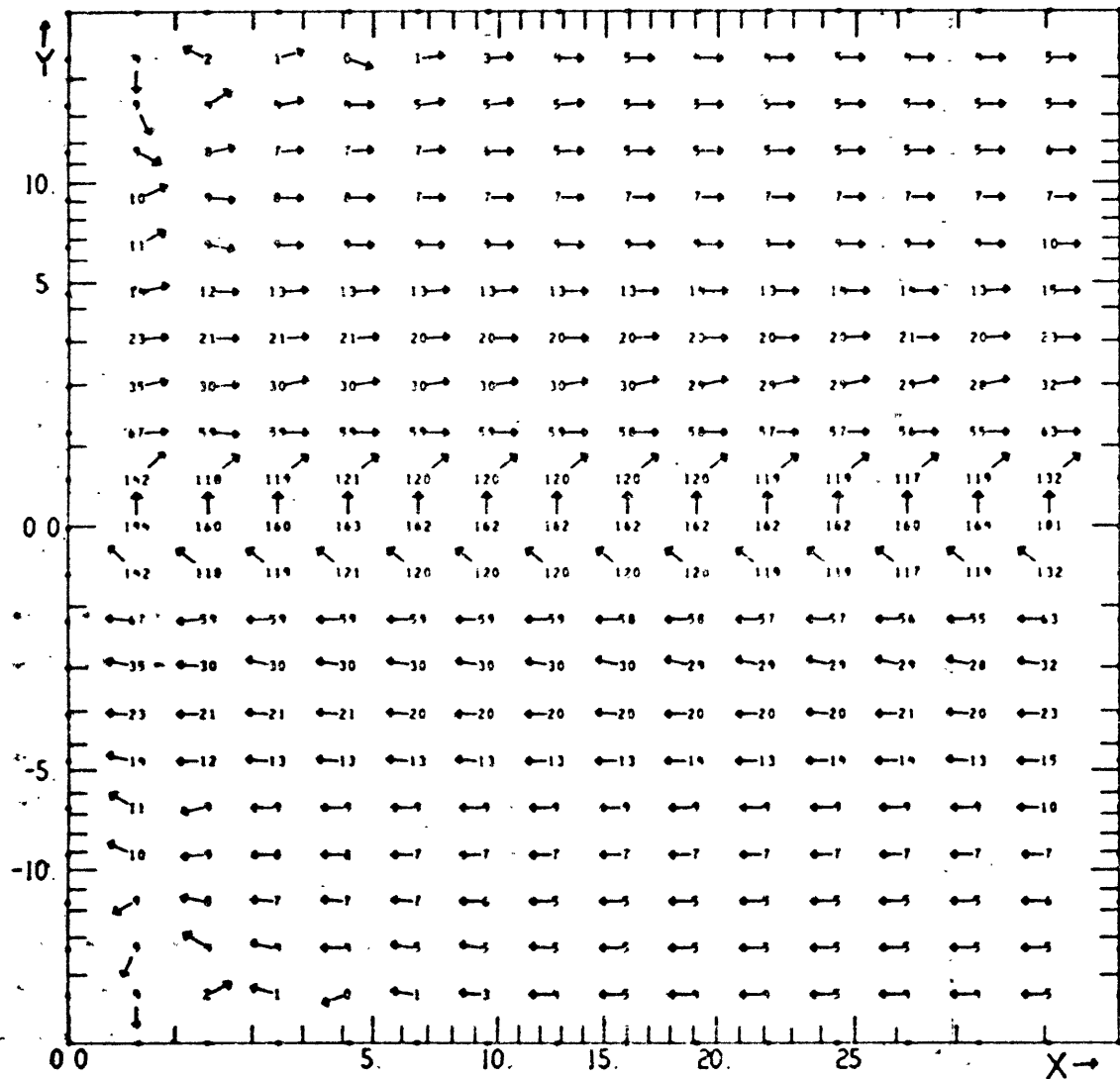


Fig. 5.8 Meridional sections of \bar{u} to day 398 at $x=14.3^\circ$. Linear. South wind.

(i.e., 5° S to 5° N) has already reached its final value. The points at 12° N and 12° S do not adjust until day 100. At the center of the basin ($x = 14.3^{\circ}$) the $n = 4$ mode passes at day 64 after which the equatorial region is spun up; the points at 12° take about 300 days to reach their final state. The comparable times for $x = 3.2^{\circ}$ are 114 and over 400 days respectively. We may say that the equatorial region spins up on the order of 100 days. Fig. 5.8 showed a similar picture for the zonal transport at the center of the basin.

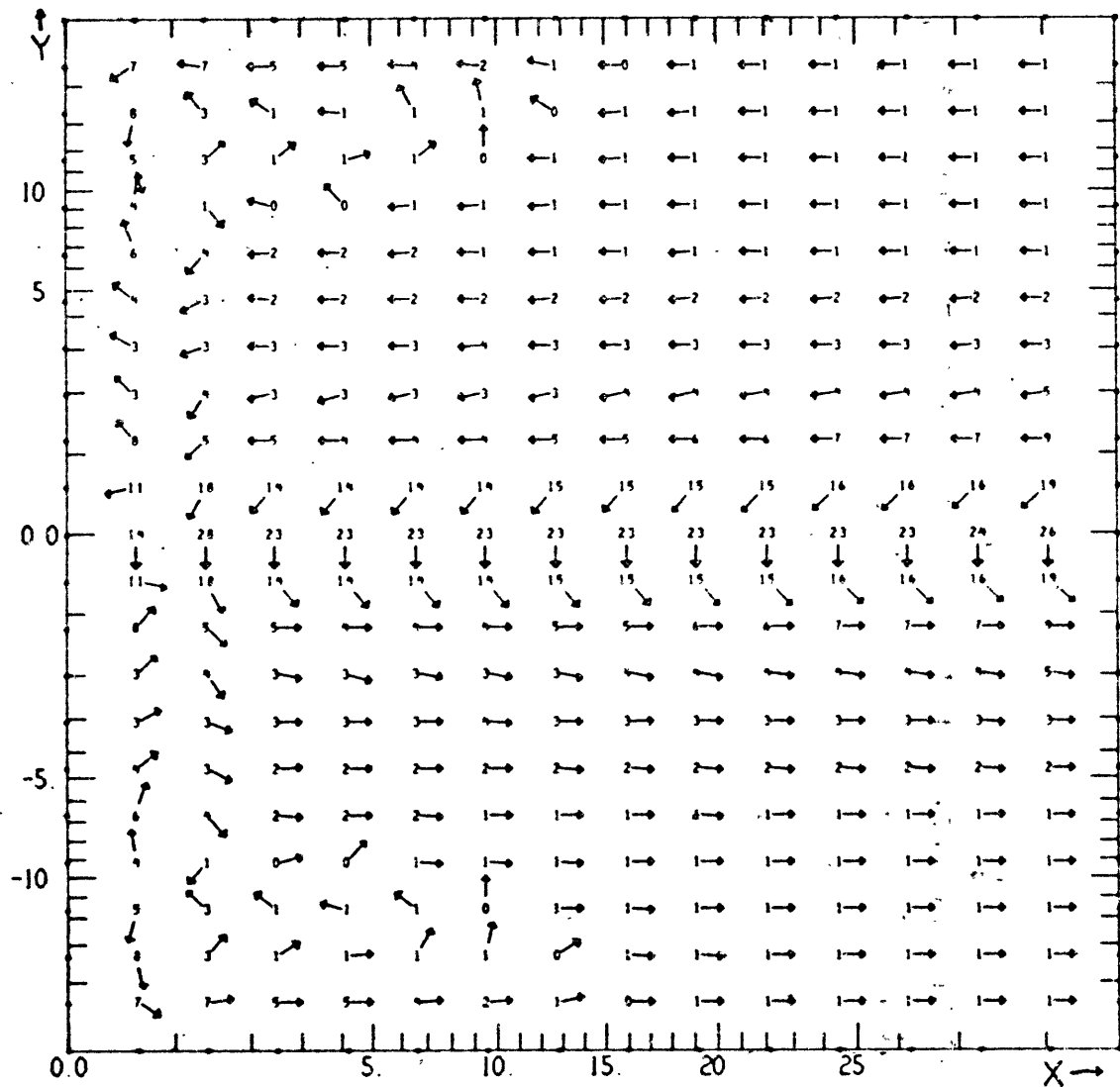
Figs. 5.9 and 5.10 show the currents, the layer depths and the contours of the zonally integrated transports at 398 days. The layer depth contours (Fig. 5.9c) reveal the extent to which adjustment is complete. The contours are by and large zonally oriented, sloping upward from a displacement below the mean depth of 22 m at the southern edge of the basin to one 22 m above it at the north. Only a small region at the northwest and southwest corners deviate from this pattern. The surface currents show zonal wind drift currents together with the meridional current in the equatorial friction layer. In most of the basin the lower layer currents are just those needed to reduce the vertically integrated transports to zero. The zonal component of these currents is in geostrophic balance with h . The exceptions to this description can be seen in Fig. 5.10, which depicts the vertically integrated transports. There is a substantial northward transport at the western



U LAYER 5

DAY 397 89 (T- 5000 00 MODEL STEP 10000) X- 0 0 TO 28 6 Y--15 0 TO 15 0
 LZES N4CM3 30X44STR DELT-.S.E-1 E-8.88-B1- 001 WIND- 5 SOUTH EVERYWHERE 07/23/14

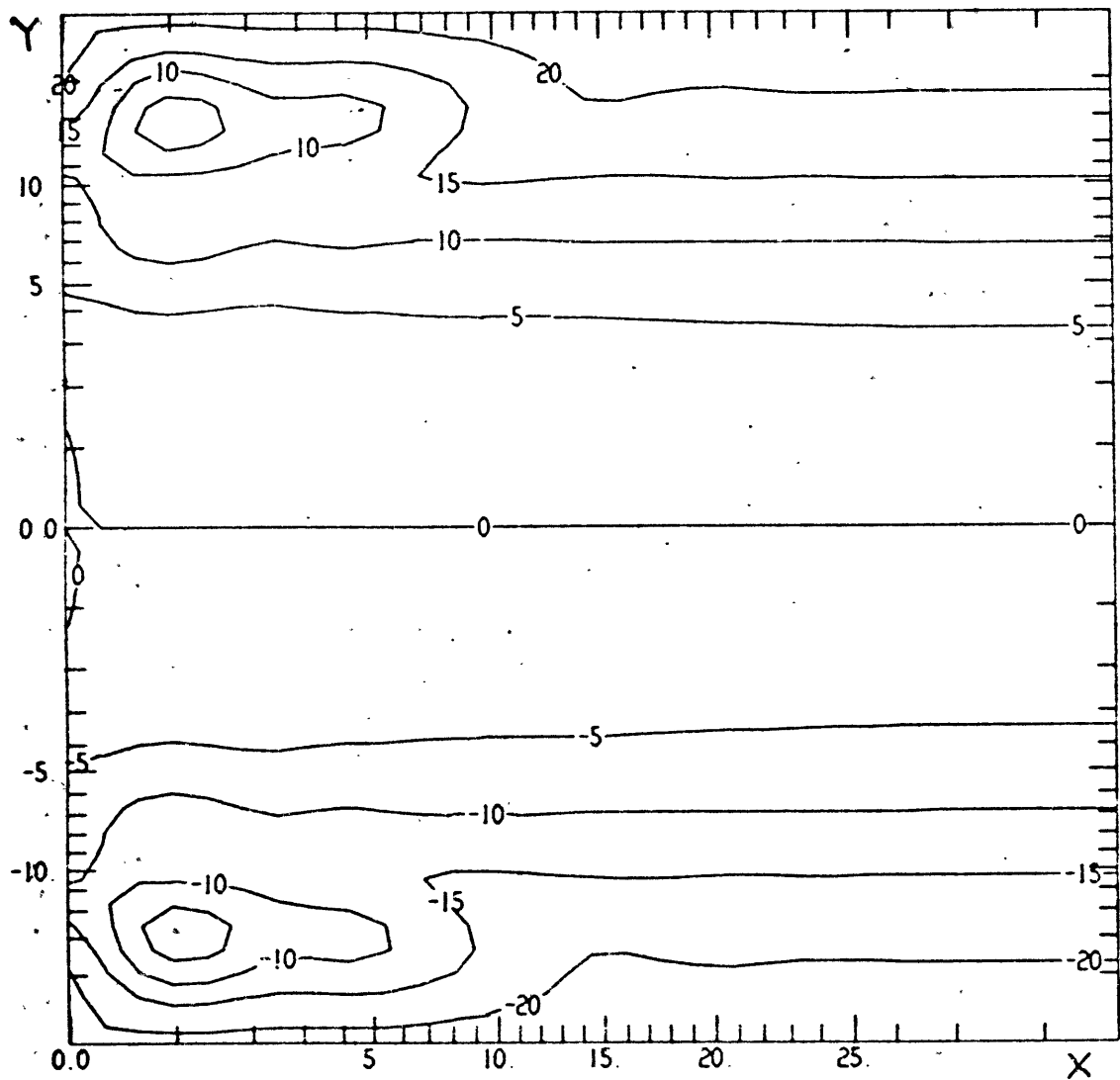
Fig. 5.9a u^s vectors at 398 days. Linear. South wind.



U LAYER 1

DAY 397.89 (T= 5000.00 MODEL STEP 10000) X= 0.0 TO 28.6 Y=-15.0 TO 15.0
 L2E3 N4CH3 30X44STR DELT= 5 E-1 E-8.BB-BI-.001 WIND= 5 SOUTH EVERYWHERE 07/23/1

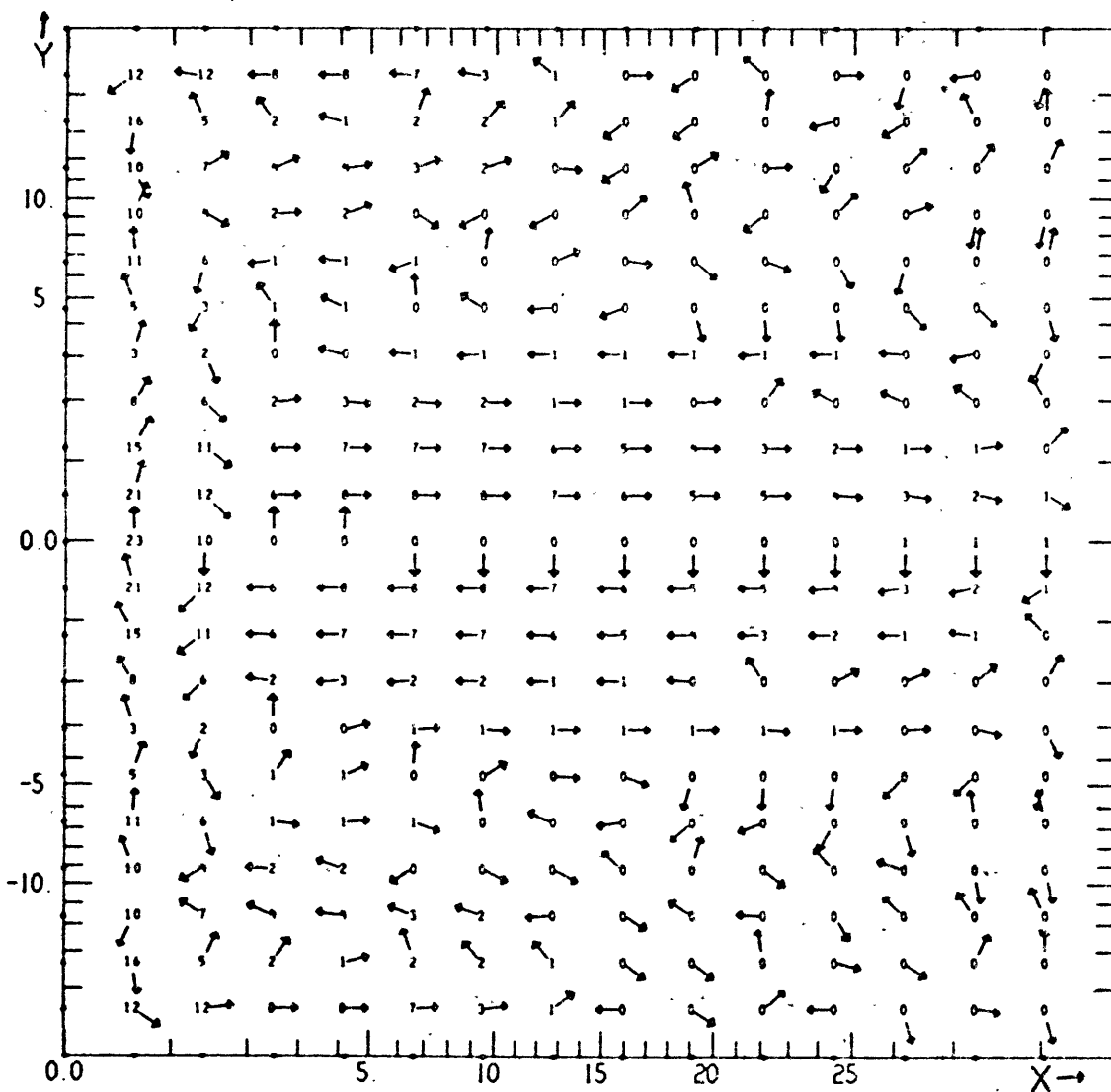
Fig. 5.9b \vec{u}^1 vectors at 398 days. Linear. South wind.



LAYER DEPTH LOV--2 19E-01 HIGH+ 2 19E-01 CI+ 5+ 1 E-02

DAY: 397 89 1T+ 5000 00 MODEL STEP 10000) X+ 0 0 TO 28 6 Y+-15 0 TO 15 0
 L2E3 N4CH3 30X44STR DELT+ .5 E+1.E-8,B8+81+ 001 WIND+ 5 SOUTH EVERYWHERE 07/23/15

Fig. 5.9c h contours at 398 days. Linear. South wind.



U TRANSPORT

DAY 397 89 (T= 5000 00 MODEL STEP 10000) X= 0.0 TO 28.6 Y=-15.0 TO 15.0
L2E3 N4CH3 30X44STR DELT= 5 E=1 E=8,BB=BI= 001 WIND= 5 SOUTH EVERYWHERE 07/23/15.3

Fig. 5.10 \bar{u} vectors at 398 days. Linear. South wind.

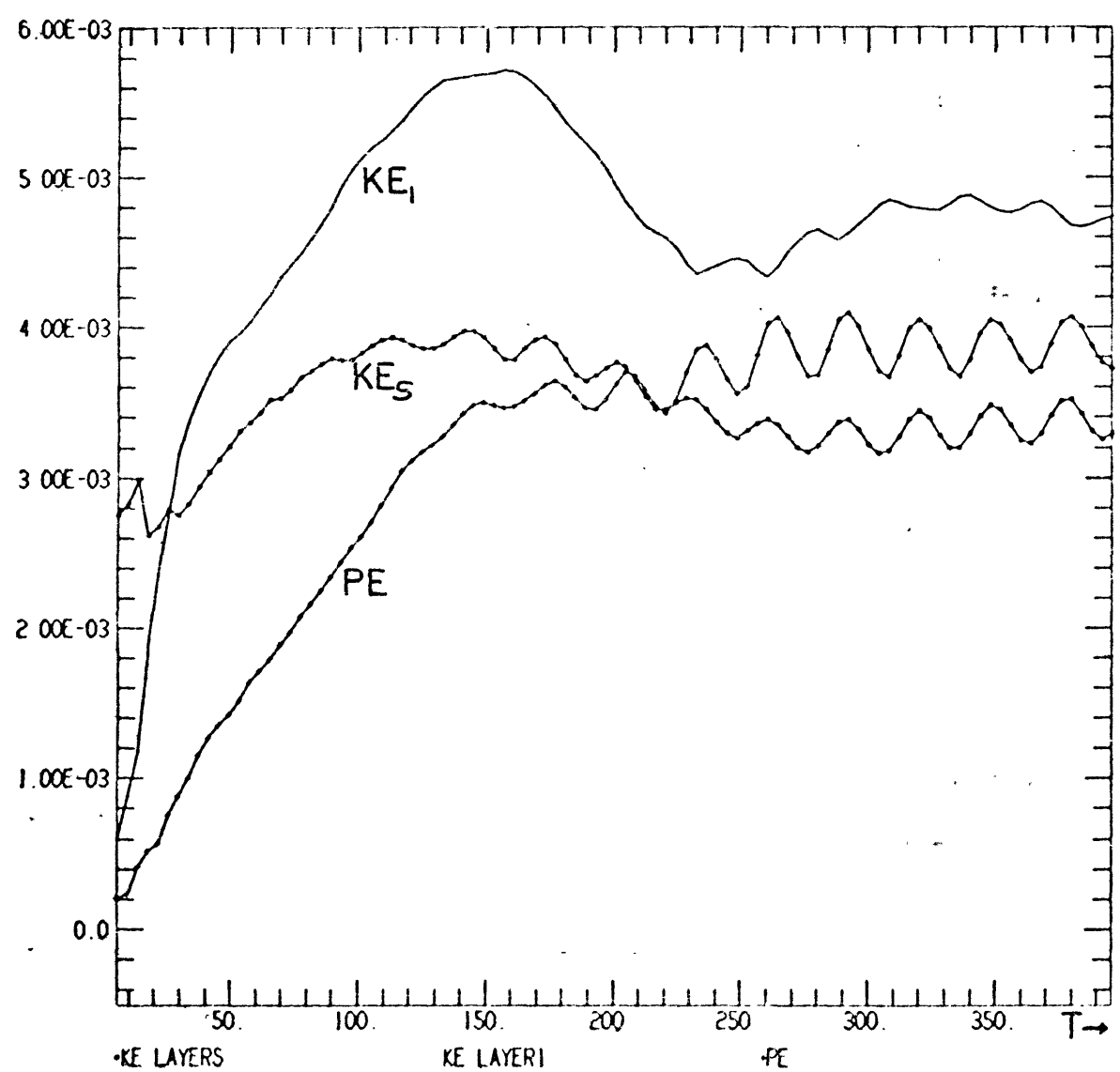
boundary (though its maximum value, $33.5 \text{ m}^2 \text{ sec}^{-1}$, is less than $1/3$ of the maximum of $118 \text{ m}^2 \text{ sec}^{-1}$ attained at day 30). Part of this -- a constantly diminishing part -- is required to move fluid from south to north to complete the overall adjustment to a final steady state. The remainder is needed to complete the circulation induced by bottom friction in an equatorial boundary layer (eq. (3.17) ff.). Away from the boundary this circulation is primarily zonal with the net transport across the equator (cf., (3.21)). As predicted, the boundary layer broadens from east to west. Superimposed on this steady-state pattern of zonal transport, one may see the wavelike pattern associated with the western boundary current. Note how similar the currents at 398 days are to those at 40 days (Fig. 5.6). The currents, even in the lower layer, are largely given by the friction component u and the frictional spin up time is on the order of 20 days. There is a marked difference in the layer depths (Figs. 5.6c and 5.9c) which adjust on the transport setup time scale, 0 (3 months) at the equator.

5.3 Nonlinear Response to a Uniform South Wind

In this section we will treat the nonlinear (Eqs. 2.8) response to a wind which is everywhere from the south. Except for the nonlinearity, this case is governed by parameters identical to those of the linear response discussed in the previous section.

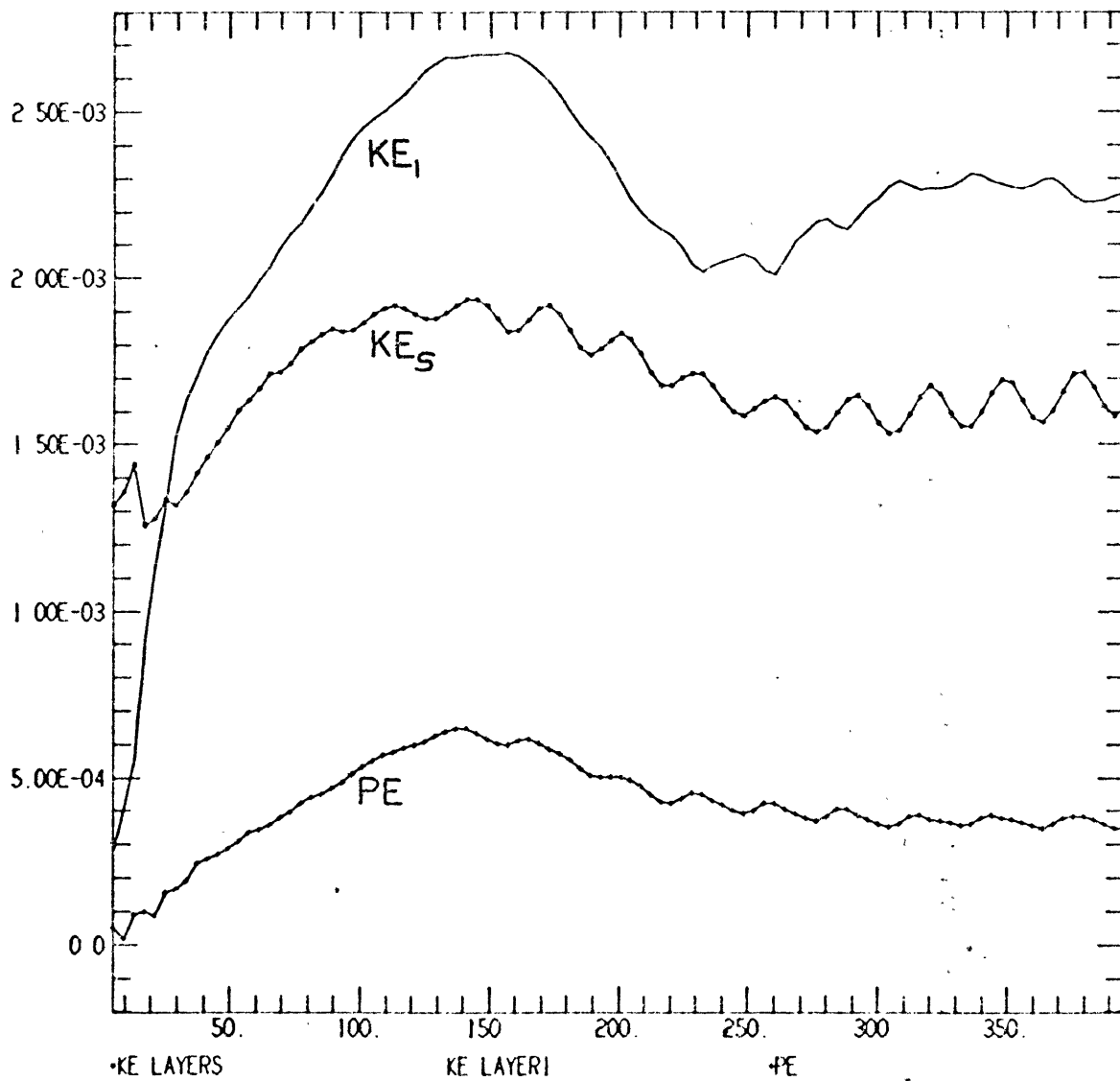
An overview of the spin up process is given by Figs. 5.11 and 5.12, which depict the energies integrated over the entire basin and the equatorial region, respectively. As in the linear case, the surface layer kinetic energy quickly (order 8 days) rises to within $1/e$ of its final value as the wind stress transfers energy to the ocean. Thereafter, the increase in surface energy is slowed, but the increase in lower layer kinetic energy and potential energy continue until about day 150, reaching peaks of 5.8×10^{-3} and 3.3×10^{-3} , respectively. Recall that in the linear case (Fig. 5.2) KE_1 was always less than 10^{-3} , while PE took 400 days to reach a value of 3×10^{-3} . The final mean value for KE_s of 3.8×10^{-3} is only slightly smaller than the linear case value of 4.4×10^{-3} . These differences suggest the importance of vertical advection as a mechanism for transferring momentum to the lower layer. After such a transfer has been made, the lower layer currents may transport significant amounts of mass. This allows for a faster buildup of potential energy than is possible when mass redistribution is accomplished primarily via the thin surface boundary layer, as is the case in the linear model. A comparison of Figs. 5.11 and 5.12 shows that about half of the kinetic energy but only about 10 per cent of the potential energy is in the region within 5.6° of the equator (about $1/3$ of the basin).

Beginning at about day 100 an oscillation with a period of 29 days may be observed in the surface kinetic energy. At



ENERGIES FOR X= 0.0 TO 28.6 Y=-15.0 TO 15.0, T= 5.25 TO 395.18 DAYS
N2E3 N4CH3 30X44STR DELT= .5 E-1.E-8,BB-BI= .001 WIND= S SOUTH EVERYWHERE 07/15/02

Fig. 5.11 Energies from 15°S to 15°N. Nonlinear. South wind.



ENERGIES FOR X= 0.0 TO 28.6 Y= -5.6 TO 5.6 , T= 5.25 TO 395.18 DAYS
 N2E3 N4CH3 30X44STR DELT= 5 E-1 E-8; BB=BI= .001 WIND= .5 SOUTH EVERYWHERE 07/15/02

Fig. 5.12 Energies from 5.6°S to 5.6°N. Nonlinear. South wind.

about day 100 an oscillation with a period of 29 days may be observed in the surface kinetic energy. At about 150 days, an oscillation in the potential energy sets in approximately in phase with this. The lower layer kinetic energy starts to decrease, eventually leveling off to oscillate about a steady value, the oscillations being out of phase with those in the other quantities. This suggests an instability which draws its energy primarily from the kinetic energy of the flow in the lower layer. Fig. 5.13 shows a plot of phase lines of the lower layer zonal velocity at the equator -- the abscissa is distance along the equator, the ordinate is time. Beginning near the western side at about day 100 and appearing later at the eastern side, a very regular progression of phase from east to west may be observed (similar plots of the other variables give essentially the same picture). These waves have a period of 29 days and a phase speed of 32.5 km/day, giving a wavelength of 950 km.

In order to understand the phenomenology of this spin up we turn to a consideration of the evolution of the currents and the layer depth. In the early stages some insight may be gained by a comparison with the linear case. Many of the features of the flow pattern can be understood by considering the kinematic effects of the vertical and meridional advectons on the linear response.

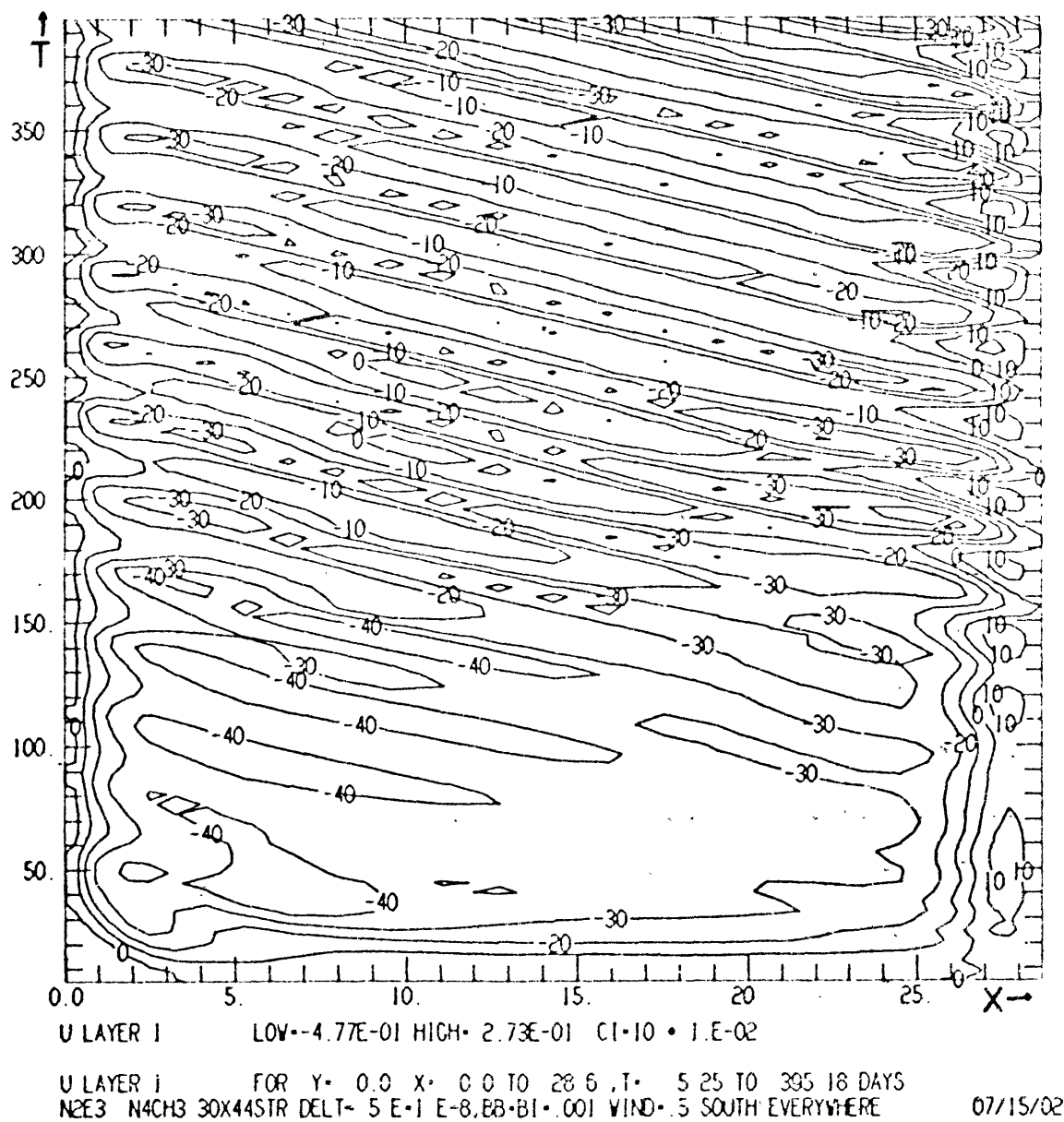
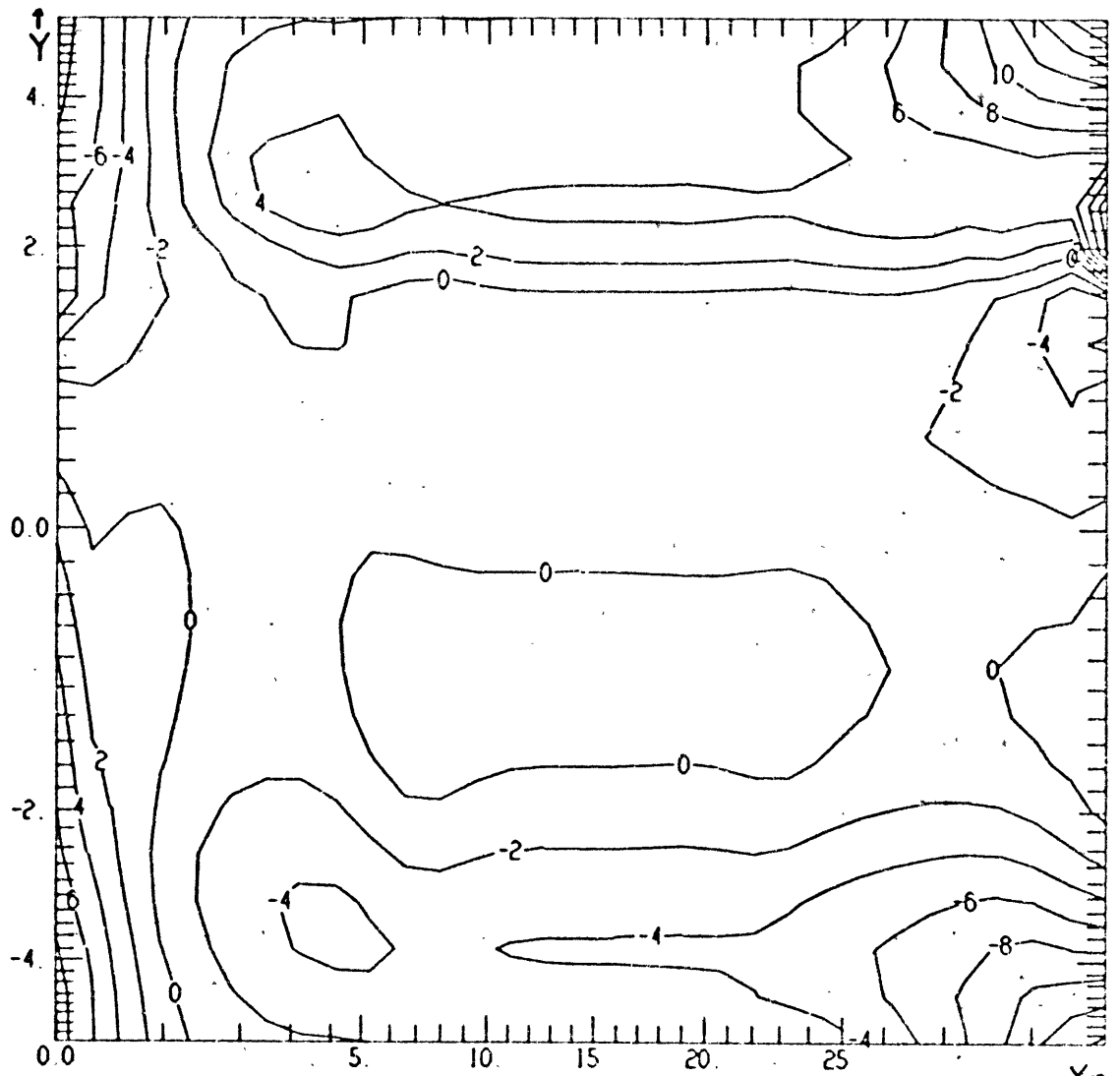


Fig. 5.13 u^1 contours at the equator to day 398. Nonlinear.
 South wind.

Fig. 5.14 shows the layer depth in the equatorial region at 8 days. With the exception of some boundary regions, this field is very nearly anti-symmetric about the equator. There is little to distinguish the interior from the linear response. The circulation pattern in both layers is similar to the linear response at this point, but some distinguishing asymmetries are already present. The principal differences may be summarized as follows.

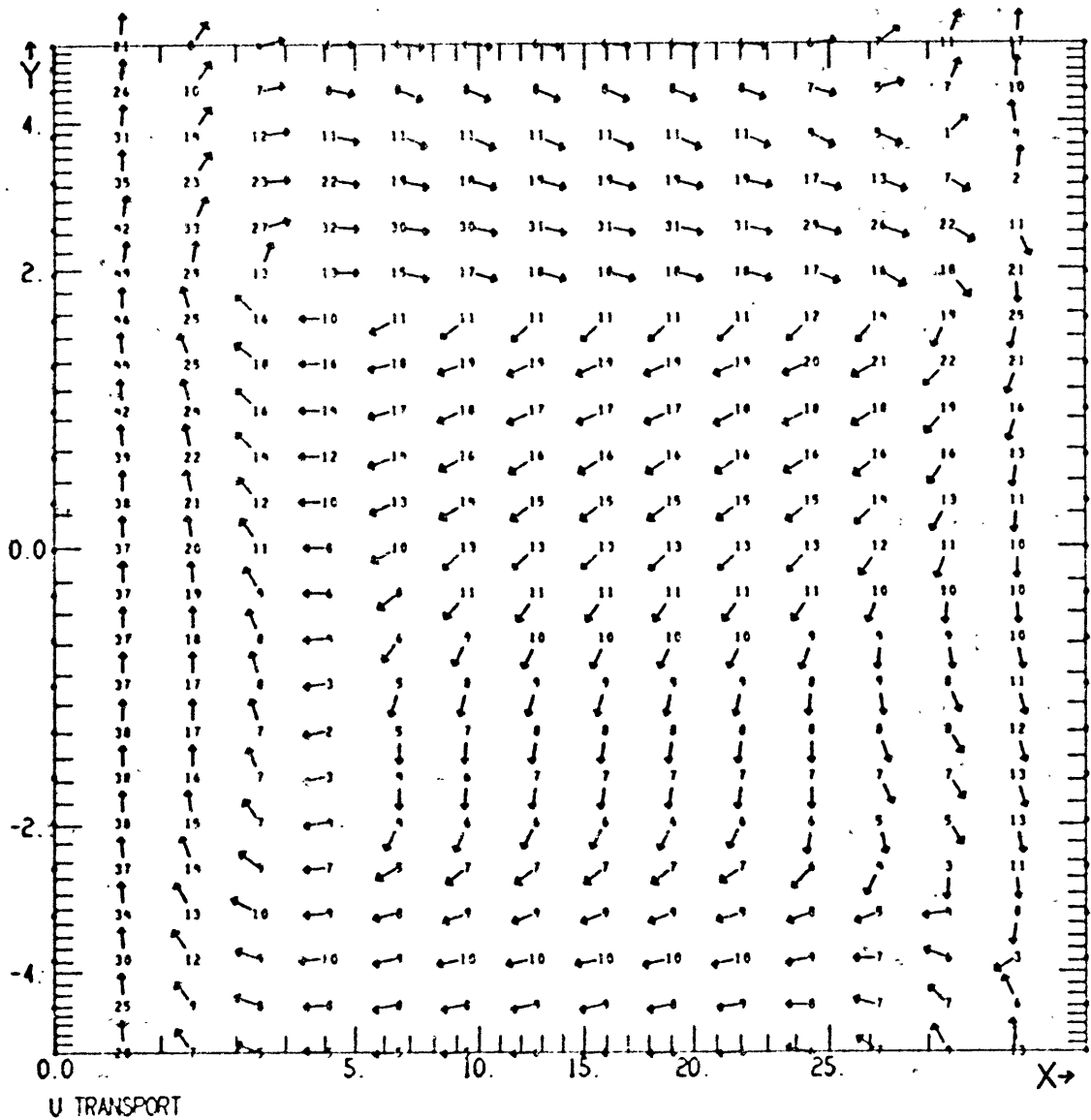
In the surface layer the maximum meridional velocity occurs at approximately 1° N, rather than on the equator as is the case for the linear response. This may be attributed to the self-advection of northward momentum by the surface currents near the equator. As in the linear case, the meridional velocity goes to zero at about 3° N and 3° S. A similar advective effect is observable in the zonal component of the surface current. The maximum westward flow still occurs at 1.2° S, but its magnitude is less ($.41 \text{ m sec}^{-1}$ compared to $.59 \text{ m sec}^{-1}$). Westward momentum has been advected northward so that the surface flow is westward to 1.2° N. The eastward momentum in the surface layer north of the equator has also been advected northward -- but not beyond 3° N, where the meridional velocity goes to zero. The effect is to compress the eastward flow into a narrower, more intense jet. The eastward flow at 2.5° N is at speeds of $.9 \text{ ms}^{-1}$, compared to



LAYER DEPTH LOV--1 45E-01 HIGH· 1.83E-01 C1· 2 · 1.E-02

DAY 7.96 (T· 100 00 MODEL STEP 200) X· 0.0 TO 28.6 Y· -5.6 TO 5.6
 N2E3 N4CH3 30X44STR DELT· .5 E-1 E-8,88·B1· 001 WIND· .5 SOUTH EVERYWHERE.. 08/05/21

Fig. 5.14 h contours at 8 days. Nonlinear. South wind.



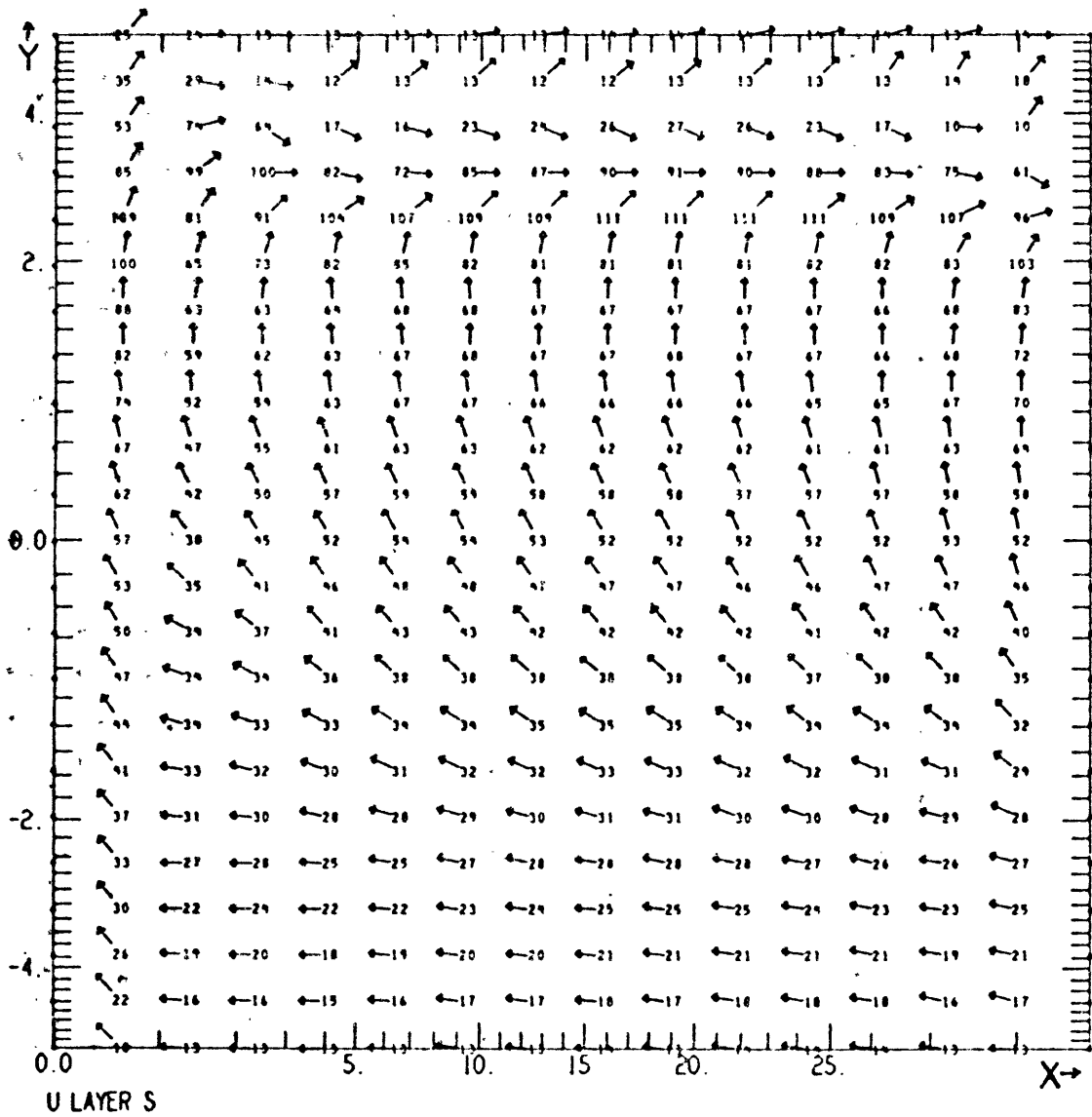
U TRANSPORT

DAY 7.96 IT= 100 00 MODEL STEP 2001 X= 0.0 TO 28.6 Y= -5.6 TO 5.6
 N2E3 N4CH3 30X44STR DELT= .5 E-1. E-8, B8-B1= .001 WIND= 5 SOUTH EVERYWHERE 08/05/21

Fig. 5.15 \bar{u} contours at 8 days. Nonlinear. South wind.

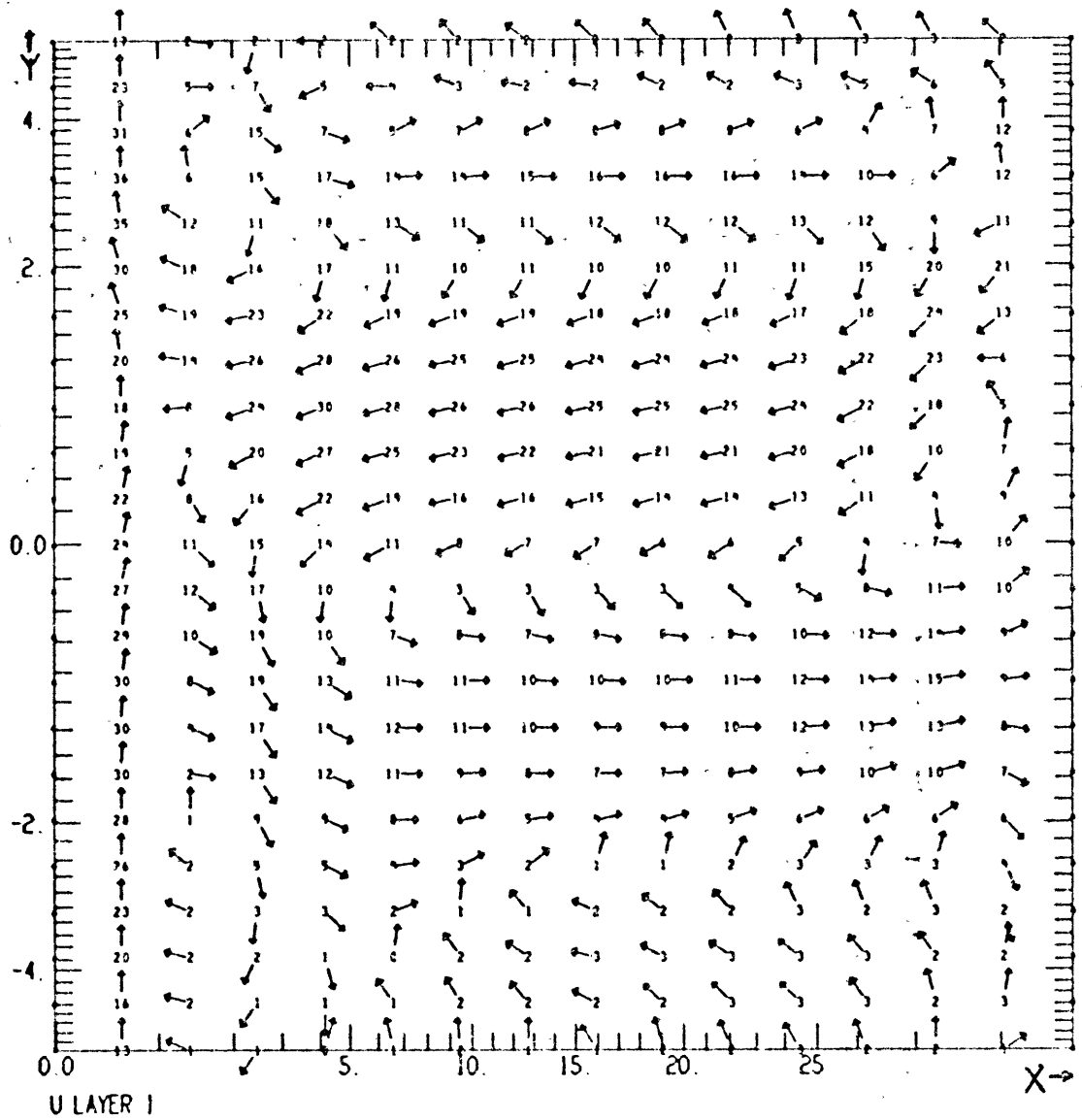
the linear maximum of $.59 \text{ ms}^{-1}$ at 1.2° N . At this time, vertical velocities are everywhere negligible in the interior; flow in the lower layer is small everywhere. The trend is thus toward the development of an eastward jet, now centered at 2.5° N with a broader, slower westward flow at the equator. This pattern is evident in the zonal transport, Fig. 5.15.

By 16 days, the degree of asymmetry is marked. The eastward jet is now centered at 3° N , where the surface flow reaches speeds of 1 m sec^{-1} (Fig. 5.16a). This jet is quite narrow; its velocity falls to less than $.2 \text{ m sec}^{-1}$ within 1° . There is a considerable horizontal convergence into the jet, resulting in a substantial downwelling ($w \approx 1.5 \times 10^{-4} \text{ ms}^{-1}$) at 3° N . Elsewhere in the interior the vertical velocity is negligible. This downwelling advects eastward momentum into the lower layer so that the flow there is also eastward (Fig. 5.16b). The result is a large vertically integrated transport to the east -- a factor of 5 larger than in the linear case (cf., Figs. 5.17 and 5.5). Returning to the surface flow, south of about 2° S the currents are essentially the wind drift, as in the linear case. From about 2° S to about 2° N , the interior flow is everywhere to the northwest. In the linear case, this was the region where the flow was given by the wind drift, plus interfacial friction solution (3.25). The nonlinear case shows a maximum meridional component north of the equator and a non-zero component to the west everywhere.



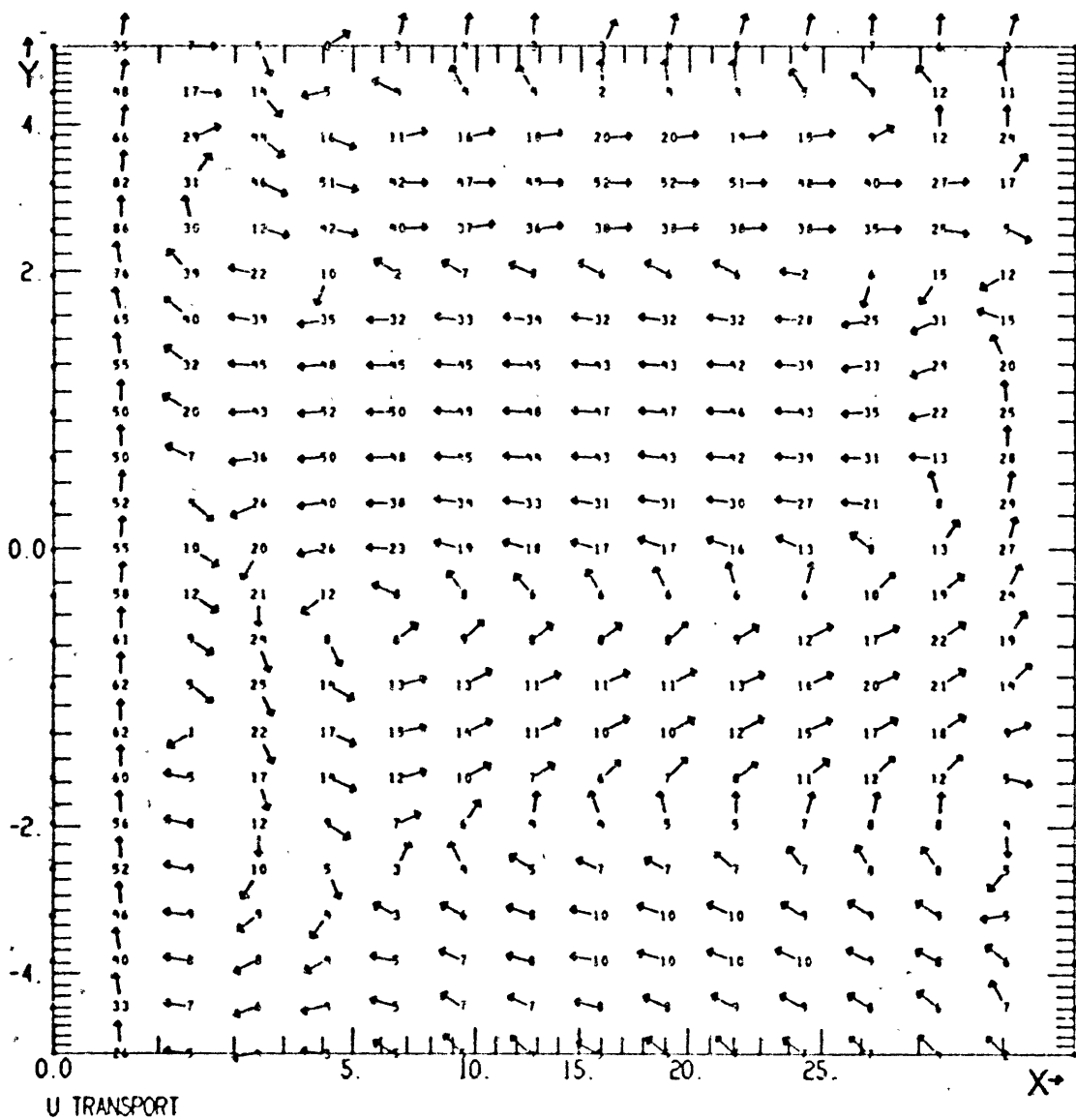
U LAYER S
 DAY: 15.92 (T= 200.00 MODEL STEP 400) X= 0.0 TO 28.6 Y= -5.6 TO 5.6
 N2E3 N4CH3 30X44STR DELT= 5 E-1 E-8,BB-BI=.001 WIND=.5 SOUTH EVERYWHERE 08/05/21

Fig. 5.16a u^S vectors at 16 days. Nonlinear. South wind..



DAY 15 92 (T= 200 00 MODEL STEP 400) X= 0 0 TO 28 6 Y= -5 6 TO 5 6
 N2E3 N4CH3 30X44STR DELT= 5 E=1 E=8, BB=BI= .001 WIND= 5 SOUTH EVERYWHERE 08/05/21 C

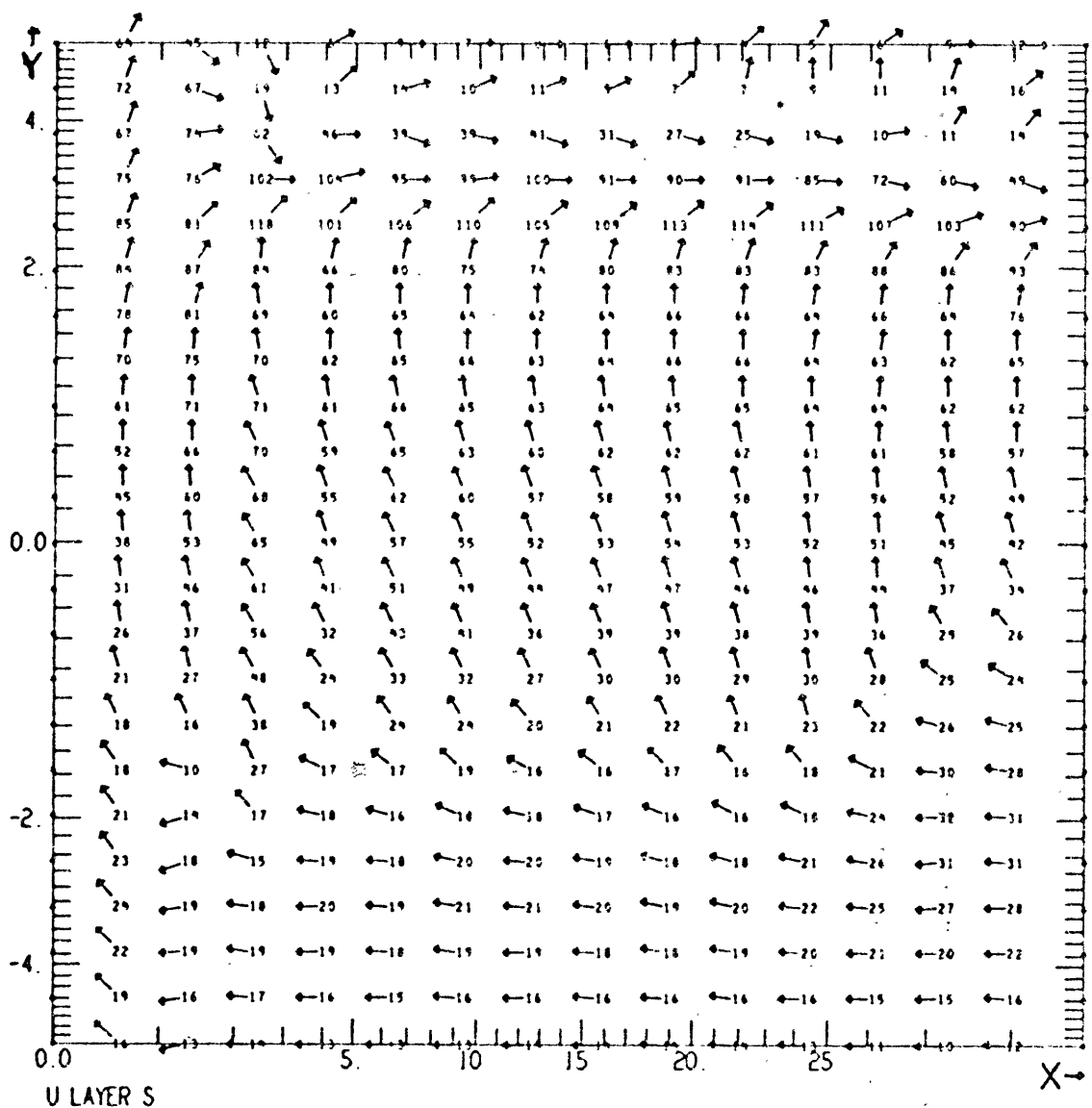
Fig. 5.16b u^1 vectors at 16 days. Nonlinear. South wind.



U TRANSPORT

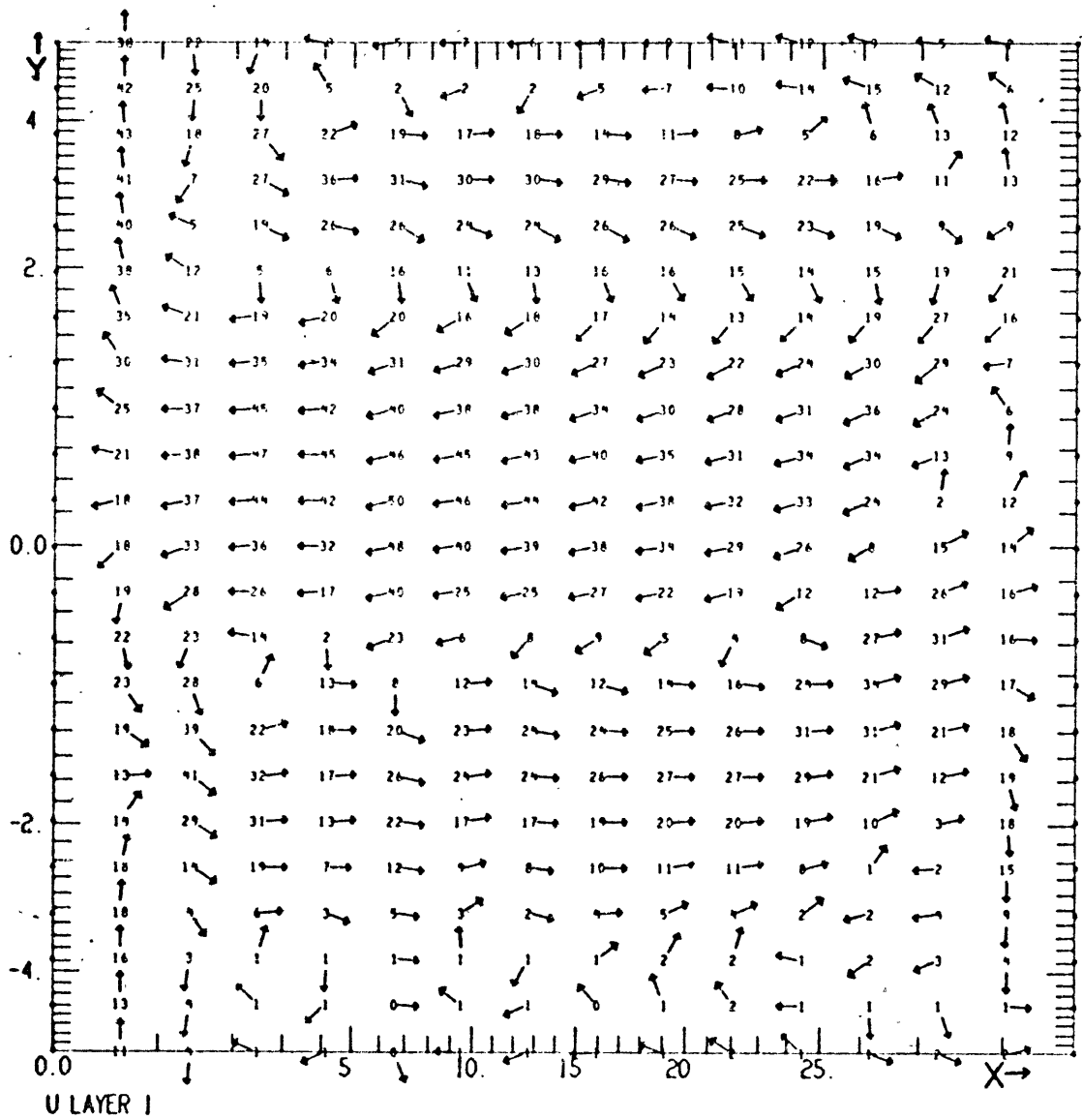
DAY 15.92 IT= 200.00 MODEL STEP 4001 X= 0.0 TO 28.6 Y= -5.6 TO 5.6
 N2E3 N4CH3 30X44STR DELT=.5 E-1.E-8.BB-B1- 001 WIND=.5 SOUTH EVERYWHERE 08/05/21.0

Fig. 5.17 \bar{u} vectors at 16 days. Nonlinear. South wind.



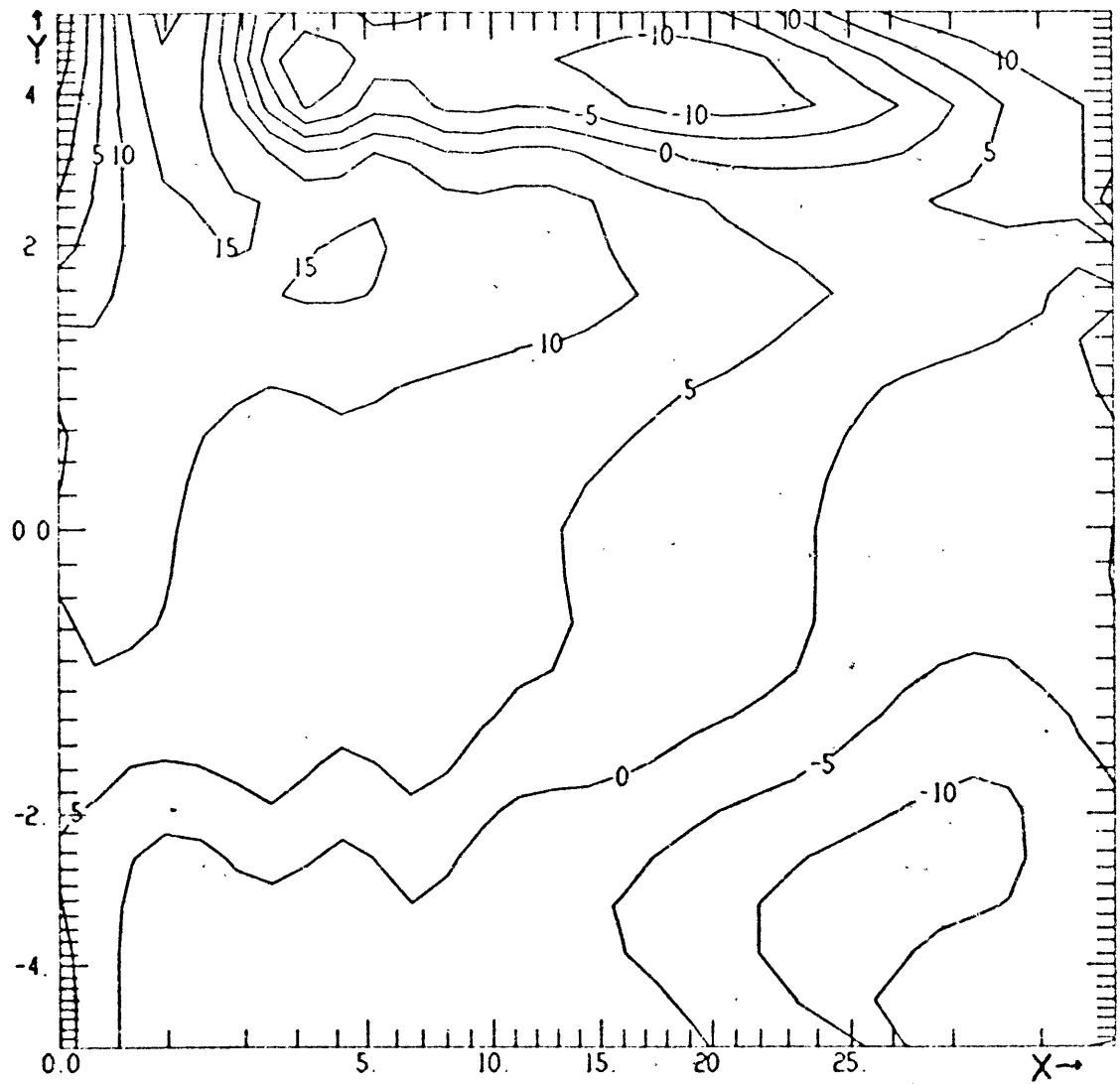
DAY 39.79 (T= 500.00 MODEL STEP 1000) X= 0.0 TO 28.6 Y= -5.6 TO 5.6
 N2E3 N4CH3 30X44STR DELT= 5 E-1 E-8;BB-B1= .001 WIND=.5 SOUTH EVERYWHERE 08/05/21 C

Fig. 5.18a \tilde{u}^S vectors at 40 days. Nonlinear: South wind.



DAY 39.79 (T= 500.00 MODEL STEP 1000) X= 0.0 TO 28.6 Y= -5.6 TO 5.6
 N2E3 N4CH3 30X44STR DELT= 5 E=1. E=8, B3-B1= .001 WIND= .5 SOUTH EVERYWHERE 07/15/0

Fig. 5.18b u^1 vectors at 40 days. Nonlinear. South wind.



LAYER DEPTH LOV=-147E-01 HIGH= 2 18E-01 CI= 5 * 1.E-02
 DAY 39 79 IT= 500 00 MODEL STEP 10001 X= 0 0 TO 28 6 Y= -5 6 TO 5 6
 N2E3 N4CH3 30X44STR DELT= .5 E=1.E-8, BB=81= .001 WIND= 5 SOUTH EVERYWHERE 07/15/02

Fig. 5.18c h contours at 40 days. Nonlinear. South wind.

As above, these effects may be understood by considering the effect of northward advection on the linear solution. The current shears are smaller here than in the linear case, and the region of substantial northward flow is broader, while the maximum northward velocity is lower by a factor of two. In the lower layer, the flow is greater than $.05 \text{ m sec}^{-1}$ only near the lateral boundaries and between 2° S and 4° N .

Figure 5.18 shows the fields at 40 days. The patterns are substantially similar to those at 16 days. We note that the interior flow is approximately steady and independent of longitude. The primary exception to this is the layer depth which shows a more uniform tilt to the north at the eastern side, similar to the linear case. It also shows a suggestion of a wavelike structure at about 4° N . The part of the interior field which is independent of x and t may be described in terms of four regions:

(1) South of about 2.5° S the response is essentially linear, like that discussed in the previous section. The dominant feature is the surface wind drift current to the left of the wind.

(2) From 2.5° S to about 2.5° N the surface flow turns from northwestward to northeastward to due east. Vertical velocities are everywhere upward and small (0 ($3 \times 10^{-5} \text{ ms}^{-1}$)), with most of the upwelling south of the equator. The zonal component of flow in the lower layer is to the west south of

1° S and to the east north of that, with a magnitude comparable to the upper layer zonal component near the equator. The meridional component is southward everywhere.

(3) From 2.5° N to 5° N there is an eastward zonal jet in both layers: at 3° N the upper layer flow is as high as 1.2 m sec^{-1} ; the lower layer flow is over $.4 \text{ m sec}^{-1}$. By this point, the meridional component of flow is negligible in both layers. There is strong convergence into the jet with large downwelling at its core ($w \approx 3 \times 10^{-4} \text{ ms}^{-1}$).

(4) North of about 5° N the model response again becomes wind drift dominated and essentially linear.

This description is in close agreement with the x-independent, steady state calculation of Charney and Spiegel (1971). (See their Figs. 11 and 12.). The only notable disagreements are that their surface velocity in the jet is smaller (less than 1 m sec^{-1}), their downwelling region is broader, and their upwelling region narrower than ours. We now seek a simple model (independent of x and t) to elucidate the physics of this flow.

Regions (1) and (4) are explicable in terms of the linear dynamics of the last section. Now consider the surface flow in region (2). A parcel in the vicinity of the equator will acquire a northward velocity component (frictional forces give it a component in the direction of the wind). As it moves northward, it acquires cyclonic planetary vorticity. Since it

(approximately) conserves its total vorticity, it must acquire anti-cyclonic relative vorticity. The effect is to turn the parcel clockwise toward the east. As long as the parcel moves northward, it is able to acquire energy from the wind stress. At some latitude the parcel's northward momentum is being converted into eastward momentum more rapidly than it is replenished by the wind. Eventually, the parcel will be travelling due east, still carrying the approximately zero total vorticity it had near the equator. To the north of this, the flow is in the wind drift regime where the vorticity of surface parcels is approximately the local planetary vorticity. The transition between the two flow regimes demands a shear layer in which the surface eastward velocity is reduced to the north, thus adding enough positive vorticity to the flow to match it to the planetary vorticity. This is accomplished by the downwelling in the jet which transports the eastward momentum downwards.

We formulate the following simple model to obtain some quantitative descriptions to accompany this qualitative description.

In region (2) the surface flow is governed by the following approximate equations

$$\frac{du}{dt} - \beta yv = 0 \quad (5.6)$$

$$\frac{dv}{dt} + \beta yu = \tau/\eta \quad (5.7)$$

where

$$\frac{d}{dt} \equiv v \frac{\partial}{\partial y}$$

so that the first equation expresses the conservation of vorticity. In addition to taking $\partial/\partial t = \partial/\partial x \equiv 0$ a number of other simplifications have been made, the least defensible of which is the neglect of interfacial friction. This was done to make the equations analytically tractable -- its inclusion would change the numerical values slightly, but not the character of the solution. The pressure gradient term is small compared to the retained term. The vertical velocity is small throughout this region and the vertical advection term is about 1/2 the retained meridional advection term in the upper layer. Its principal effect can be captured by multiplying the solution for v obtained below, (5.8), by $(2/3)^{1/2} \approx .8$. An energy equation may be formed from (5.6) and (5.7),

$$\frac{1}{2} \frac{d}{dt} (u^2 + v^2) = \frac{\tau}{\eta} v .$$

By making use of the definition $dy/dt \equiv v$, this may be integrated to yield

$$u^2 + v^2 = 2 \frac{\tau}{\eta} y + \text{Const.}$$

From (5.6)

$$u = \frac{\beta}{2} y^2 + ay + b .$$

We now simplify things further by assuming that $u = v = u_y = 0$ at the equator (actual values are $v^S \approx .6 \text{ ms}^{-1}$, $u^S \approx -.2 \text{ ms}^{-1}$, and $u_y^S \approx 10^{-7} \text{ s}^{-1}$) and so obtain

$$u \approx \frac{\beta y^2}{2} \quad v^2 \approx 2 \frac{\tau}{\eta} y - \frac{\beta^2 y^4}{4} . \quad (5.8)$$

The position of the jet is at a latitude y_J where $v = 0$:

$$y_J = 2 \frac{\tau/\eta}{\beta^2}^{1/3} \approx 340 \text{ km} \approx 3^\circ .$$

At this latitude

$$u_J = \frac{\beta y_J^2}{2} = 2 \frac{(\tau/\eta)^2}{\beta}^{1/3} \approx 1.2 \text{ m sec}^{-1} .$$

These values are in excellent agreement with the numerical calculation. We may also obtain a scale for the other velocity component by considering the latitude y_m where v is a maximum:

$$y_m = \left[\frac{2\tau/\eta}{\beta^2} \right]^{1/3} = 2^{-2/3} y_J \approx .63 y_J \approx 2^\circ$$

$$V_m \equiv v(y_m) = \left[\frac{3}{2} y_m \frac{\tau}{\eta} \right]^{1/2} = 1.37 \left[\frac{(\tau/\eta)^2}{\beta} \right]^{1/3}$$

$$\approx .8 \text{ m sec}^{-1}$$

(5.9)

This agrees quite well with the maximum in the numerical calculation, but the position is further to the north (about 2.5° N). If we had made the initial velocity at the equator non-zero, the effect would be to increase V_m and to move Y_J and Y_m slightly to the north. We also note that the jet must, in fact, form before the meridional velocity is identically zero in order to permit the downwelling required to maintain the zonal momentum balance. Turning to the jet itself, the requirement that the vorticity of the flow be brought up to the local planetary vorticity in order to match onto the linear regime gives a scale for the width Y of the shear zone.

$$\beta (Y_J + Y) \sim U_J/Y \Rightarrow Y \approx .35 Y_J \approx 1.1^\circ.$$

This is the right order but slightly too wide (the model results show $Y = .8^\circ$). The principal neglected term is the downwelling term (the model's analogue to the vortex stretching term) which would tend to make the jet wider. One feature of this description which agrees well with the numerical calculation and that of Charney and Spiegel (loc. cit.) is that the zonal velocity of the jet falls off more rapidly to the north than to the south.

The fluid which descends in the jet arrives in the lower layer with considerable eastward momentum and negative relative vorticity. The meridional velocity component in region (2) is southward in order to satisfy the continuity equation

$$(hv^1)_y = -v_y^s \quad (5.10)$$

and the (approximate) condition that $v^1 = v^s = 0$ at the southern edge of the region. Parcels will approximately conserve their total vorticity because vertical exchanges are small and because both f and variations in the layer depth are small (so that the variation of potential vorticity is given by the variation of vorticity). As a parcel travels southward, its planetary vorticity decreases so its relative vorticity must become less negative and may even become positive.

Let us now trace a parcel southward after it leaves the region of the jet. Its initial conditions (i.e., $u > 0$ and $u_y > 0$) mean that it starts out with an eastward velocity which becomes progressively more westward as it travels south. Note that a parcel which makes it to the eastern side before turning east slows its westward flows and "uses" its vorticity to enhance its meridional flow. There is a region of large southward transport at the eastern side centered at about 1.8° N. As the parcels flow toward the west-southwest the westward component of flow increases, but at a decreasing rate. This latter effect is due to the increase of relative vorticity (i.e., u_y) goes to zero. In our calculation this occurs at about $.3^\circ$ N. Note that north of this point the flow impinging on the western boundary turns clockwise to the north (its relative vorticity $\zeta < 0$) while south of it the flow turns

counterclockwise to the south ($\zeta > 0$). This flow continues south along the boundary until it meets a northward current, which, since it comes from the south, must have negative relative vorticity. Both currents then turn eastward (this junction is at 1.5° S at 40 days and at 3° S at 80 days). Parcels which travel this far south in the interior must also begin to flow eastward as their relative vorticity increases. We note that there is an eastward flow with currents larger than $.1 \text{ m sec}^{-1}$ in the region from 1° S to about 3° S. At the eastern side of this region some of the water turns north and some south, consistent with the idea that the flow contained parcels with both positive and negative relative vorticity. The upwelling in this area is not large. The vertical exchanges in this model are characterized by a weak upwelling almost everywhere, with narrow regions of strong downwelling at the western side in the vicinity of the equator and in the jet at 3° N (especially at its eastern end).

Before continuing the discussion of the evolution of the model calculation we wish to make two remarks about the foregoing discussion. It is pleasing to be able to obtain an explanation of the motion which is independent of the value of the frictional parameters since these are so uncertain. The neglect of friction in (5.6) and (5.7) is justified if the vertical friction coefficient K/η in (2.6) is small compared to the advective operator $v^0/\partial y$. The latter may be estimated from (5.9):

$$v \frac{\partial}{\partial y} \sim V_m / y_m = \left[\frac{3^{3/2}}{4} \beta \frac{\tau}{M} \right]^{1/3} \approx 9 \times 10^{-7} \text{ sec}^{-1}$$

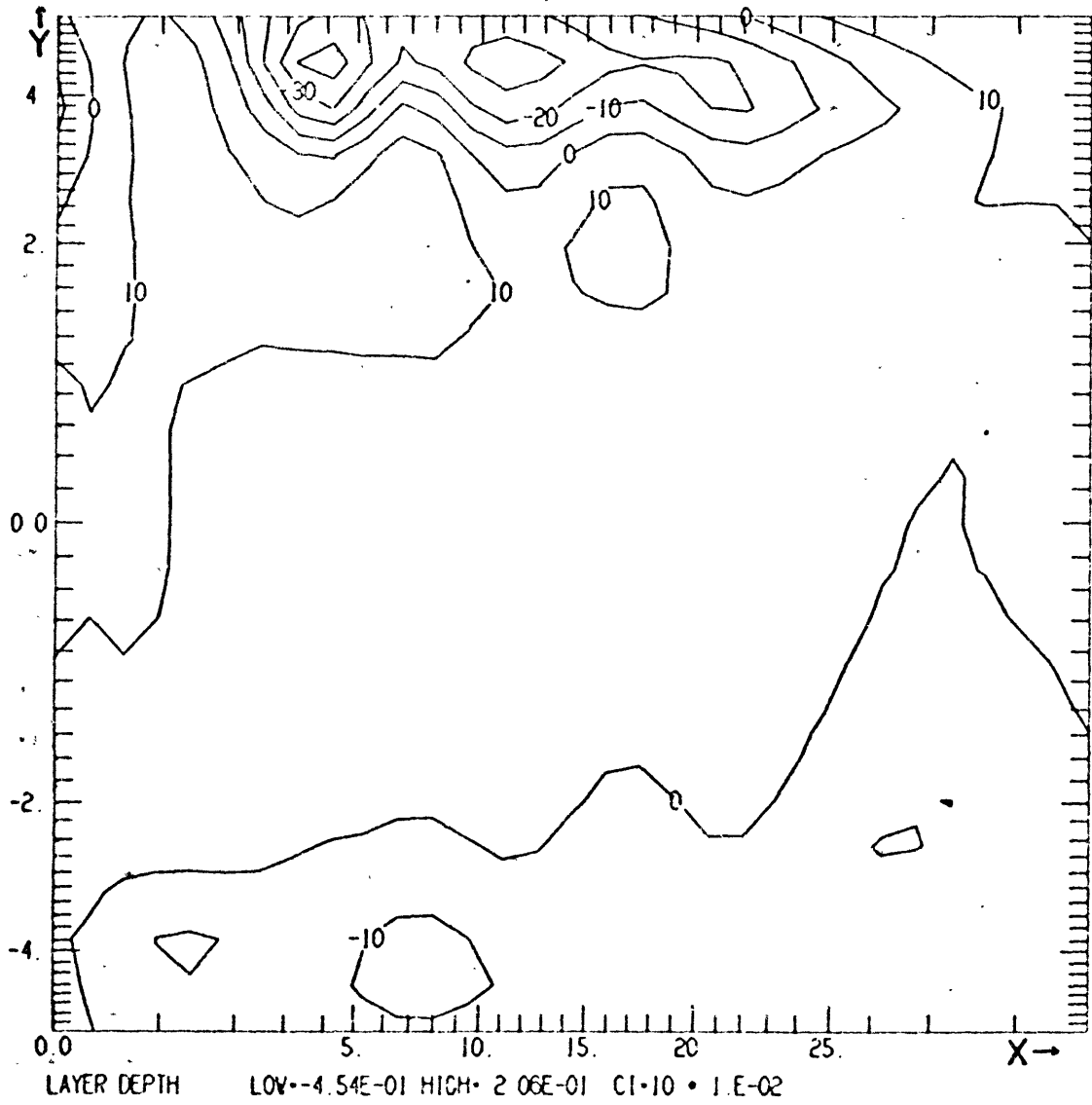
while with the values in Table 1 the friction coefficient is $6 \times 10^{-7} \text{ sec}^{-1}$. The excellent agreement of our analysis with the numerical results is probably due to the neglect of friction being compensated by underestimating the actual initial velocity in obtaining (5.8).

Our second remark serves as a preface to the further evolution of the flow. It concerns the implications of the foregoing analysis for the susceptibility of the flow to shear instability -- the distinguishing characteristic being that the growing perturbation draws its energy from the kinetic energy of the mean flow). For non-divergent inviscid flow a necessary condition for instability is that the vorticity -- $f - u_y$, in our case -- have an extremum. Though our situation is more complicated, this simple criterion still serves as a useful guide (see discussion below). This condition is usually not met by geophysical flows because the gradient of planetary vorticity, β , is large enough to ensure that the gradient of total vorticity, $\beta - u_{yy}$, is monotonic. The flow in region (2) described above was characterized by the conservation of total vorticity, thereby neutralizing the stabilizing effect of beta. Recall that the key ingredients that create this situation are a non-zero meridional velocity, to permit exchanges of relative

and planetary vorticity, and the absence of a wind stress curl to alter the total vorticity. A number of considerations permitted our description to be greatly simplified. In particular, the fact that throughout the region vertical velocities are not large and the layer depth does not vary greatly allowed us to consider the vorticity balances within each layer separately. The fact that the flow was approximately x-independent reduced the relative vorticity to the meridional shear of the zonal flow.

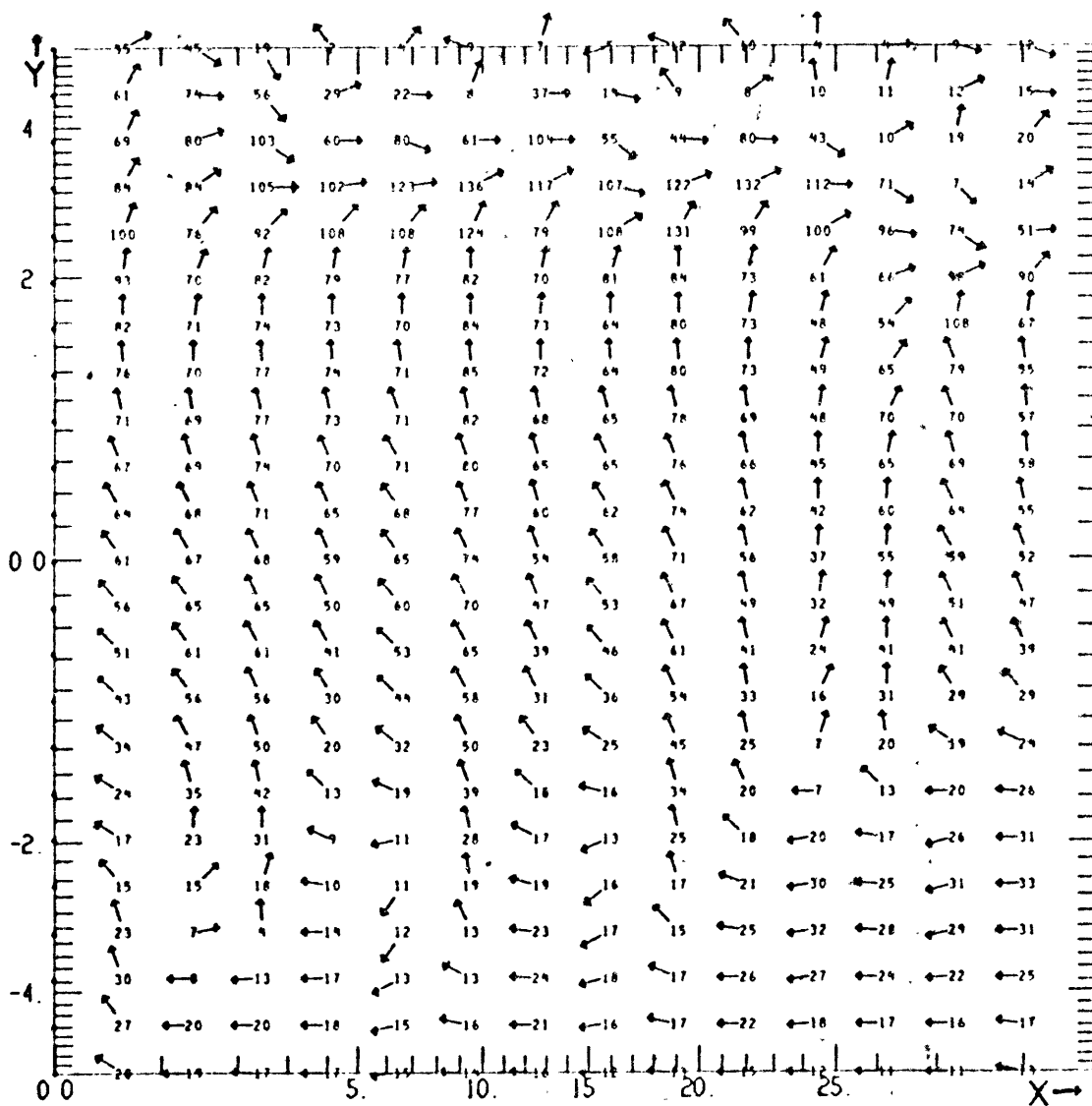
Since the vorticity gradient is constant, the flow is marginally unstable; an additional process which produced a region of stronger (or weaker) shear will cause this necessary (but not sufficient) condition for instability to be met. The model calculation does exhibit numerous extrema in the profile of $f - u_y$. For example, after 80 days of model time at a longitude 9.5° from the western boundary, the upper layer has a maxima at 0.3° N and 1.5° N and minima at 0.9° N and 2.5° N; the lower layer has maxima at 0.6° S and 0.9° N and minima at 0.3° N and 1.5° N.

We resume the discussion of the evolution of the flow with Fig. 5.19, which shows h at 119 days. The waviness suggested in the earlier figures at 4° N (Fig. 5.18) is now clearly evident. Note that it now extends further to the east and that there is a wavy pattern developing at 4° S as well. Recall that the energy graphs (figs. 5.11 and 5.12) show some



DAY 119.37 (T= 1500 CG MODEL STEP 3000) X= 0.0 TO 28.6 Y= -5.6 TO 5.6
 N2E3 N4CH3 30X44STR DELT= 5 E-1 E-8, BB=BI= 001 WIND= .5 SOUTH EVERYWHERE 07/15/02

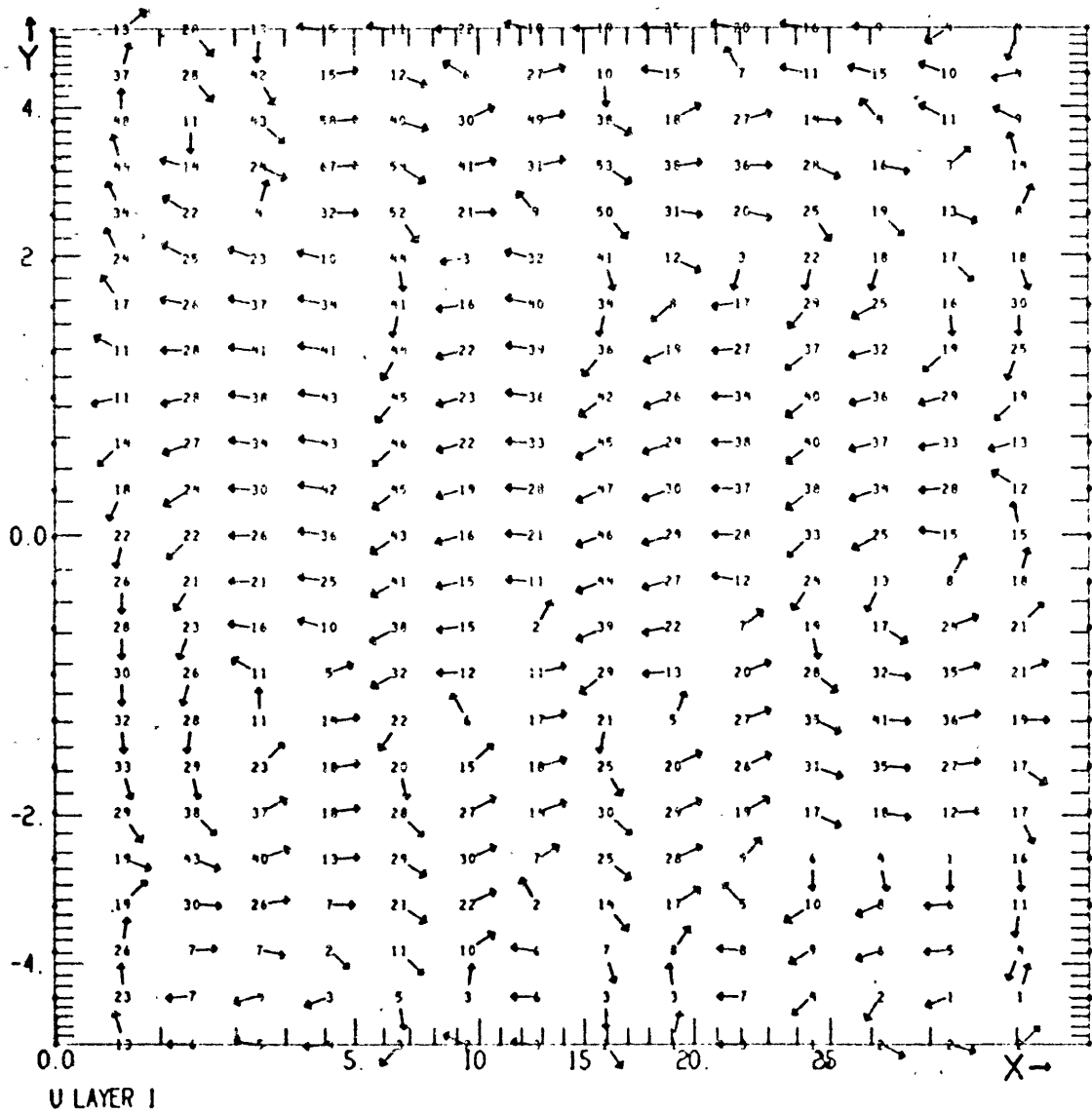
Fig. 5.19 h contours at 119 days. Nonlinear. South wind.



U LAYER S

DAY 159.16 IT=2000.00 MODEL STEP=40001 X= 0.0 TO 28.6 Y=-5.6 TO 5.6
 N2E3 N4CH3 30X44STR DELT=.5 E=1 E=8,BB=BI=.001 WIND=.5 SOUTH EVERYWHERE 07/15/00

Fig. 5.20a \vec{u}^S vectors at 159 days. Nonlinear. South wind.



DAY +159.16 (T= 2000.00 MODEL STEP= 4000) X= 0.0 TO 28.6 Y= -5.6 TO 5.6
 N2E3 N4CH3 30X44STR DELT= .5 E=1.E-8, BB=BI=.001 WIND= 5 SOUTH EVERYWHERE 07/15/02

Fig. 5.20b \underline{u}^1 vectors at 159 days. Nonlinear. South wind.

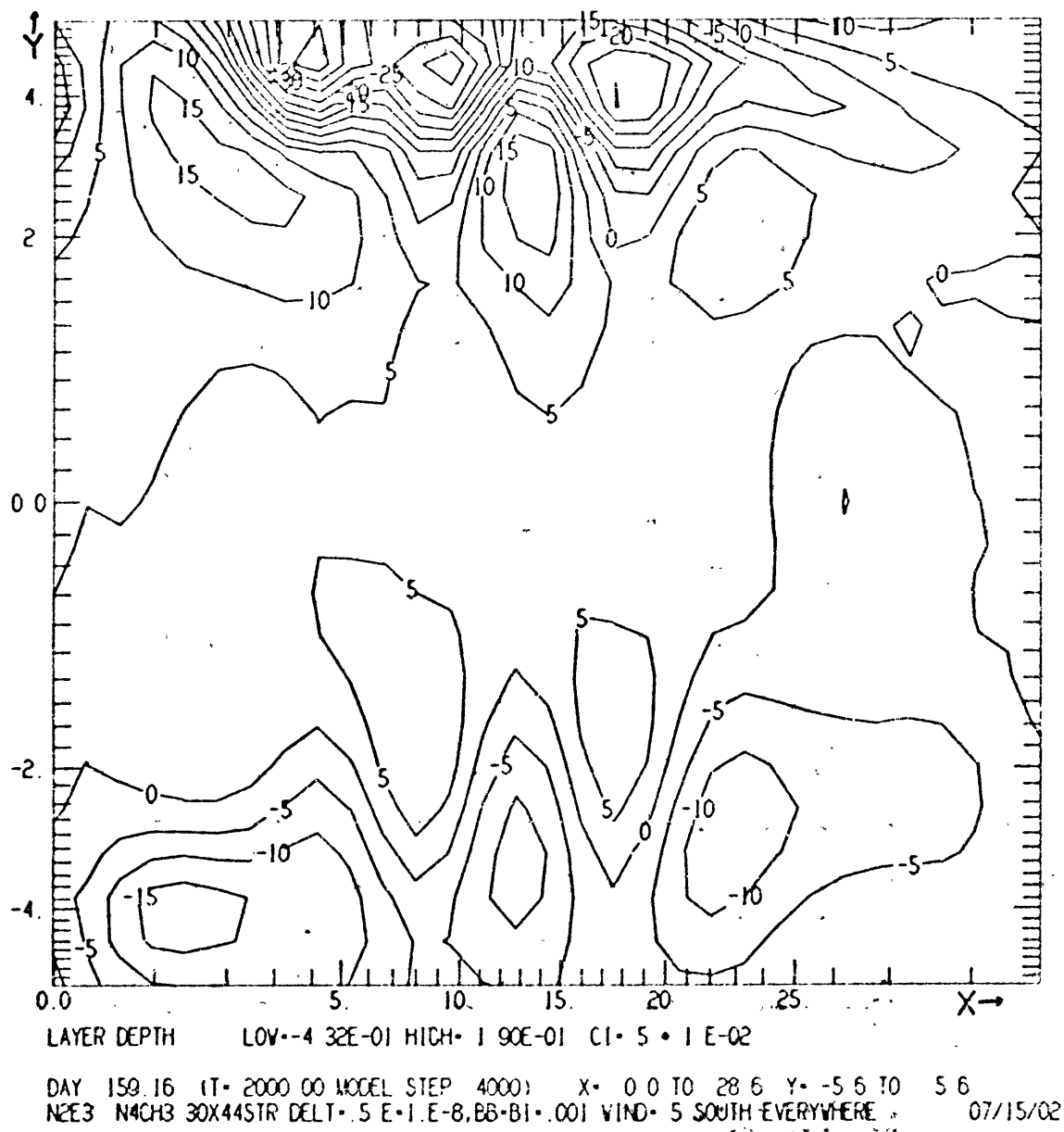
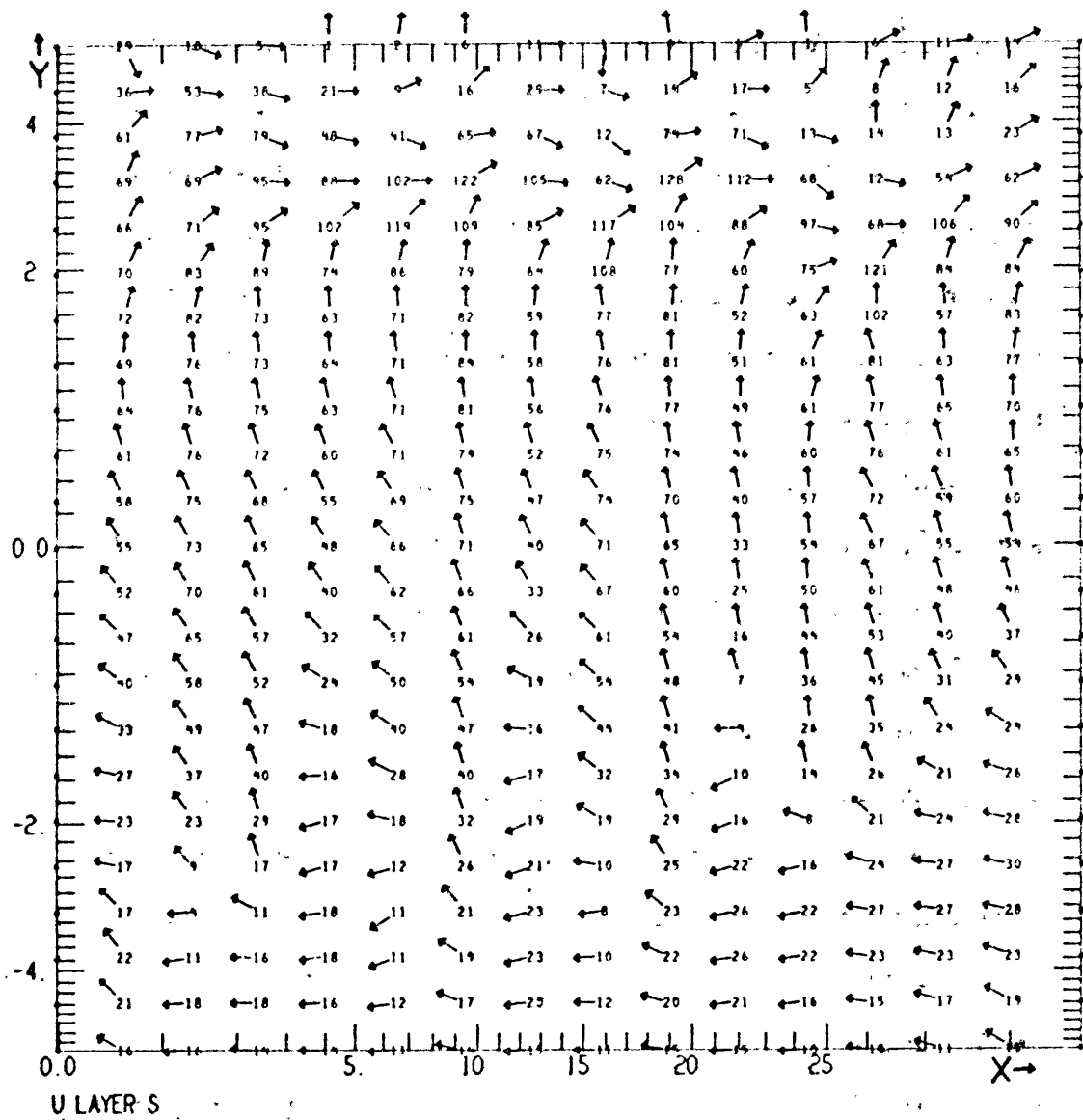


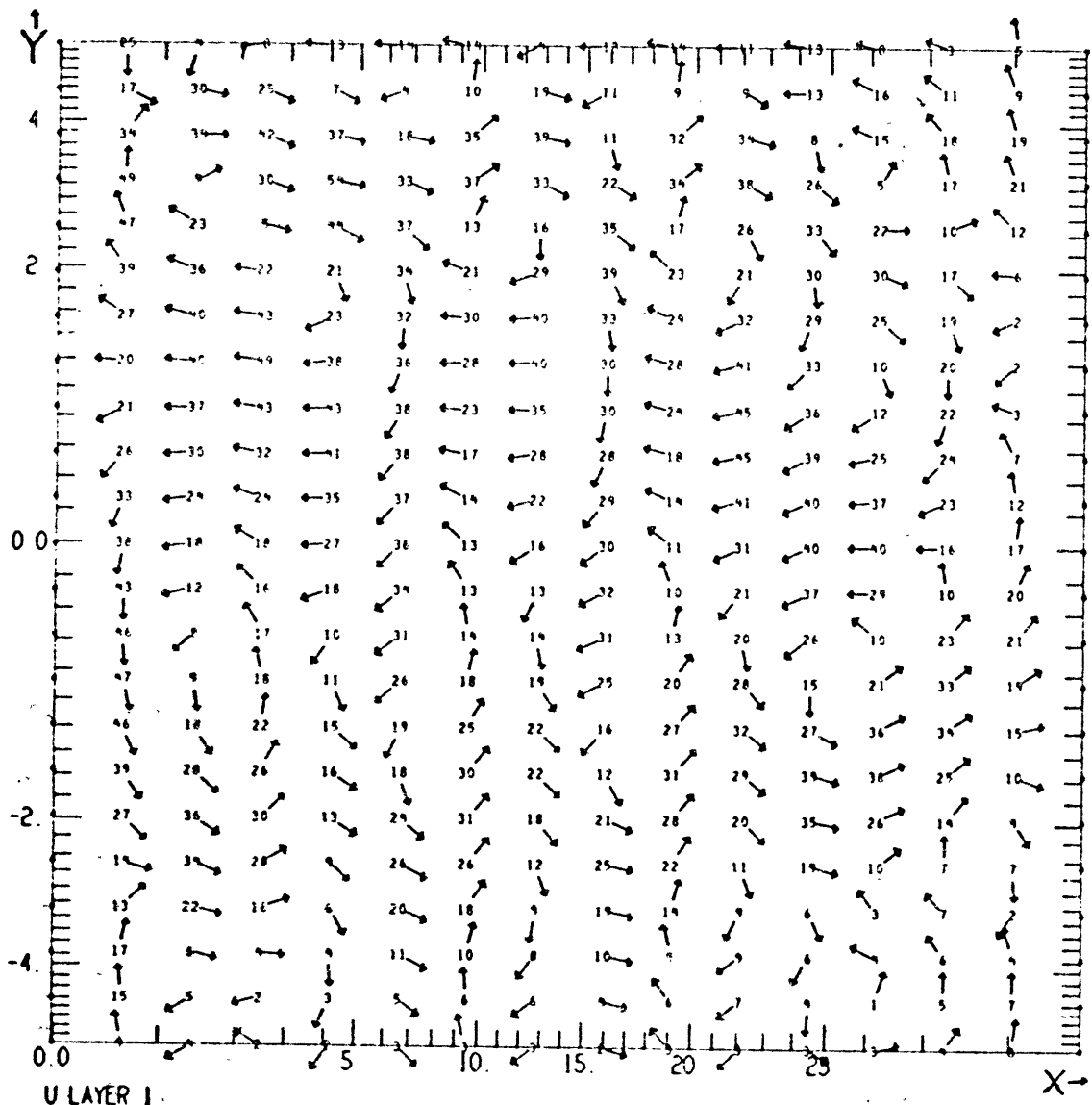
Fig. 5.20c h contours at 159 days. Nonlinear. South wind,

evidence of an instability by this time. At 160 days the lower layer kinetic energy reaches a peak and the instability is readily apparent. Fig. 5.20 shows the flow at this time. The overall pattern in the velocity fields is similar to that described above for day 40, but there is an additional wavelike disturbance, especially evident in the lower layer velocities, Fig. 5.20b. This is no longer confined to the western side, but is present in equal amplitude across the width of the basin. By about day 200, the flow settles into a repeated pattern with wavelike disturbances propagating (in the phase sense) across the basin from east to west (see Fig. 5.13). Figs. 5.21 show the fields in the entire basin during this final period of the flow's evolution. The surface velocities exhibit a marked x-independent pattern, though superimposed on this there is a wavelike pattern of approximately 1/3 the amplitude of the (zonally averaged) mean flow. In the lower layer flow (Fig. 5.21b), the x-independent pattern is barely discernible; the amplitude of the instability is approximately equal to that of the mean flow. The variations in the layer depth (Fig. 5.21c) are dominated by this instability from 7° S to 7° N. Poleward of these latitudes it exhibits a general south to north tilt similar to the linear case (cf., Fig. 5.7). The maximum amplitudes of the wave occur at 5° N and 4° S. Figs. 5.22a, b show the zonal and meridional transport. The wave-pattern is particularly clear in the v component because the x-independent



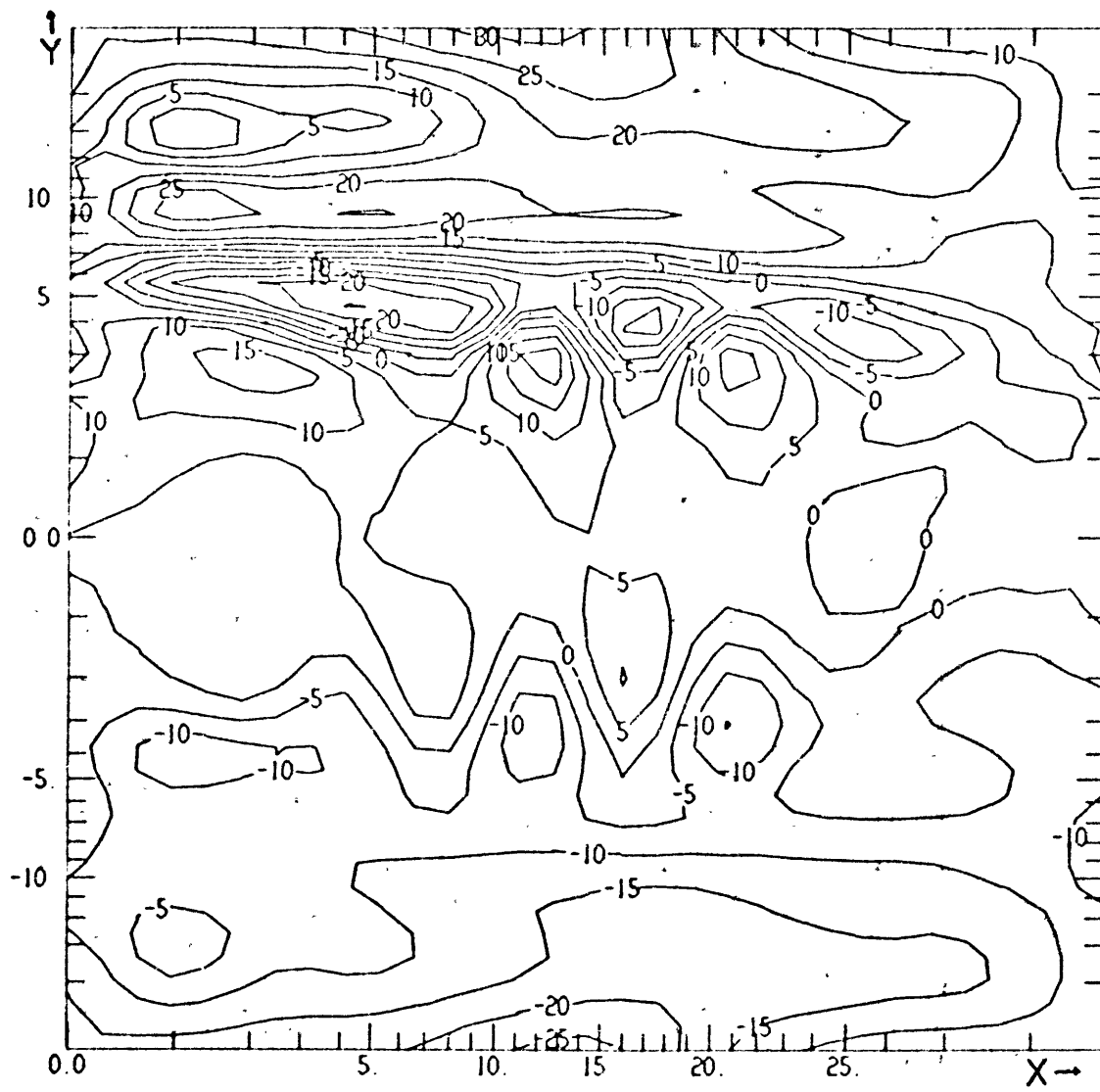
DAY 397.89 (T= 5000.00 MODEL STEP 10000) X= 0.0 TO 28.6 Y= -5.6 TO 5.6
 N2E3 N4CH3 30X44STR DELT= .5 E=1.E-8, B8=BI= .001 WIND= 5 SOUTH EVERYWHERE 07/15/02

Fig. 5.21a u^s vectors at 398 days. Nonlinear. South wind.



DAY 397.89 (T= 5000.00 MODEL STEP 10000) X= 0.0 TO 28.6 Y= -5.6 TO 5.6
 N2E3 N4CH3 30X44STR DELT= 5 E=1 E=8.88-B1= 001 WIND= 5 SOUTH EVERYWHERE 07/15/02

Fig: 5.21b u^1 vectors at 398 days. Nonlinear. South wind.



LAYER DEPTH LOW=-2.65E-01 HIGH=3.17E-01 CI=5.0 I.E-02
 DAY 397.89 IT=5000.00 MODEL STEP 100001 X= 0.0 TO 28.6 Y=-15.0 TO 15.0
 N2E3 N4CH3 30X44STR DELT= 5 E-1.E-8.88-B1= .001 WIND= .5 SOUTH EVERYWHERE 07/15/02..

Fig. 5.21c h contours at 398 days. Nonlinear. South wind.

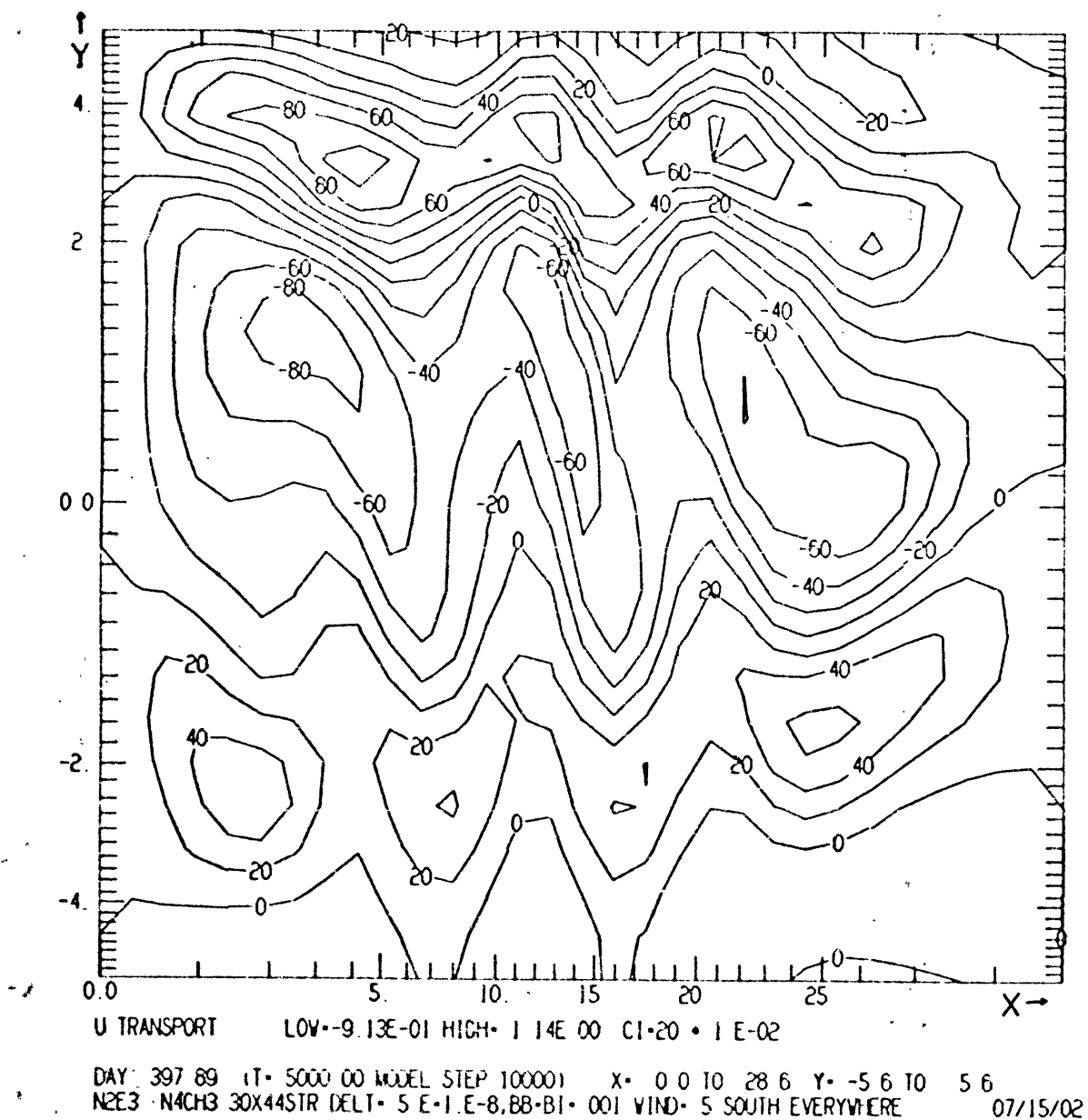
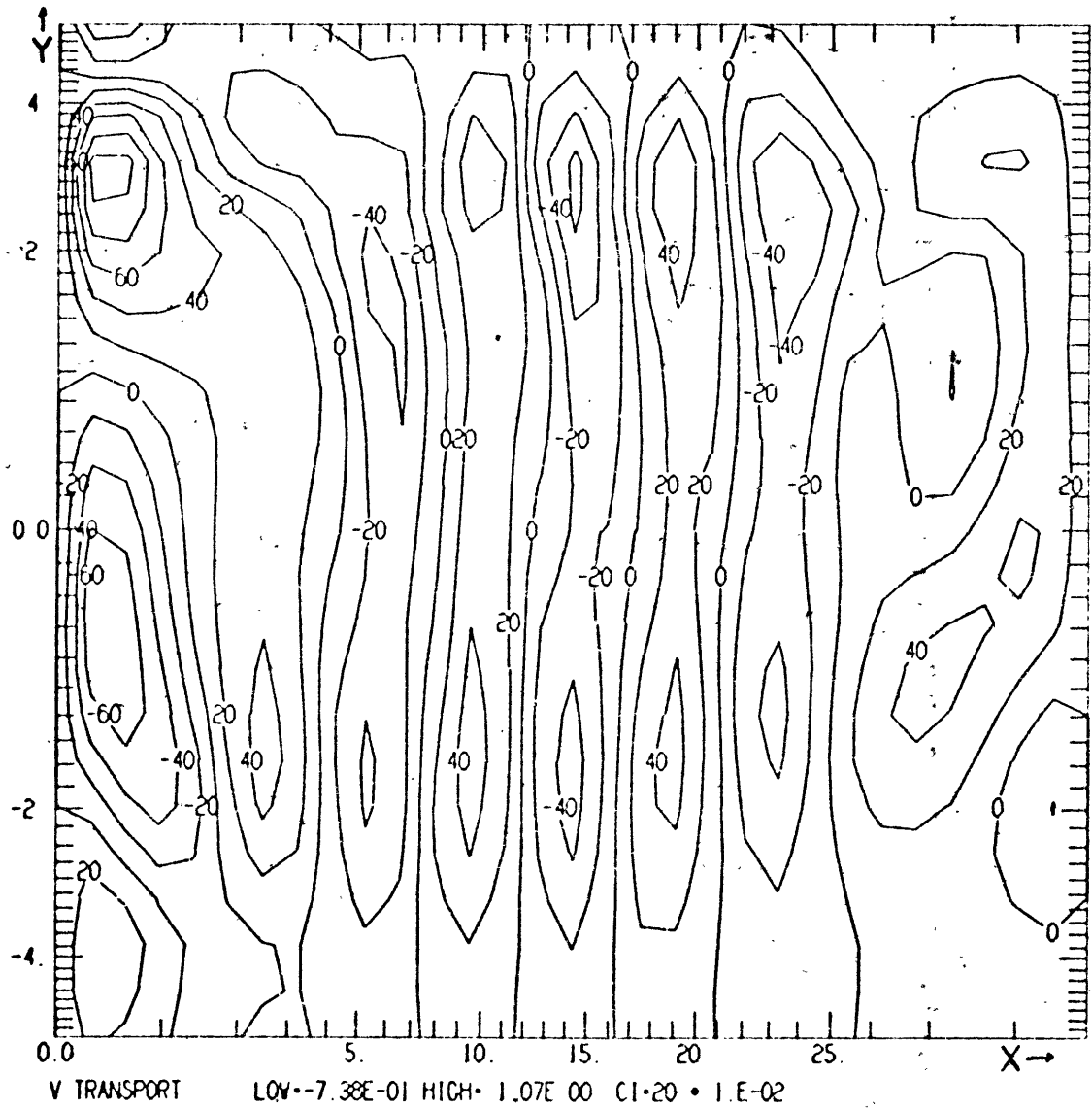


Fig. 5.22a \bar{u} contours at 398 days. Nonlinear. South wind.



DAY 397 89 (T= 5000 00 MODEL STEP 10000) X= 0 0 TO 28 6 Y=-5 6 TO 5 6
 N2E3 N4CH3 30X44STR DELT=.5 E-1 E-8,BB-B1= .001 WIND= 5 SOUTH EVERYWHERE 07/15/02

Fig. 5.22b \bar{v} contours at 398 days. Nonlinear. South wind.

part of the meridional transport is approximately zero (cf. (5.10)). The amplitude maxima of \bar{v} occurs at approximately 1.6° S and 2.6° N. The maxima of the wavy part of \bar{u} at approximately 2.4° S, 1.2° N, and 3.6° N. These positions vary slightly with longitude. The approximate phase relations are: u^S and u^1 are out of phase, while v^S and v^1 are in phase. The v components lead u^S by $1/4$ wavelength; u^S and h are in phase. As mentioned above, the frequency is 29 days and the wavelength is 950 km.

It is of interest to compare our results with the results for the stability of equatorial currents given by Philander (1975). On the basis of the vertically averaged zonal velocity we can crudely fit the model currents to a sech^2 profile, viz.

$$U = U_0 \text{sech}^2 y/L + U_1 ,$$

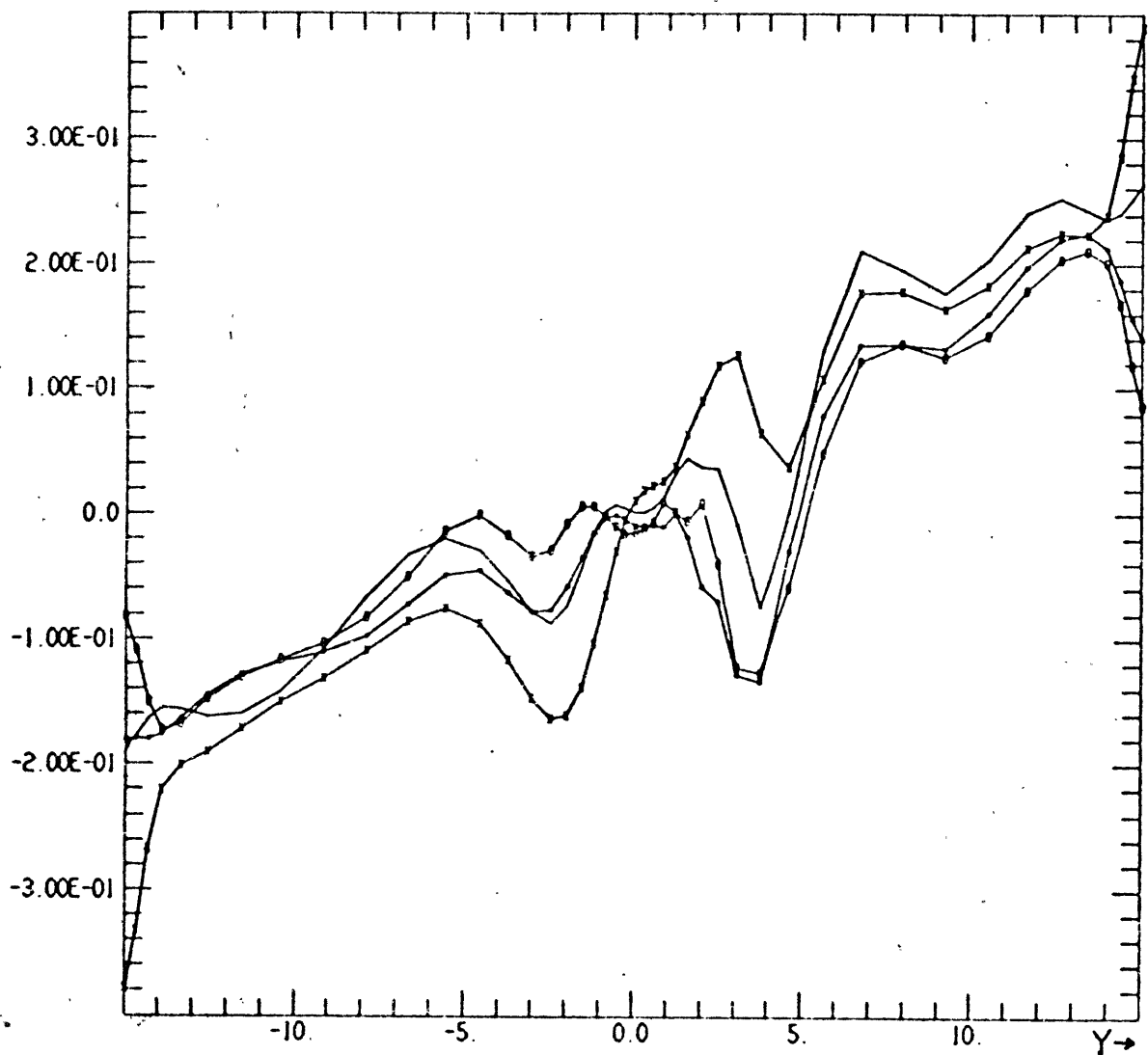
by taking $U_0 \approx -0.7 \text{ ms}^{-1}$, $U_1 = +0.4 \text{ ms}^{-1}$ and $L \approx 100 - 200 \text{ km}$.

Then

$$R_i = \frac{gH}{U_0^2} \approx 8 \quad R_o = \frac{U_0}{BL^2} \approx -1 \text{ to } -4 .$$

From Fig. 3 of Philander (loc. cit.) the wavelength of the fastest growing wave for these parameter values is approximately $2\pi L$ -- between 600 and 1,200 km in our case. This is consistent with the model results.

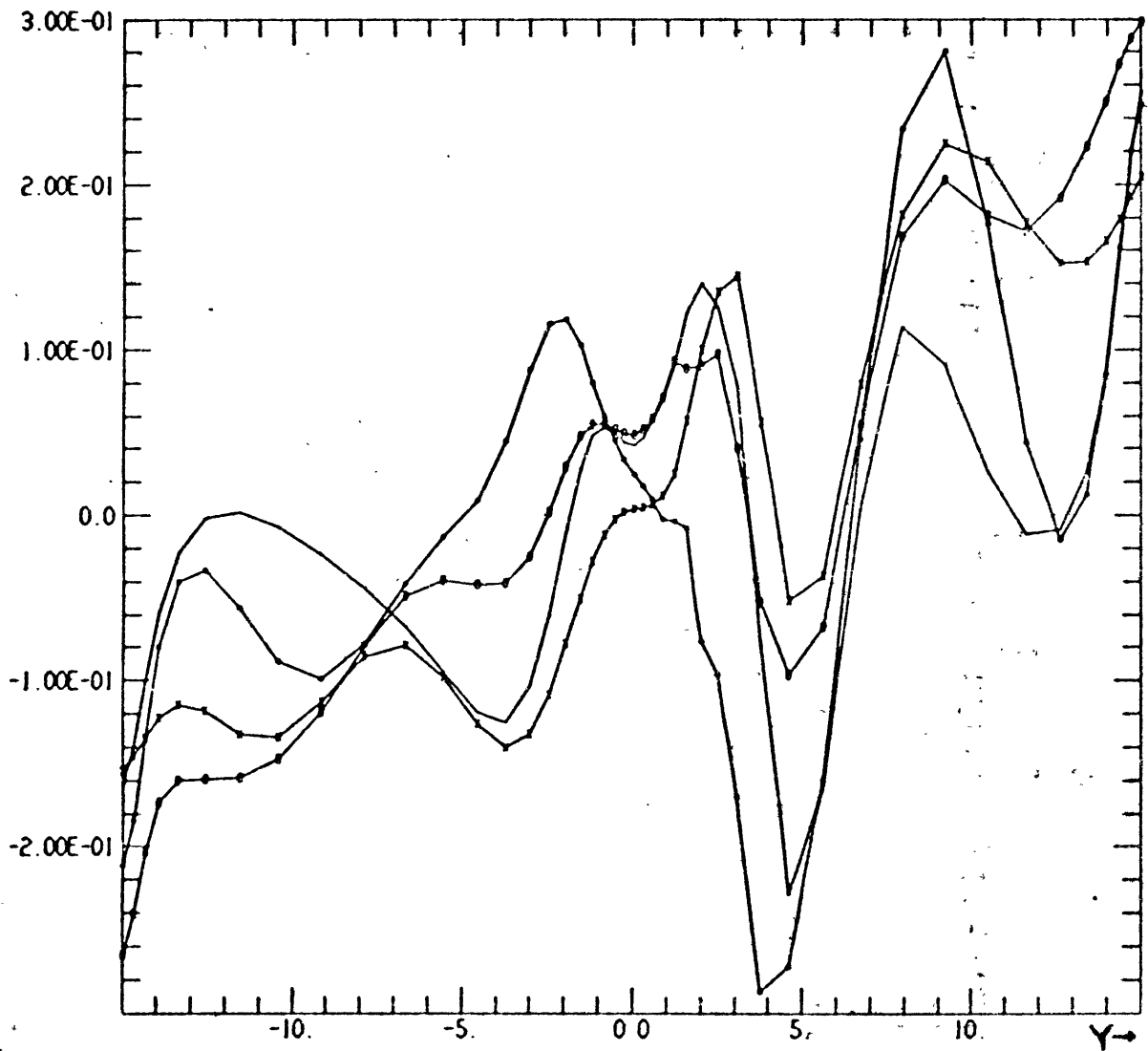
Fig. 5.23 shows meridional sections of the layer depth h at various longitudes. These should be compared with the similar figures for the linear case (Fig. 5.7). In the large there is a tilt upward from south to north at all longitudes, with this feature being barely evident at the western side (Fig. 5.23c) and becoming increasingly pronounced as one moves eastward. The adjustment is more like the linear case at the eastern end. At all longitudes there is a tendency for h to adjust toward a final state poleward of about 7° , while oscillating about a mean state equatorward of those latitudes. The extra-equatorial adjustment occurs more rapidly at the eastern side (Fig. 5.23a) than in the center of the basin (Fig. 5.23b) as in the linear case. Even after 400 days the flow at the western side appears to be very different from the expected final state. The oscillations in the equatorial region are clearly a result of the instability. The mean profile shows that at all longitudes the general tilt to the north is interrupted to allow for troughs (and the associated ridges) are a result of the tendency of h to be in geostrophic balance with the strong zonal currents in the lower layer. These features are more pronounced at the western side than they are at the eastern side. Fig. 5.24 shows a meridional section of the zonal transports at the center of the basin, comparable to Fig. 5.8 for the linear case. The transports are more than an order of magnitude larger than those in the linear case. As



$T = 99.47$ DAYS
 $T = 397.89$ DAYS
 LAYER DEPTH FOR $X = 25.4$ $Y = -15.0$ TO 15.0 , $T = 99.47$ TO 397.89 DAYS
 $N2E3$ $N4CH3$ $30X44STR$ $DELT = .5$ $E = 1.E-8$ $B8 = B1 = .001$ $WIND = .5$ SOUTH EVERYWHERE

08/05/21 0

Fig. 5.23a Meridional sections of h to day 398 at $x = 25.4^\circ$.
 Nonlinear. South wind.



·T· 99.47 DAYS ·T· 198.94 DAYS ·T· 298.42 DAYS
 ·T· 397.89 DAYS
 LAYER DEPTH FOR X= 14.3 Y=-15.0 TO 15.0 ·T· 99.47 TO 397.89 DAYS
 N2E3 N4CH3 30X44STR DELT· 5 E·1.E-8, BB·BI·.001 WIND· 5 SOUTH EVERYWHERE. 08/05/21 C

Fig. 5.23b Meridional sections of h to day 398 at x=14.3° ,
 Nonlinear South wind.

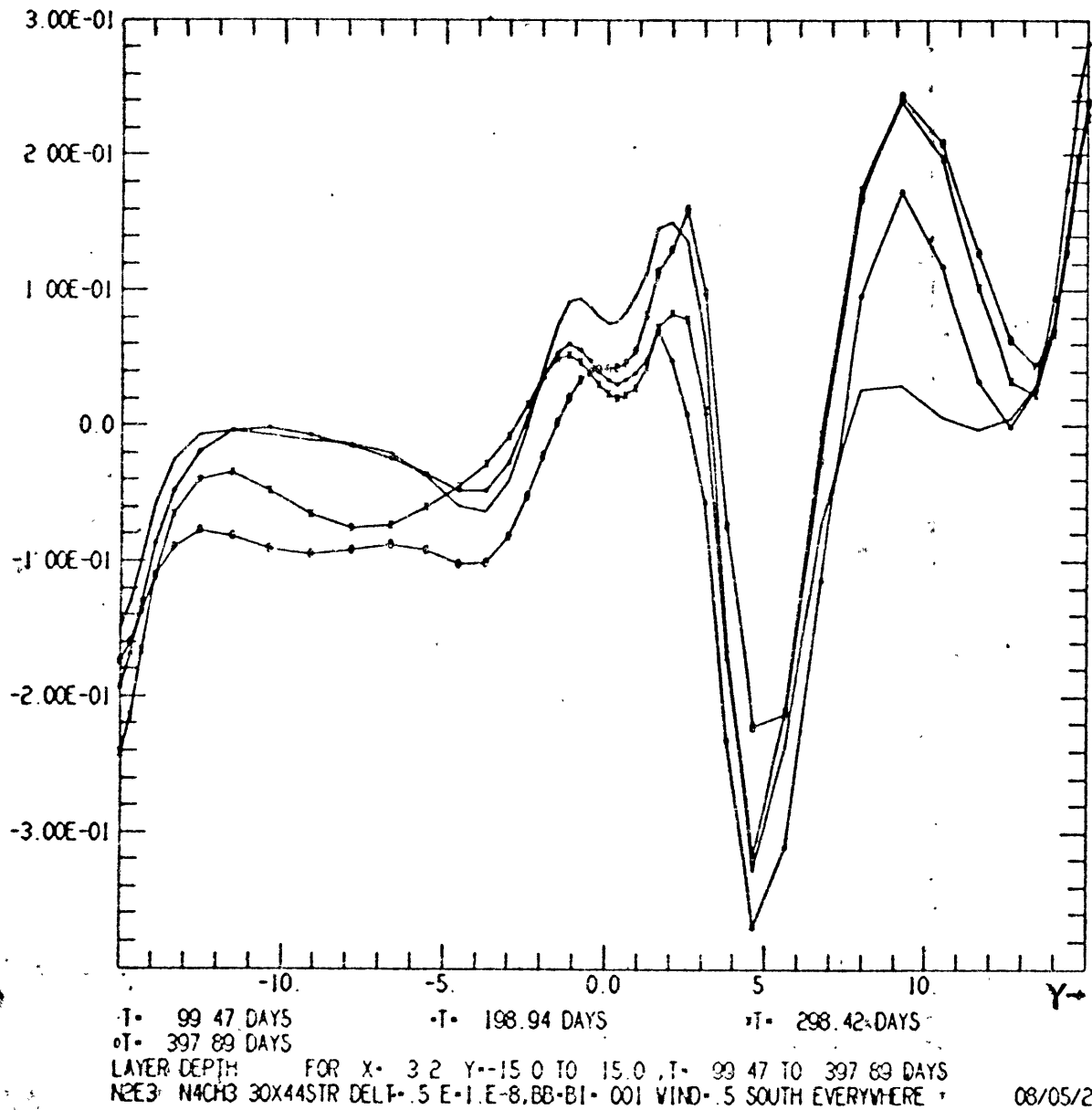


Fig. 5.23c Meridional sections of h to day 398 at $x=3.2^\circ$.
Nonlinear. South wind.

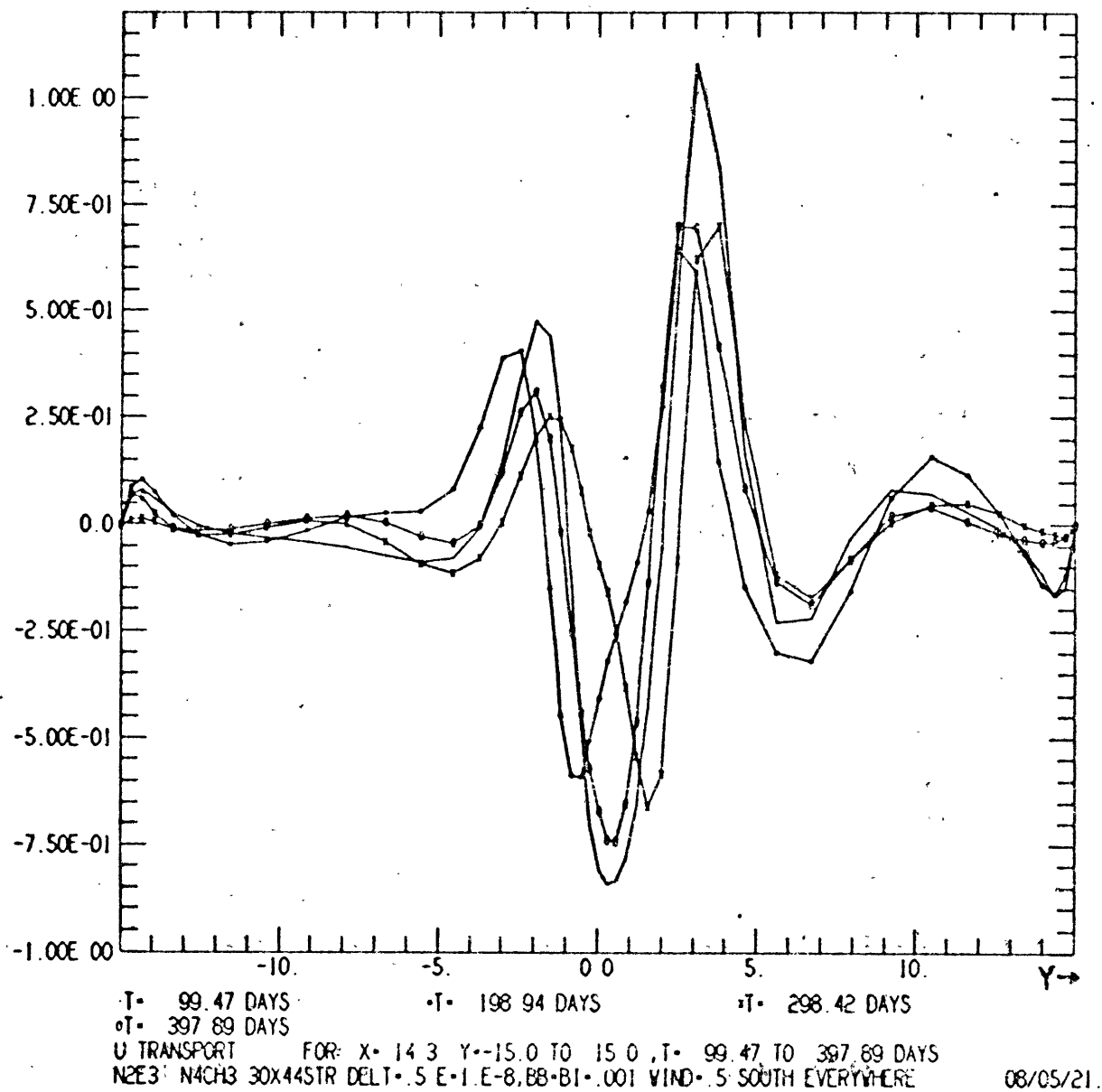


Fig. 5.24 Meridional sections of \bar{u} to day 398 at $x=14.3^\circ$.
 Nonlinear. South wind.

with the layer depths, there is an adjustment toward a final state extra-equatorially and an oscillation about a mean in the vicinity of the equator.

5.4 Linear Response to an East Wind

In this section we are concerned with the linear response of the model to a wind of constant magnitude which is everywhere from the east. (See Section 5.2 for a precise specification of parameters; the sole difference here is that the wind stress of $.465 \text{ dynes cm}^{-2}$ is from the east rather than the south.) We begin by applying the analytic results of chapters 3 and 4 apply to this case.

The solution for the boundary layer velocity \tilde{u} defined by (3.8) is given by (3.25). It evolves to a steady state on the frictional timescale of 20 days. Extra-equatorially, \tilde{u} approaches the Ekman wind drift solution; flow is poleward in both hemispheres. Consequently, there is a strong upwelling at the equator. The flow at the equator is westward, in the direction of the wind ($u = \tau^{(x)} E^{-1} (1 - e^{-Et})$, $\tilde{v} = 0$). There is a boundary layer extending about 300 km from the equator in which interfacial friction is important. Within this layer the flow turns from being zonal to being meridional. The non-zero u component requires sidewall boundary layers of width $O(A^{1/2})$ where A is the horizontal Ekman number. An upwelling region at the eastern end of the equator and a downwelling layer at the

western end are needed to complete the fluid circuit. Downwelling layers will also be required at the northern and southern boundaries of the basin to bring \bar{v} to zero. (See Section 3.3).

The time dependent solution for the vertically integrated transports and the layer depth h may be found by the methods of Chapter 4. It will have \bar{u} and h symmetric and \bar{v} antisymmetric about the equator. In the absence of boundaries, this part of the model response would consist of inertia-gravity waves together with functions of the form (4.19), viz.,

$$(\bar{u}, \bar{v}, h) = (U(y)t, V(y), H(y)t) \quad (5.11)$$

These functions are depicted in Fig. 4.2 for the wind stress $F=1$, which is just the negative of the present case (also see (4.15) - (4.17) and (E16)). Note that U and H are equatorially confined, while V goes to zero at the equator and approaches $-F/y$ as y increases. Most of the energy put in by the wind goes into (5.11); relatively little goes into the inertia-gravity waves.

The boundary effects on the inertia-gravity waves are similar to those for the south wind case discussed in Section 5.2. Briefly, these waves are reflected at the meridional boundaries but they lose a part of their initial energy to boundary-trapped modes with each reflection at the eastern side. It is clear that the adjustment to a final state will be accomplished by the boundary effects on the secularly growing part of (5.11). As with the south wind we anticipate that the final state will be one in which there is no motion and the sea

surface tilts up uniformly from east to west to balance the wind stress; this is consistent with the Sverdrup relation (3.15). If we choose a velocity scale so that $F = -1$, then this state is

$$\bar{u} = \bar{v} = 0; \quad h = -(x - x_E)/2 \quad (5.12)$$

There are some crucial differences from the south wind case which make the spin up process far more complex with an easterly wind stress. First, the unbounded response (5.11) is not steady. More importantly, this response is composed of both Rossby modes and a Kelvin mode, so that not all propagating modes have group velocity in the same direction.

Denote the Kelvin mode of (5.11) by K_0 and the Rossby modes collectively by R_0 . U and H being equatorially confined implies that the amplitude of the Rossby modes falls off rapidly with n [cf. (4.16) and (E16)]. The eastern boundary response to R_0 is a sum of Rossby modes which we will denote collectively by R_1 [these modes have the form (4.22)]. The n^{th} such mode propagates away from the boundary with group velocity $(2n+1)^{-1}$ so that the response extends farthest from the boundary at low latitudes. R_1 is an infinite set of modes; if all modes were present at a point x , then $R_0 + R_1 + V(y)$ would have zero velocity components and $h = -(x - x_E)$, except that the Kelvin mode component required for such a state is missing. That is, the eastern boundary reflection of R_0 tends to adjust toward zero velocities and a height sloping upward to the west independent of time. Note that it tends to make the height too low everywhere:

$h = -(x-x_E)$ instead of (5.12). This part of the response is analogous to the process that affected the adjustment in the south wind case. Here it is not sufficient to bring the ocean to a steady state.

R_1 are not the only Rossby modes generated at the eastern boundary. The Kelvin mode K_0 is reflected as a series of Rossby modes R_1' ; these have a linear time dependence (see Eq. (E13)). At the eastern boundary they asymptote extra-equatorially to a coastal Kelvin mode which will turn the corners at the northern and southern boundaries of the basin.

At the western side, the response to K_0 is a Kelvin mode K_1 (4.23) propagating eastward with unit group velocity such that

$$K_0 + K_1 = d_{-1} \times \phi_{-1} = -\pi^{-1/4} \times \phi_{-1}$$

thus eliminating the secularly growing K_0 . In response to R_0 there is a $K_1' \approx -\frac{\pi^{1/4}}{5} (t-x) \phi_{-1}$ (E17), so that not all such growth has been eliminated. In addition, the reflection R_0 is composed of boundary trapped Rossby modes (E15); these have only a minor role in the spin up of the basin.

At time $t = x_E$ modes K_1 and K_1' arrive at the eastern boundary, thus altering the form of the reflection of the Kelvin mode there. K_1 changes the secularly growing set of modes R_1' into a set R_2 , each of which has constant amplitude in time and space. The reflection of K_1' is a secularly growing set R_2'

but with smaller amplitude than R_1' . This reflection thus tends to bring the basin closer to a steady state.

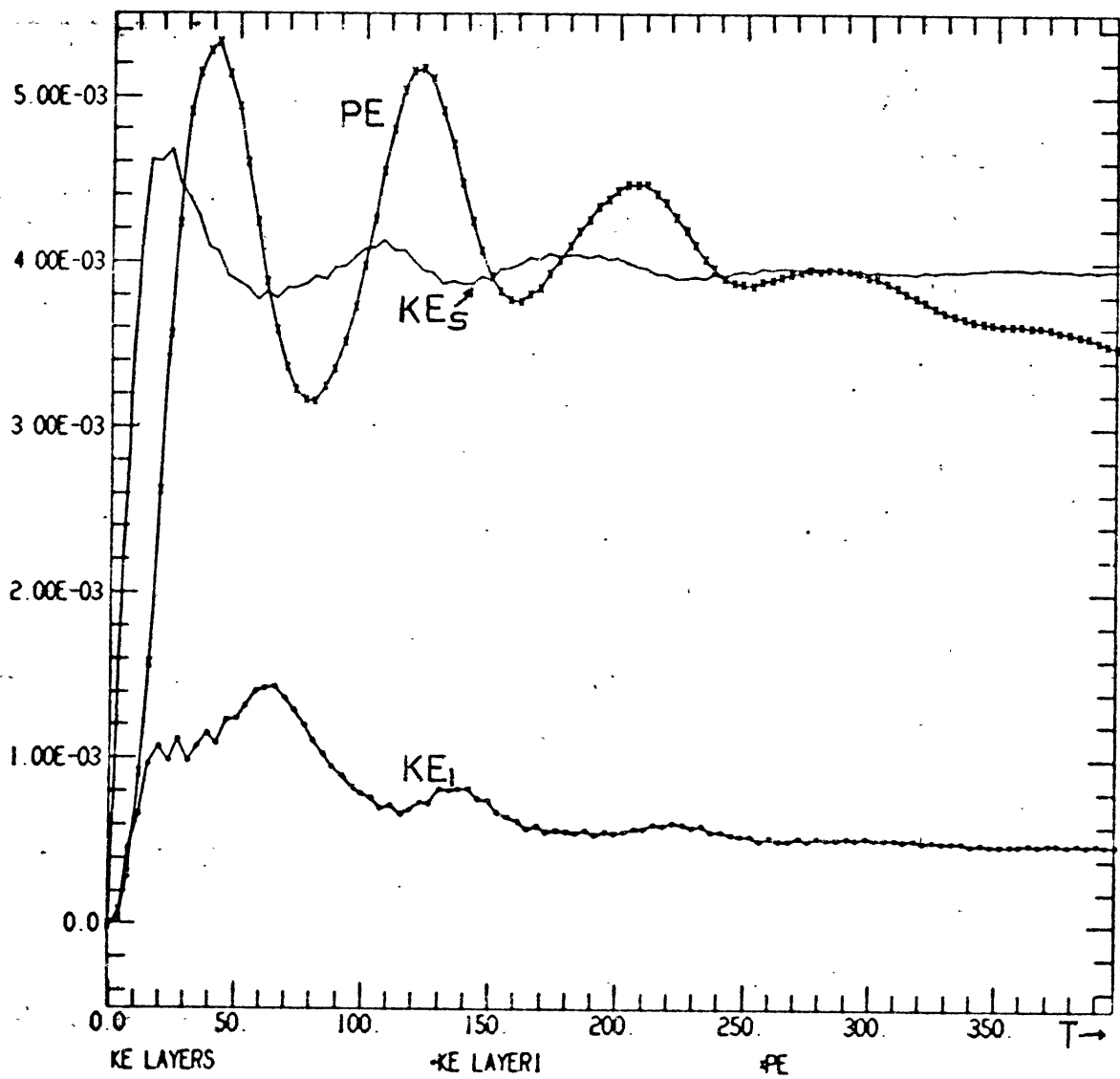
At $t = 3x_E$ the leading edge (or wave front) of R_1 and R_1' (the $n = 1$ Rossby mode) has crossed the basin from east to west. The presence of R_1 at the western side alters the time dependent Kelvin mode reflection K_1' to a steady (in space and time) Kelvin mode K_2 . The reflection of R_1' creates another time growing Kelvin mode K_2' , but with smaller amplitude than K_1' .

At $t = 4x_E$ the leading edge of R_2 and R_2' reaches the western boundary, while K_2 and K_2' just reach the eastern boundary. Again, the reflections of the unprimed terms have constant amplitude, while the primed terms' reflections are non-steady. At this time there are no R's or K's with their leading edge in the interior of the basin. In this sense, the situation is similar to conditions at $t = 0$ and a cycle has been completed; there is a periodicity with period $4x_E$. It is not yet clear how many such cycles it takes before (5.11) is approached arbitrarily closely. This information is most readily obtained from the numerical simulation.

Before turning to those results however, we wish to remark further on some of the features of the preceding description. Both the eastern and western boundaries participate actively in the adjustment process, because the fact that the forcing excites the Kelvin mode makes it impossible for the

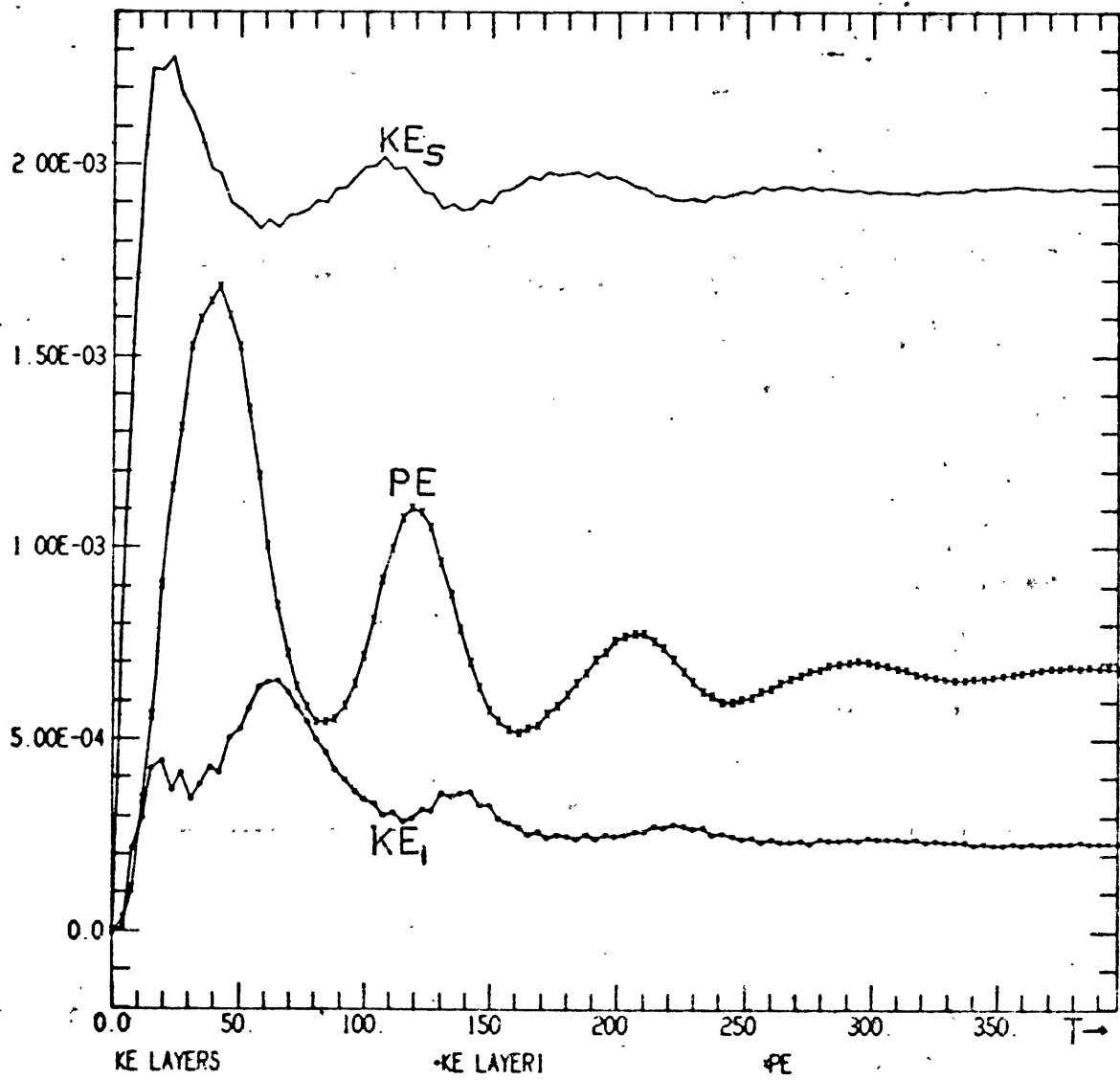
adjustment to proceed solely from the east. The final state is not approached monotonically; for example, the gradient of the layer depth tends to "overshoot" its final value. In appearance, this is reminiscent of the response of a tilted pan of water, though the mechanism responsible here is not gravity waves. As before, the more equatorially confined modes travel the most rapidly, but here it does not follow immediately that the equatorial region adjusts more rapidly (though this does turn out to be the case). The Kelvin wave has negligible amplitude extra-equatorially, influencing that region only via the coastal Kelvin modes generated when it is reflected at the eastern end of the equator. Hence, all the extra-equatorial adjustment proceeds from east to west.

Figs. 5.25 and 5.26 show the energies for the basin as a whole and for the equatorial region, respectively. The upper layer kinetic energy reaches its maximum value in the frictional spin up time (20 days). Since there is no vertical advection of momentum, the lower layer kinetic energy remains much smaller than that of the upper layer. This was also true of the previous linear case, Fig. 5.2. The most striking feature of these plots is the damped oscillations which appear in all fields, though they are most clearly seen in the potential energy curves. This oscillation has an 80 day period; the initial peak is at day 42 and the first minimum at day 82. The crest to trough difference from day 200 to 240 has 30



ENERGIES FOR X= 0.0 TO 28.6 Y=-15.0 TO 15.0 T= 0.0 TO 397.25 DAYS
 L2E2 N4CH3 30X44STR DELT= 5 E-1 E-8.88-61-.001 WIND= .5 EAST EVERYWHERE 07/22/03 0

Fig. 5.25. Energies from 15°S to 15°N. Linear. East wind.



ENERGIES FOR X= 0.0 TO 28.6 Y= -5.6 TO 5.6 T= 0.0 TO 397.25 DAYS
 L2E2 N4CH3 30X44STR DELT= 5 E-1 E-8 BB-BI= 001 WIND= 5 EAST EVERYWHERE 07/22/03

Fig. 5.26 Energies from 5.6°S to 5.6°N. Linear. East wind.

percent of the amplitude of that from day 42 to day 82.

These oscillations in the energies are obviously related to the reflections from the basin walls described above. The fundamental time period that emerged in that analysis is the time it takes for a Kelvin wave to cross the basin, $t = x_E$ with the scaling of Chapter 3. For the model parameters used here, this time is 19.2 days. It was remarked earlier that the adjustment pattern repeated after 4 such time periods; this agrees well with the observed 80 day period. The potential energy is a minimum at $t = 80, 160, \dots$ days. At these times, the leading edges of the last Kelvin mode generated has just reached the eastern boundary, while that of the last Rossby modes has just reached the west. The PE maxima occur at $t = 40, 120, \dots$ days. At 40 days the leading edge of the first Rossby modes generated at the eastern side (R_1 and R_1') are two-thirds of the way across the basin while the second set of such modes (R_2 and R_2') are one-third of the way across.

Figs. 5.27 and 5.28 show profiles of the layer depth at the equator at various times. If the height were set up to balance the wind stress (5.12), the layer depth profile would be a straight line 21.8 m below it at the eastern side (the dotted line in Fig. 5.27). During the course of the adjustment the profile tends to be below this final value everywhere. The profile at 8 days (Fig. 5.27) shows a flat center section in which the boundary influences have not been felt; here h is

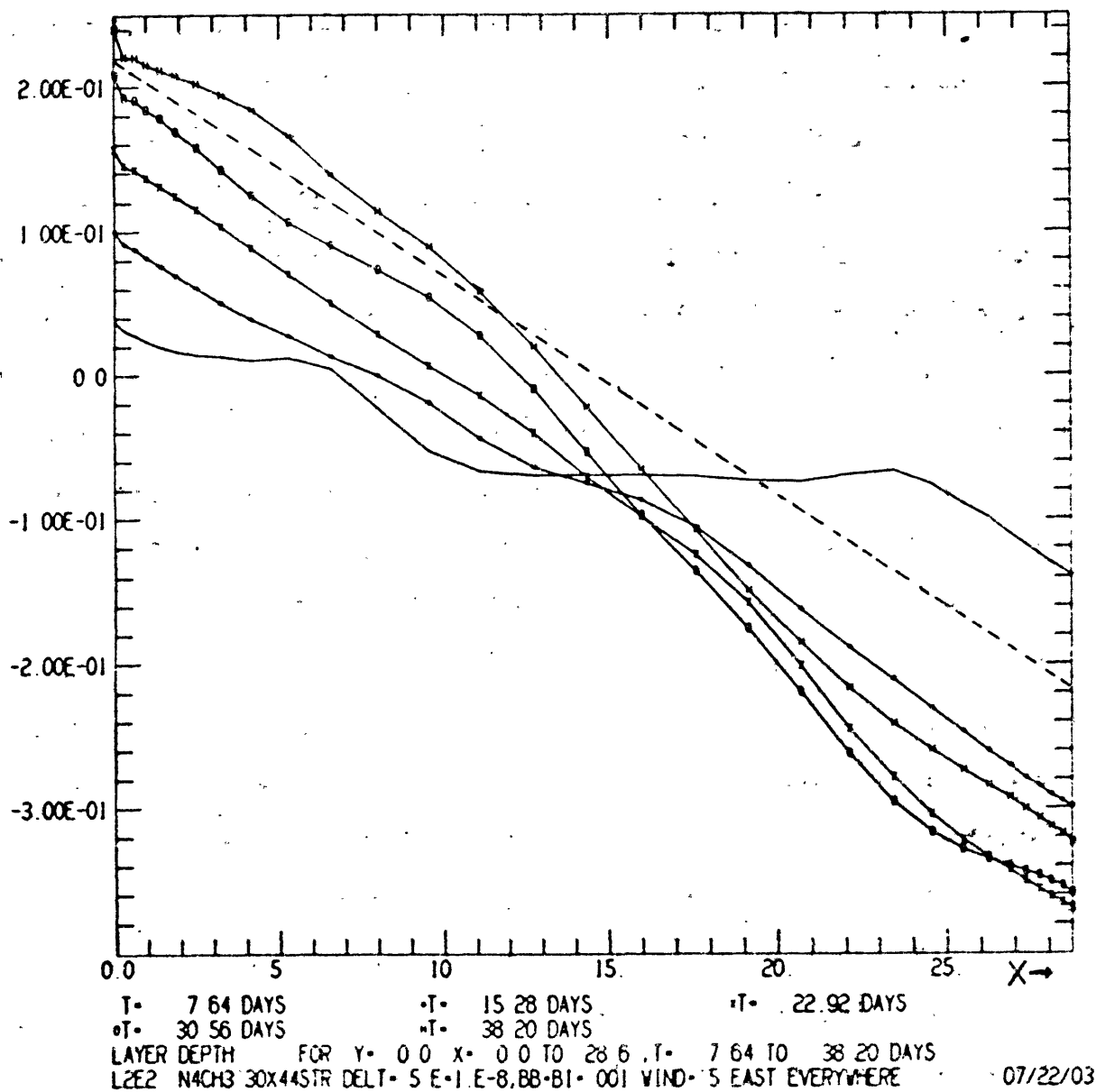


Fig. 5.27 Sections of h along the equator to day 38. Linear. East wind.

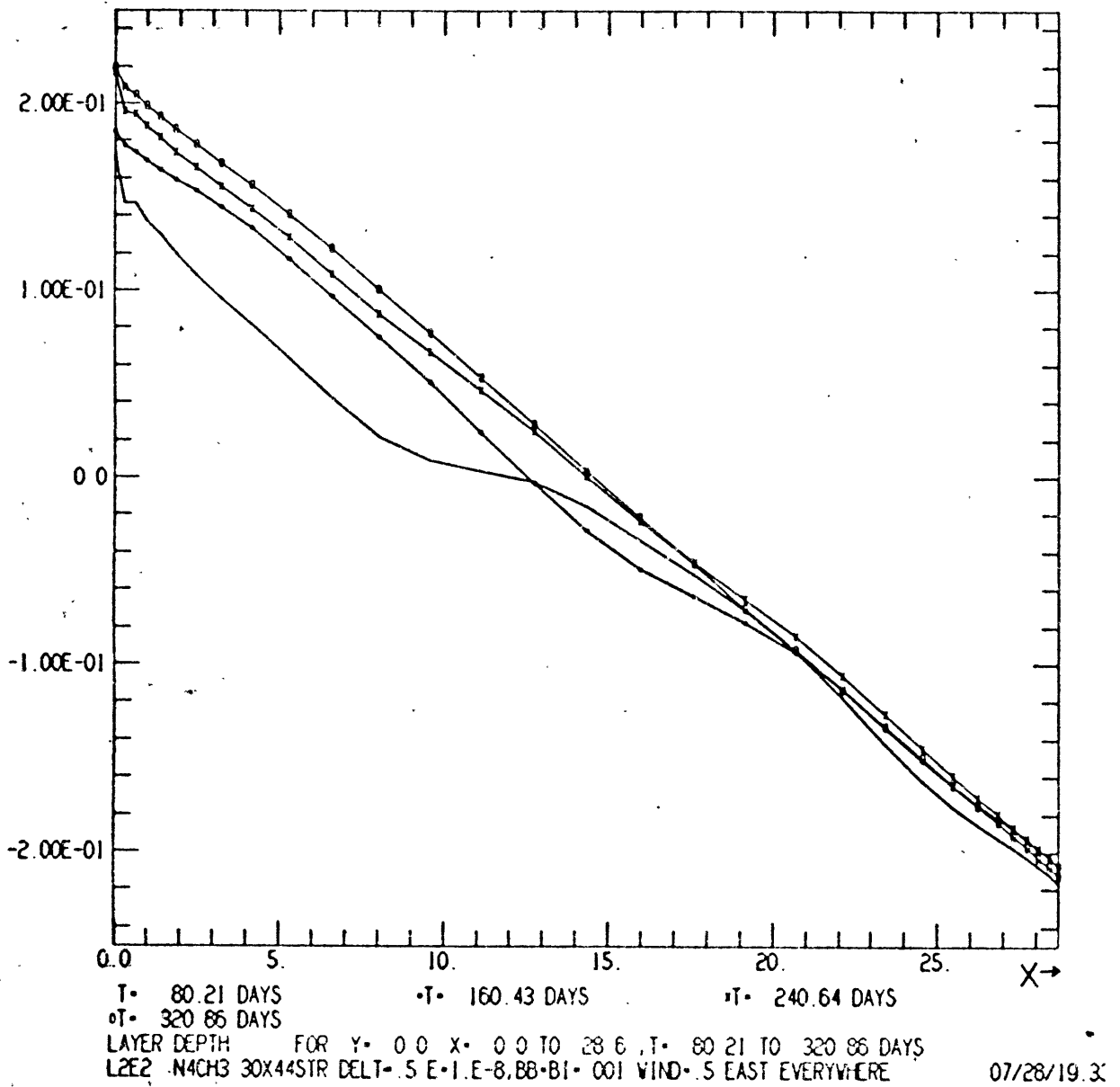


Fig. 5.28 Sections of h along the equator to day 398. Linear. East wind.

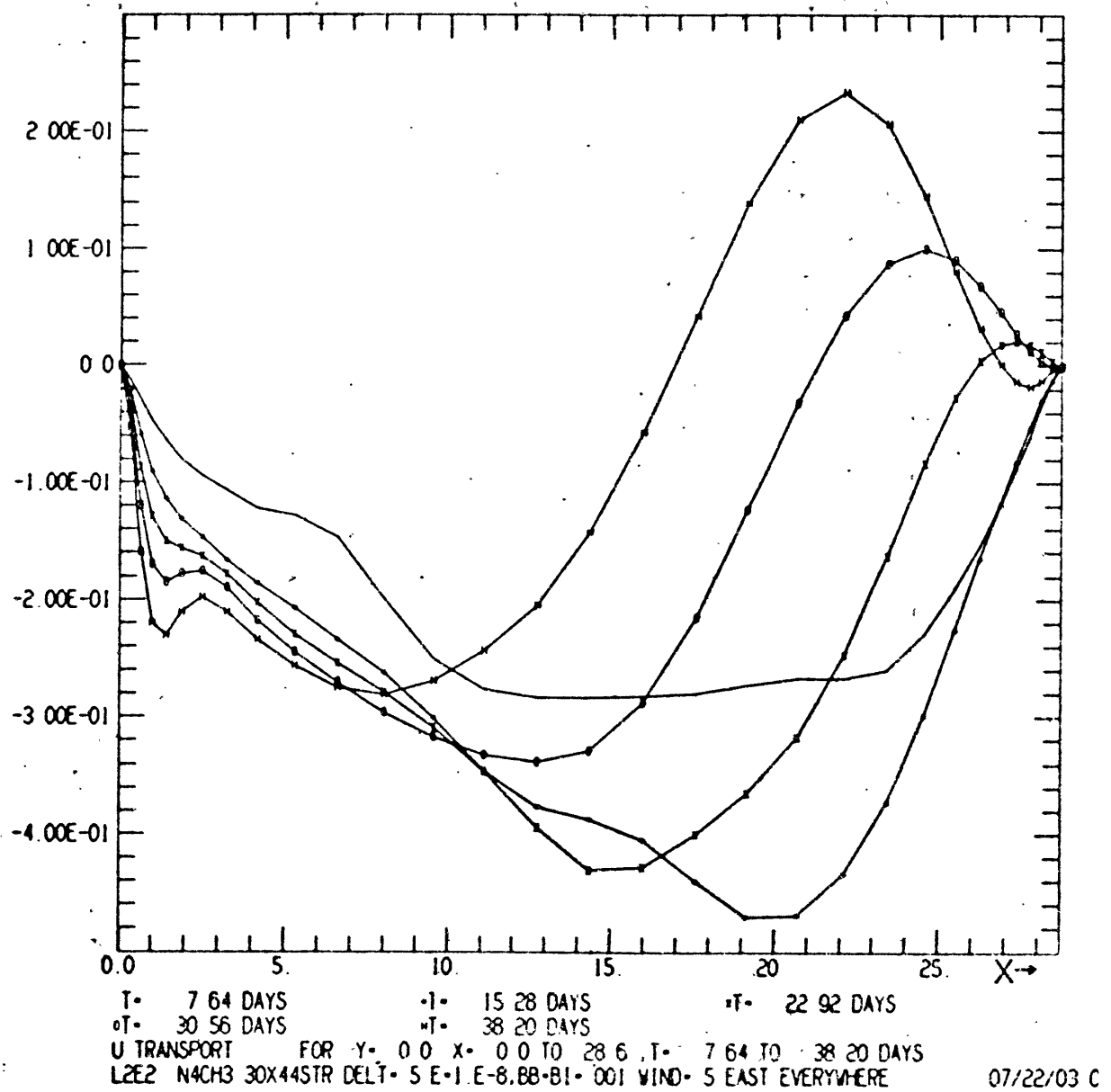


Fig. 5.29 Sections of \bar{u} along the equator to day 38. Linear. East wind.

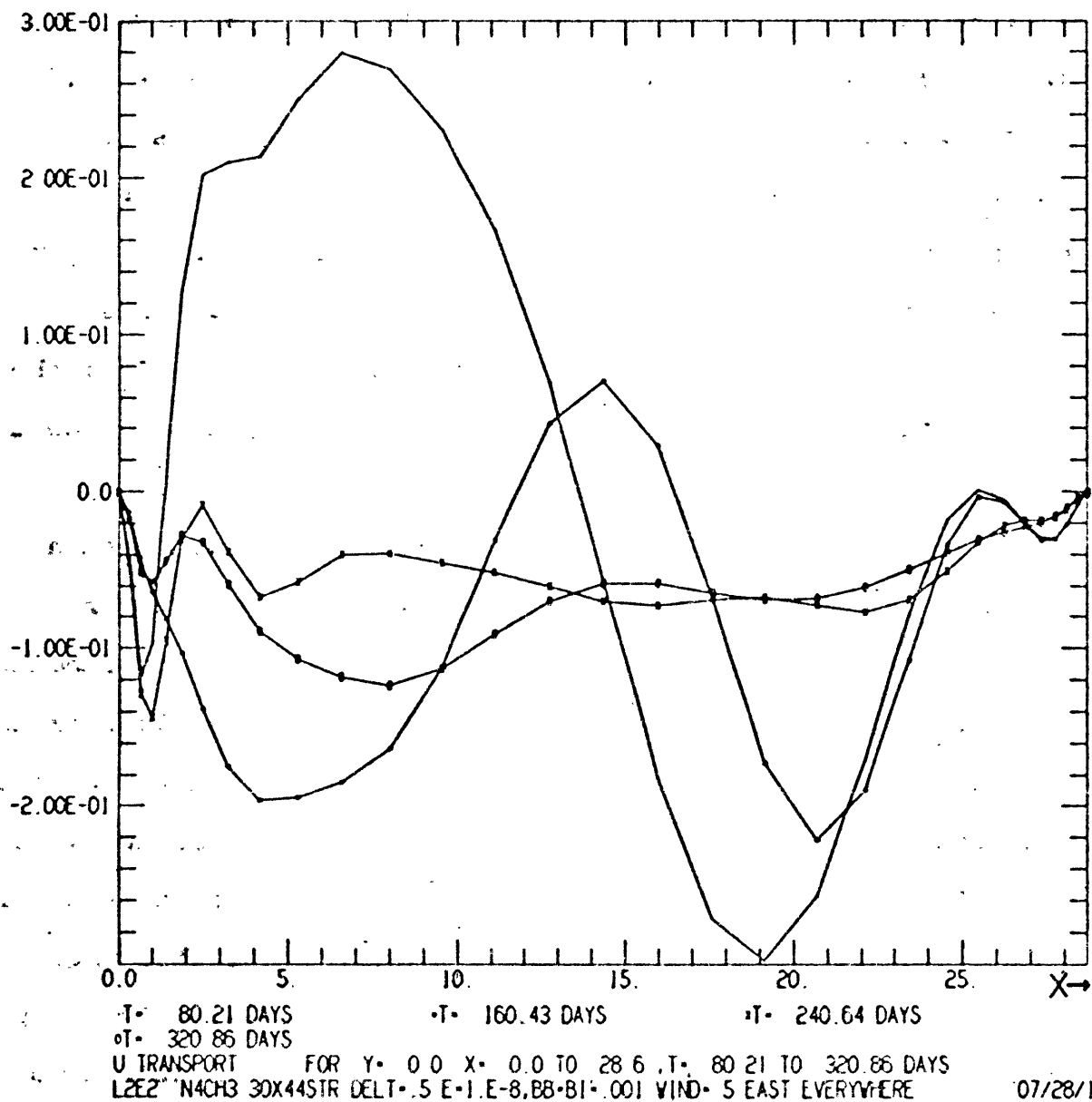


Fig. 5.30 Sections of \bar{u} along the equator to day 398. Linear. East wind.

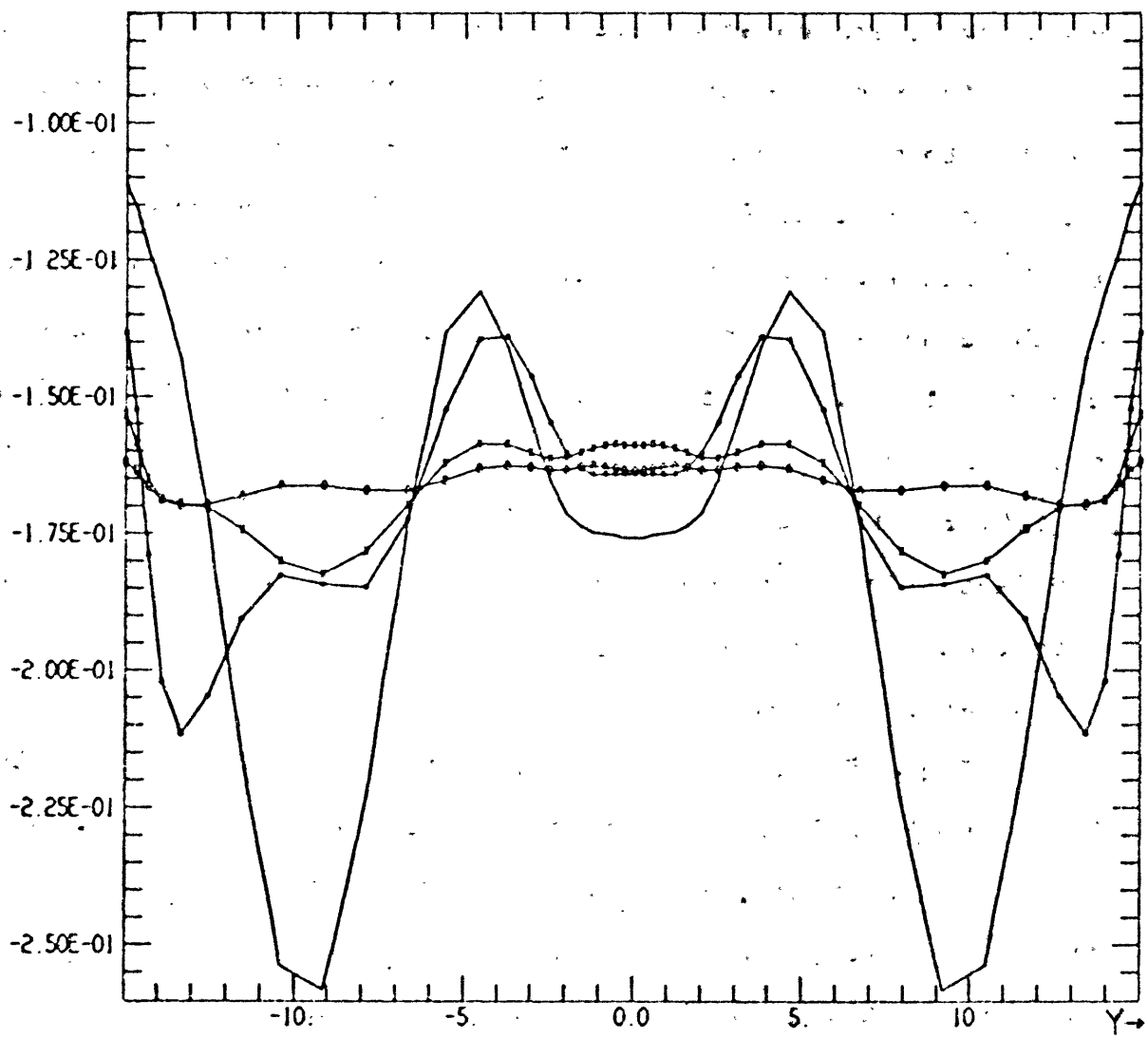
decreasing in accordance with the unbounded solution (5.11). At this time, the Kelvin mode generated at the western boundary ($K_1 + K_1'$) has propagated 12° into the basin. This is evident in the sloping region at the western side of the basin. Near the wall there is also evidence of the effect of the boundary trapped modes. At the eastern side there is another sloping piece to the profile extending 4° into the basin. This is due to the Rossby modes generated at the boundary ($R_1 + R_1'$); the fastest of these, the one with meridional index $n = 1$, would have propagated 4° at this time.

At 14 days the two boundary influences would meet at a point three-quarters of the way across the basin. Up until this time, the magnitude of the zonal transport at this point has increased according to (5.11). Hereafter the slope of the height field at all longitudes on the equator will be up toward the west, thus reducing the zonal acceleration. In fact, it is evident from Fig. 5.27 that by 24 days this gradient is generally sufficient to balance the wind stress so that the magnitude of the westward transport will no longer increase. The slopes at the eastern side become steeper than what is required to balance the wind stress so that the transport here becomes eastward and the layer deepens. All of these comments about the transport are confirmed by Fig. 5.29. This region of eastward flow is behind the front formed by the Rossby modes ($R_2 + R_2'$) which are the reflection of the first Kelvin mode ($K_1 + K_1'$) to

cross the basin. The region propagates out from the eastern boundary beginning at day 20.

The profiles at day 40 (Fig. 5.27) and day 80 indicate why the former time is a potential energy maxima and the latter a minima. Fig. 5.28 shows that the later minima are very close to the final state. Fig. 5.30, which shows the zonal transports at the equator, indicates that the equatorial region takes approximately 250 days to spin up to something like its final steady state. This time scale agrees with the energy diagram, Fig. 5.26. Fig. 5.30 also shows that it takes on the order of 200 days before the zonal transports are uniformly westward. Note that the adjustment appears to occur at the eastern side at an earlier time.

Figs. 5.31a, b, and c show north-south sections of the layer depth at longitudes near the eastern boundary, at the center of the basin, and near the western boundary, respectively. At each longitude the steady state profile would be a horizontal line. At all longitudes this is approximated more rapidly at latitudes close to the equator. Near the eastern wall $h \approx -16.5$ m at all latitudes after 300 days. At the center of the basin the expected final value $h = 0$ is approximated only within about 7° of the equator even after 400 days. There is still a strong tilt at the northern and southern walls to geostrophically balance the boundary jets present there (Fig. 5.35). The profile at 3.2° of longitude (Fig. 5.31c) is even further from



T= 80.21 DAYS T= 160.43 DAYS T= 240.64 DAYS
 T= 320.86 DAYS
 LAYER DEPTH FOR X= 25.4 Y=-15.0 TO 15.0 T= 80.21 TO 320.86 DAYS
 L2E2 N4CH3 30X44STR DELT= .5 E=1 E=8.88=BI= .00! WIND= .5 EAST EVERYWHERE -

07/28/19 33

Fig. 5.31a Meridional sections of h to day 397 at x=25.4°. Linear. East wind.

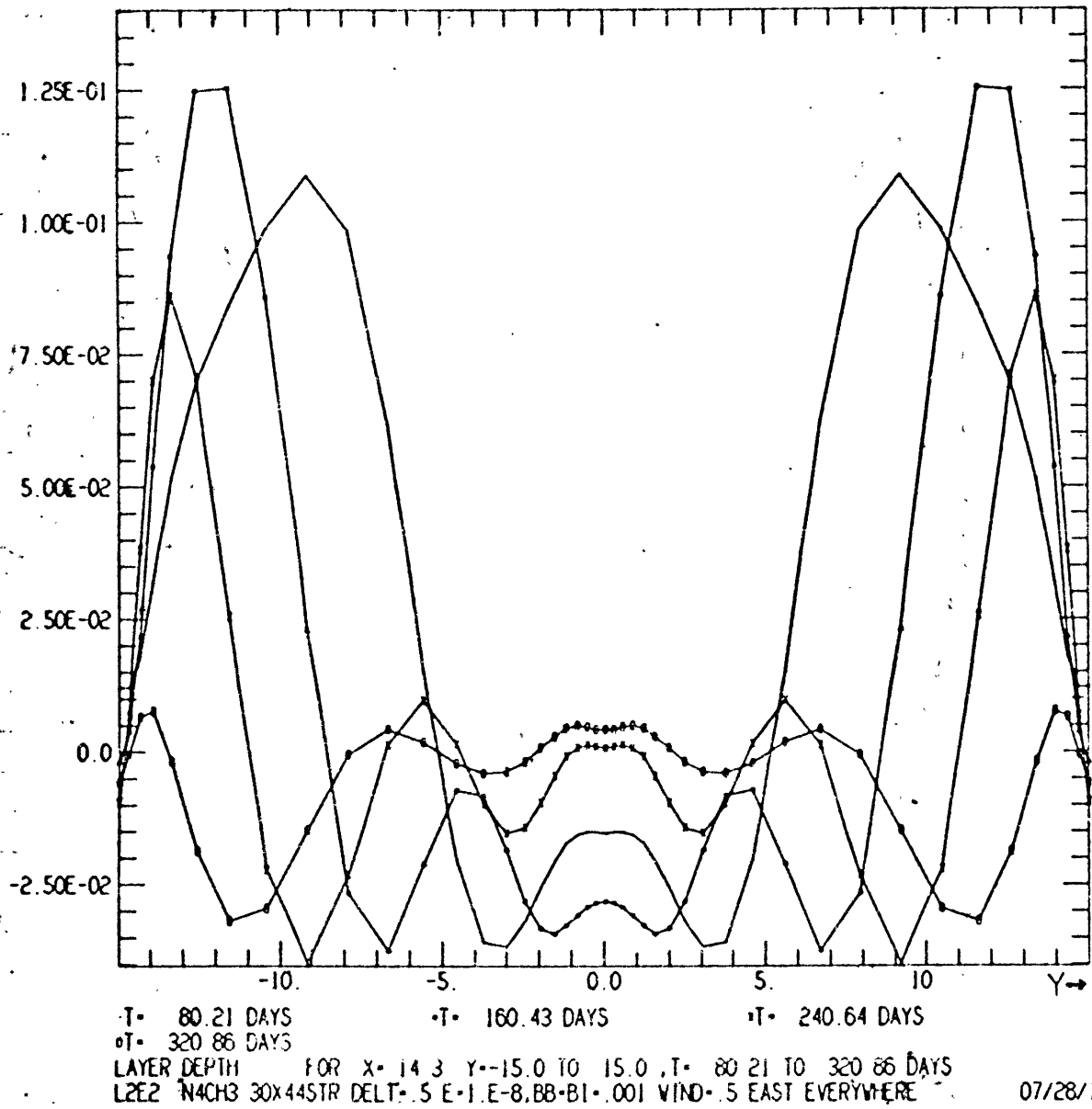


Fig. 5.31b Meridional sections of h to day 397 at $x=14.3^\circ$.
Linear. East wind.

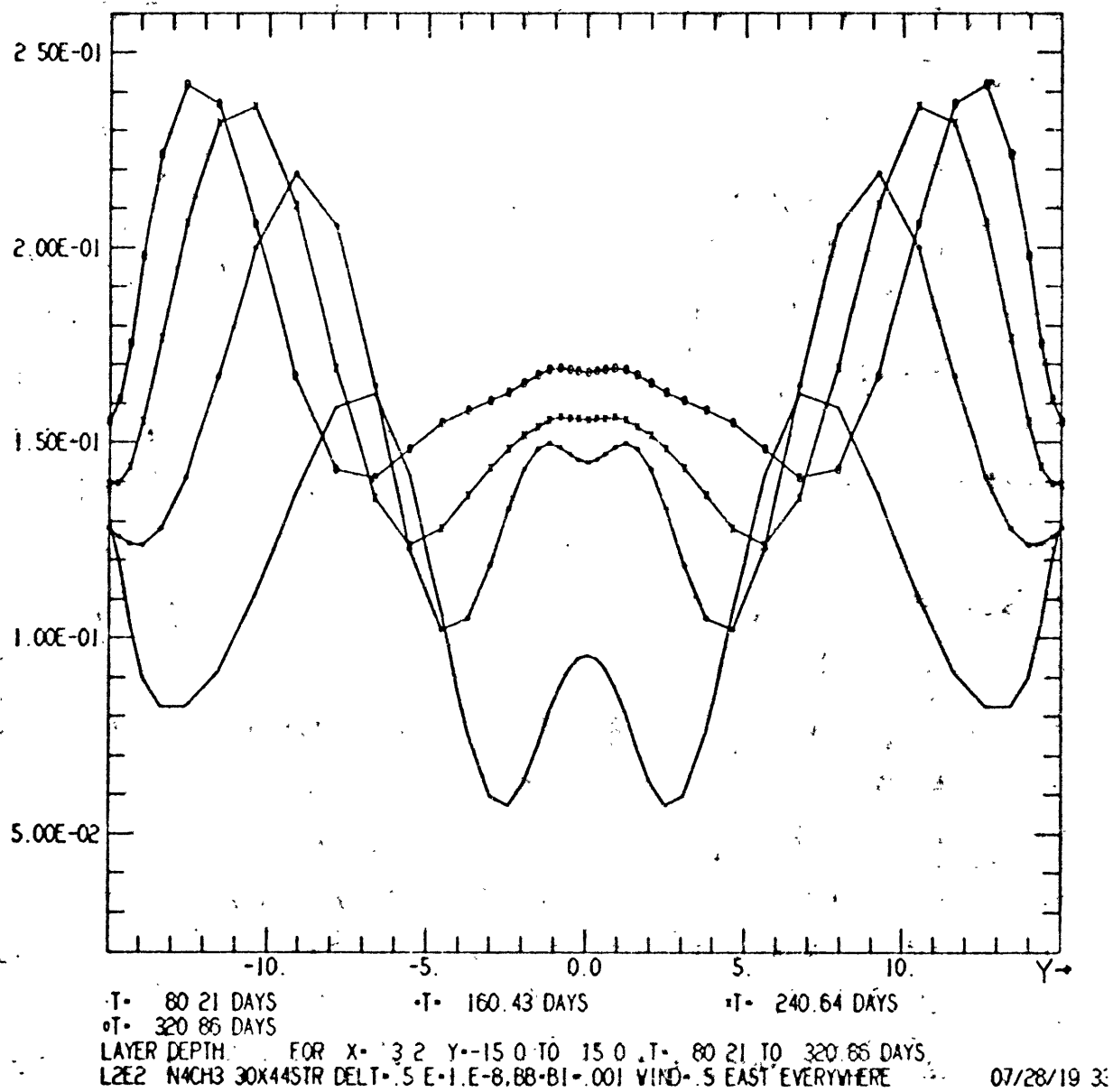
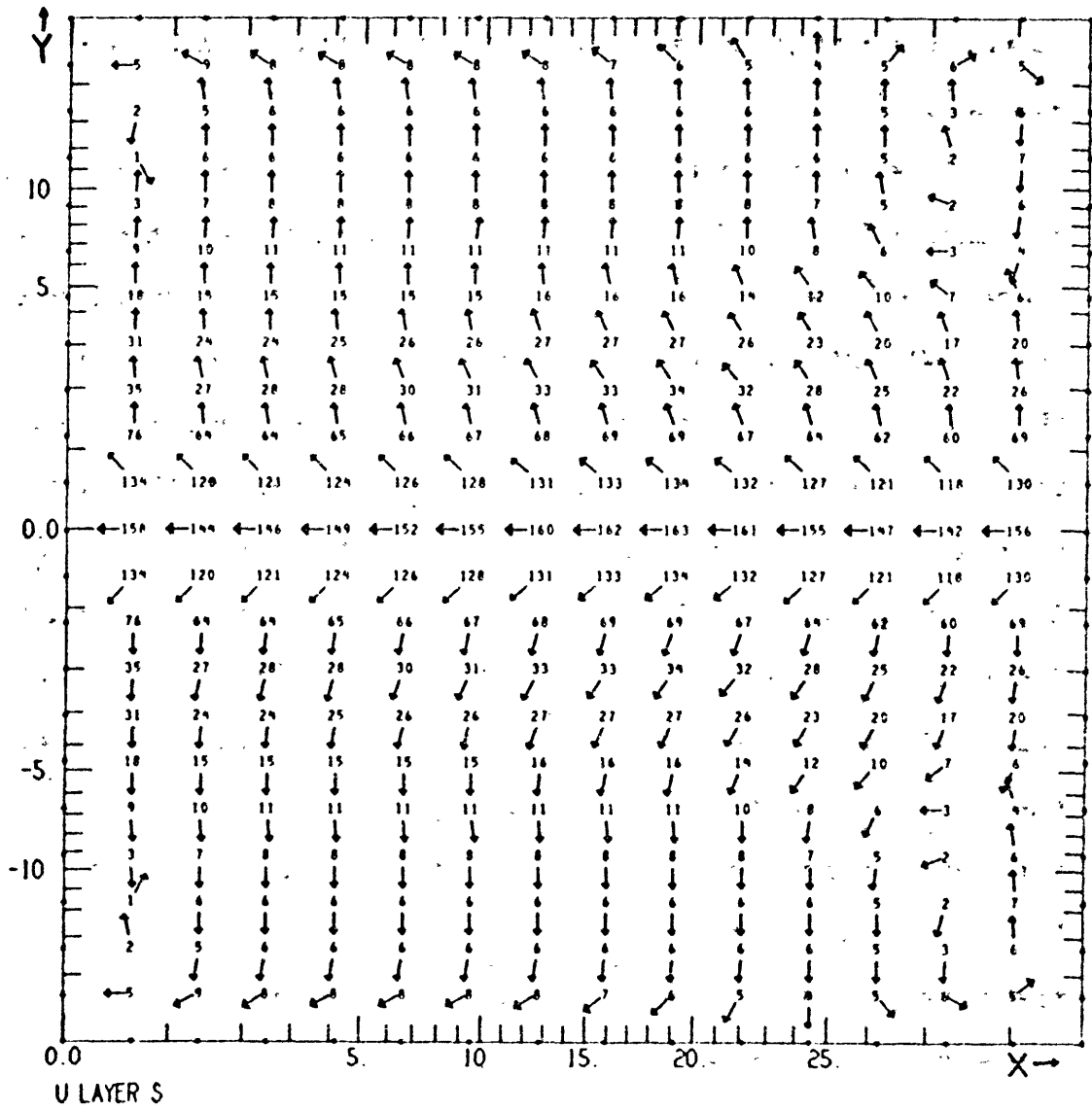


Fig. 5.31c Meridional sections of h to day 397 at $x=3.2^\circ$.
Linear. East wind.

its steady state value ($h \approx + 16.5$ m at all latitudes), though it could be argued that this is approximated within 6° of the equator.

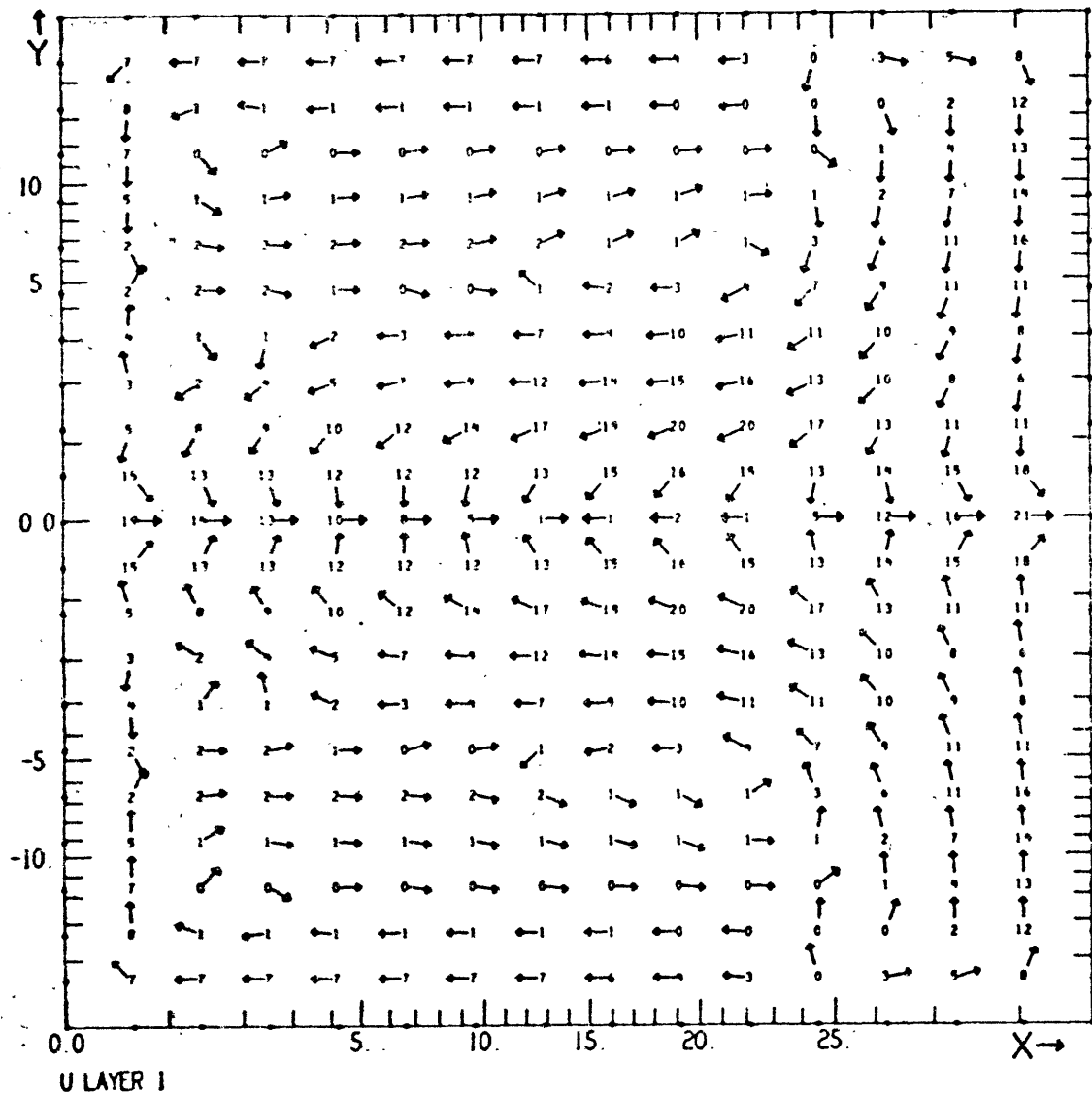
The preceding discussion has touched on most of the elements of the spin up process. A more integrated view is presented in Figs. 5.32 to 5.35 which show the model variables at 16, 40, 200 and 400 days, respectively. In the upper layer, the wind driving is much greater than the pressure forces and the currents behave like \tilde{u} . The velocities at the equator are ^{west} eastward; they turn to be poleward within 4° of the equator. By 16 days, the transports associated with these currents have decreased the layer depth at the eastern end of the equator and raised it at the western end. Near both sides the gradient is steep enough so that the lower layer flow there is counter to the wind direction. Almost everywhere else, interfacial friction has dragged the currents in the same direction as those in the upper layer. The exceptions are the meridional flow near the equator and the eastern boundary. At the zonal boundaries there is a narrow flow in the direction of the wind. It may be shown (Moore 1968) that these coastal Kelvin modes are the $n=0$ infinite equatorial beta plane modes which were rejected because u and h became unbounded at infinity (cf., Section 4.2).

At 40 days (Fig. 5.33) the layer depth changes are largely confined to the boundaries, an area with 7° of the equator, and the eastern side. The Kelvin modes along the



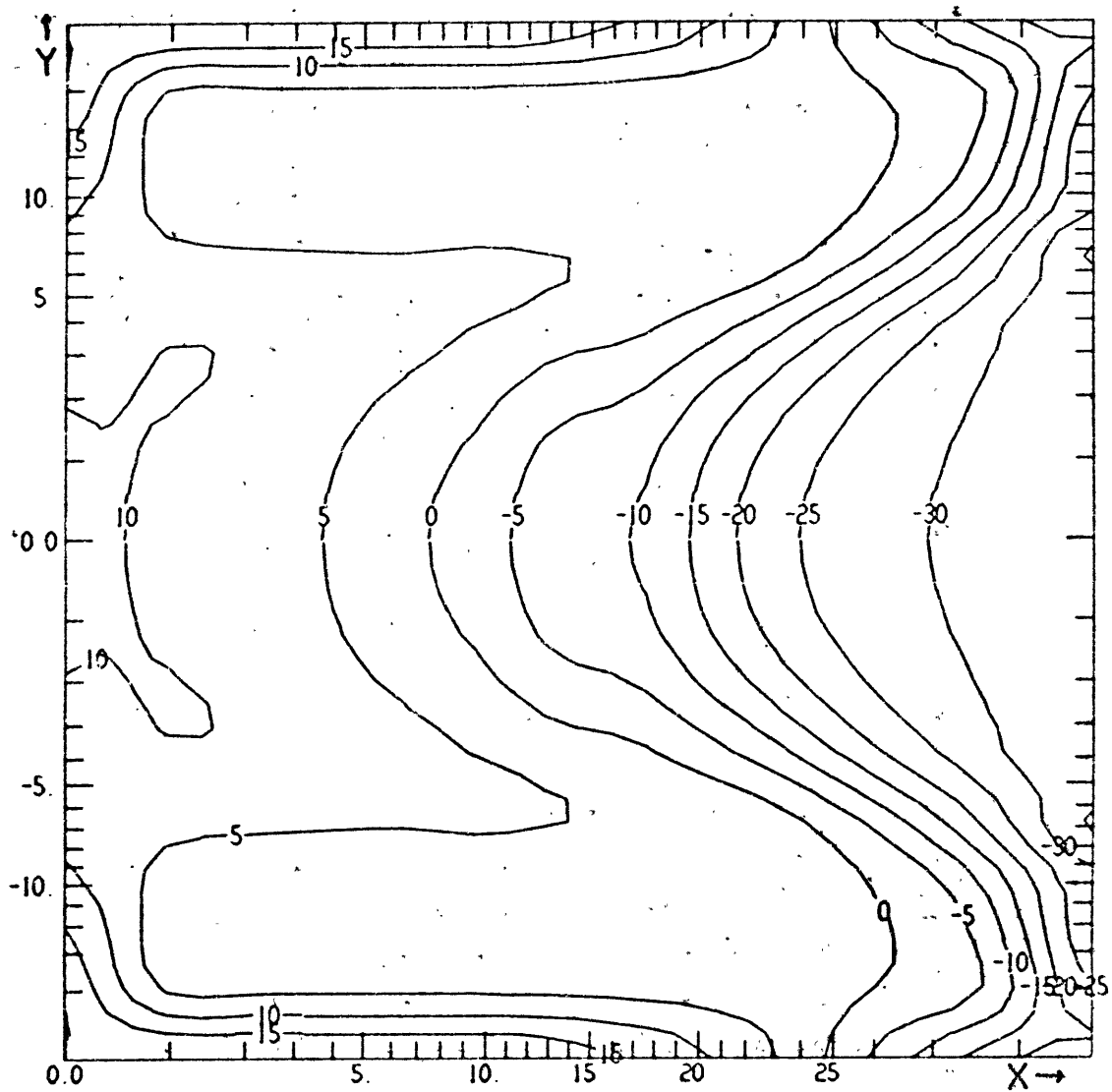
DAY 16.23 IT- 204 00 MODEL STEP 408: X- 0.0 TO 28.6 Y- -15.0 TO 15.0
 L2E2 N4CH3 30X44STR DELT- .5 E-1 E-8,BB-B1-.001 WIND- 5 EAST EVERYWHERE 07/15/02

Fig. 5.32a \vec{u}^S vectors at 16 days. Linear. East wind.



DAY: 16 23 (T- 204 00 MODEL STEP 408) X- 0.0 TO 28.6 Y--15.0 TO 15.0
 L2E2- N4CH3 30X44STR DELT- 5 E-1.E-8.BB-B1- 001 WIND- 5 EAST EVERYWHERE 07/22/03

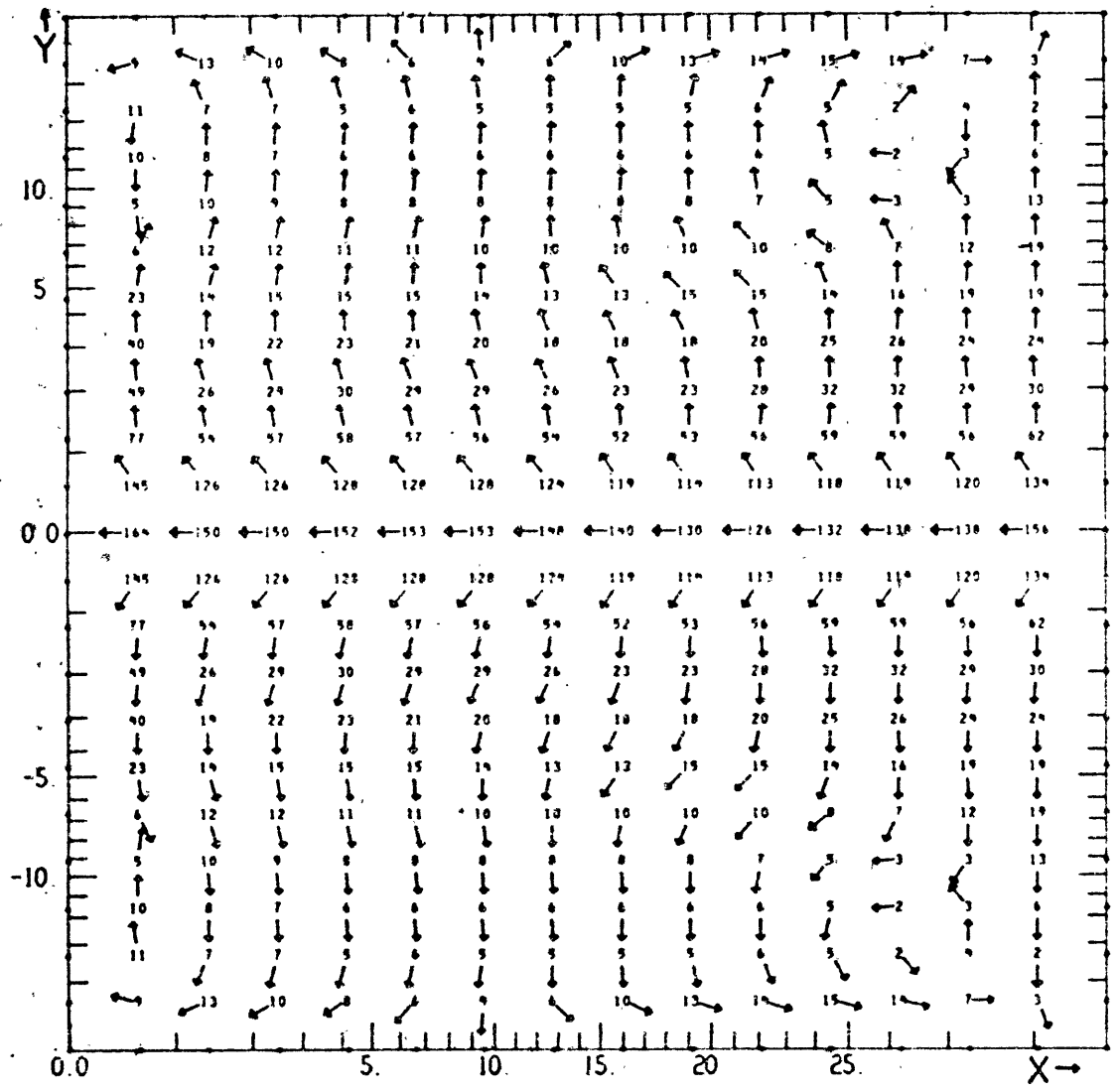
Fig. 5.32b u^1 vectors at 16 days. Linear. East wind.



LAYER: DEPTH LOW: -3.58E-01 HIGH: 2.04E-01 CI: 5 * 1.E-02

DAY 16 23 IT: 204 00 MODEL STEP: 4081 X: 0.0 TO 28.6 Y: -15.0 TO 15.0
 L2E2 N4CH3 30X44STR DELT: 5 E-1 E: 8.88+BI: .001 WIND: 5 EAST EVERYWHERE 07/22/03.1

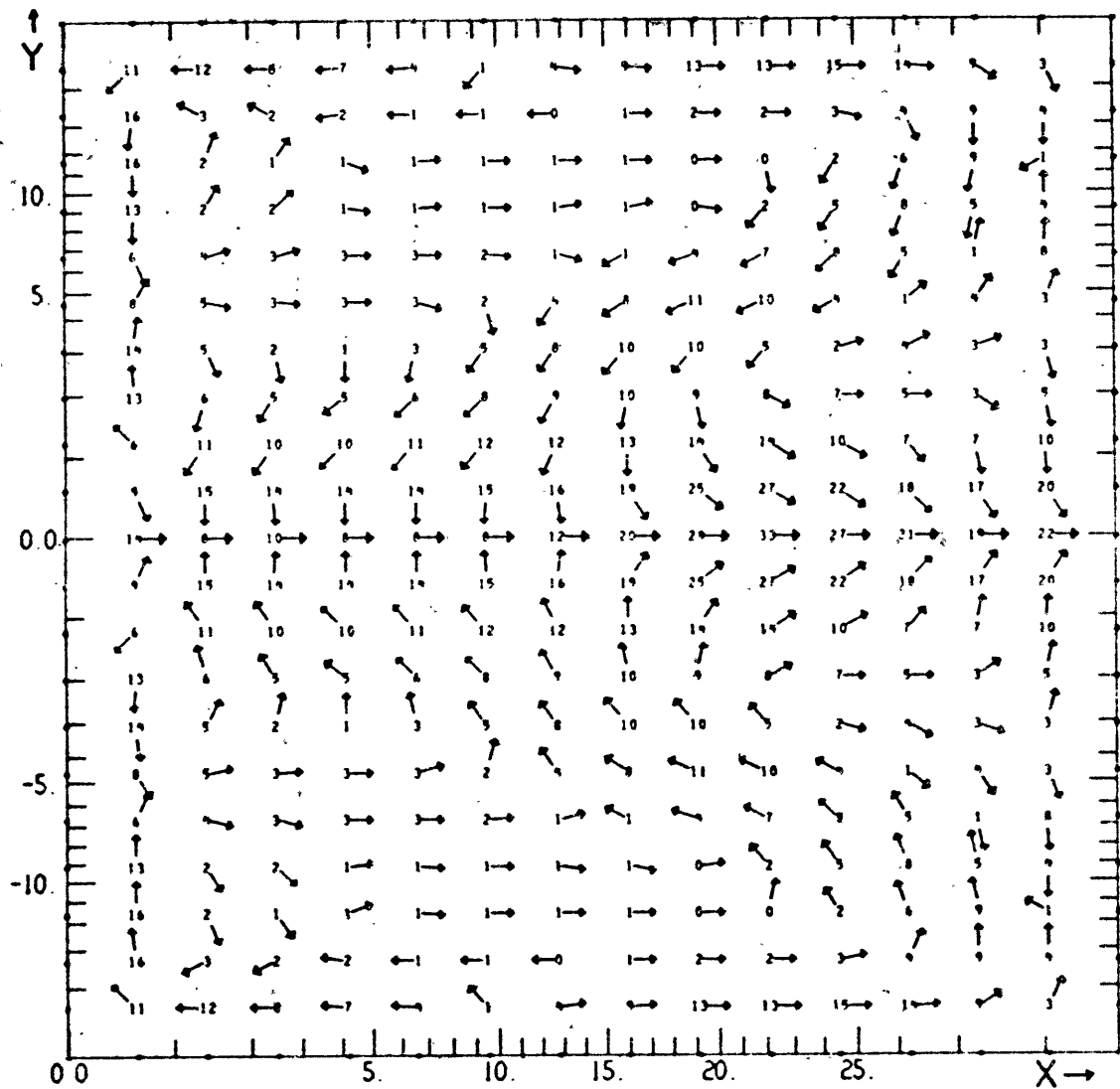
Fig. 5.32c: h contours at 16 days. Linear. East wind.



U LAYER S

DAY 40.11 (T= 504.00 MODEL STEP 1008) X= 0.0 TO 28.6 Y=-15.0 TO 15.0
 L2E2 N4CH3 30X44STR DELT=.5 E=1.E-8.88*81= .001 WIND=.5 EAST EVERYWHERE 07/22/03

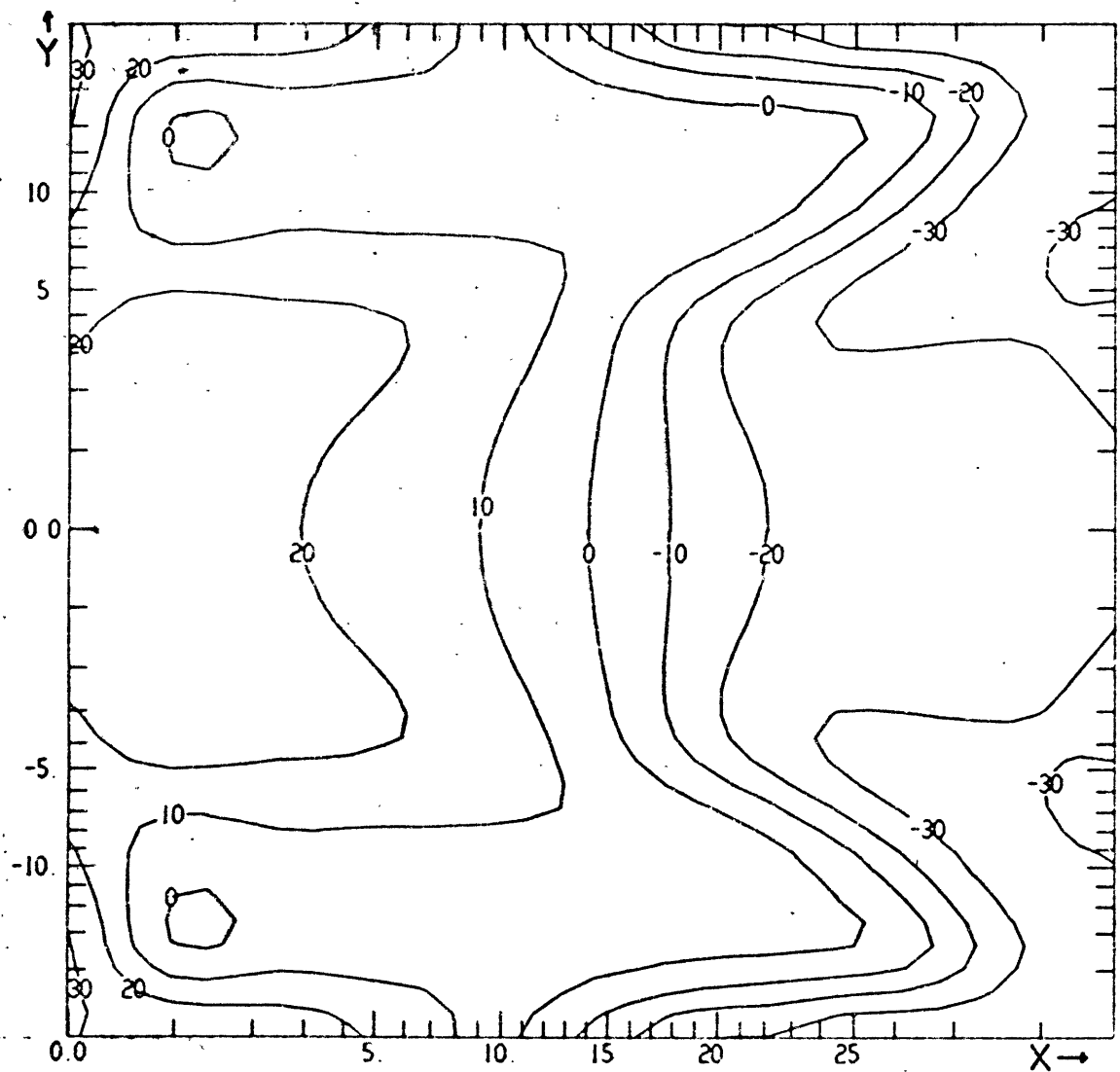
Fig. 5.33a u^S vectors at 40 days. Linear. East wind.



U LAYER 1

DAY 40.11 (T= 504.00 MODEL STEP 1008) X= 0.0 TO 28.6 Y=-15.0 TO 15.0
 L2E2 N4CH3 30X44STR DELT= .5 E=1 E=8,BB=B1= 001 WIND= 5 EAST EVERYWHERE 07/22/03

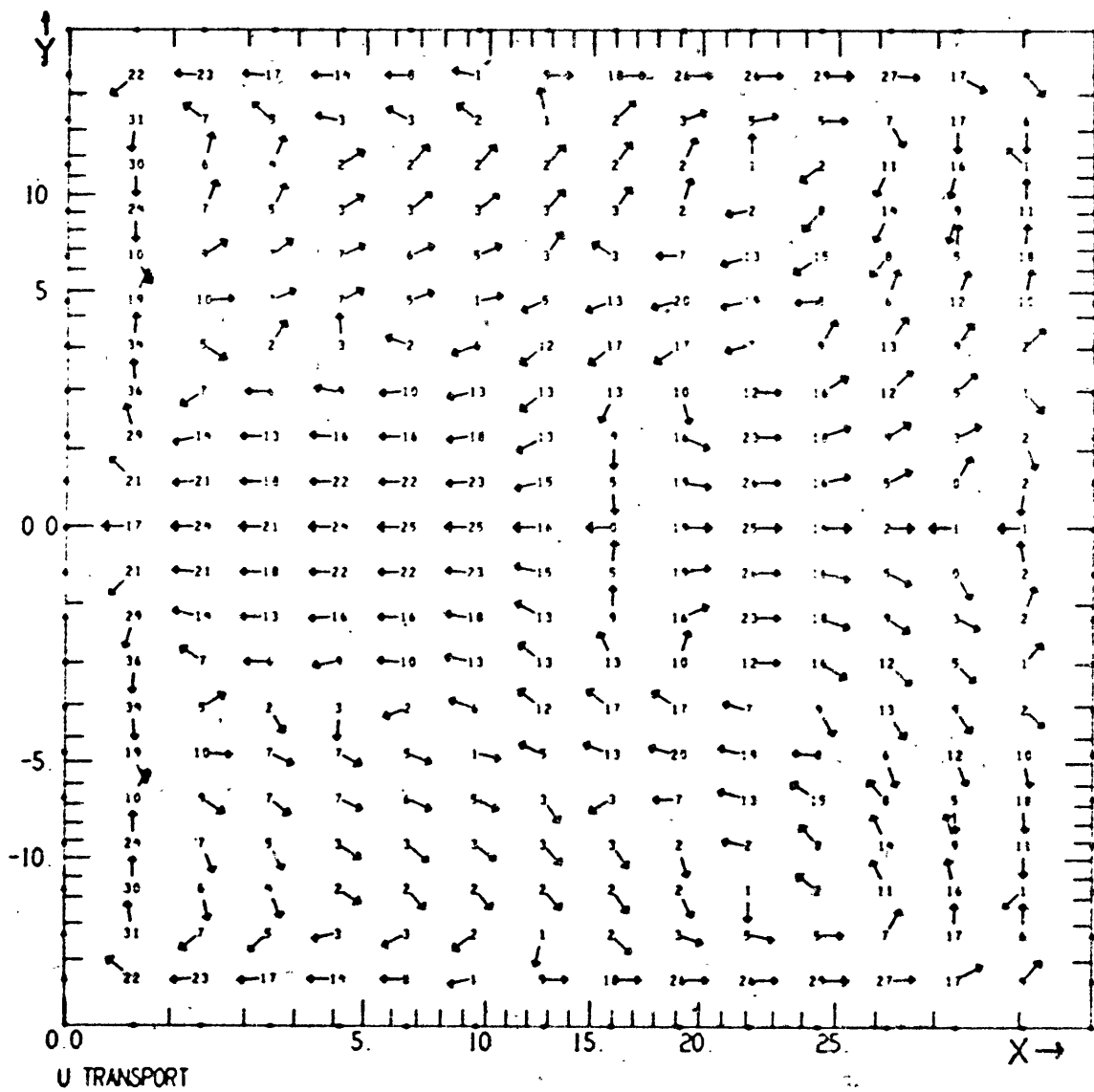
Fig. 5.33b u^1 vectors at 40 days. Linear. East wind.



LAYER DEPTH LOW--3 79E-01 HIGH- 3 24E-01 CI-10. * 1 E-02

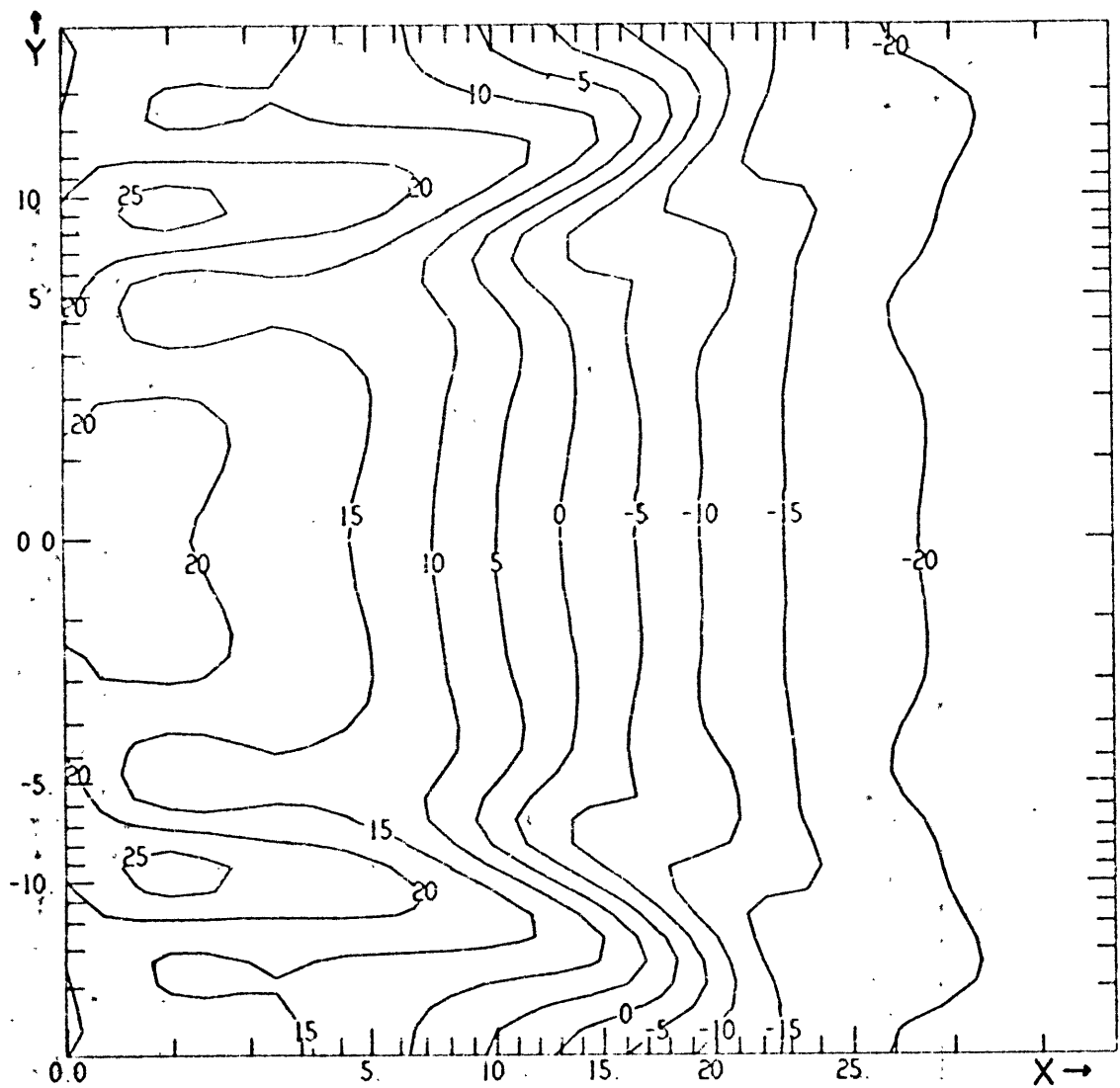
DAY. 40.11: 17- 504 00 MODEL STEP 10081 X- 0 0 TO 28 6 Y--15 0 TO 15 0
 L2E2 N4CH3 30X44STR DELT-.5 E-1 E-8.88-B1- 001 WIND-.5 EAST EVERYWHERE 07/22/03 C

Fig. 5.33c h contours at 40 days. Linear. East wind.



DAY 40 11 (T= 504:00 MODEL STEP 1008) X= 0.0 TO 28.6 Y=-15.0 TO 15.0
 LZEE N4CH3 30X44STR DELT= .5 E=1 E=8.88-B1= .001 WIND= .5 EAST EVERYWHERE 07/22/03 (

Fig. 5.33d \bar{u} vectors at 40 days. Linear. East wind.



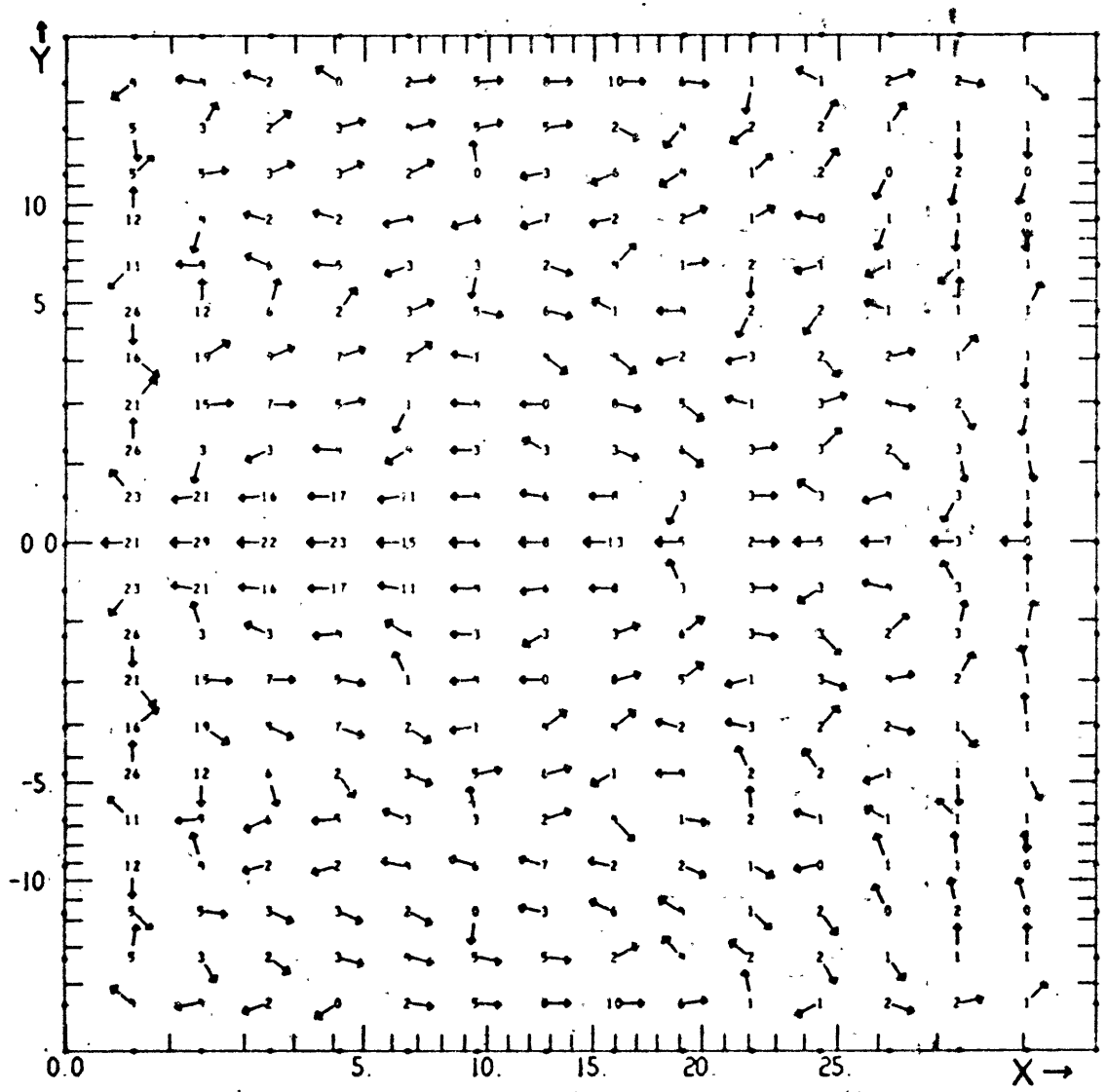
LAYER DEPTH LOW \cdot 2.37E-01 HIGH \cdot 2.75E-01 CI \cdot 5 \cdot 1 E-02

DAY 199.58 IT \cdot 2508 00 MODEL STEP 50161 X \cdot 0 0 TO 28 0 Y \cdot -15 0 TO 15 0

L2E2: N4CH3 30X44STR DELT \cdot 5 E-1 E-8,BB-BI \cdot .001 WIND \cdot .5 EAST EVERYWHERE

07/15/0x

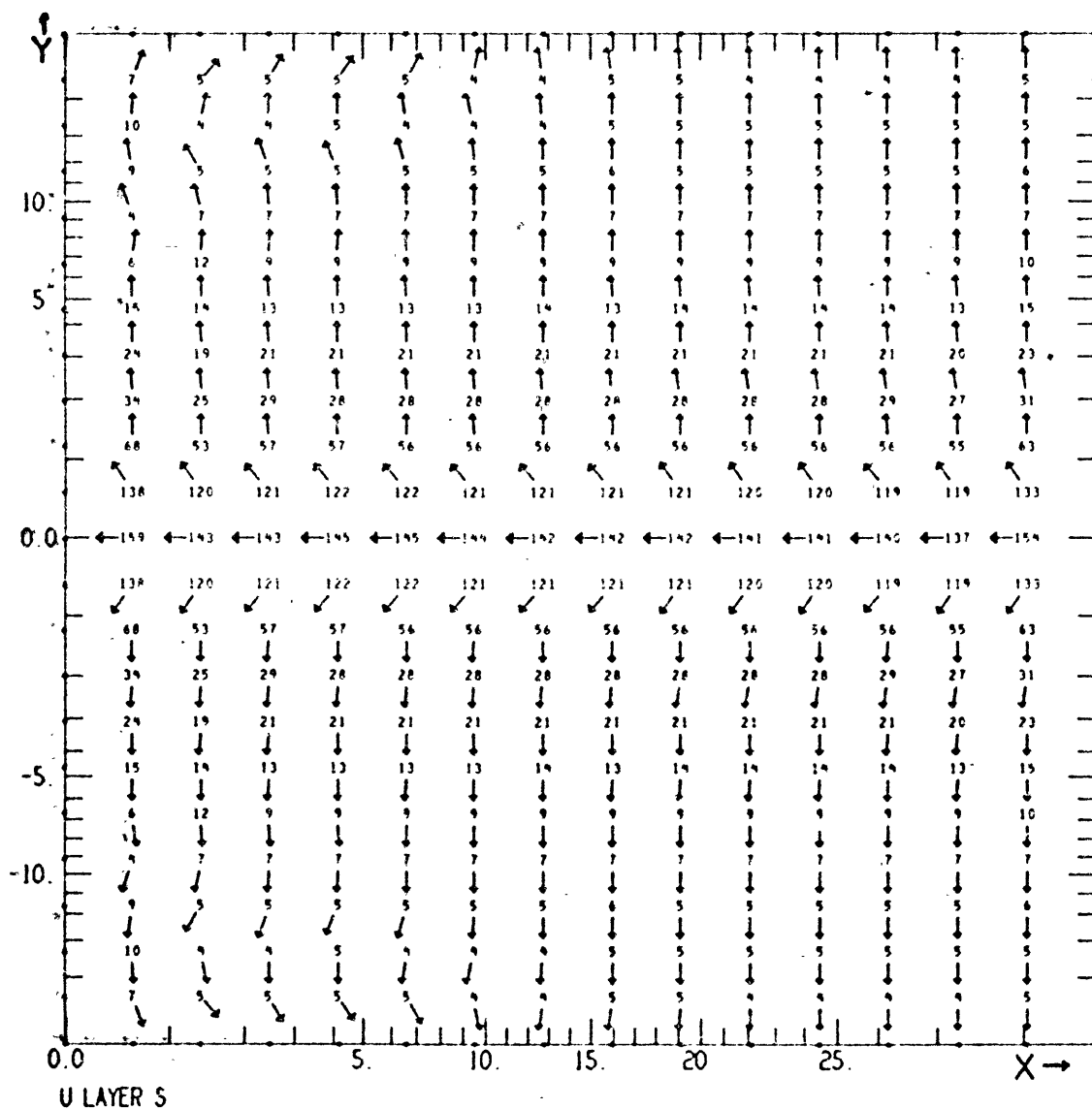
Fig. 5.34a h contours at 200 days. Linear. East wind.



U TRANSPORT

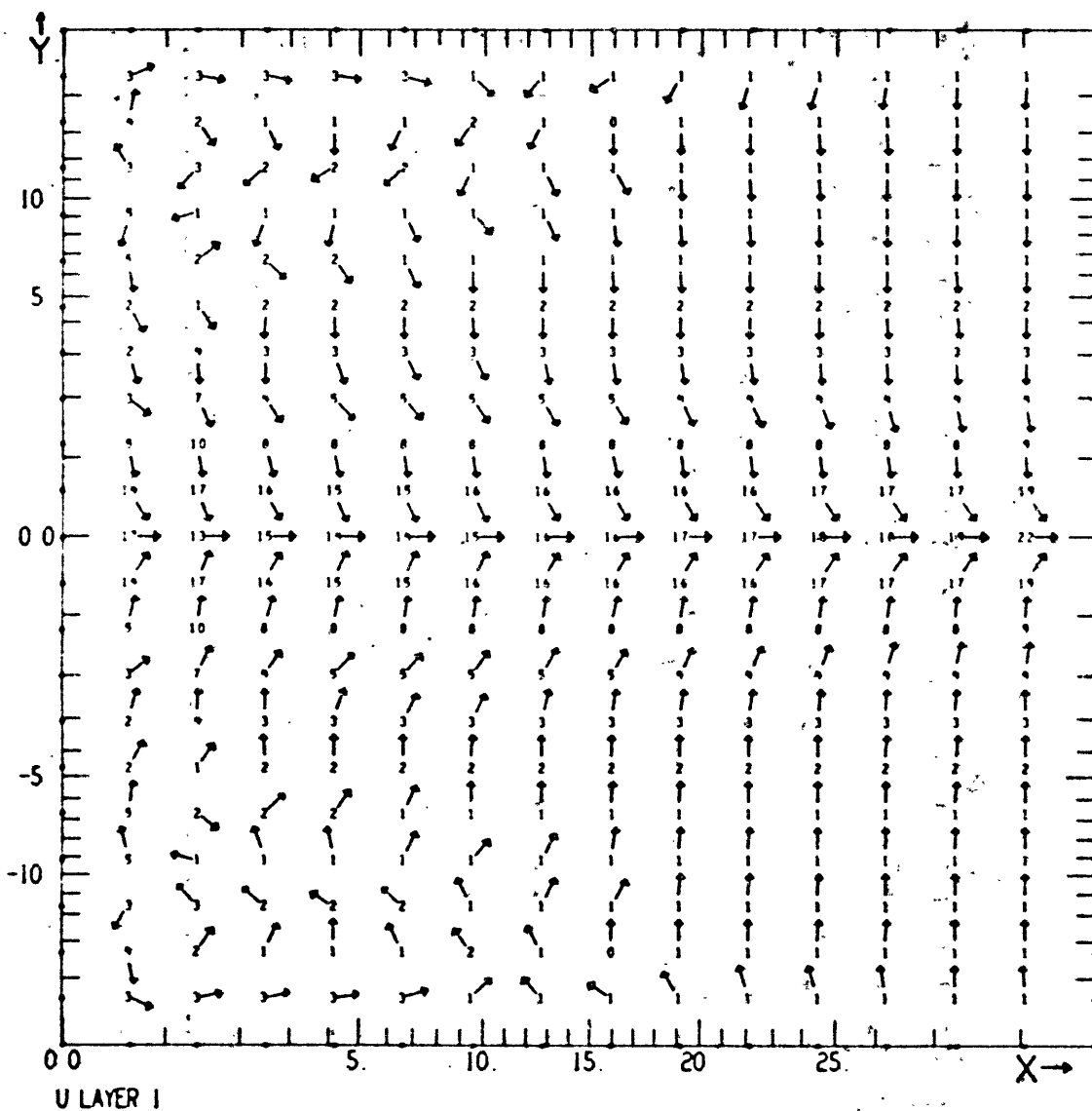
DAY 199 58 (T= 2508.00 MODEL STEP 5016) X= 0.0 TO 28.6 Y= -15.0 TO 15.0
 L2E2 N4CH3 30X44STR DELT= 5 E-1 E-8, BB-B1= 001 VIND= 5 EAST EVERYWHERE 07/22/03

Fig. 5.34b \bar{u} vectors at 200 days. Linear. East wind.



DAY 397 25 (T= 4992.00 MODEL STEP 9984) X= 0.0 TO 28.6 Y=-15.0 TO 15.0
 L2E2 N4CH3 30X44STR DELT= .5,E-1.E-8,BB-BI= 001 WIND= 5 EAST EVERYWHERE 07/15/02

Fig. 5.35a u^s vectors at 397 days. Linear. East wind.



DAY 397 25 (T= 4992 00 MODEL STEP 9984) X= 0.0 TO 28.6 Y= -15.0 TO 15.0
 L2E2 N4CH3 30X44STR DELT= .5 E=1.E-8,BB=81-.001 WIND= .5 EAST EVERYWHERE; 07/22/03 0

Fig. 5.35b \vec{u}^1 vectors at 397 days. Linear. East wind.

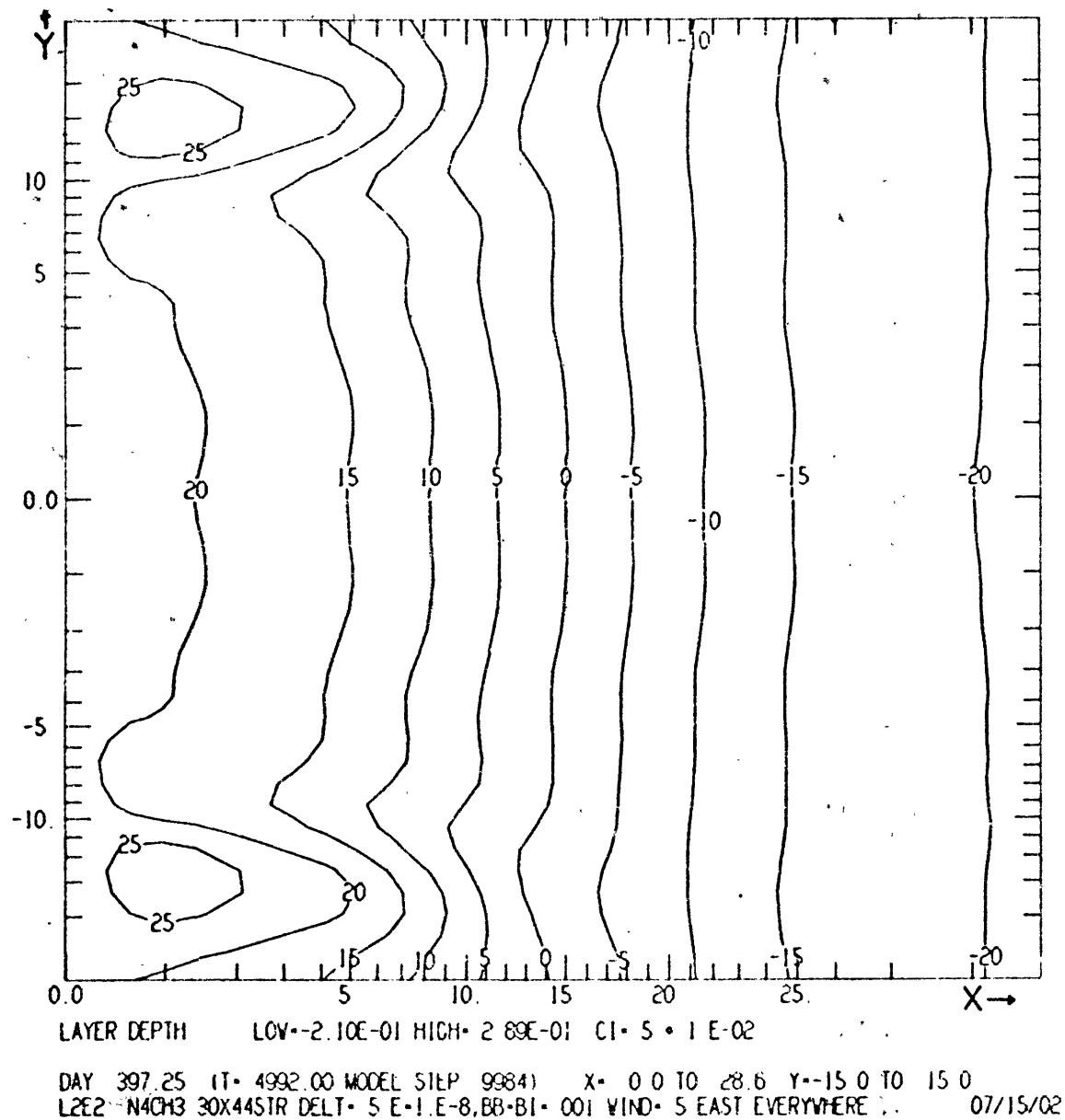
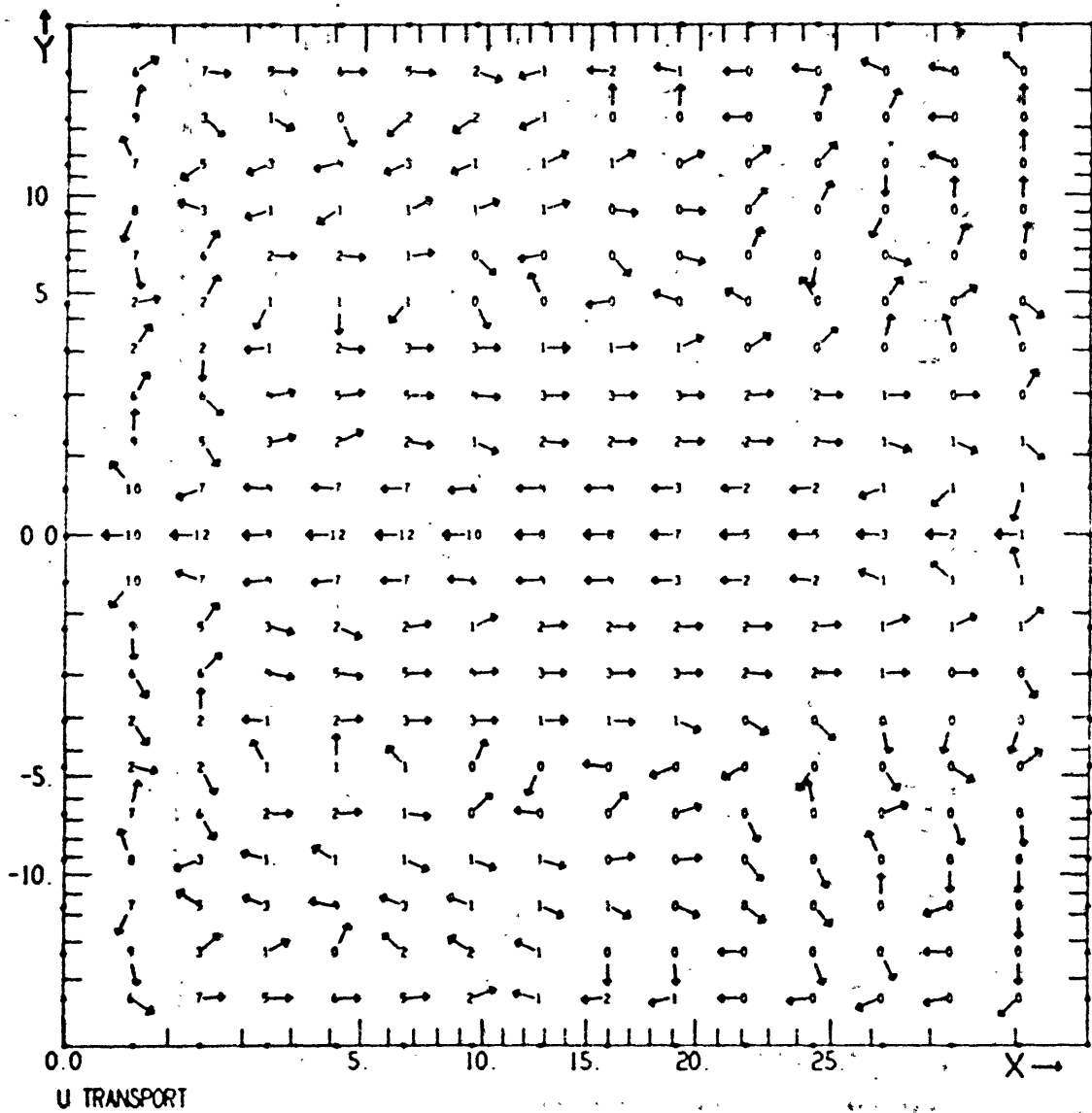


Fig. 5.35c h contours at 397 days. Linear. East wind.



DAY 397 25 (T= 4992 00 MODEL STEP 9984) X= 0 0 TO 28.6 Y=-15 0 TO 15 0
 L2E2 N4CH3 30X44STR DELT= 5 E-1 E-8.88-B1= .001 WIND= 5 EAST EVERYWHERE. 07/22/03

Fig. 5.35d \bar{u} vectors at 397 days. Linear. East wind.

eastern boundary have propagated to the zonal boundaries and turned the corner. For example, the flow along the northern boundary is now opposite to the wind at the eastern side. The coastal flow further to the west has now turned the corner and is headed toward the equator along the western boundary. In order to accomplish this it first built up the sea surface height in the corner so the turn could be made geostrophically. Further south the boundary flow remains poleward. At the eastern side some of the slowly propagating Rossby modes generated from $t = 0$ have moved away from the boundary. This is clear from the extra-equatorial flow pattern. Behind (i.e., to the east of) this region of equatorward flow in the lower layer (Fig. 5.33b) there is a region of poleward flow due to the reflection of the Kelvin modes which arrived at the eastern side at day 20. Fig. 5.33d shows the transports at day 40. The largest meridional transports are those associated with the western boundary currents near the equator. These are now larger than the zonal transports anywhere in the basin. There is an area of eastward transport at the eastern side of the equator. This is needed to increase the layer depth there (Fig. 5.27). The lower layer flow is eastward at all longitudes on the equator. This "undercurrent" is very narrow, with a half-width of less than 50 km at the center of the basin. The scale is determined frictionally. The undercurrent comes about because the transport in the upper layer, which is due to the

balance between the wind stress and the interfacial friction term, is everywhere more westward than the vertically integrated transport required at this stage of the evolution. The direct cause of the eastward flow at depth is the pressure gradient force (Charney 1960). As we have mentioned before, an important signature of the observed undercurrent not reproduced by a linear model is that the vertically integrated transport at the equator be large and eastward. The maximum u^1 is less than $.1 \text{ m sec}^{-1}$ at day 40.

Fig. 5.34 shows the layer depth and transports at 200 days. The former is close to its final value near the equator and near the zonal boundaries. Transports at the equator are in the direction of the wind at almost all longitudes.

By 400 days (Fig. 5.35) the model ocean is close to its final state everywhere in the basin with the exception of the northwest and southwest corners. The upper layer is given primarily by the wind-drift-frictional solution (3.12) with the lower flow having an equal and opposite mass flux so that the vertically integrated transport is zero. There is significant downwelling at the northern and southern boundaries, the western end of the equator, as well as the region near the equator ($\approx \pm 1^\circ$) where v^S is decreasing rapidly in magnitude. There is significant upwelling along the equator, with the maximum vertical velocity ($1.5 \times 10^{-3} \text{ m sec}^{-1}$) in the entire basin occurring at its eastern end. There are no exceptionally

fast boundary currents. The "undercurrent" maximum velocity is only $.2 \text{ m sec}^{-1}$ and its half-width is only $.5^\circ$. Both of these numbers are determined primarily by the vertical eddy viscosity.

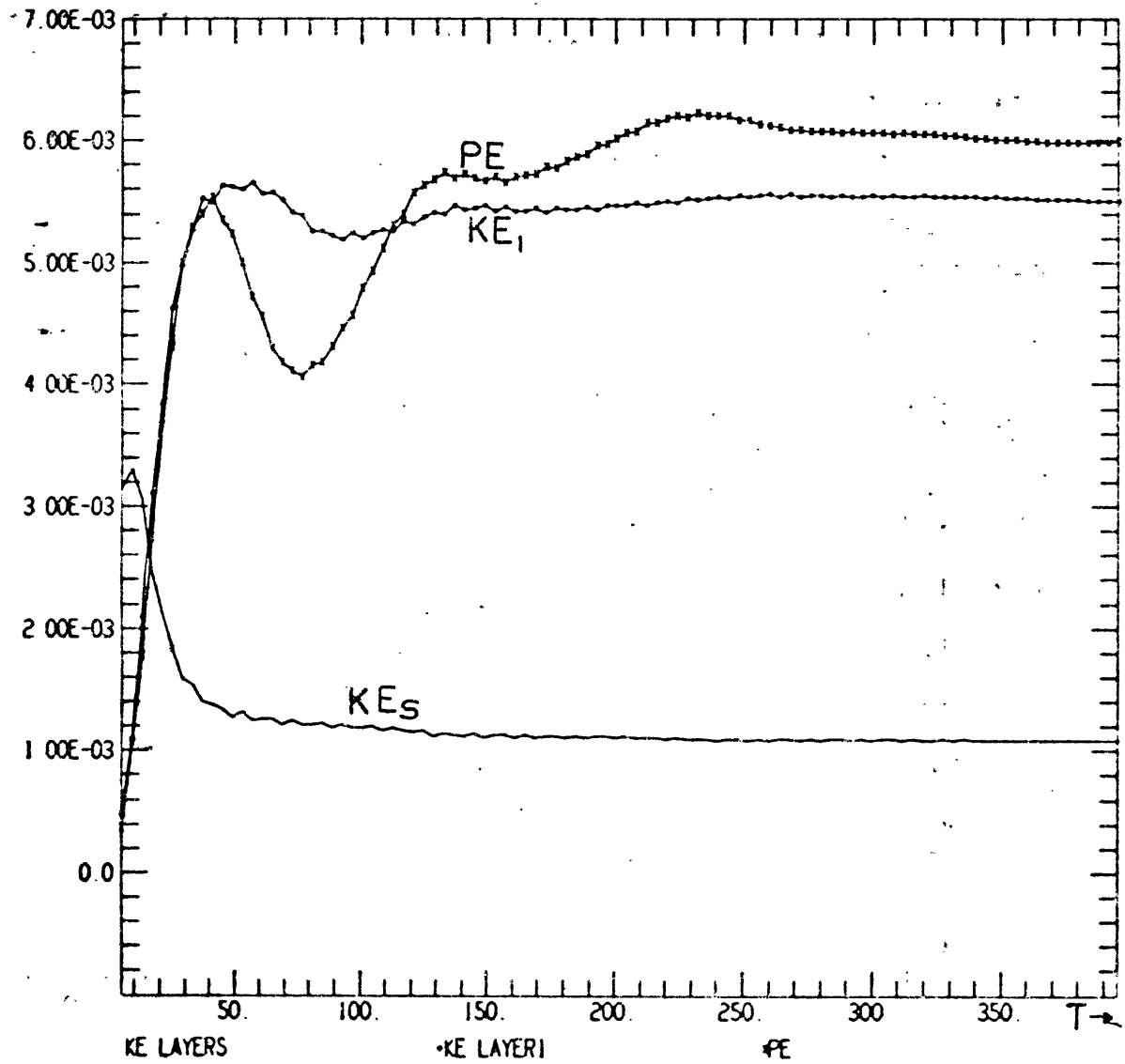
The principal feature omitted by this description is the net transport evident in Fig. 5.35d. Such a circulation was predicted in Section 3.3. Recall that this net transport is induced by the friction at the bottom of the lower active layer; without this bottom friction the transport would be zero everywhere. As predicted, this circulation occurs in an equatorial boundary layer which thickens from east to west. The transports are predominately zonal and increase toward the west. Transport at the equator is in the direction of the wind; there is a return transport at higher latitudes with a meridional "leakage" of fluid toward the equator. The fluid circuit is closed by a western boundary current. The layer depth deviation associated with this circulation is present in Fig. 5.35c, but is more readily seen in Fig. 5.31.

5.5 Nonlinear Response to a Uniform East Wind

In this section we consider the nonlinear response to a uniform east wind. Except for the nonlinearity the governing parameters are identical to those in the previous section. Among the simple wind stress patterns this is the case which is most closely related to the observed undercurrent; the wind stress mimics the component of the wind which is predominant in the Atlantic and Pacific Oceans.

The energy plots (Figs. 5.36, 5.37) exhibit striking differences from those for the linear response to the same forcing (Figs. 5.25, 5.26). As with the south wind cases the inclusion of vertical momentum advections results in much greater kinetic energy in the lower layer. And, as with the south wind cases, the surface layer kinetic energy is less in the nonlinear case--here by a factor of 4. The upper layer kinetic energy reaches a peak after three days, after which it falls off rapidly until day 40. During this initial 40 day period the potential energy and lower layer kinetic energy both rise to a peak. As we shall see, the flow that evolves has surface currents directed opposite to the wind stress. The loss of surface layer energy to the lower active layer via vertical advections is not fully compensated by the transfer of energy from the winds to the ocean.

There is a strong contrast between the linear and nonlinear responses in the oscillations in the energy curves. (These oscillations may be used as an index of the tendency to "overshoot" the final adjusted state as the flow evolves.) Consider, for example, the potential energy in the equatorial region, Figs. 5.26, 5.37. The linear response shows three marked peaks and troughs. After the third of these (day 240) the potential energy is approximately constant. This final value is close to the value at the troughs. The nonlinear response also shows a peak at day 40 and a trough at day 80.



ENERGIES FOR X= 0.0 TO 28.6 Y=-15.0 TO 15.0, T= 4.93 TO 394.86 DAYS
 N2E2 N4CH3 30X44STR DELT= 5 E=1. E=8.88-B1= 001 WIND= 5 EAST EVERYWHERE 07/23/19

Fig. 5.36 Energies from 15°S to 15°N. Nonlinear. East wind.

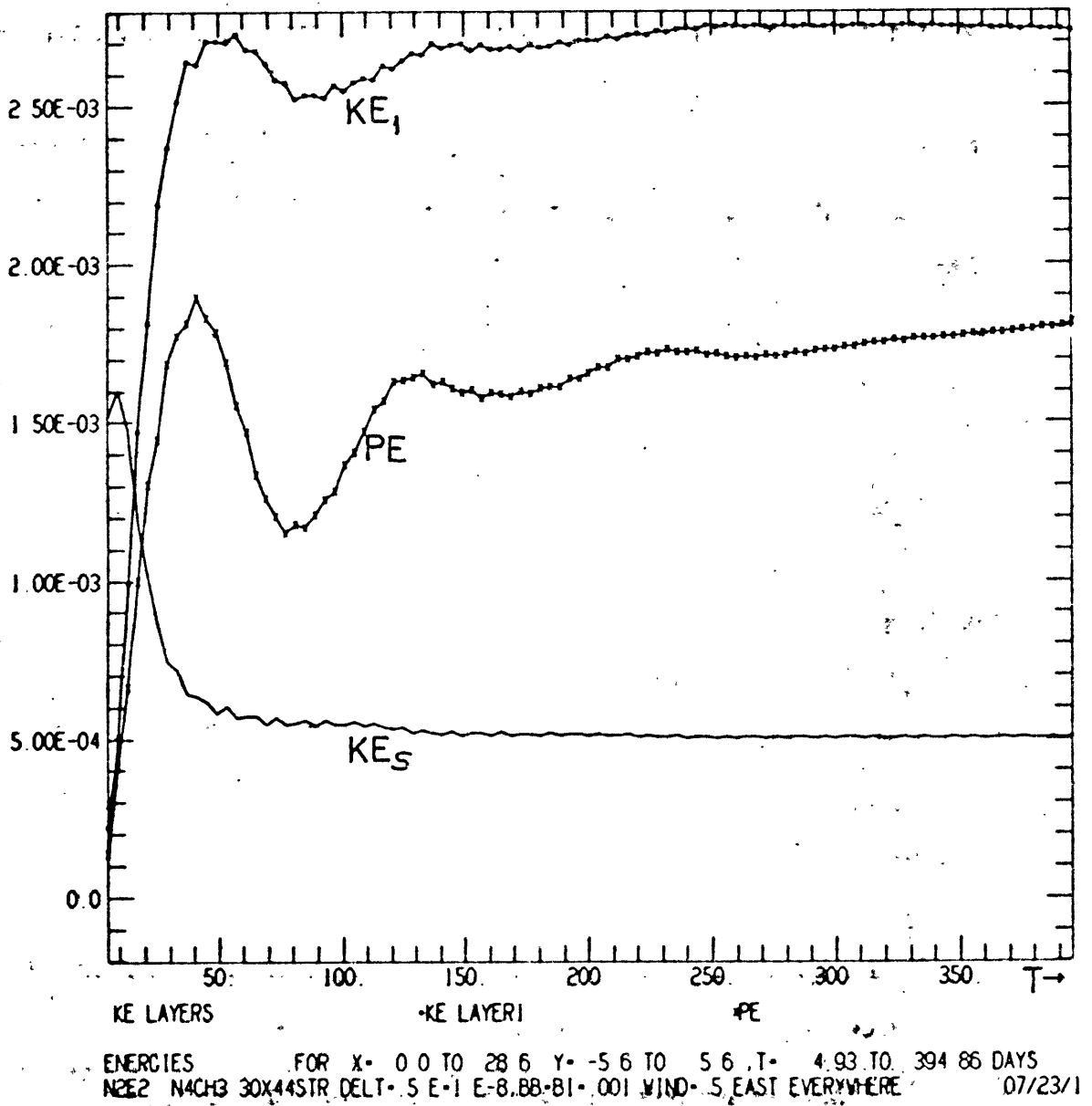


Fig. 5.37 Energies from 5.6°S to 5.6°N. Nonlinear. East wind.

The peak value is roughly 10% higher than that of the linear case, but the amplitude of the oscillation is less than 60% of the linear one. The curve rises to a second peak at day 140 and remains close to this peak value thereafter. The addition of nonlinear effects has damped the tendency to oscillate about a final steady state. Furthermore, the nonlinear steady state is one with potential energy close to the maximum value the system attains in the course of its evolution, while the linear steady state is close to a minimum.

We can gain some understanding of how these differences arise by considering sections of layer depth h and zonal transport \bar{u} at the equator. Figs. 5.38 and 5.27 show h at the equator for the first 40 days in the nonlinear and linear cases respectively. At 8 days the two sections are very similar; the differences are only that the slope at the eastern side is greater in the linear case and there is an additional narrow (one grid point wide) boundary layer at the western wall in the nonlinear case. Through day 40 there is little difference in the two cases, except at the eastern side. Recall that over the first 20 days, the linear response built up a steeper height gradient than was needed to balance the wind stress. After that the reflection of the first Kelvin mode to arrive from the western side caused the layer depth to decrease (Fig. 5.27). The nonlinear case is similar for the first 20 days, but the eastern boundary response to the first signals arriving from

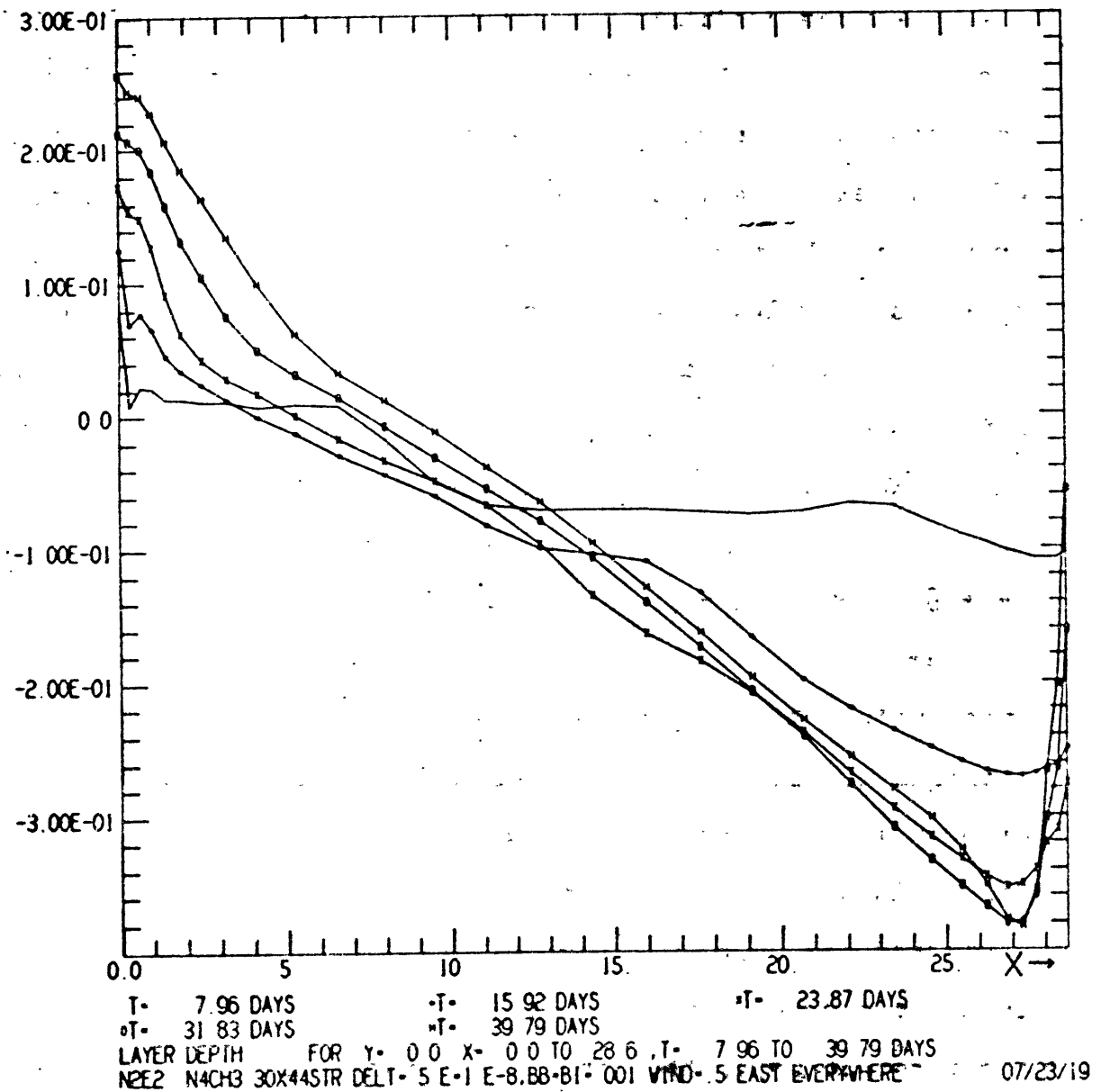


Fig. 5.38 Sections of h along the equator to day 40. Nonlinear. East wind.

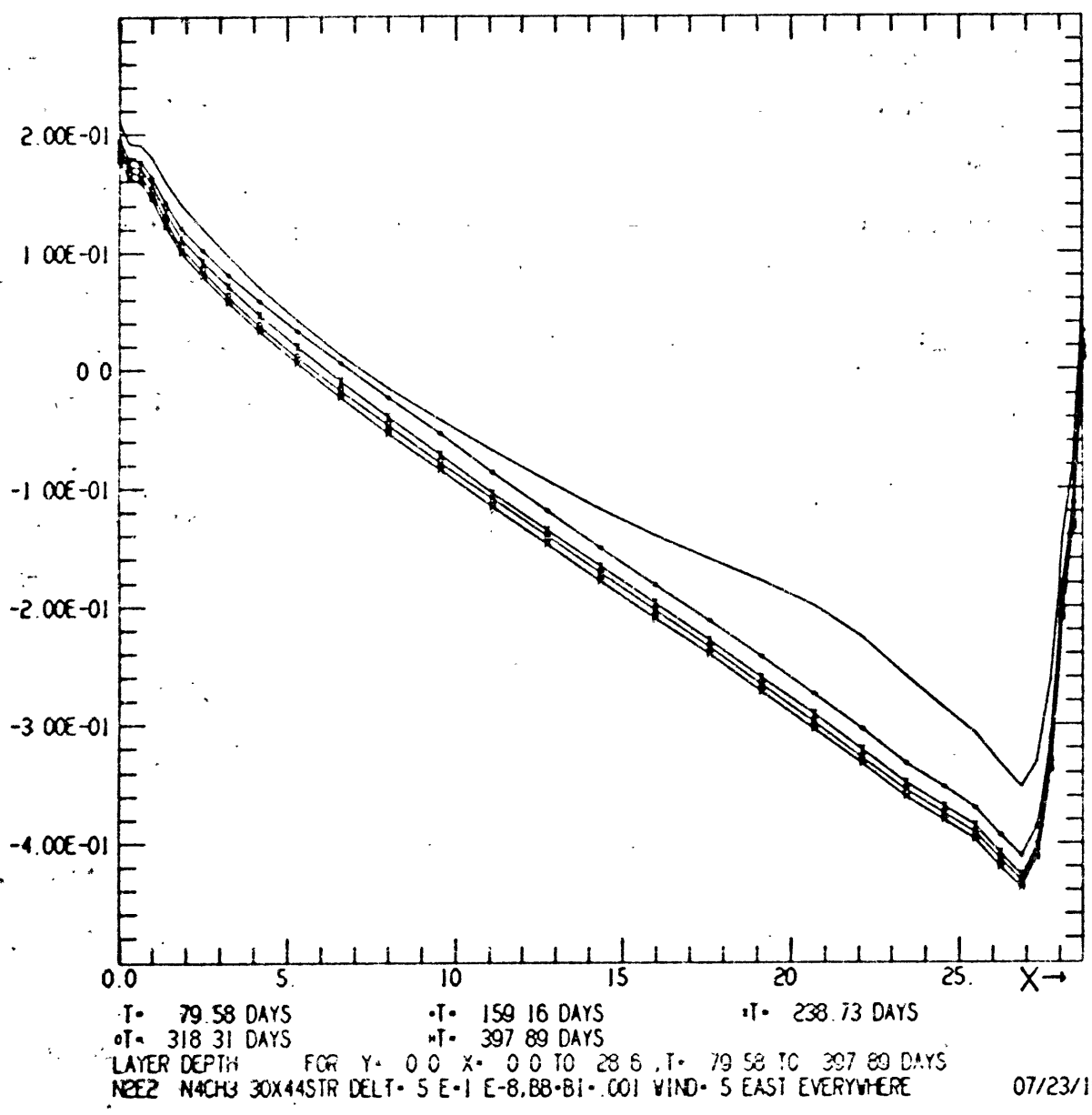


Fig. 5.39 Sections of h along the equator to day 398. Nonlinear. East wind.

the western side is quite different. The slope of h remains steep throughout the basin with a strong boundary layer forming at the eastern wall. Within this narrow (1.5° wide) layer the transports impinging on the eastern wall are turned to the north and south. We might say that the nonlinear dynamics respond to the incoming currents at the equator by forming an inertial boundary layer whereas the linear response is a reflection. The Rossby modes which comprise the reflection of the Kelvin mode in the linear theory all propagate too slowly to the west to escape from the boundary in the face of the fast eastward current that exists at the equator. Therefore, they are trapped at the eastern wall on the equator and a boundary layer forms. Fig. 5.39 shows that the layer depth profile evident at day 40 persists thereafter, with its minimum becoming more pronounced with time. After 160 days it varies little.

Now consider the contrast between the linear (Fig. 5.28, 5.29) and nonlinear (Figs. 5.40, 5.41) transports at the equator. After one month has elapsed the transports in the nonlinear case are almost an order of magnitude larger. By 16 days the nonlinear transports are everywhere eastward, a feature which persists thereafter. The linear transports eventually become westward everywhere, but they take on the order of 200 days to do so at all longitudes. The differences may be attributed to the inclusion of relative vorticity in the nonlinear vorticity balance (cf., Fofonoff & Montgomery 1955, Charney 1960; also,

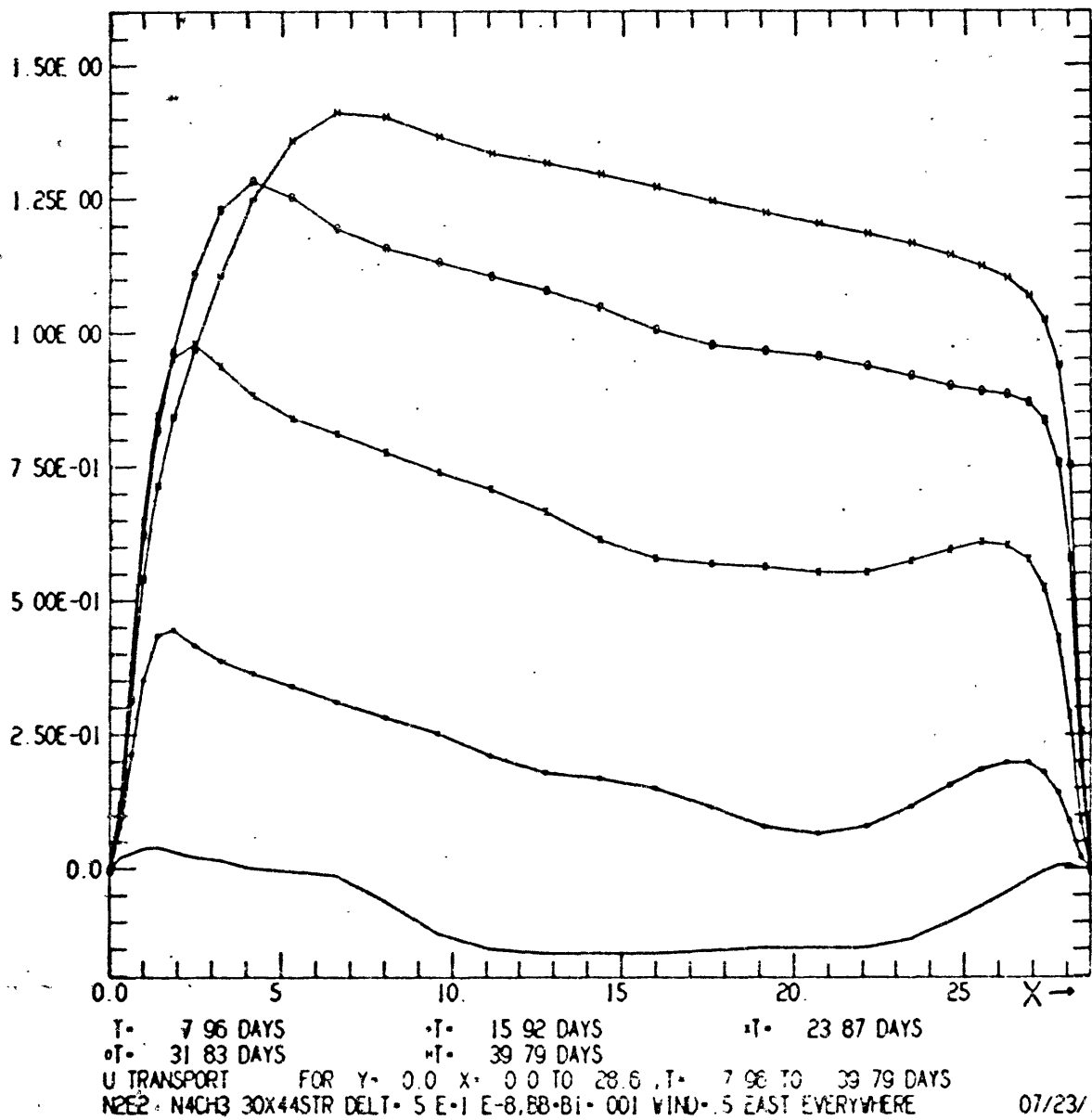
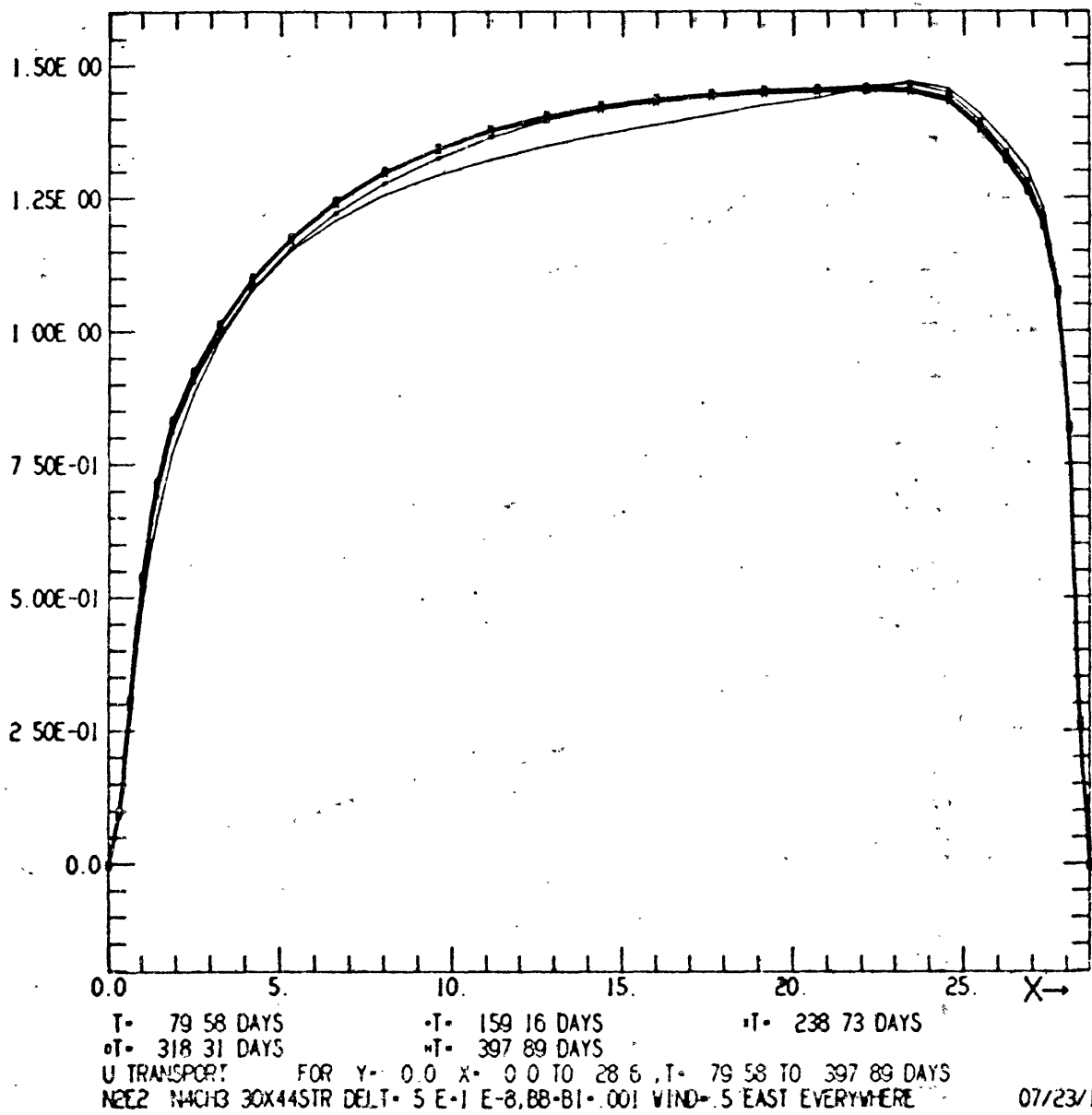


Fig. 5.40 Sections of \bar{u} along the equator to day 40. Nonlinear. East wind.

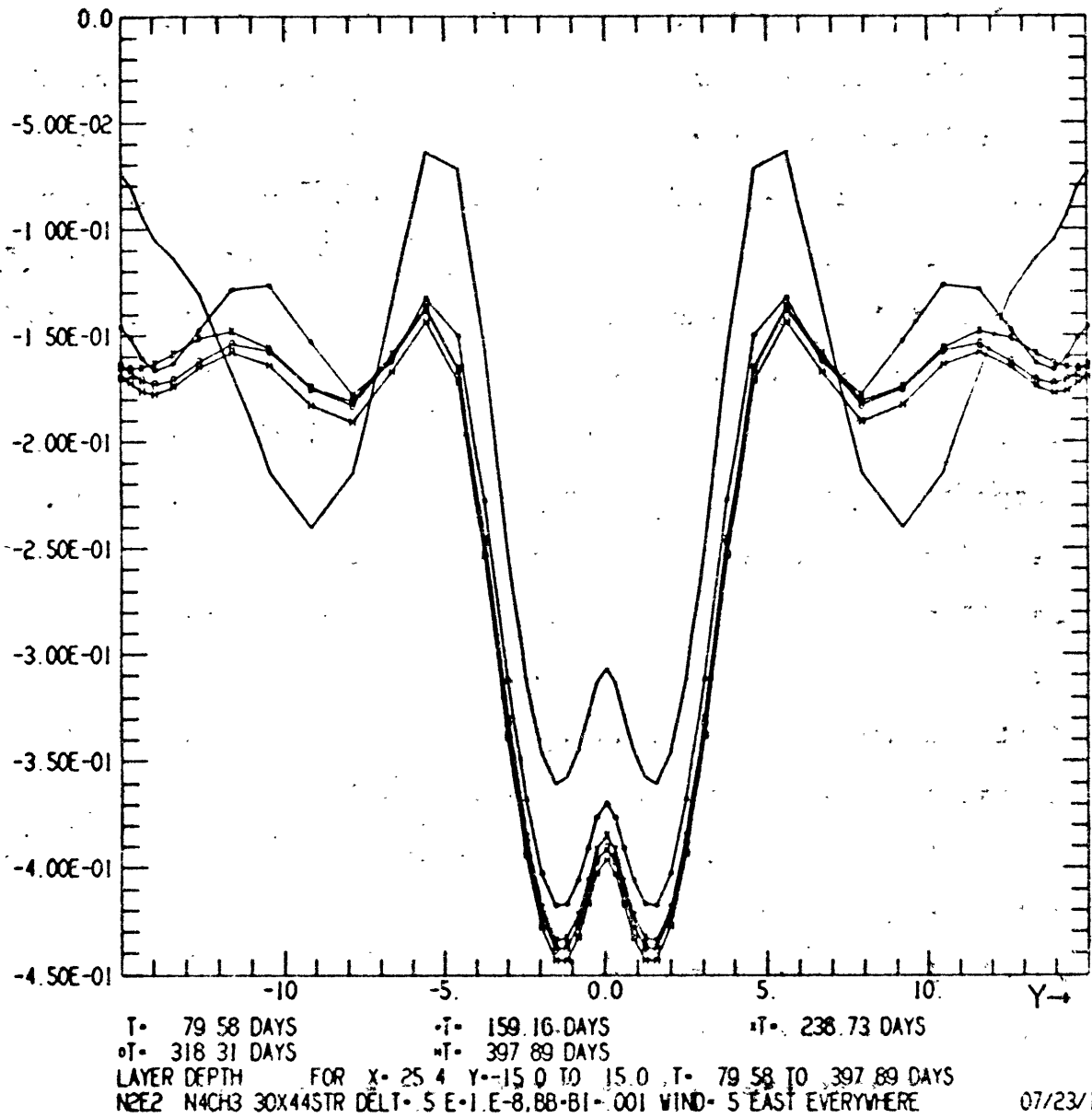


07/23/19

Fig. 5.41 Sections of \bar{u} along the equator to day 398. Nonlinear. East wind.

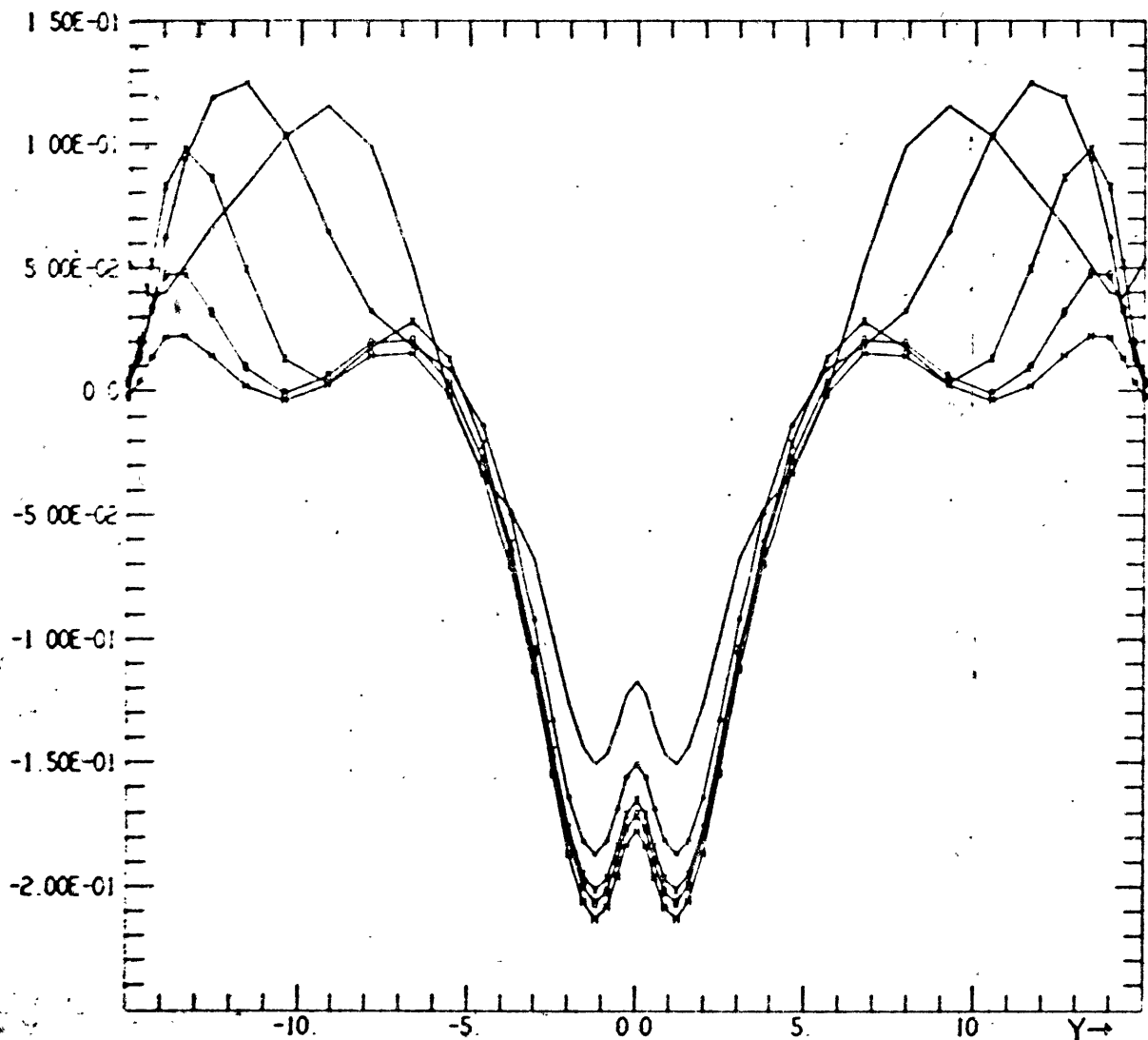
Chapter 1). The lower layer meridional velocities are equatorward near the equator. As a fluid parcel approaches the equator it compensates the change in its planetary vorticity by acquiring relative vorticity. The result is eastward flow at the equator, regardless of which hemisphere the parcel originated in. The transport is reduced to zero at the walls by boundary layers at both the eastern and western sides. Inertial effects apparently broaden the western boundary layer relative to the linear case (compare Fig. 5.41 with Fig. 5.30). The linear response has no transport boundary layer at the eastern side. As a final point about Figs. 5.40 and 5.41 we note that from day 60 onward the transport in the interior increases downstream while at day 40 it decreases from west to east. The latter behavior is more in accord with observations in the Atlantic and Pacific. (See the discussion in Chapter 6.)

Thus far we have considered the solution at the equator only. Figs. 5.42a, b, c show profiles of h across the basin. At all longitudes the greatest difference from the corresponding linear sections (Figs. 5.31a, b, c) is the deep trough within 5.6° of the equator. This trough is symmetric about the equator; h slopes downward from 5.6°N to 1.2°N to geostrophically balance the westward current in the lower layer at those latitudes. From 1.2° to 0° it slopes upward to geostrophically balance the undercurrent. By 160 days this trough is close to its final shape. This time scale for adjustment agrees



07/23/19

Fig. 5.42a Meridional sections of h to day 398 at $x=25.4^\circ$.
Nonlinear. East wind.



T• 79.58 DAYS •T• 159.16 DAYS •T• 238.73 DAYS
 •T• 318.31 DAYS •T• 397.89 DAYS
 LAYER DEPTH FOR X=14.3 Y=-15.0 TO 15.0, T= 79.58 TO 397.89 DAYS
 N2E2, N4CH3 30X44STR DELT=.5 E-1 E-8, BB-BI=.001 WIND= 5 EAST EVERYWHERE.

07/23/19

Fig. 5.42b Meridional sections of h to day 398 at $x=14.3^\circ$.
 Nonlinear. East wind.

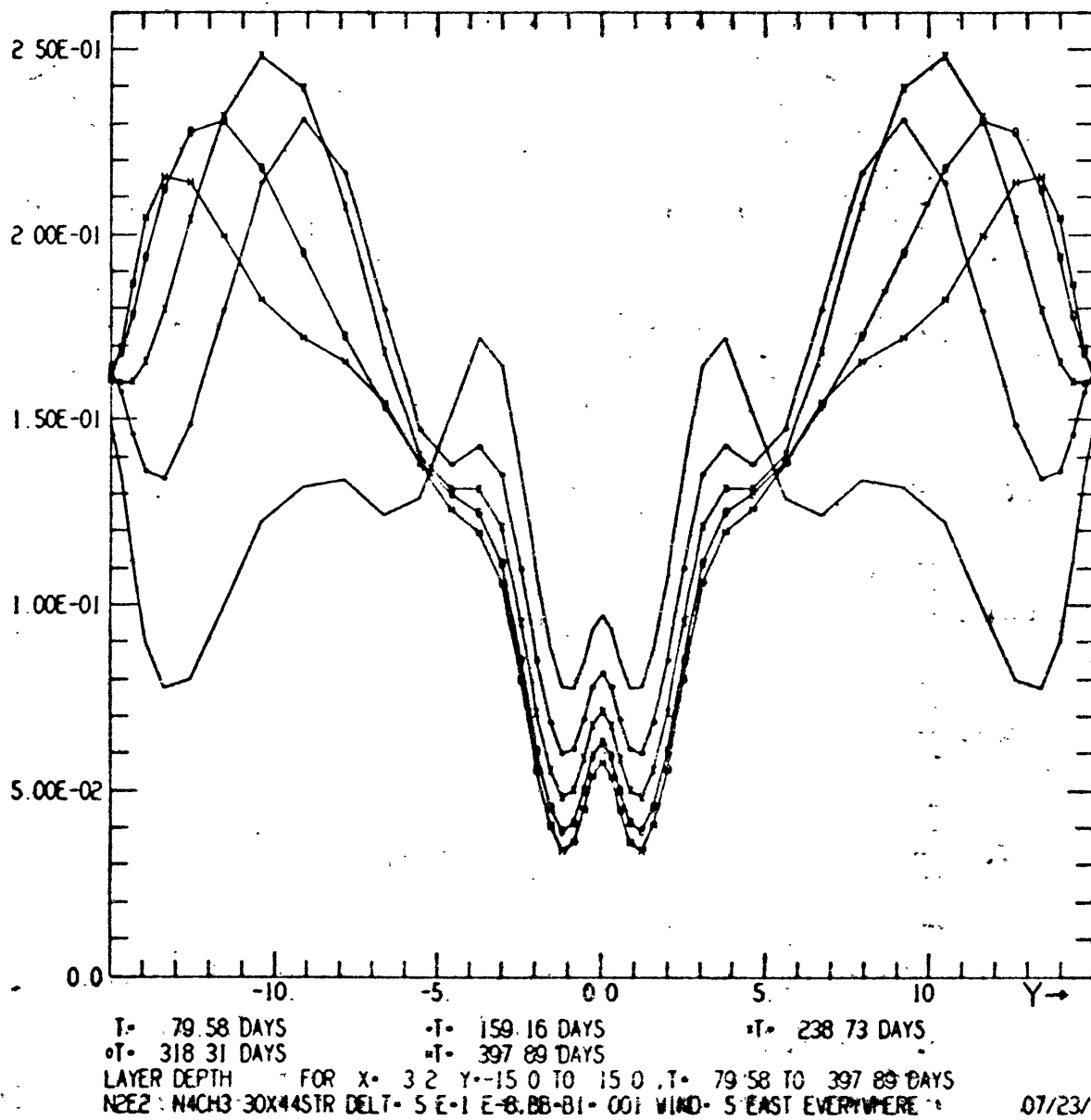


Fig. 5.42c Meridional sections of h to day 398. at $x=3.2^\circ$. . .
 Nonlinear. East wind.

with that given by the energies (Fig. 5.37) and the vertically integrated transport at the equator (Fig. 5.41). Within this equatorial region there is some tendency for the adjustment to occur soonest at the eastern side, particularly poleward of about 3° . Poleward of 5.6° the adjustment clearly proceeds from east to west and is more rapid the nearer to the equator one is. The time scales for this extra-equatorial process are comparable to those for the linear case (Figs. 5.31a, b, c), although h shows some influence from nonlinear effects at all latitudes.

Figs. 5.43 and 5.44 show sections of the zonal transport at the central longitude of the basin. Except for the regions near the equator and the northern and southern walls, very little happens in the first 40 days. By day 80 the transport has reached its final value within 2° of the equator. The adjusted region extends to 5.6° by day 160, and continues to expand meridionally as time goes on.

Figs. 45a, b, c show the flow at 16 days. Comparison with the linear case shows striking differences. The surface layer currents near the equator are weaker and more zonally oriented in the nonlinear case. This is a result of the fact that parcels north of the equator tend to turn clockwise as they move north and lose relative vorticity to make up for the gain in planetary vorticity. (The flow south of the equator shows similar behavior.) In the non-linear case the lower

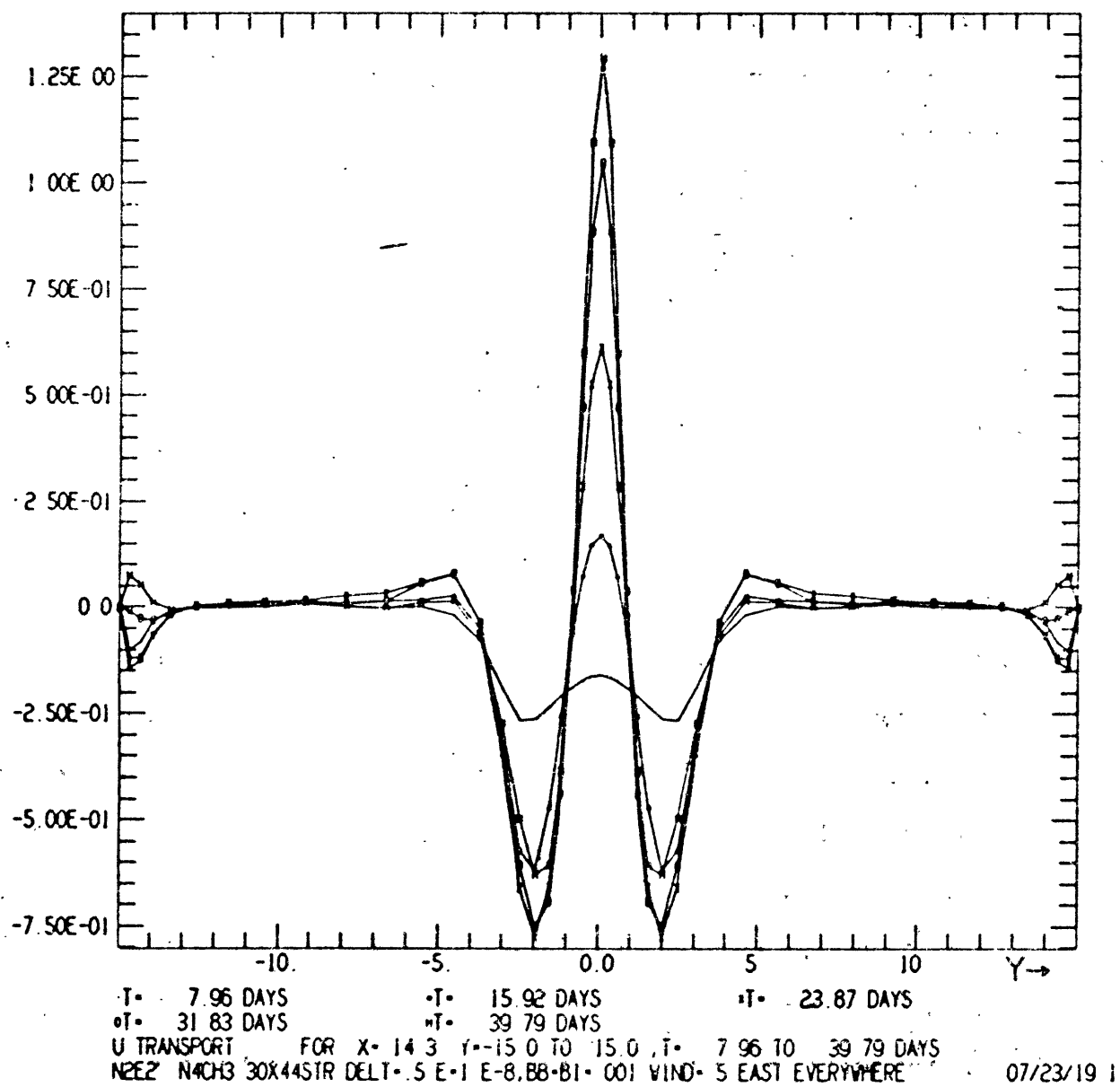
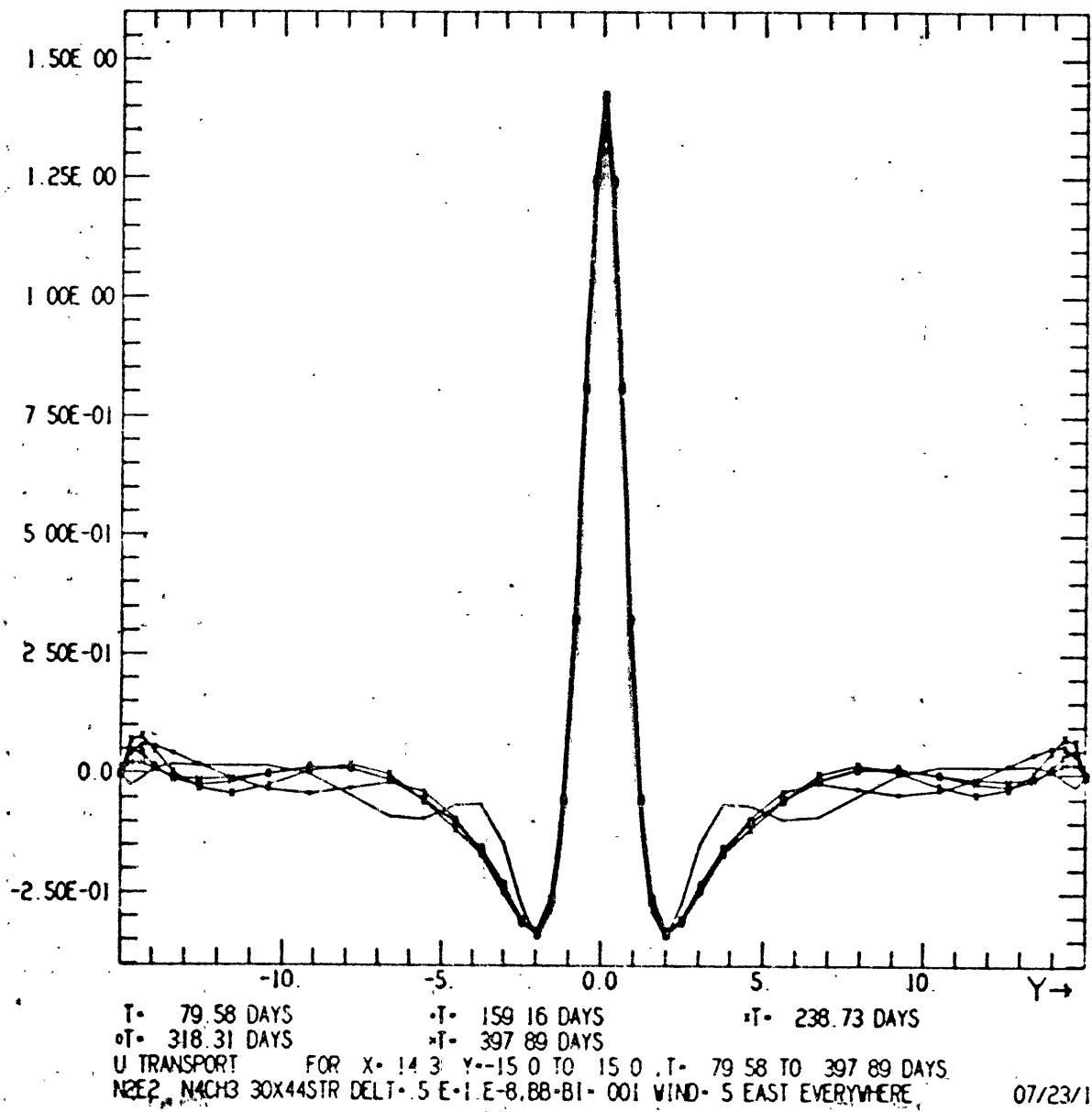
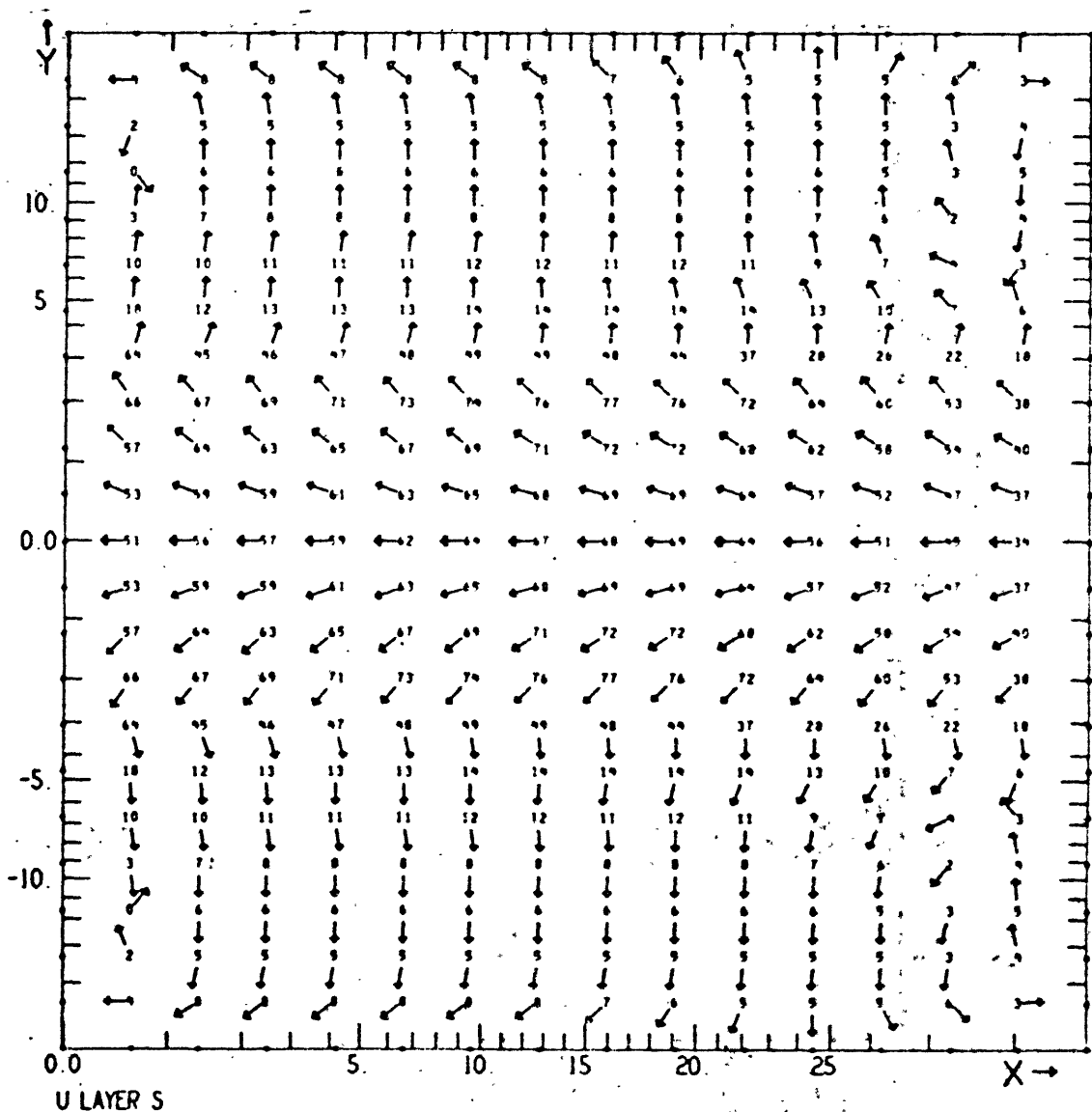


Fig. 5.43 Meridional sections of \bar{u} to day 40 at $x=14.3^\circ$.
Nonlinear. East wind.



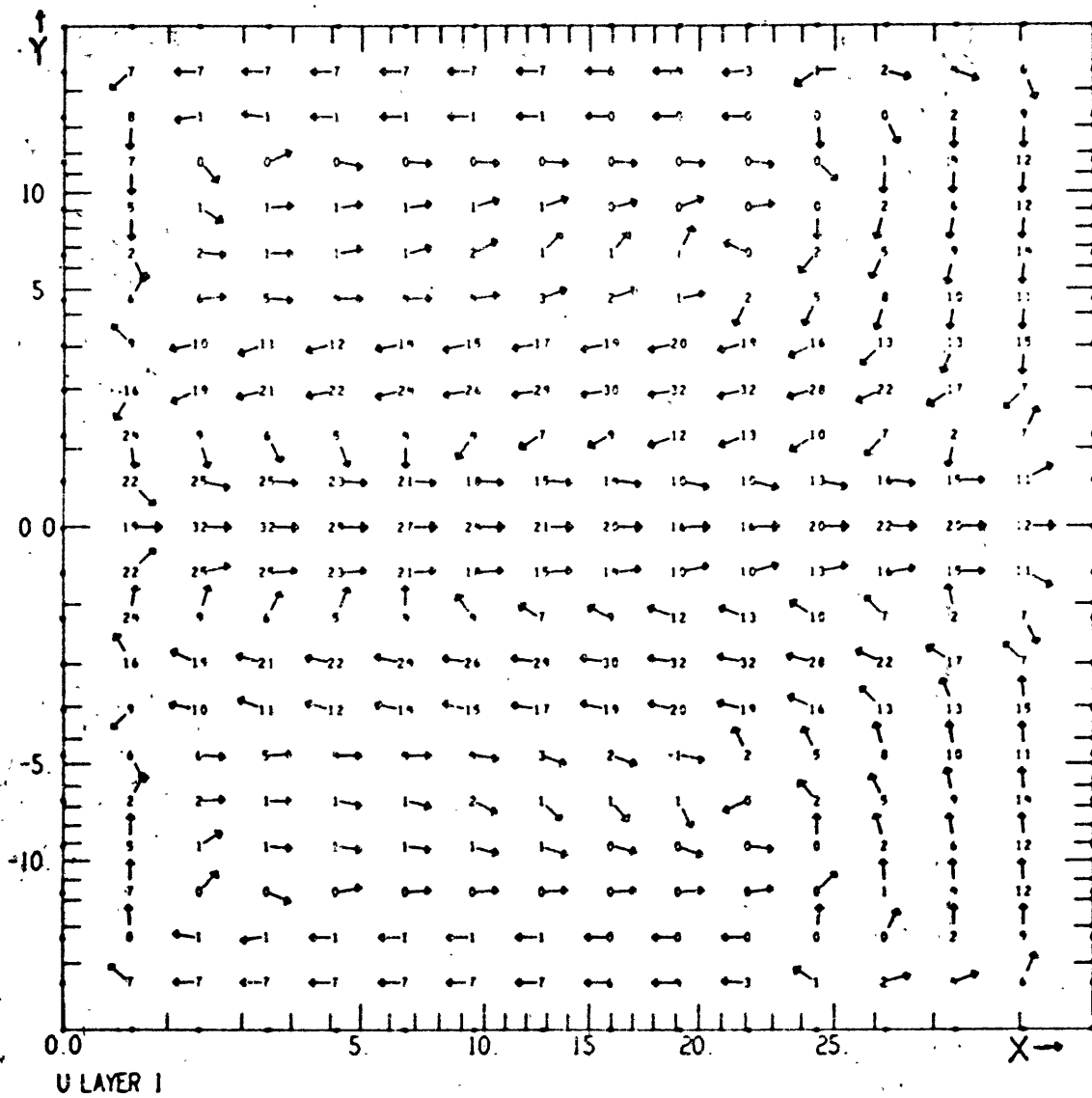
07/23/19

Fig. 5.44 Meridional sections of \bar{u} to day 398 at $x=14.3^\circ$.
Nonlinear. East wind.



DAY 15 92 (T= 200 00 MODEL STEP 400) X= 0.0 TO 28.6 Y=15.0 TO 15.0
 NEE2 N4CH3 30X44STR DELT= .5 E-1 E-8.88-B1- 001 WIND= .5 EAST EVERYWHERE 07/23/19

Fig. 5.45a u^s vectors at 16 days. Nonlinear. East wind.



DAY 15.92 (T= 200.00 MODEL STEP 400) X= 0.0 TO 28.6 Y=-15.0 TO 15.0
 N2E2 N4CH3-30X44STR DELT=.5 E=1 E=8.88=B1-001 WIND= 5 EAST EVERYWHERE 07/23/19

Fig. 5.45b u^1 vectors at 16 days. Nonlinear. East wind.

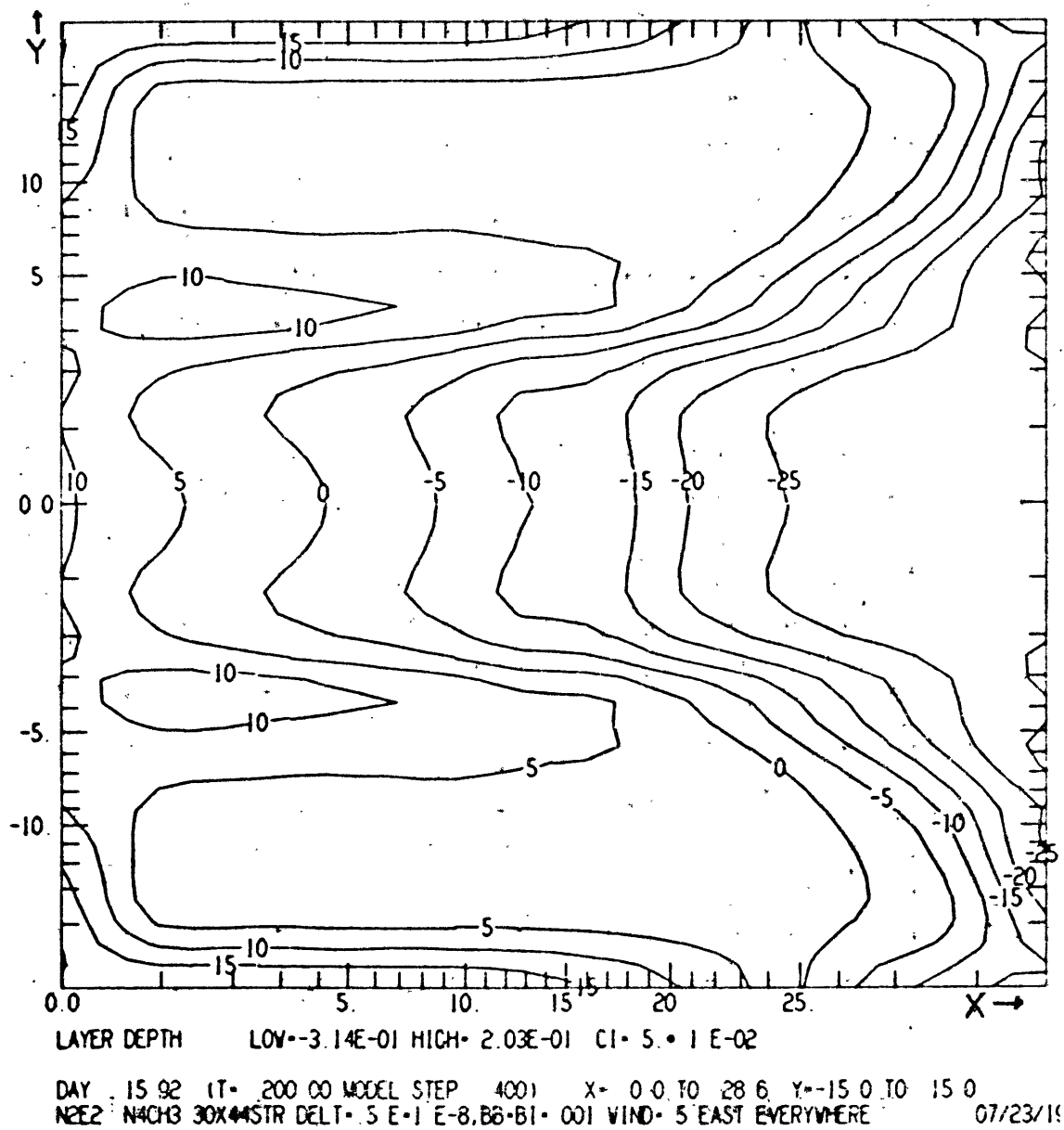
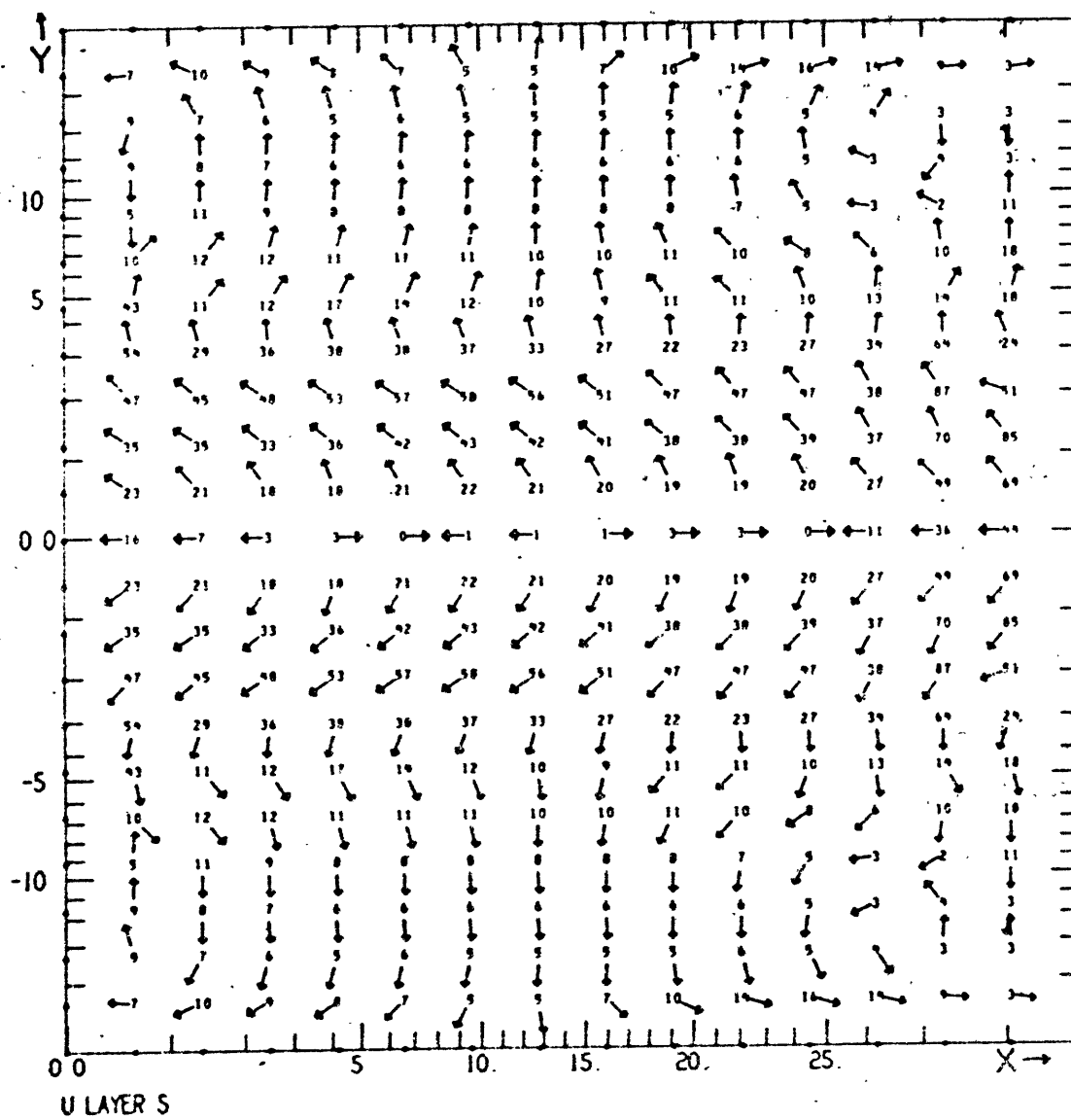


Fig. 5.45c h contours at 16 days. Nonlinear. East wind.

layer already shows a strong eastward flow (speeds at the equator above $.3\text{m sec}^{-1}$) within 1.2° of the equator. The flow to the west centered at $\pm 3^\circ$ tends to balance the eastward transport of the undercurrent and is much stronger than in the linear case. The layer depth h (Fig. 5.45c) already tends to bow up at the equator in order to geostrophically balance the undercurrent.

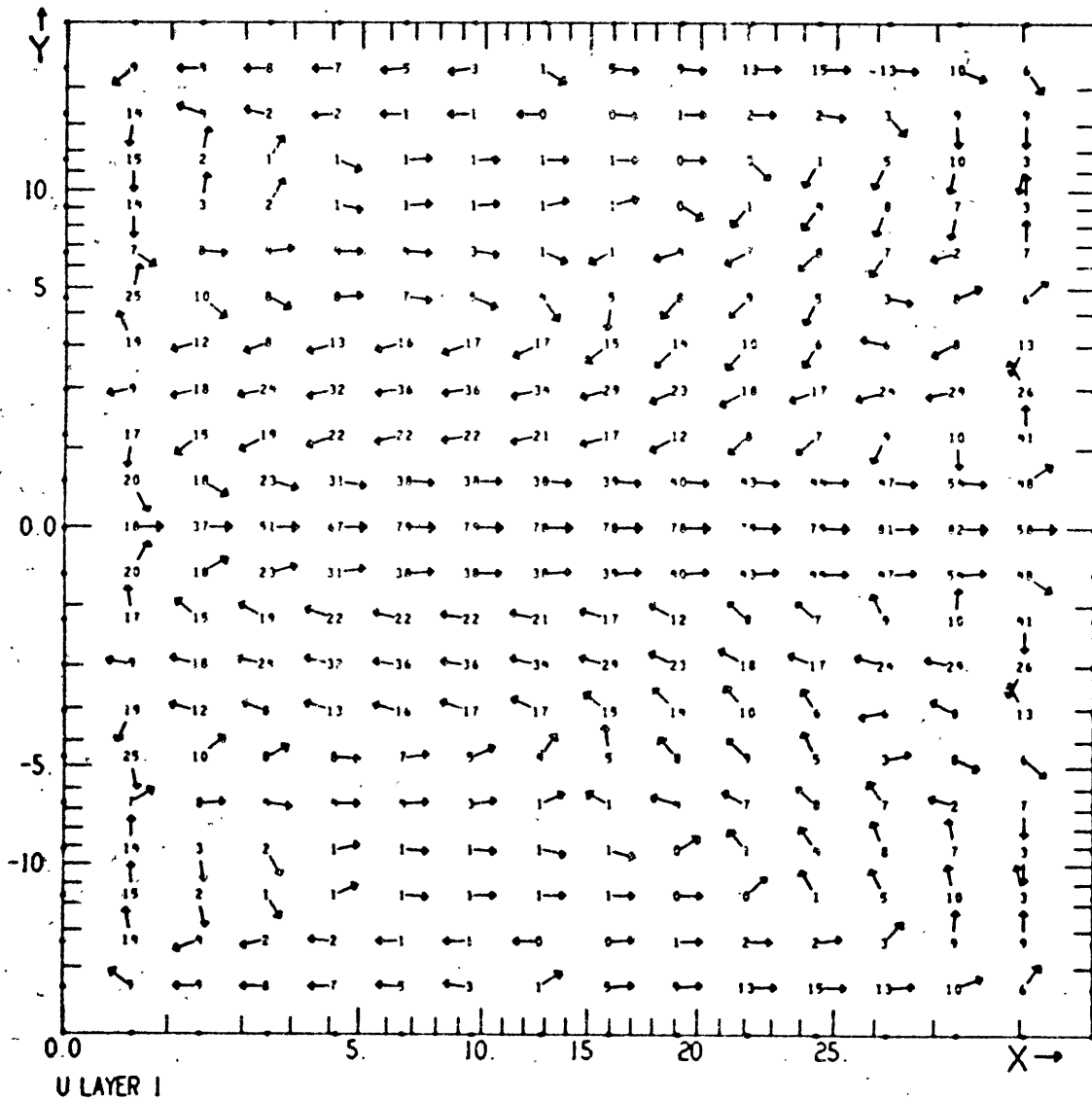
By day 40 the effects of upwelling, vertical friction and the pressure gradient have reduced the surface layer zonal velocity (Fig. 5.46a) to near zero at the equator, except at the sidewall boundaries. Vertical advection of eastward momentum from the lower active layer is the most important factor in bringing about this weak surface flow. The maximum undercurrent velocity is now above $.8\text{m sec}^{-1}$ and occurs near the eastern boundary (Fig. 5.46b). The boundary layer at the eastern terminus of the undercurrent shows strong poleward flow in both active layers, with lower layer flow being approximately geostrophic (Figs. 5.46b,c). This poleward flow turns eastward about 2° from the equator. The western boundary transports are weaker than those at the eastern side: flow in the surface layer is poleward, while that in the lower layer is equatorward, feeding the undercurrent. The only large meridional transports are at the meridional boundaries (Fig. 5.46d).

Figs. 5.47a,b,c,d show the fields after 398 days. At this time the steady state solution is closely approximated



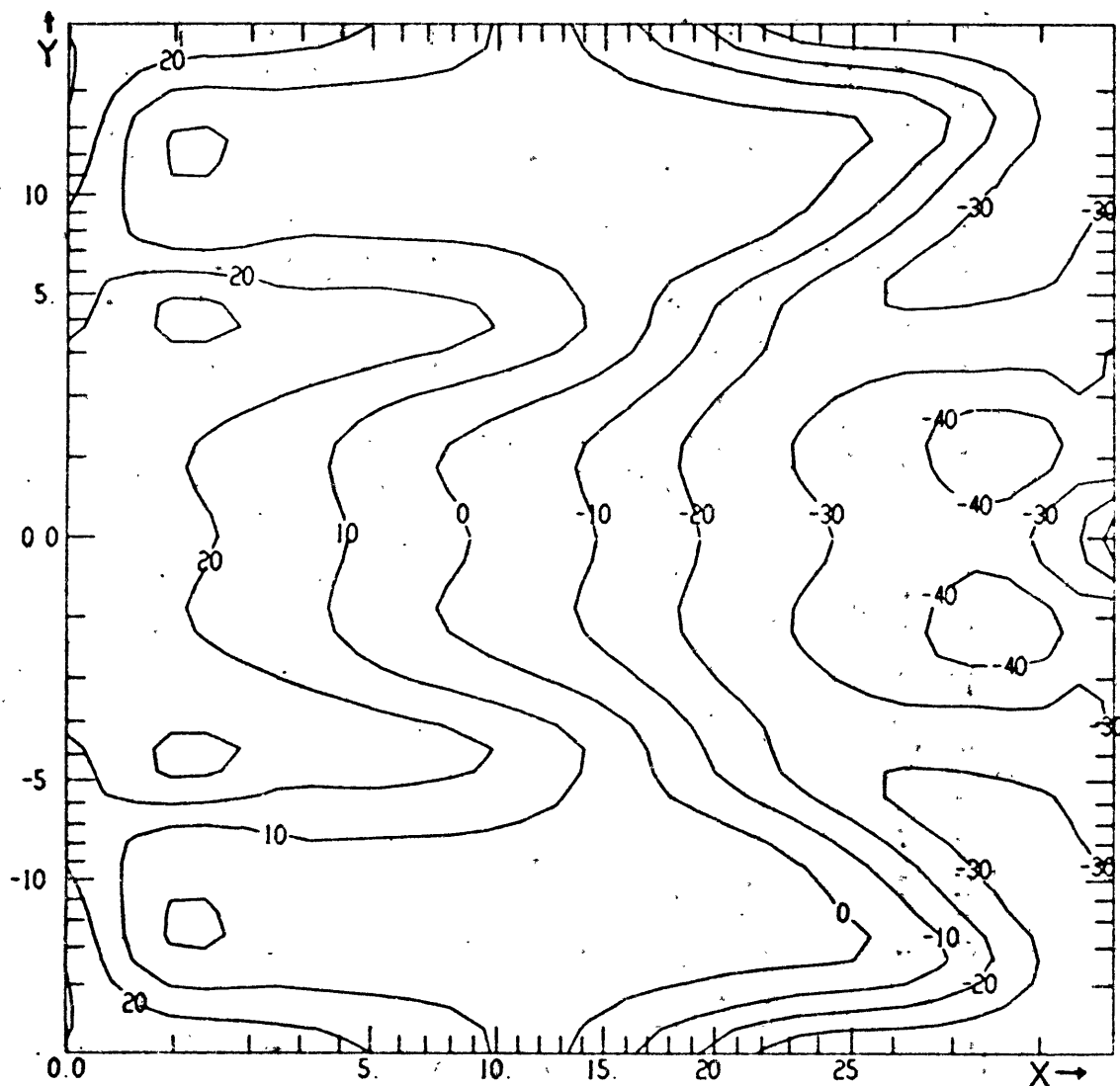
DAY 39.79 IT- 500 00 MODEL STEP 10001 X- 0 0 TO 28 6 Y--15 0 TO 15 0
 N2E2 N4CH3 30X44STR DELT- 5 E-1 E-8.88-B1-.001 WIND- 5 EAST EVERYWHERE 07/23/19

Fig. 5.46a u^s vectors at 40 days. Nonlinear. East wind.



DAY 39.79 (T= 500.00 MODEL STEP 1000) X= 0.0 TO 28.6 Y=-15.0 TO 15.0
 N2E2 N4CH3 30X44STR DELT=.5 E-1.E-8,BB-BI-.001 WIND= 5 EAST EVERYWHERE 07/23/19.

Fig. 5.46b u^1 vectors at 40 days. Nonlinear. East wind.

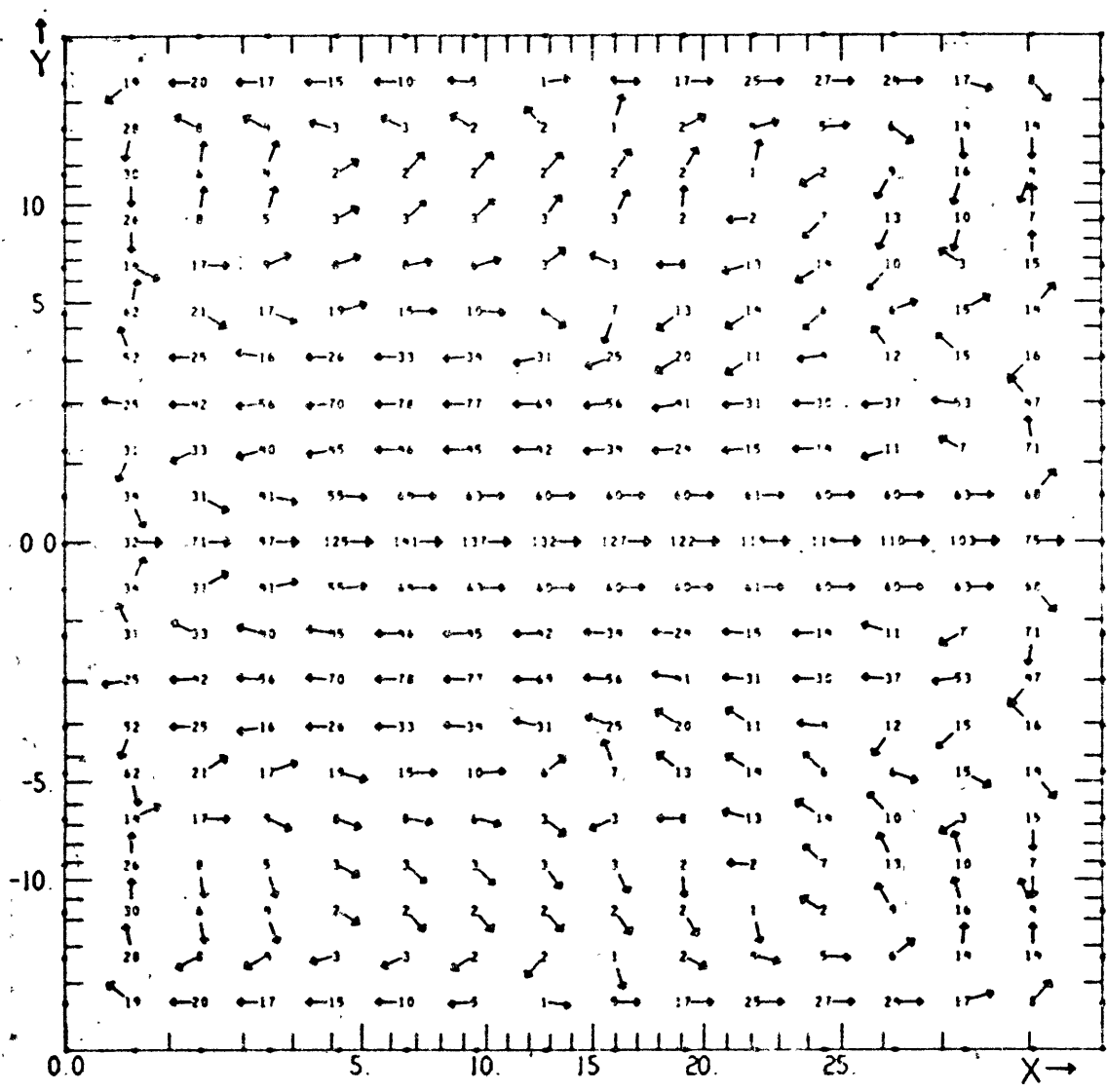


LAYER DEPTH LOV--4 71E-01 HIGH• 3.17E-01 CI-10 • 1 E-02

DAY 39.79 (T- 500 00 MODEL STEP 1000) X- 0.0 TO 28.6 Y--15.0 TO 15.0

NZEE2 NACH3 30X44STR DELT- 5 E-1 E-8, BB-B1- 001 WIND- 5 EAST EVERYWHERE 07/23/19

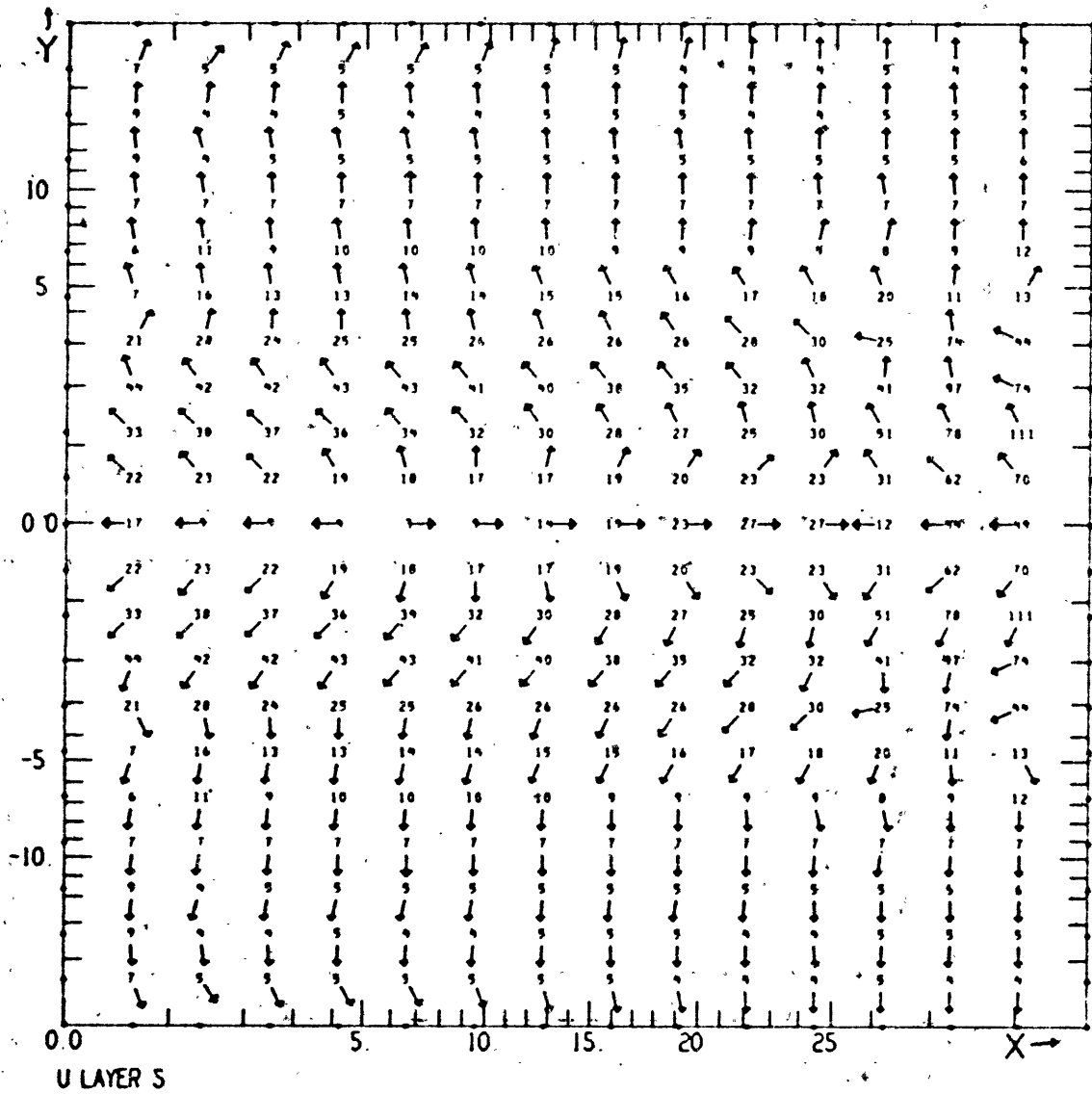
Fig. 5.46c h contours at 40 days. Nonlinear. East wind.



U TRANSPORT

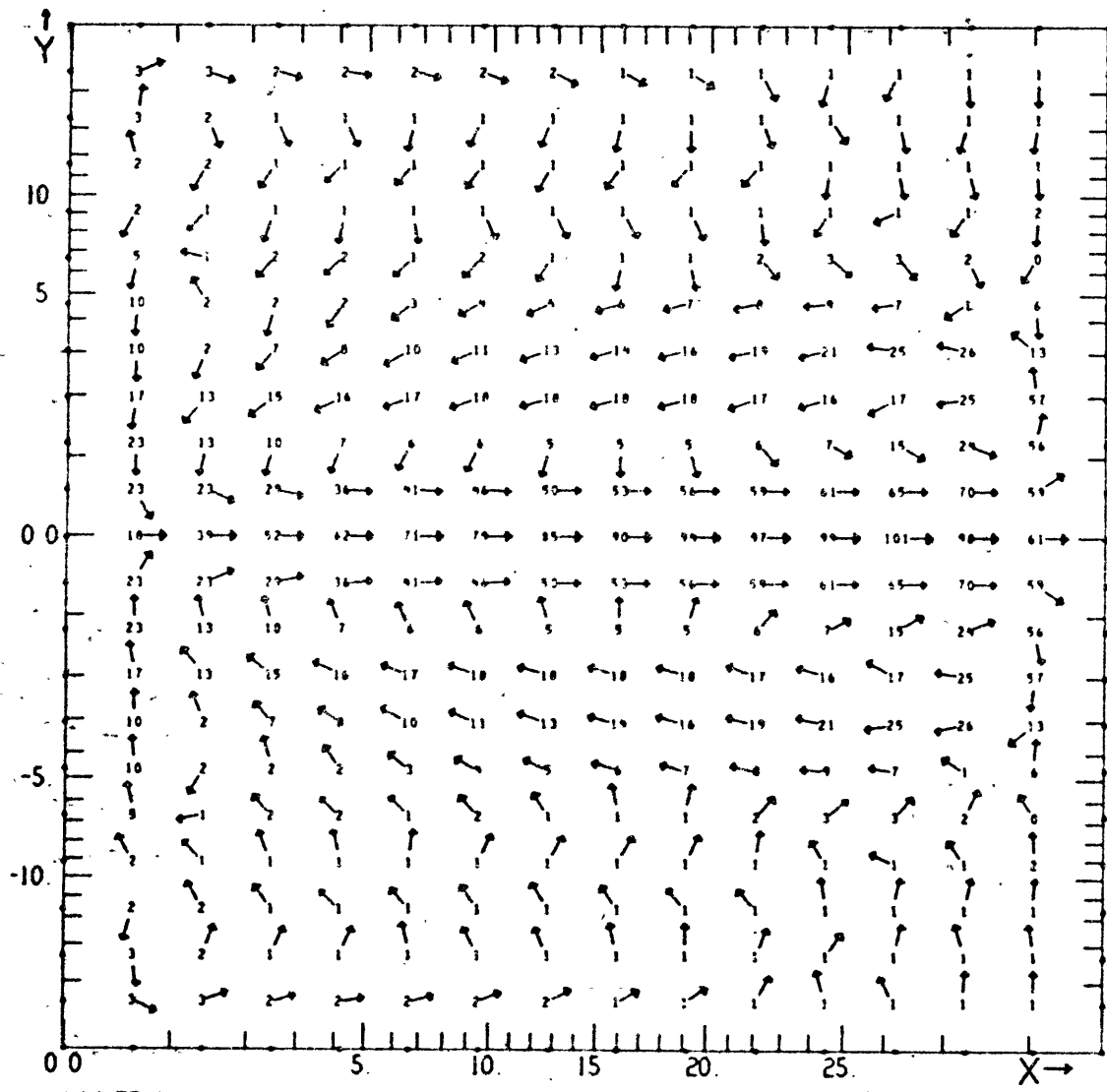
DAY 39 79. (T= 500 00 MODEL STEP 1000) X= 0 0 TO 28 6 Y=-15 0 TO 15 0
 NPE2 N4CH3 30X44STR DELT=.5 E=1.E-8,B8-B1=.001 WIND= 5 EAST EVERYWHERE 07/23/19

Fig. 5.46d \bar{u} vectors at 40 days. Nonlinear. East wind.



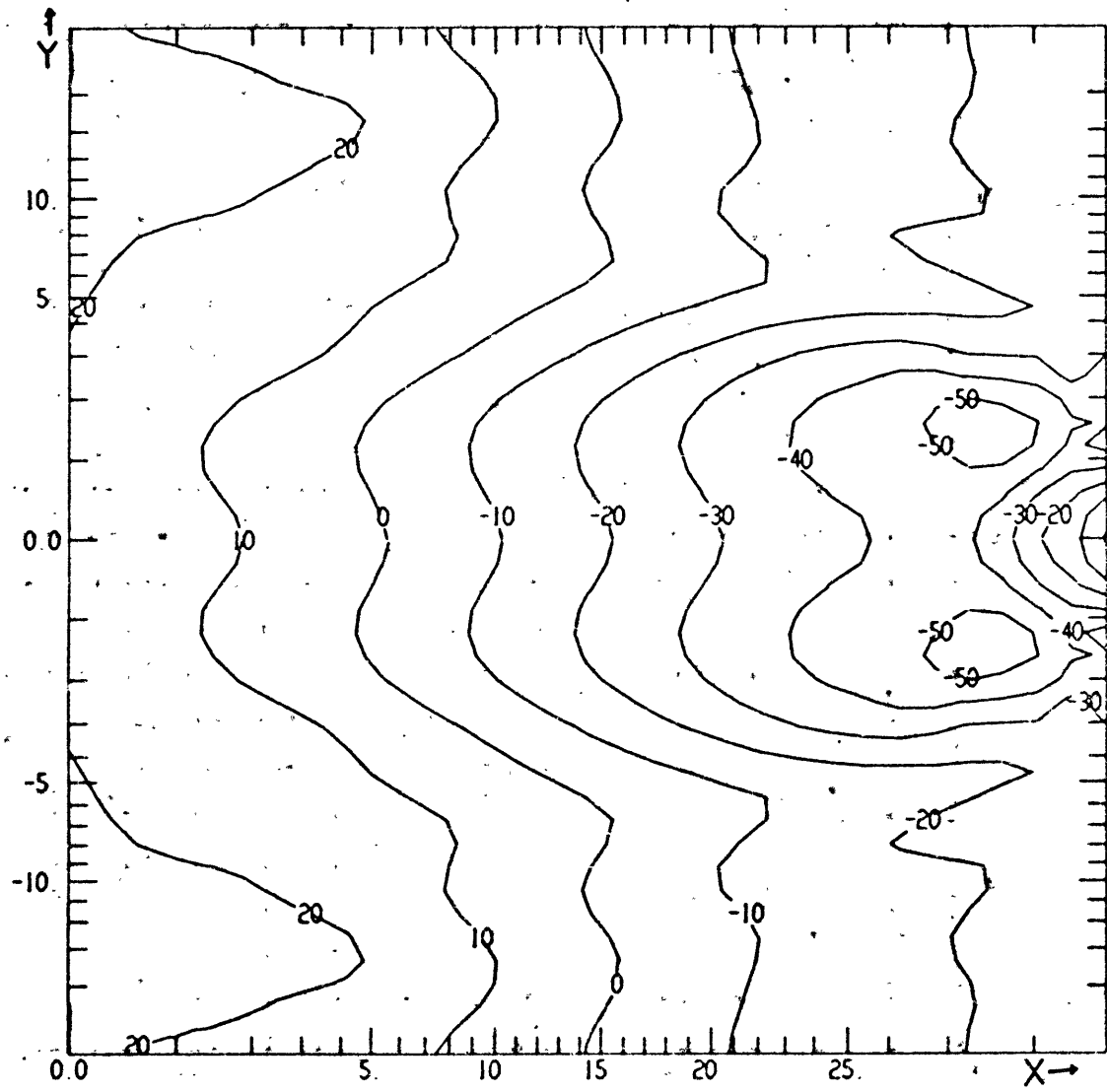
DAY 397 89 IT= 5000 00 MODEL STEP 100001 X= 0.0 TO 28.6 Y=-15.0 TO 15.0
 N2E2 N4CH3 30X44STR DELT= 5 E-1 E-8.88-81- 001 WIND= 5 EAST EVERYWHERE 07/23/19 1'

Fig. 5.47a u^S vectors at 400 days. Nonlinear. East wind.



DAY 397.89 (T= 5000 (00-MODEL STEP 10000) X= 0.0 TO 28.6 Y=-15.0 TO 15.0
 N2E2 N4CH3 30X44STR DELT= .5 E-1 E-8.88-B1= .001 WIND= 5 EAST EVERYWHERE 07/23/1

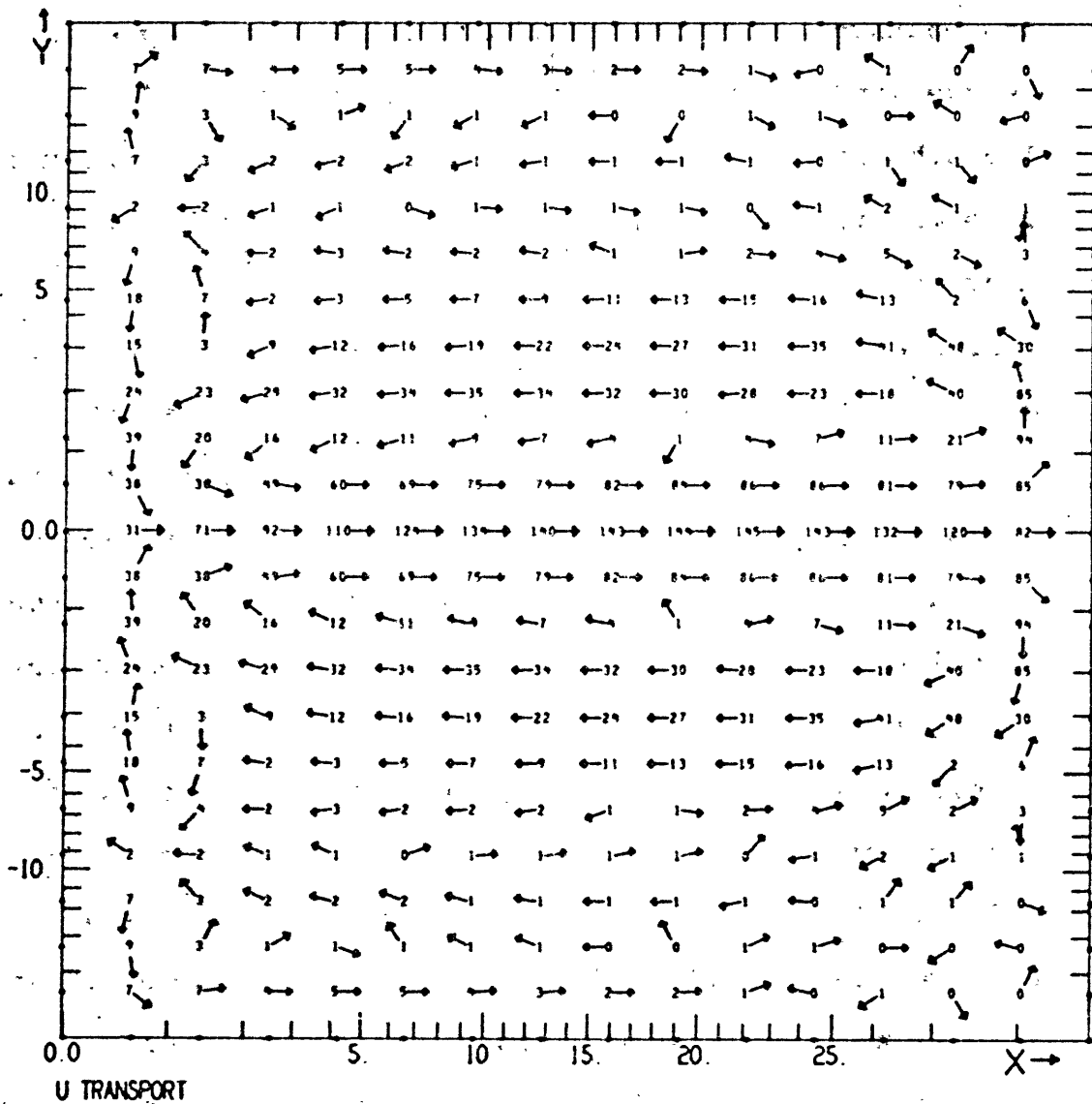
Fig. 5.47b u^1 vectors at 400 days. Nonlinear. East wind.



LAYER DEPTH LOW=-5.50E-01 HIGH= 2.72E-01 CI=10 * 1.E-02

DAY 397.89 (T= 5000 DO MODEL STEP 10000) X= 0.0 TO 28.6 Y=-15.0 TO 15.0
 N2E2 N4C3 30X44STR DELT= 5 E-1 E-8.88-81- 001 WIND= 5 EAST EVERYWHERE 07/23/19

Fig. 5.47c h contours at 400 days. Nonlinear. East wind.



DAY 397 89 (T= 5000 00 MODEL STEP 10000) X= 0.0 TO 28.6 Y=-15.0 TO 15.0
 N2E2 N4CH3 30X44STR DELT= .5 E-1 E-8,BB-BI= .001 WIND= 5 EAST EVERYWHERE 07/23/19

Fig. 5.47d \bar{u} vectors at 400 days. Nonlinear. East wind.

everywhere in the basin with the exception of the northwest and southwest corners. Poleward of 5° the surface layer flow is the wind drift solution given by the linear theory, (3.12). The subsurface flow combines with this to give approximately zero vertically integrated transport, consistent with (3.15). Many of the prominent features near the equator in the interior are in good agreement with the y-z plane calculation of Charney and Spiegel (1971). (See their Figs. 1b and 2b.) Specifically, in both our calculation and theirs the halfwidth of the undercurrent is about 1° and the velocity at the equator averaged at all depths below 25m (i.e. the mean undercurrent velocity) is about $.80\text{m sec}^{-1}$. Both have eastward flow at the surface; as noted above this is primarily due to the strong upwelling at the equator. Eastward flow at the surface with easterly winds has been observed in the Pacific by Taft, et. al. (1974). Both calculations show the strongest westward subsurface flow (on the order of $.10\text{m sec}^{-1}$) between 2° and 3° .

The principal features of the flow may be explained qualitatively by considering the vorticity balance, as in Fofonoff and Montgomery (1955). (Also see Charney, 1960 and Charney and Spiegel, 1971). The easterly wind produces a poleward Ekman drift in the surface layers. This requires upwelling at the equator and therefore an equatorward flow at depth. Parcels moving toward the equator lose planetary vorticity. If we assume that total vorticity is approximately

conserved these parcels must acquire relative vorticity as they approach the equator resulting in an eastward flow there. A calculation similar to that leading to (5.8) shows that a parcel originating at a latitude y_0 with approximately zero relative vorticity and zero zonal velocity has an eastward velocity of approximately $\beta y_0^2/2$ at the equator. For undercurrent velocities of .75 to 1.00 m sec⁻¹ y_0 is between 2.5° and 3°; this is consistent with our calculation. A similar line of reasoning may be used to determine the position of the westward currents. Fluid parcels in the undercurrent that reach the eastern side are turned poleward in narrow boundary currents. As they travel away from the equator they gain planetary vorticity. In order to approximately conserve their vorticity they must lose relative vorticity so that their poleward velocity must decrease (since in these currents relative vorticity $\zeta \sim V_x$). In particular, if the vorticity of such a parcel is βy_0 it cannot progress poleward beyond latitude y_0 and we conclude that this will be the latitude of the currents required to complete fluid circuits which include the undercurrent.

The argument in the preceding paragraph does not give the complete story. It not only ignores the effects of both upwelling and friction, which must become important near the equator, but it provides no independent way of determining the latitude y_0 . Poleward of y_0 the advection of planetary vorticity in the lower layer is balanced by the vortex stretching term $f\omega$;

y_0 is the point where nonlinear terms enter the vorticity balance. In Section 2.2 we established (see (2.10) ff.) that the linear dynamics of the Ekman layer break down at a latitude $y_c \sim 2^\circ$ when inertial terms become important in the Ekman layer. The latitude y_0 must be the same order as y_c since the layers are coupled by vertical motions. These considerations allow us to find an inertial scaling for Eqs. (3.1), valid when the Ekman layer Rossby number $\epsilon_E > \gamma^{5/2}$, where $\epsilon_E = \epsilon \gamma^{-1/2}$ (see (3.2) for the definitions of ϵ and γ . For the parameter values in Table 1, $\epsilon_E \sim .2$ and $\gamma \sim 10^{-2}$.) The arguments of Section 2.2 give the following rescalings in Eqs. (3.1):

$$y = \epsilon_E^{2/5} y', \quad \alpha = \epsilon_E^{-1/5} \gamma^{1/2} \alpha', \quad \gamma_I = \epsilon_E^{1/5} \gamma^{1/2} / \alpha' \quad (5.13)$$

(Unlike the linear scaling (3.3) it is necessary to take account of the inertial dependence in the determination of η and hence of α .) We assume that the scale in the x direction is long enough so that zonal variations may be neglected except in the pressure gradient term. (It is this term which drives the undercurrent. See Chapter 1.) It then follows from (5.13) that the remaining variables may be written (cf., Philander 1971, p. 239):

$$(u^s, v^s, u^t) = \epsilon_E^{-1/5} \gamma^{-1/2} (u^{s'}, v^{s'}, u^{t'})$$

$$V^t = \epsilon_E^{-2/5} V^{t'}, \quad W = \epsilon_E^{-4/5} W' \quad (5.14)$$

$$h = \int^x \hat{\tau}^{(x)}(y=0) dx + \gamma^{-1/2} \epsilon_E^{3/5} p$$

Dropping primes and taking $\alpha' = 1$ for simplicity the steady state version of (3.1) is

$$V^s u_y^s + \frac{W}{2} (u^s - u^t) - \gamma v^s - \hat{\tau}^{(x)} = -\epsilon_E^{2/5} [p_x + u^s u_x^s] \quad (5.15a)$$

$$V^s v_y^s + \frac{W}{2} v^s + \gamma u^s + p_y = -\epsilon_E^{2/5} u^s v_x^s \quad (5.15b)$$

$$V^t u_y^t + \frac{W}{2} (u^s - u^t) - \gamma v^t + \hat{\tau}^{(x)} = -\gamma^{-1/2} \epsilon_E^{3/5} (u^t u_x^t + p_x) \quad (5.15c)$$

$$\gamma u^t + p_y = -\gamma^{1/2} \epsilon_E^{1/5} u^t v_x^t \quad (5.15d)$$

$$V_y^s + V_y^t = -\gamma^{-1/2} \epsilon_E^{3/5} u_x^t \quad (5.15e)$$

(The highest order x-dependent terms are exhibited on the right hand sides of these equations; they will be considered below.)

We have now obtained scales for all variables in the equatorial region that are determined in terms of the governing parameters. In dimensional terms the meridional scale for the

equatorial circulation is 1.5° . The scale for the surface velocities and the subsurface zonal velocity is $[\tau_0^4/4\beta v_V^2]^{1/5}$; this is about $.5m \cdot sec^{-1}$. (We have again taken $K \approx 2v_V/\bar{H}$).

The meridional sections of the layer depth that we calculate closely resemble a similar section presented by Charney and Spiegel. (Compare their Fig. 15 with our Fig. 5.42.) These profiles agree qualitatively with the bowing of isotherms which is usually observed beneath the undercurrent (e.g., Knauss 1966). Eq. (5.15d) requires that the pressure gradient be in geostrophic balance with the lower layer zonal velocity. This accounts for the meridional profile of the pressure gradient. For example, at the center of the basin at $.3^\circ N$ the term fu and $g'h_y$ balance to within 10%. At $3^\circ N$ the balance is within 15%.

There are a number of differences between our calculation and that of Charney and Spiegel. These are largely attributable to the different simplifications in the model geometries. Our model has no way of producing the downwelling region which they find beneath the undercurrent maximum. (See their Fig. 2). They argue that longitudinal variations may be neglected because the inertially determined cross stream scale $\delta = u/\beta$ is so much smaller than the downstream scale L_x . (There is no intrinsic longitudinal scale; L_x is taken as the length of the basin). A related argument leads to the conclusion that the zonal pressure gradient exactly balances the wind stress.

divided by the layer depth. In our model longitudinal variations are permitted and the zonal pressure gradient is free to seek its own value. The most stringent condition for neglecting the zonal dependences arises from (5.15c) and (5.15e); viz, that

$$L_x > \gamma^{-1/2} \epsilon_E^{3/5} \quad (5.16)$$

This is about 1300 km for our parameter values. The condition based on a simple comparison of length scales (i.e. $L_x > \epsilon^{2/5}$) is inappropriate because the subsurface velocity components have different scales. Charney and Spiegel's (1971) calculations failed to converge when the viscosity was reduced to the point where the right hand side of (5.16) was on the order of 2000 km. This suggests that in such a parameter range it is necessary to include the effect of the zonal gradients in limiting the growth of zonal momentum.

In our model there will be some zonal variation in the interior regardless of the zonal length scale L_x because the layer depth varies across the basin. This comes about because the layer depth is a multiple of the pressure and zonal variation of the pressure must be allowed in order to drive the undercurrent. The effects of the layer depth variation enter (5.15) at order $\epsilon_E^{8/5}$ relative to the retained terms and hence do not substantially influence the dynamics. The more important zonal variations are due to the terms on the right hand sides

of (5.15c) and (5.15e). For example, because the undercurrent velocity increases downstream the vertically integrated transport increases downstream despite the decrease in the depth of the layer.

Since the undercurrent transport increases downstream the boundary current at the eastern end of the equator will be stronger than that at the west. It also follows that the vertically integrated meridional transport \bar{v} will be equatorward (and not zero). At a latitude where inertial terms are negligible the vertically integrated zonal momentum equation is approximately (with the scaling of Chapter 3)

$$-y\bar{v} \approx -h_x + \hat{\tau}^{(x)}$$

Since $\tau^{(x)} < 0$ and $-y\bar{v} > 0$ it follows that

$$h_x = (1+a)\hat{\tau}^{(x)}, \quad a > 0 \quad (5.17)$$

so that the pressure gradient overbalances the wind stress. All of the features described in the preceding paragraph are present in our numerical computation. From Fig. 5.47c it is evident that $a > 0$ from about 5°S to about 5°N . At the equator (Fig. 5.39) $a \approx .3$.

The preceding paragraph shows that $p_x < 0$ if $u_x^1 > 0$. Similarly, $p_x < 0$ if $u_x^1 > 0$. That u_x^1 is nonzero follows from the form taken by (5.15a) and (5.15c) at the equator. Subtract the latter from the former to obtain

$$-2\hat{\tau}^{(x)} \approx \gamma^{-1/2} E_E^{3/5} (u^2 u_x^2 + p_x) \quad (5.18)$$

Since geostrophy (5.15d) holds up to the equator and u^1 peaks sharply at the equator, it follows that the undercurrent velocity must increase downstream. Considering only the left hand sides (5.15a) says that the vertical advection term balances the wind stress while (5.15c) demands that the same term balance the zonal pressure gradient $(-\tau^{(x)})$. Since the surface stress and the pressure gradient are of opposite sign this is not possible. So other terms must enter into the balance. In our model the advection of zonal momentum comes in before the vertical friction term for L_x less than $\gamma^{-1} \epsilon^{2/5} = 10^4 \text{ km}$ with our parameters. Charney and Spiegel (1971) failed to obtain convergence for small values of v_v , perhaps because there was no term available to balance the left hand side of (5.15c).

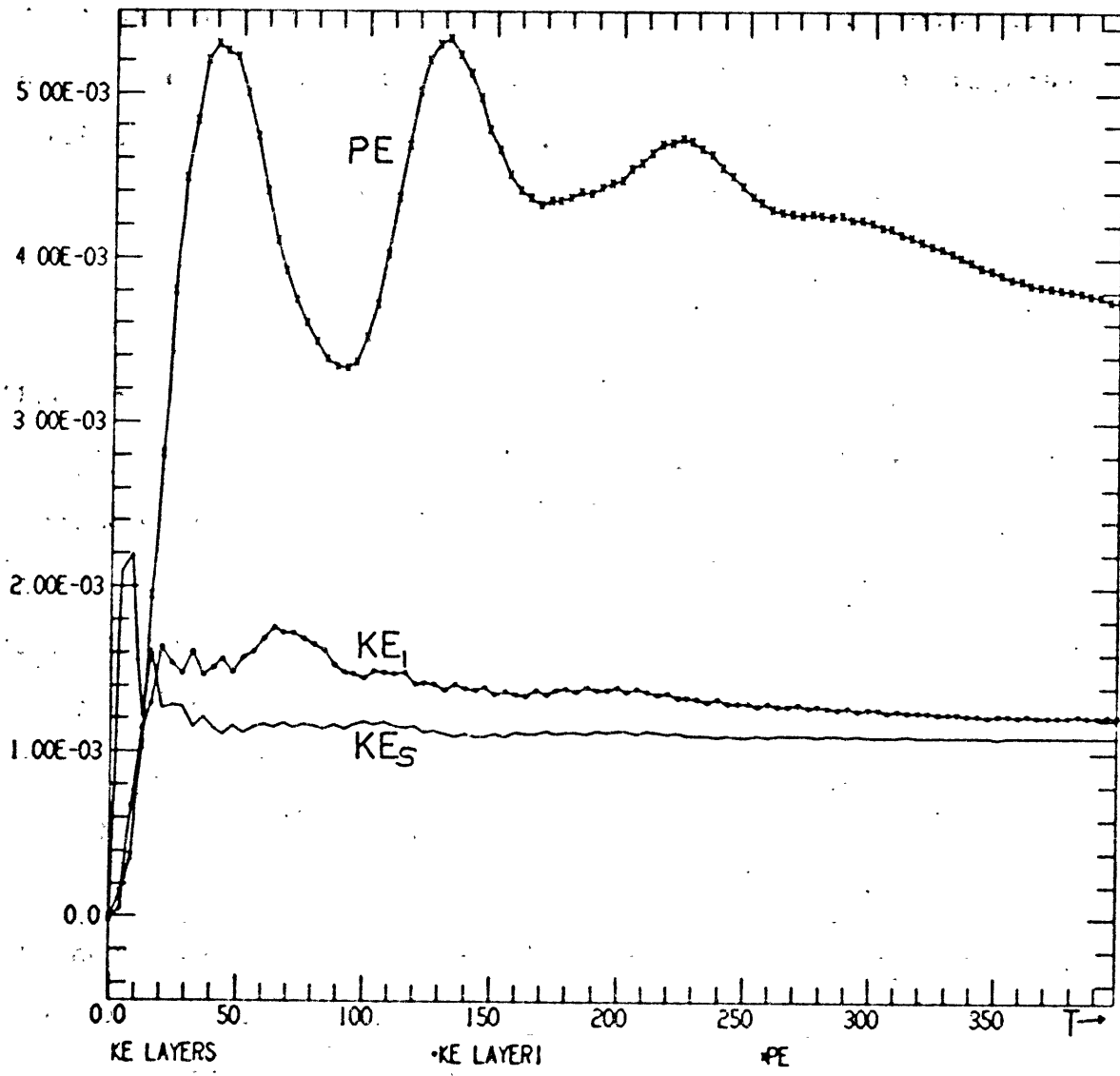
As we remarked earlier, the observational evidence is that the undercurrent transport decreases downstream. In order to reproduce this feature it appears to be necessary to include some physical mechanism which allows the pressure gradient force to be uncoupled from the vertical extent of the undercurrent. One such possibility is the equatorial effect of the thermohaline circulation (Philander, 1973a). It appears that a successful model of the undercurrent must be fully three dimensional. Perhaps the most significant result of our undercurrent simulation concerns what did not happen; there was no evidence at all of any hydrodynamic instabilities and the current system remained stable throughout the course of

its evolution. This is consistent with Philander's (1975) stability analysis.

5.6 Nonlinear Response to a Uniform West Wind

In this section we consider the nonlinear response to a uniform westerly wind stress of $.465 \text{ dyn cm}^{-2}$. The only difference between this case and that of the previous section is in the wind direction. Because of east-west asymmetries in the ocean dynamics due to the beta effect the responses in the two nonlinear cases are quite different. The linear response to an east wind (Section 5.4) is easily interpreted as a west wind response: simply change the sign of all variables (h into -h, u^S into $-u^S$, etc.). The pattern of the response is unchanged.

The energy graphs for this case (Figs. 5.48, 5.49) are much more similar to the linear east wind energy graphs (Figs. 5.25, 5.26) than they are to the nonlinear ones (Figs. 5.36, 5.37). We will focus our attention on the curves for equatorial region (5.6°S to 5.6°N). The potential energy curve for the present case is almost identical to that for the linear case: the amplitudes are approximately the same and the oscillations have the same periods with an initial peak at about day 40. In Section 5.4 these oscillations were explained in terms of the reflections of Rossby and Kelvin waves at the meridional boundaries. The same phenomena appear to be present in this nonlinear case. The kinetic energy curves behave differently.



ENERGIES FOR X= 0.0 TO 28.6 Y=-15.0 TO 15.0 T= 0.0 TO 397.89 DAYS
NBEIR N4CH3 30X44STR DELT= 5 E-1 E-8.88-B1= 001 WIND=1 5.0 EVERYWHERE 07/23/18

Fig. 5.48 Energies from 15°S to 15°N. Nonlinear. West wind.

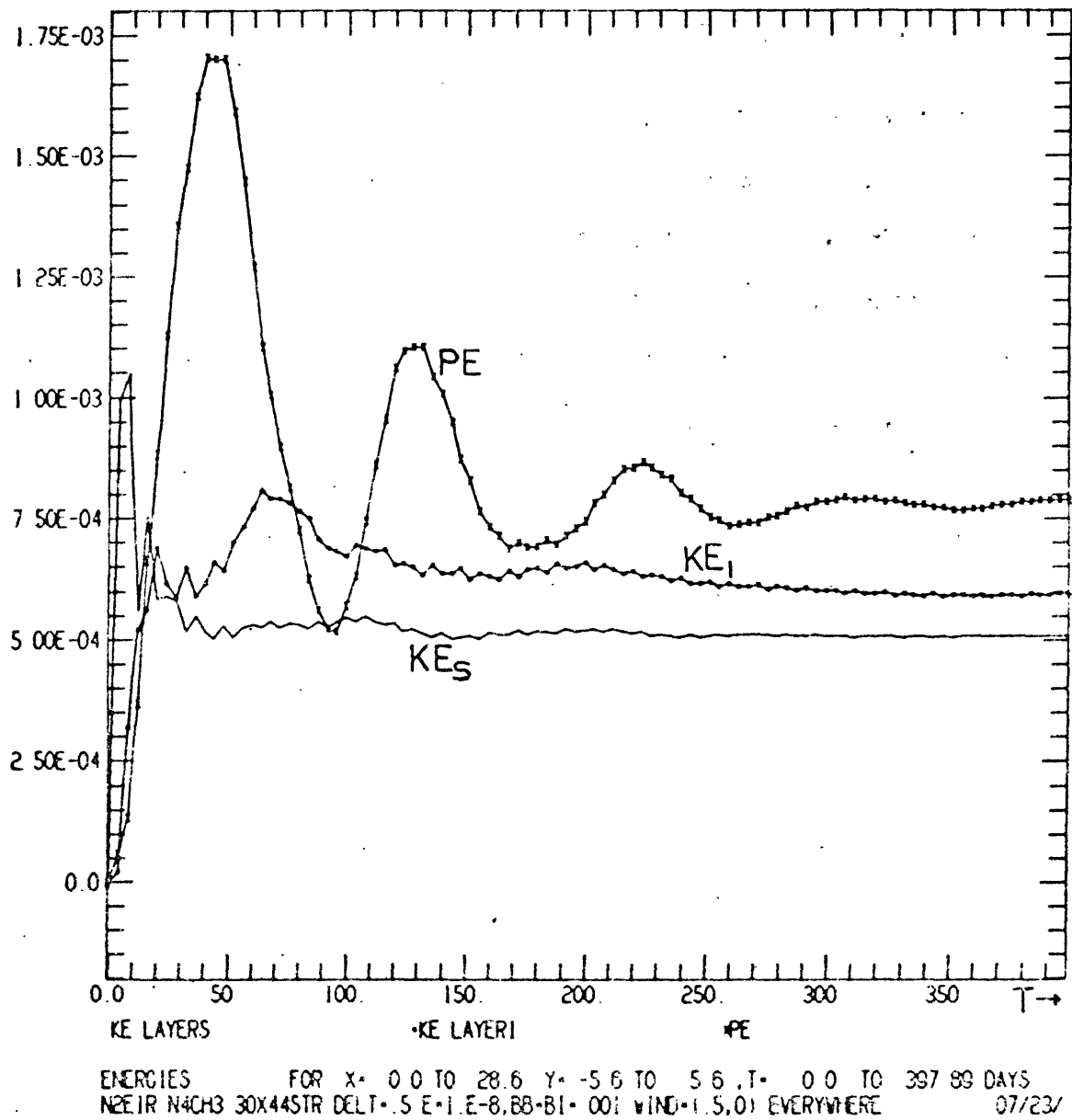


Fig. 5.49 Energies from 5.6°S to 5.6°N. Nonlinear. West wind.

The surface layer has less, and the lower layer more kinetic energy than in the linear case. The former is about the same as the east wind nonlinear case but the latter is less by almost a factor of 5. After about 80 days the kinetic energy curves show little oscillation compared with the linear case.

Fig. 5.50 shows sections of the layer depth across the equator for the first 40 days. As was true of the east wind nonlinear response (Fig. 5.38), these sections are very similar to the linear zonal wind response (Fig. 5.27) except near the boundaries. In particular the effects of the Kelvin mode moving in from the western boundary are evident. Fig. 5.51 shows that by day 80 h at the equator is close to its final value; closer than the previous zonal wind cases (Figs. 5.26, 5.28, 5.39) at the same time. The slope of h in the final profile is nearer to the linear result than was the east wind h profile. The boundary layer at the western side is 2.5° wide while that at the east is only one grid point (0.3°) wide.

Fig. 5.52 shows that at the equator \bar{u} becomes close to its final interior value within 8 days. There is some oscillation about this final value of about $75 \text{ m}^2 \text{ sec}^{-1}$ until about day 160 (Fig. 5.53). The nonlinear east wind case (Figs 5.40 5.41) takes about 24 days to reach a value of $75 \text{ m}^2 \text{ sec}^{-1}$ and about 40 days to approximate its final value of $125 \text{ m}^2 \text{ sec}^{-1}$. Figs. 5.55 and 5.56 show the early and late evolution, respectively, of meridional sections of the zonal transport \bar{u} .

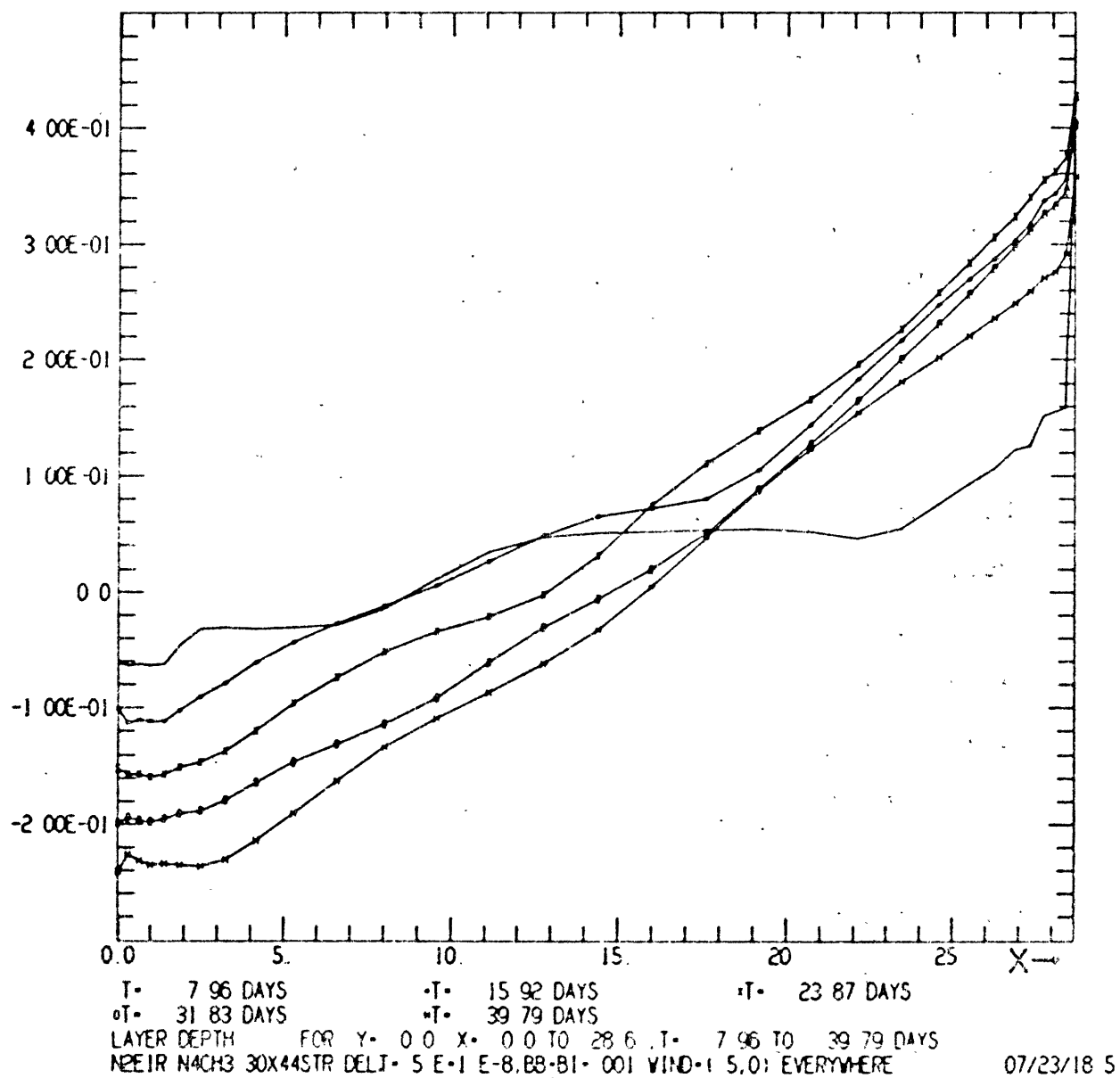


Fig. 5.50 Sections of h along the equator to day 40. Nonlinear. West wind.

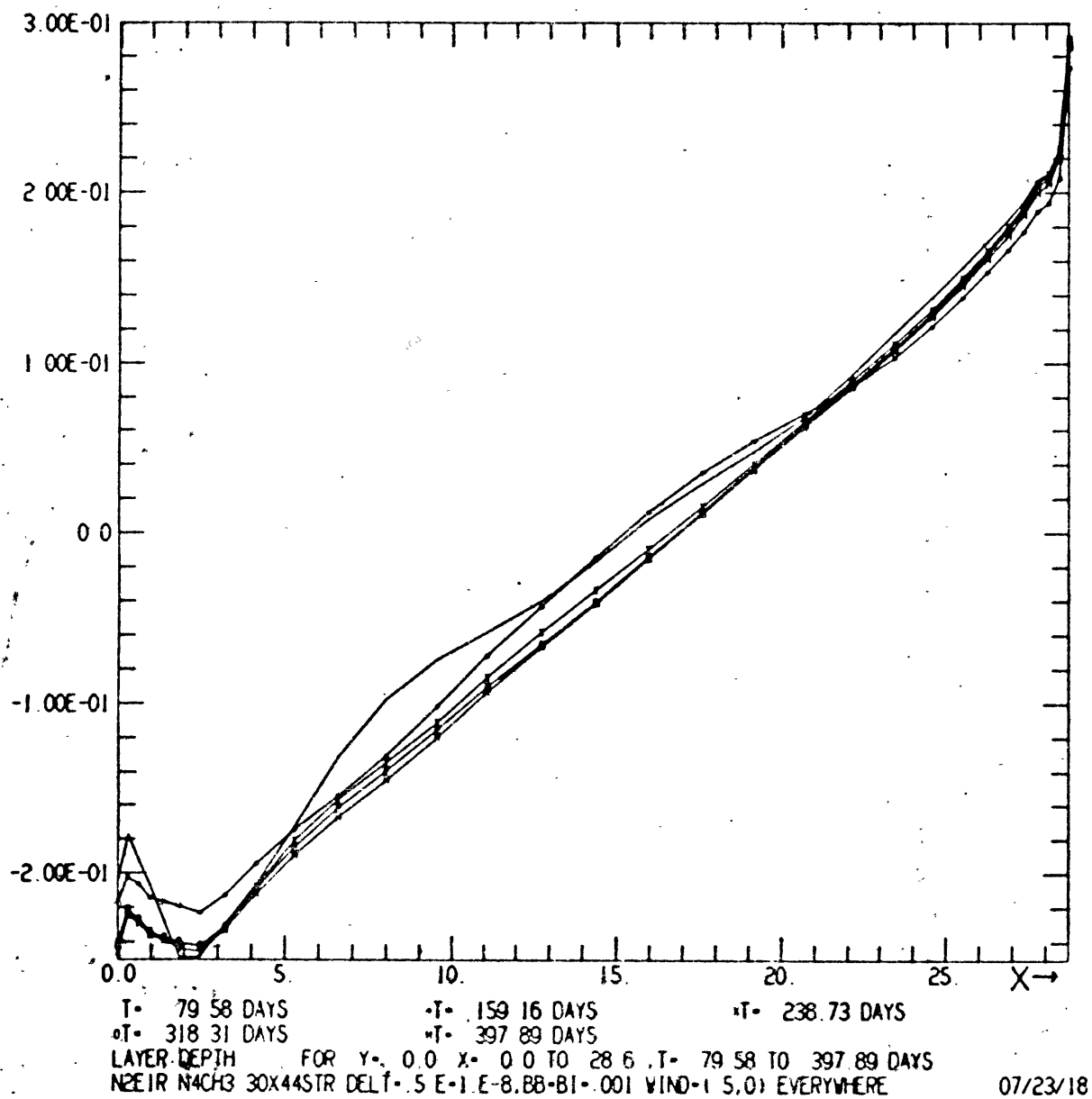


Fig. 5.51 Sections of h along the equator to day 398. Nonlinear. West wind.

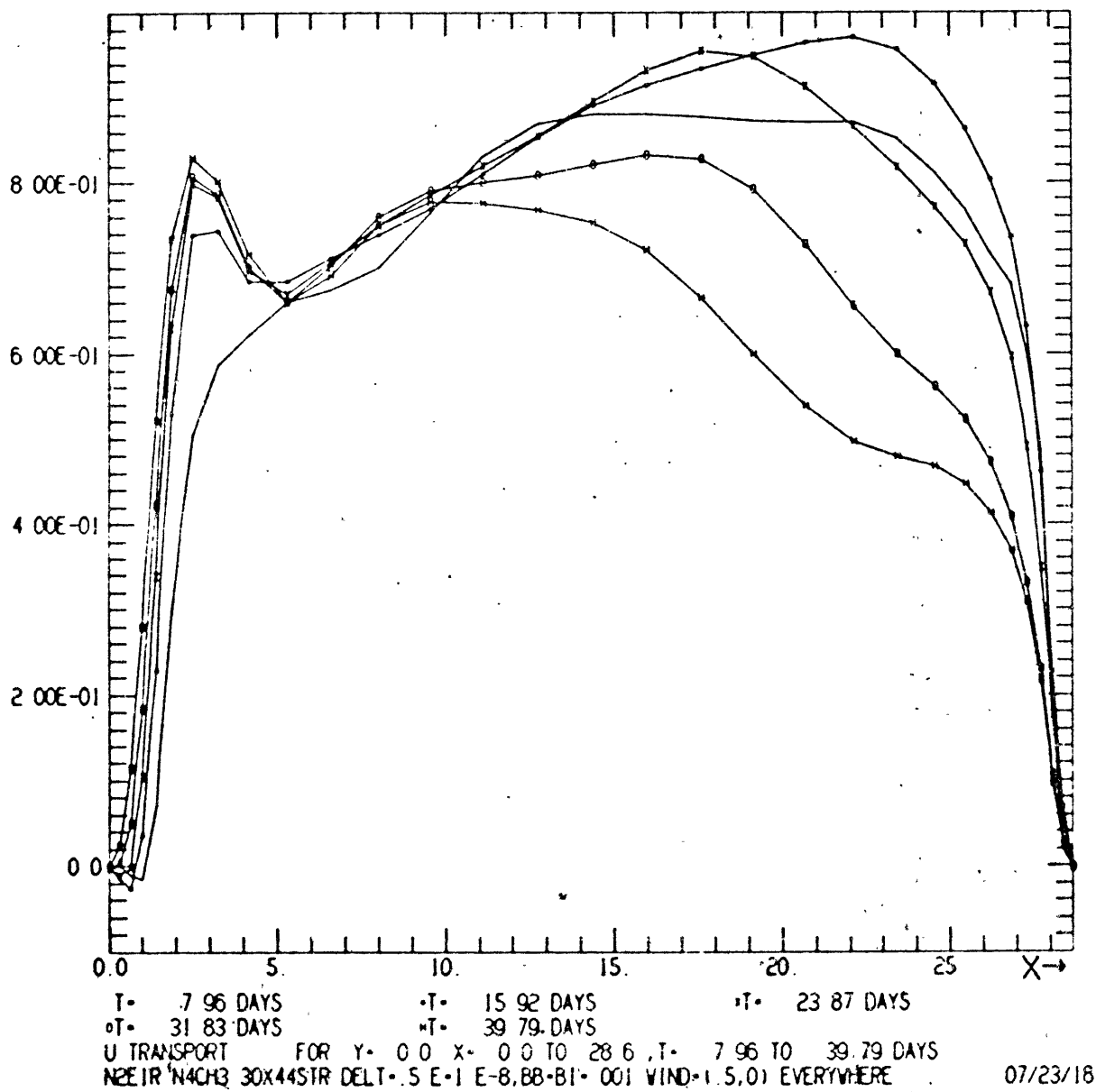


Fig. 5.52 Sections of \bar{u} along the equator to day 40. Nonlinear. West wind.

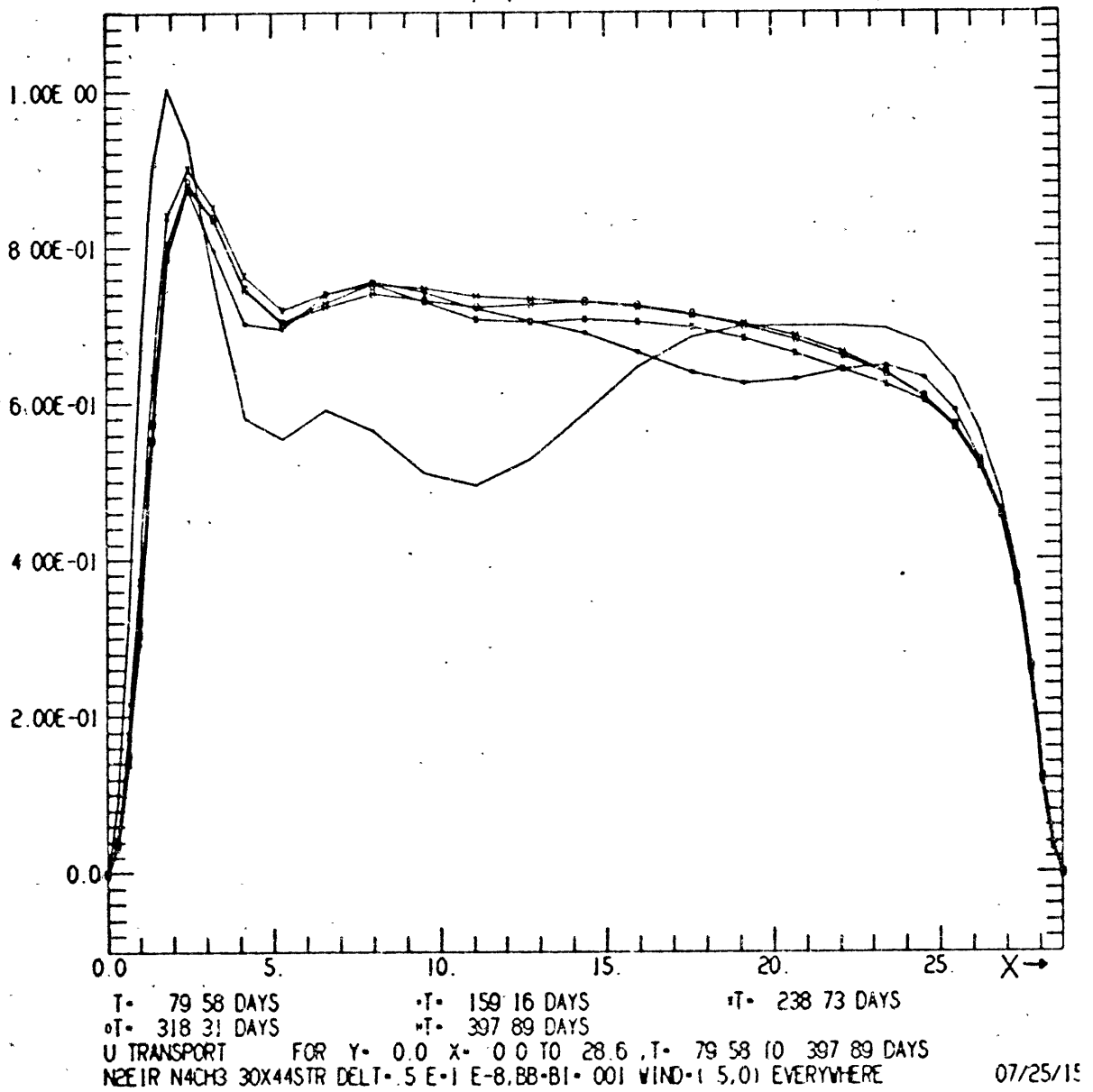


Fig. 5.53 Sections of \bar{u} along the equator to day 398. Nonlinear. West wind.

They should be compared with the similar figures for the east wind case, Figs. 5.43 and 5.44. In the west wind case, the eastward transport at the equator is quickly established. Westward currents will be required in the steady state to return to the west the water that has travelled to the eastern side at the equator. These currents, centered at 2°S and 2°N , take longer to become established. This is reasonable, since in the early stages there is a net transport of water from west to east in order to establish a pressure gradient opposite to the wind. For the same reason the westward flowing currents are set up before the eastward flowing undercurrent when the wind is from the east.

Figs. 5.54a, b, c show meridional sections of h at various longitudes. As with all previous cases adjustment "propagates" from east to west and occurs sooner near the equator than extra-equatorially.

Figs. 5.57a, b, c show the flow fields at 16 days. Surface flow at the equator is in the direction of the wind and is limited by the interfacial friction between the two active layers. Extra-equatorially the surface currents are wind drift currents, resulting in convergence at the equator. The downwelling at the equator due to this convergence transports eastward momentum downwards so that the lower layer also has eastward currents at the equator. Unlike the east wind case, in this case the surface flow is faster than the flow at depth.

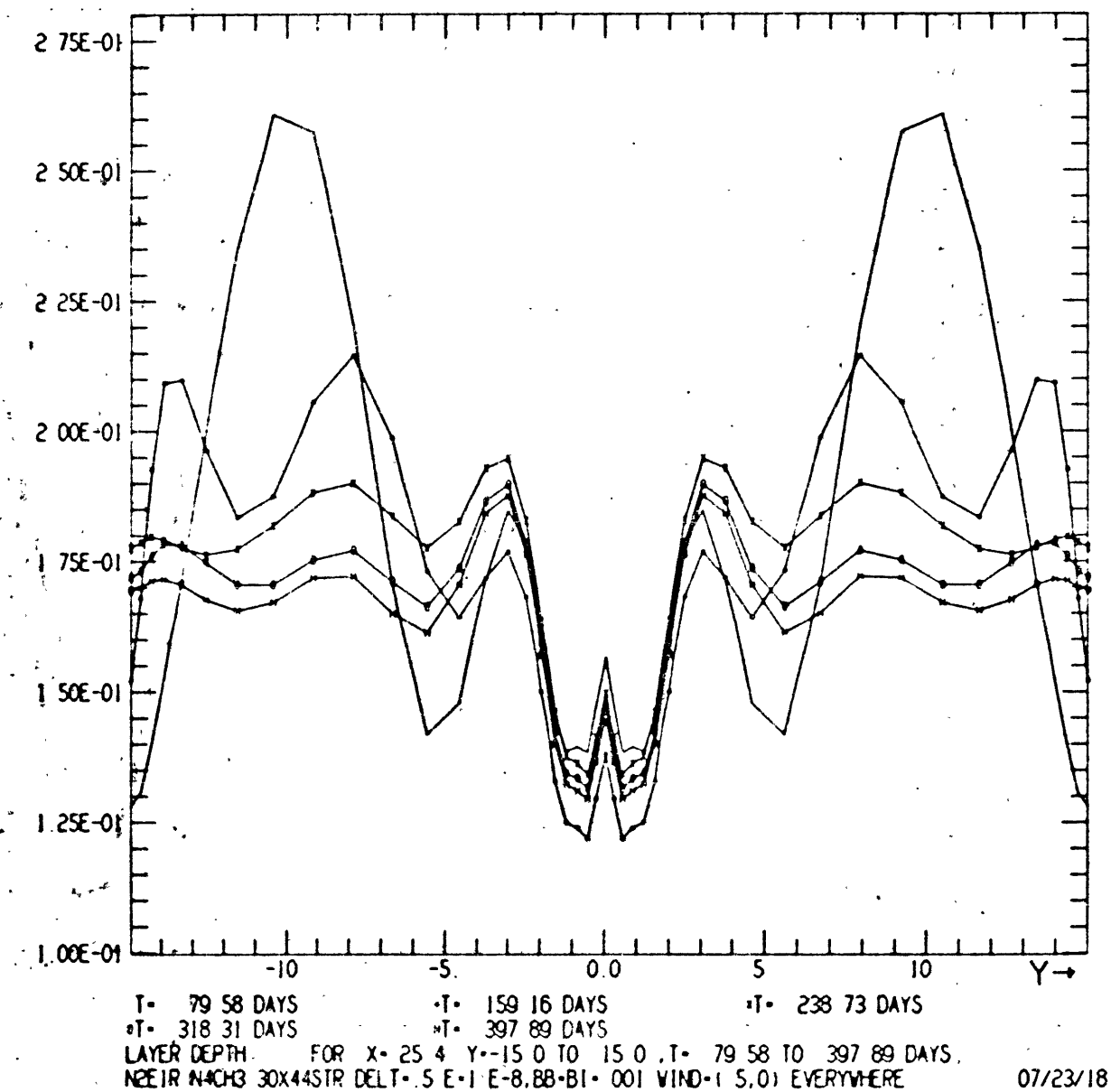
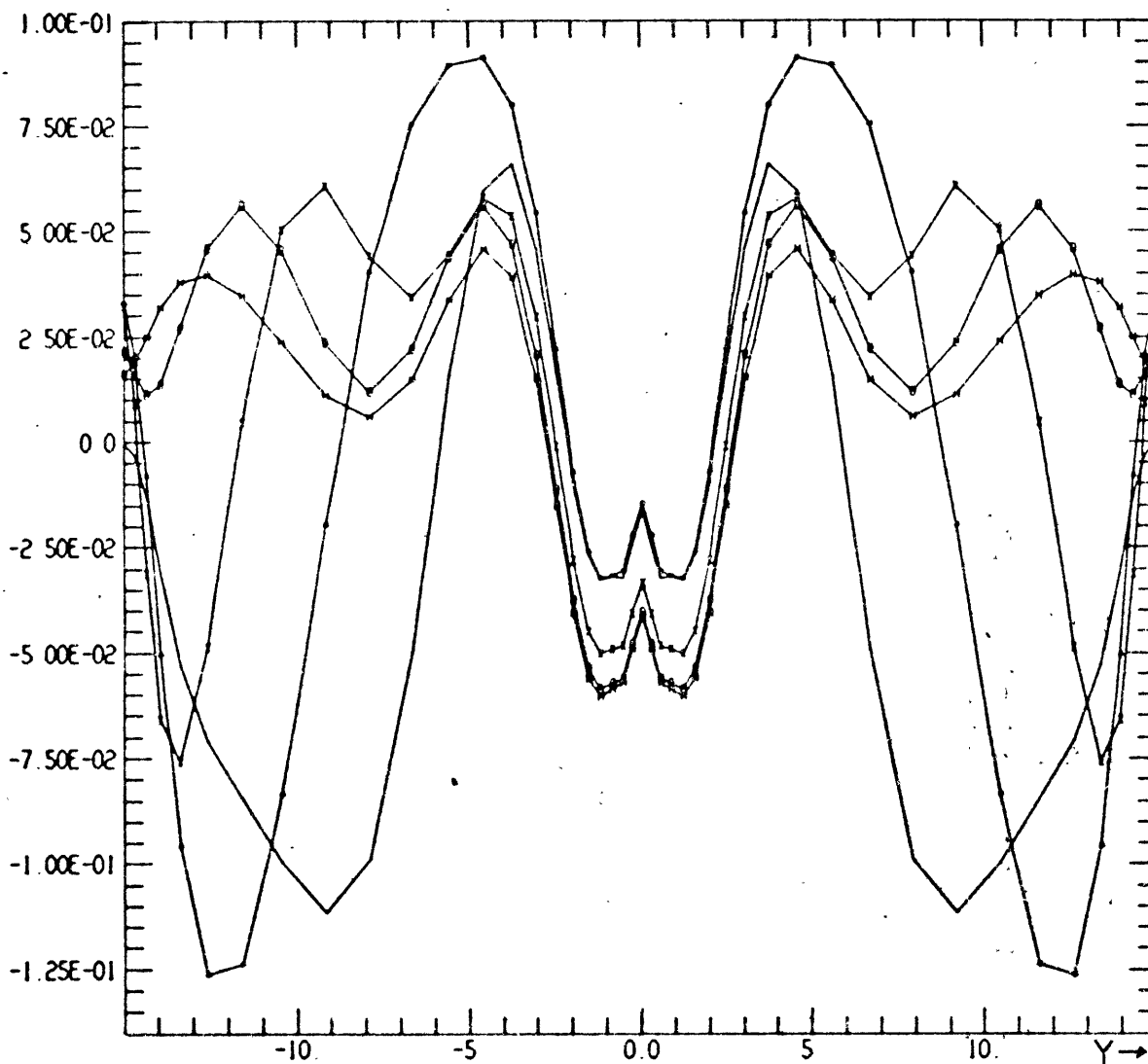


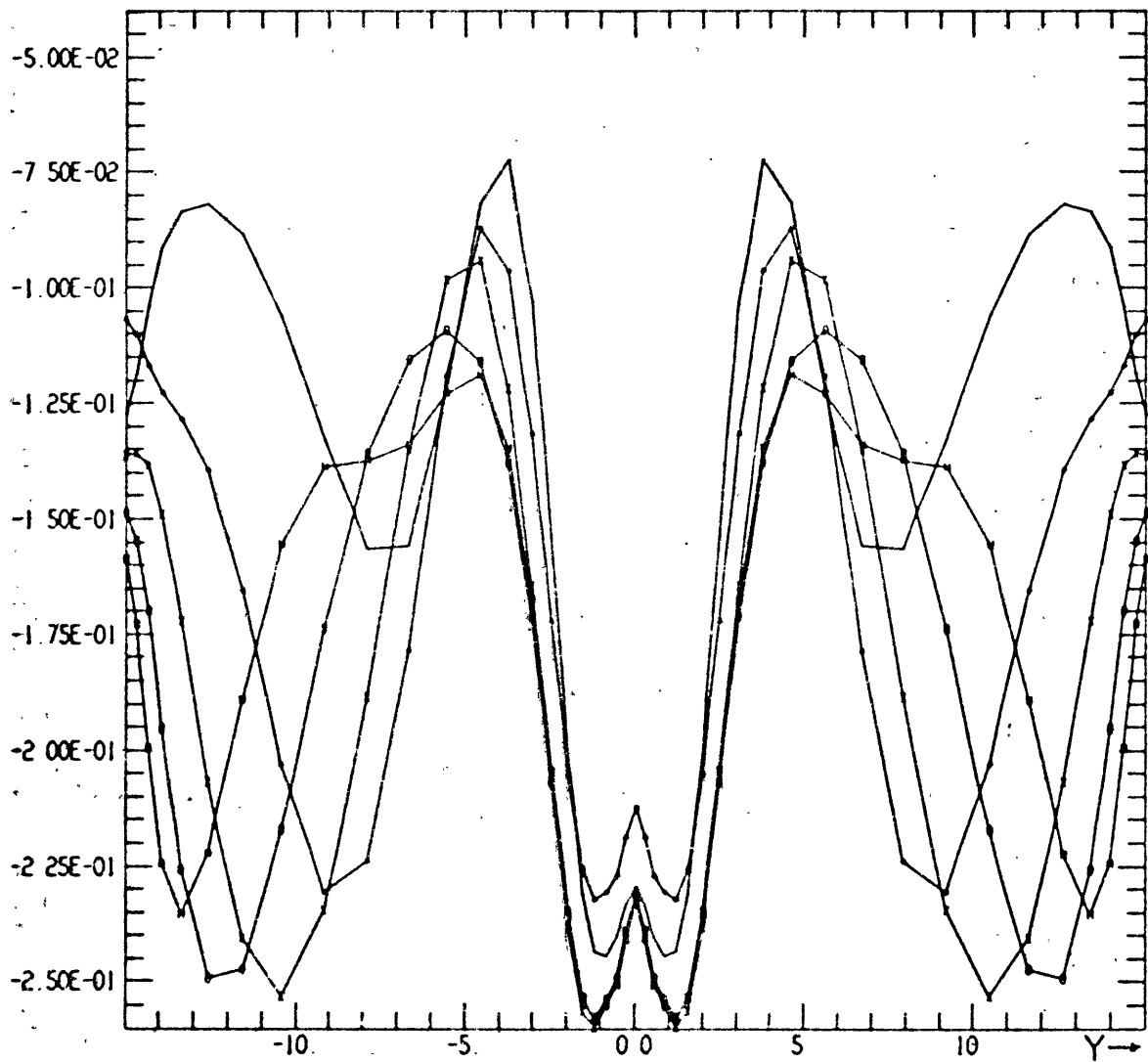
Fig. 5.54a Meridional sections of h to day 398 at $x=25.4^\circ$.
 Nonlinear. West wind.



T- 79.58 DAYS -T- 159.16 DAYS +T- 238.73 DAYS
 oT- 318.31 DAYS -T- 397.89 DAYS
 LAYER DEPTH FOR X=14.3 Y=-15.0 TO 15.0 T= 79.58 TO 397.89 DAYS
 NZEIR N4CH3 30X44STR DELT= 5 E-1 E-8, BB-BI= .001 WIND=(1.5,0) EVERYWHERE.

07/23/18 5

Fig. 5.54b Meridional sections of h to day 398 at $x=14.3^\circ$.
 Nonlinear. West wind.



T- 79.58 DAYS -T- 159.16 DAYS T- 238.73 DAYS
 t- 318.31 DAYS t- 397.89 DAYS
 LAYER DEPTH FOR X- 3.2 Y-15.0 TO 15.0 T- 79.58 TO 397.89 DAYS
 NZEIR NACH3 30X44STR DELT- .5 E-1 E-8, BB-B1- .001 WIND-1 5.0) EVERYWHERE. 07/23/18 53

Fig. 5.54c Meridional sections of h to day 398 at $x=3.2^\circ$.
 Nonlinear. West wind.

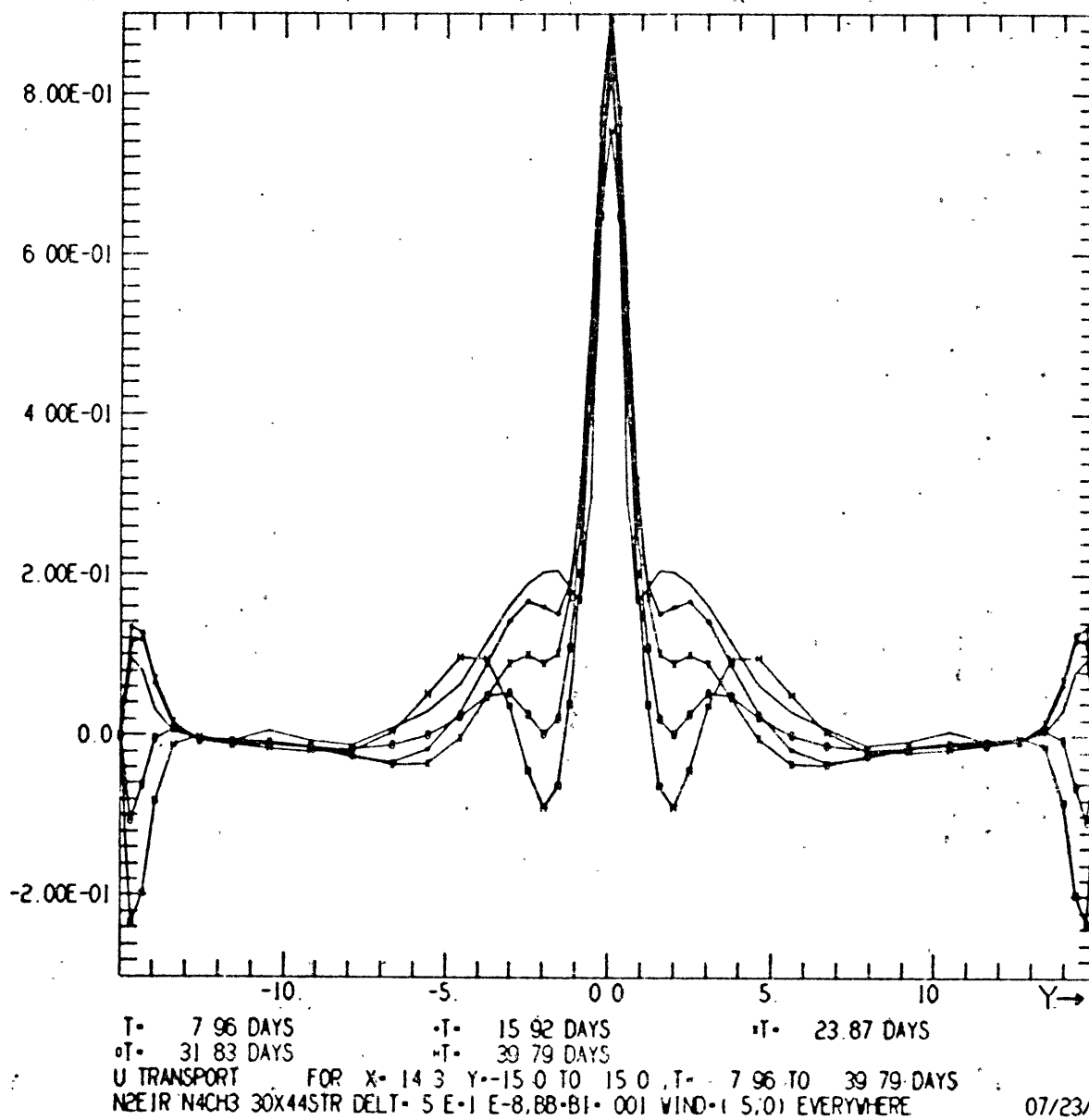


Fig. 5.55 Meridional sections of \bar{u} to day 40 at $x=14.3^\circ$.
Nonlinear, West wind.

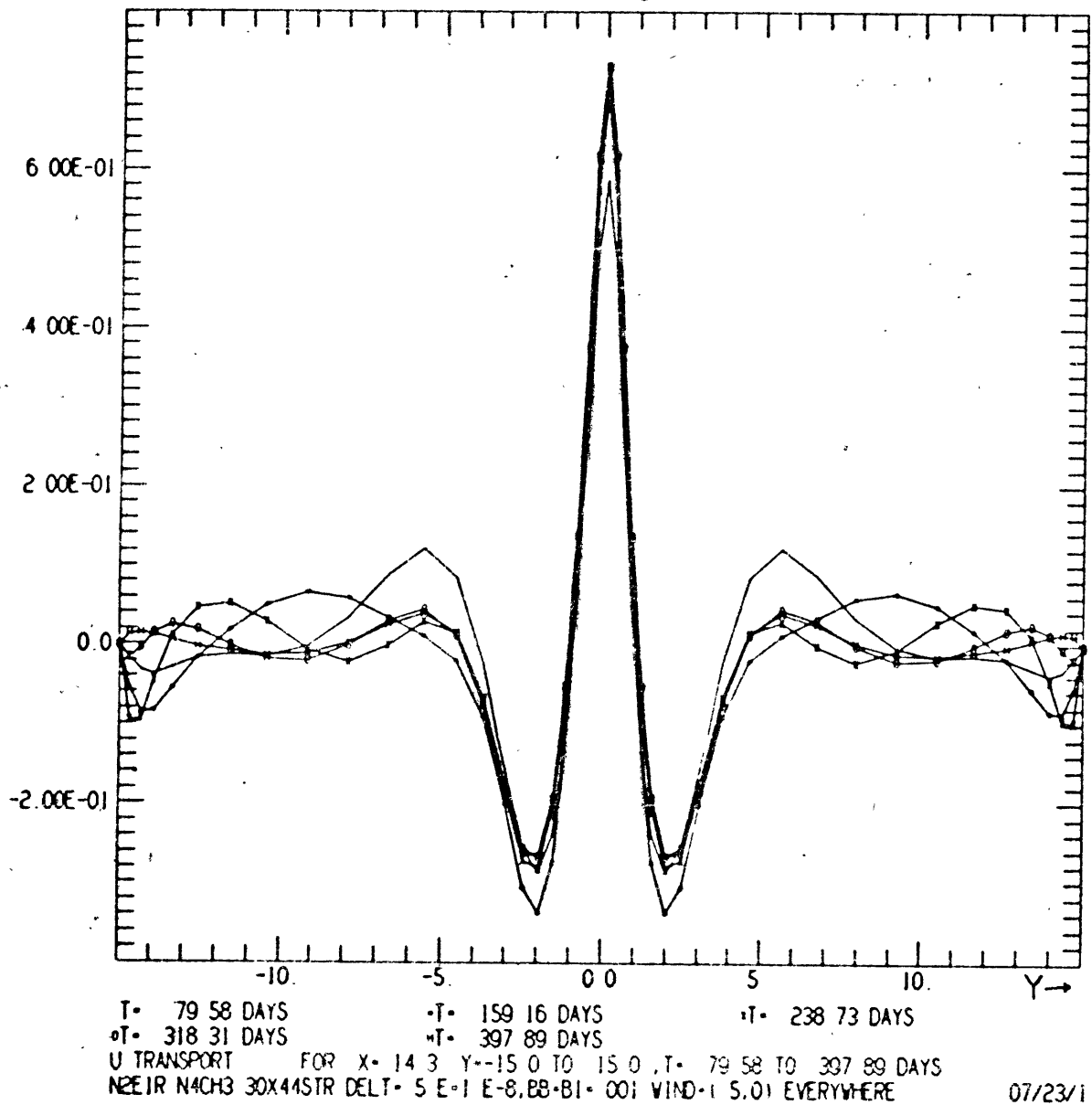


Fig. 5.56 Meridional sections of \bar{u} to day 398 at $x=14.3^\circ$.
Nonlinear. West wind.

The meridional components of the lower layer velocities near the equator are poleward so that the vertically integrated meridional transport is small. Contours of the layer depth h at 16 days reveal a pattern that is familiar from the other zonal wind cases. Most of the variation from the initial state occurs near the equator and along the eastern and zonal boundaries. Since the more equatorially confined Rossby waves propagate most rapidly the sloping region at the eastern side is broadest near the equator. At that side the poleward travelling coastal Kelvin waves have already reached the northern and southern walls and turned the corners there. The layer depths at the western ends of the zonal walls have decreased in order to geostrophically balance the eastward currents along these boundaries. The coastal Kelvin waves have westward group velocity; they have turned the corners at the western end of the zonal boundaries. At the equator h bows up in order to geostrophically balance the zonal current in the lower layer. This is similar to the east wind pattern (Fig. 5.47c). At the western end of the equator the currents are poleward in both layers in order to supply water to the eastward jet along the equator. At the eastern end the surface layer flow is still equatorial (in the wind drift direction) but the currents in the lower layer are poleward so that the vertically integrated transport at the eastern side is poleward.

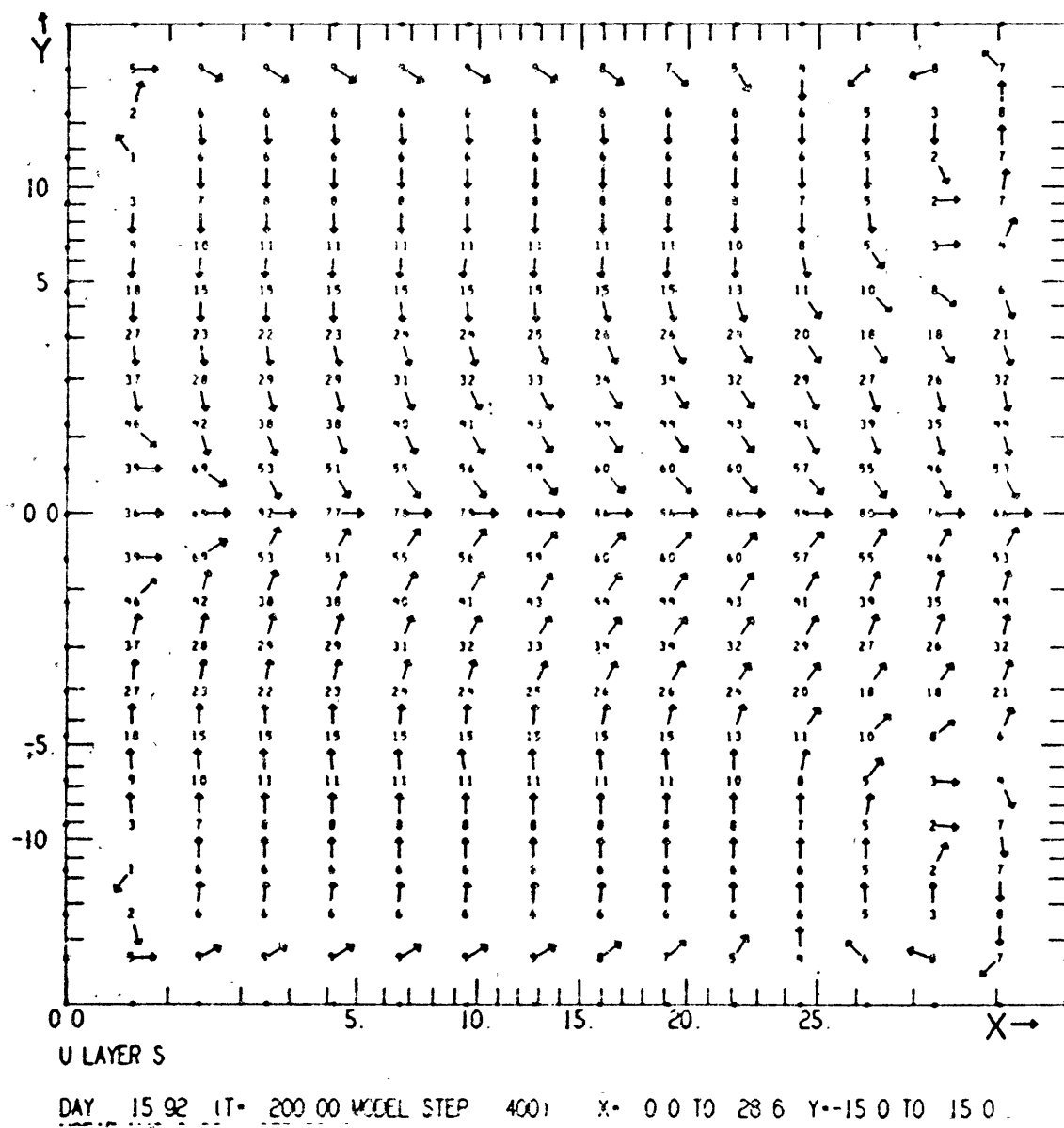
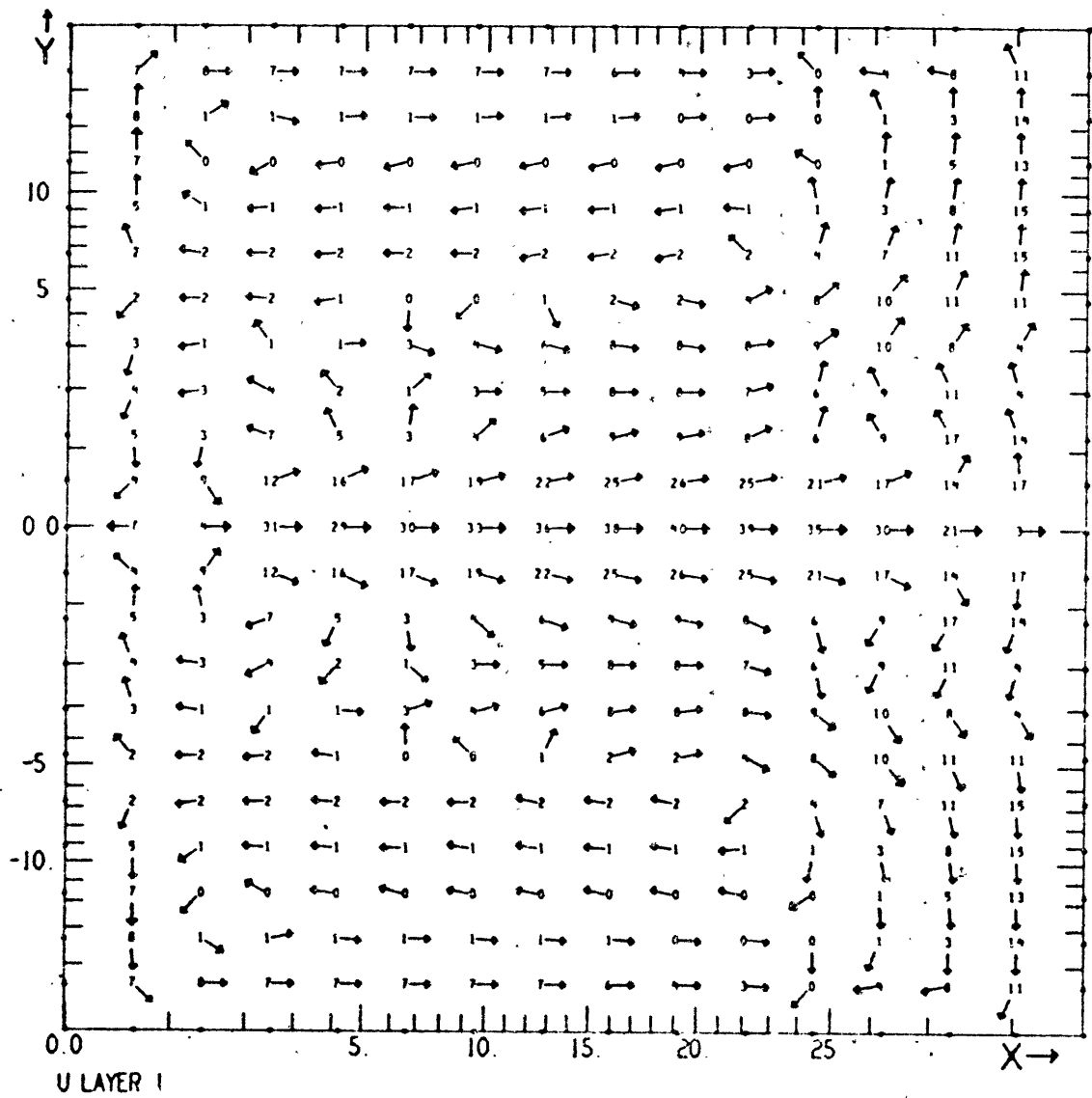


Fig. 5.57a u^S vectors at 16 days. Nonlinear. West wind.



DAY 15 92 IT= 200 00 MODEL STEP 400) X= 0 0 TO 28 6 Y=-15 0 TO 15 0
 NZE1R N4CH3 30X44STR DELT= 5 E-1 E-8,BB-BI= 001 WIND=(5,0) EVERYWHERE 07/23/18 5.

Fig. 5.57b \underline{u}^1 vectors at 16 days. Nonlinear. West wind.

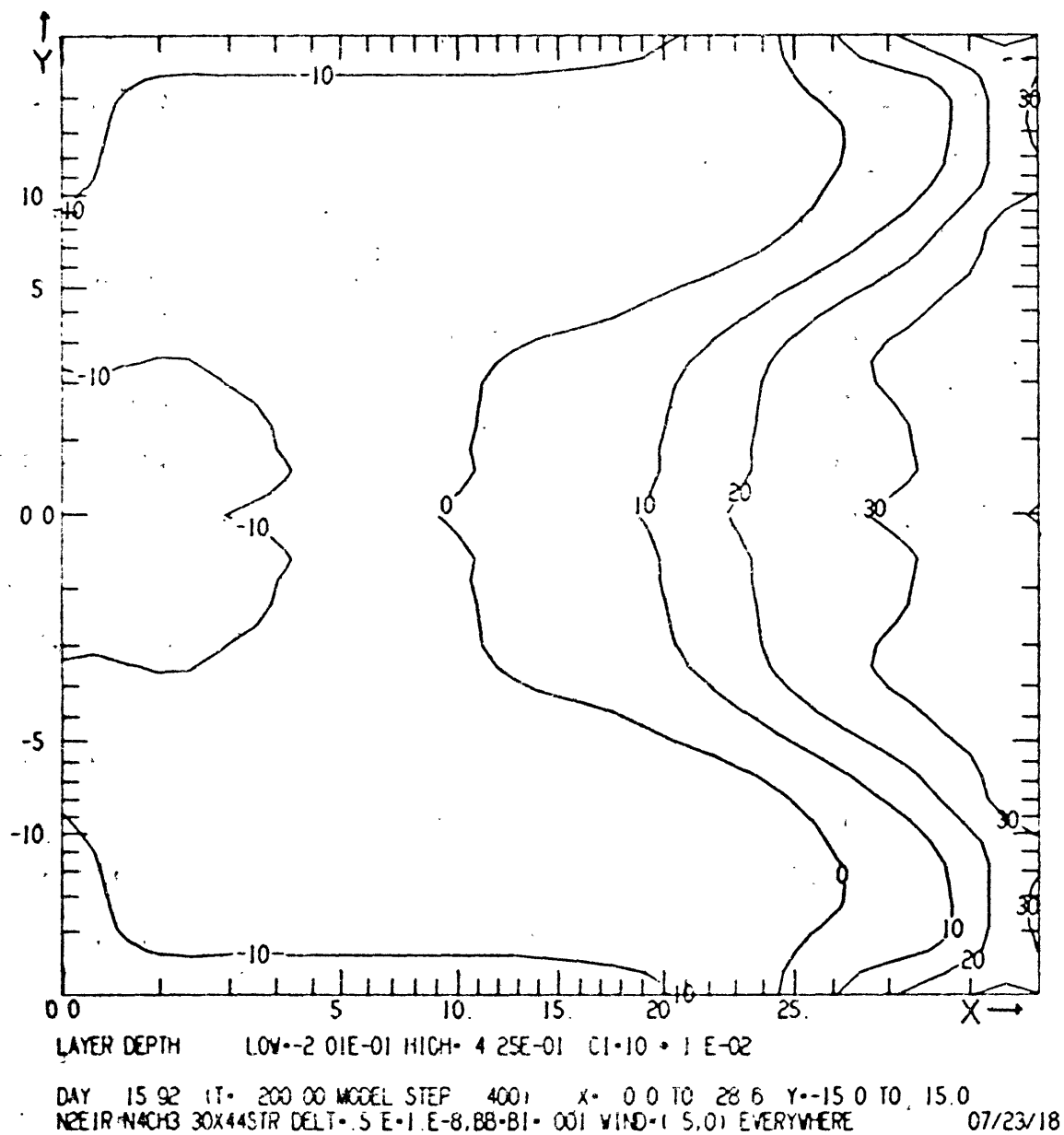
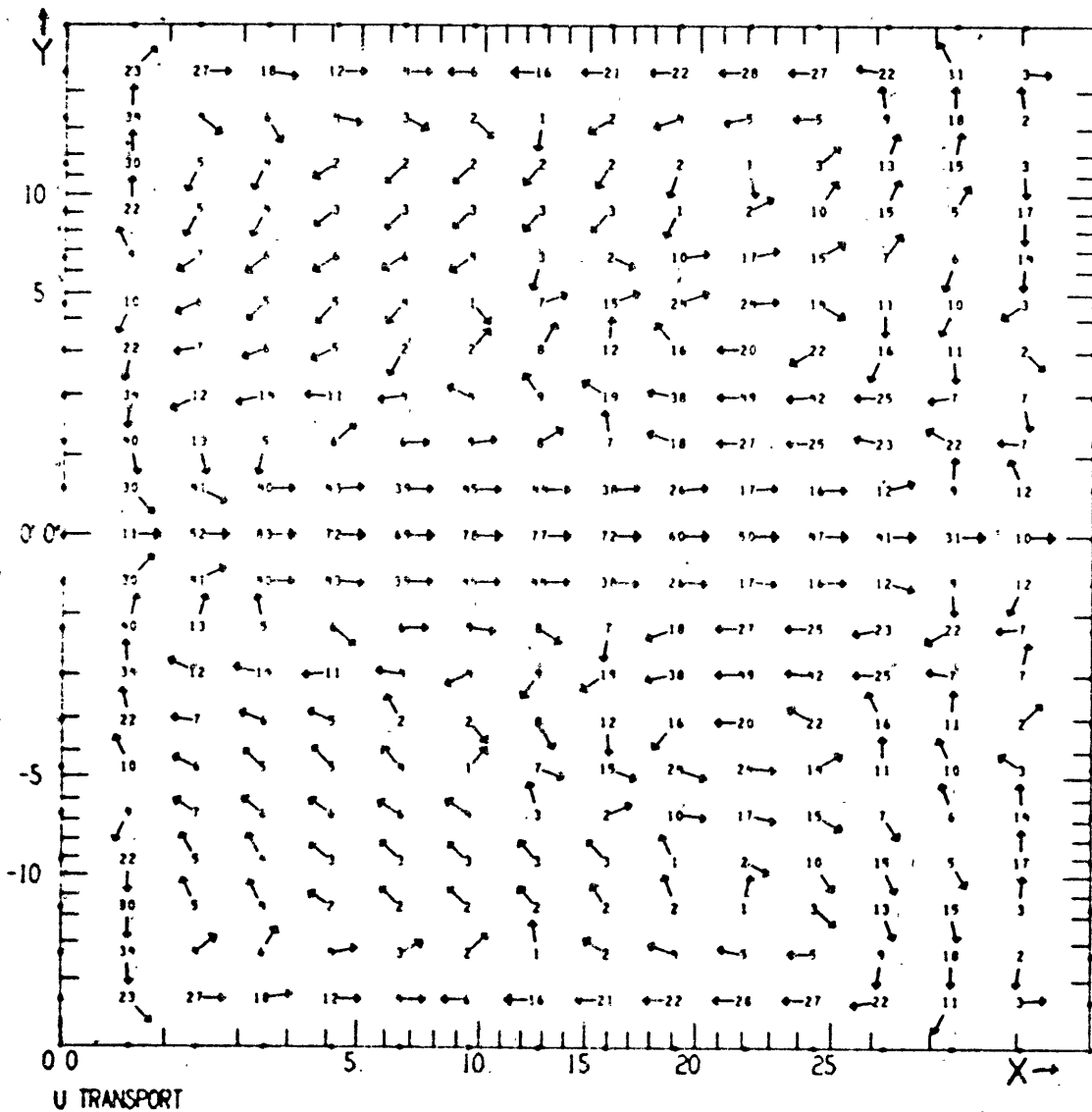


Fig. 5.57c h contours at 16 days. Nonlinear. West wind.

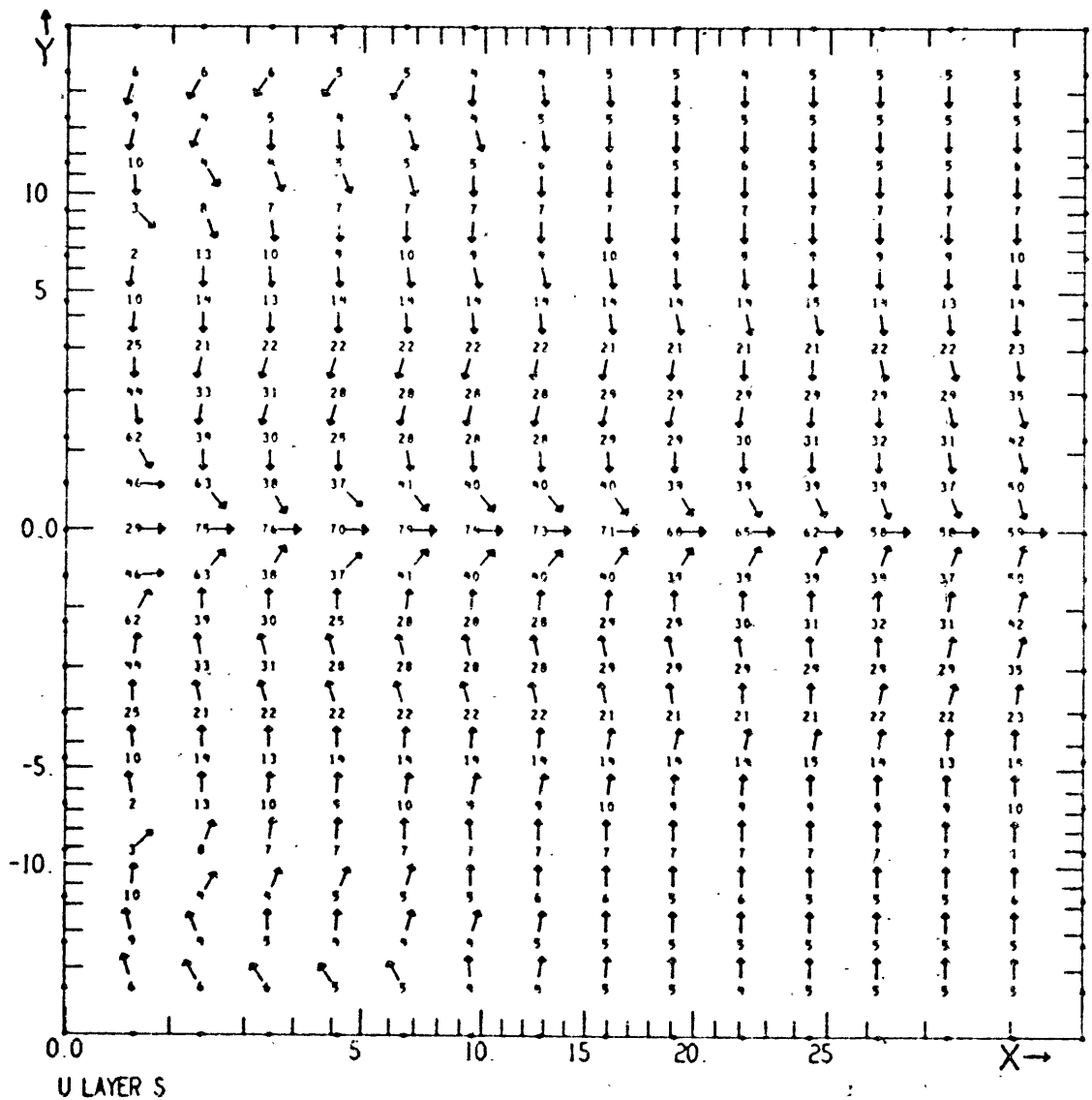
The circulation at 40 days is not very different than it was at 16 days. The gradients of h are generally greater, especially at the eastern end of the equator (cf., Fig. 5.50). The major difference from the earlier time is that the lower layer currents now have a westward component poleward of 1° from the equator. The vertically integrated transport at those latitudes is now westward (Fig. 5.58).

By day 398 (Figs. 5.59a, b, c, d) a steady state is closely approximated everywhere in the model basin with the exception of the northwest and southwest corners. The surface layer currents are very much as they were at day 16; they are largely determined by the wind drift interfacial friction solution (3.12), except that inertial effects become important within a few degrees of the equator (cf., Section 5.5). In the lower layer there is an eastward jet at the equator with a half width of 1° . The water transported eastward at the equator in both layers is returned to the west in lower layer currents extending from about 1° to about 4° on both sides of the equator. There is very strong downwelling at the eastern end of the equator in order to transport the upper layer water into the lower layer so that it may return to the west. Both the equatorial jet and the westward countercurrents broaden and strengthen from east to west so that the zonal transports at the equator decrease downstream. (The exception to this is a feature of the western boundary layer. The zonal currents in



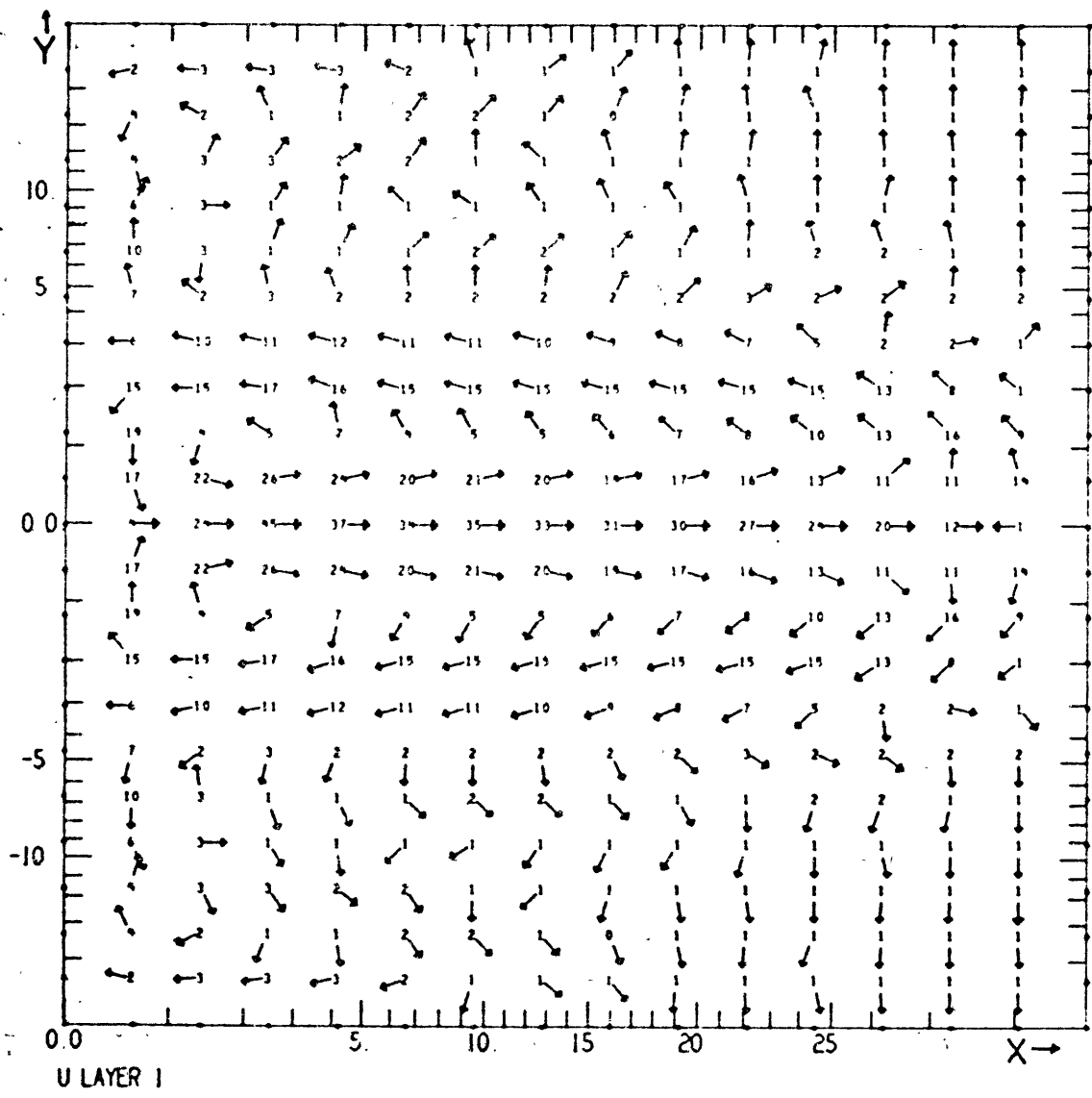
DAY 39 79 (T= 500 00 MODEL STEP 1000) X= 0 0 TO 28 6 Y=-15 0 TO 15 0
 NCEIR N4CH3 30X44STR DELT= 5 E-1 E-8.88-81= 001 WIND=(5,0) EVERYWHERE 07/23/18 5

Fig. 5.58 \bar{u} vectors at 40 days. Nonlinear. West wind.



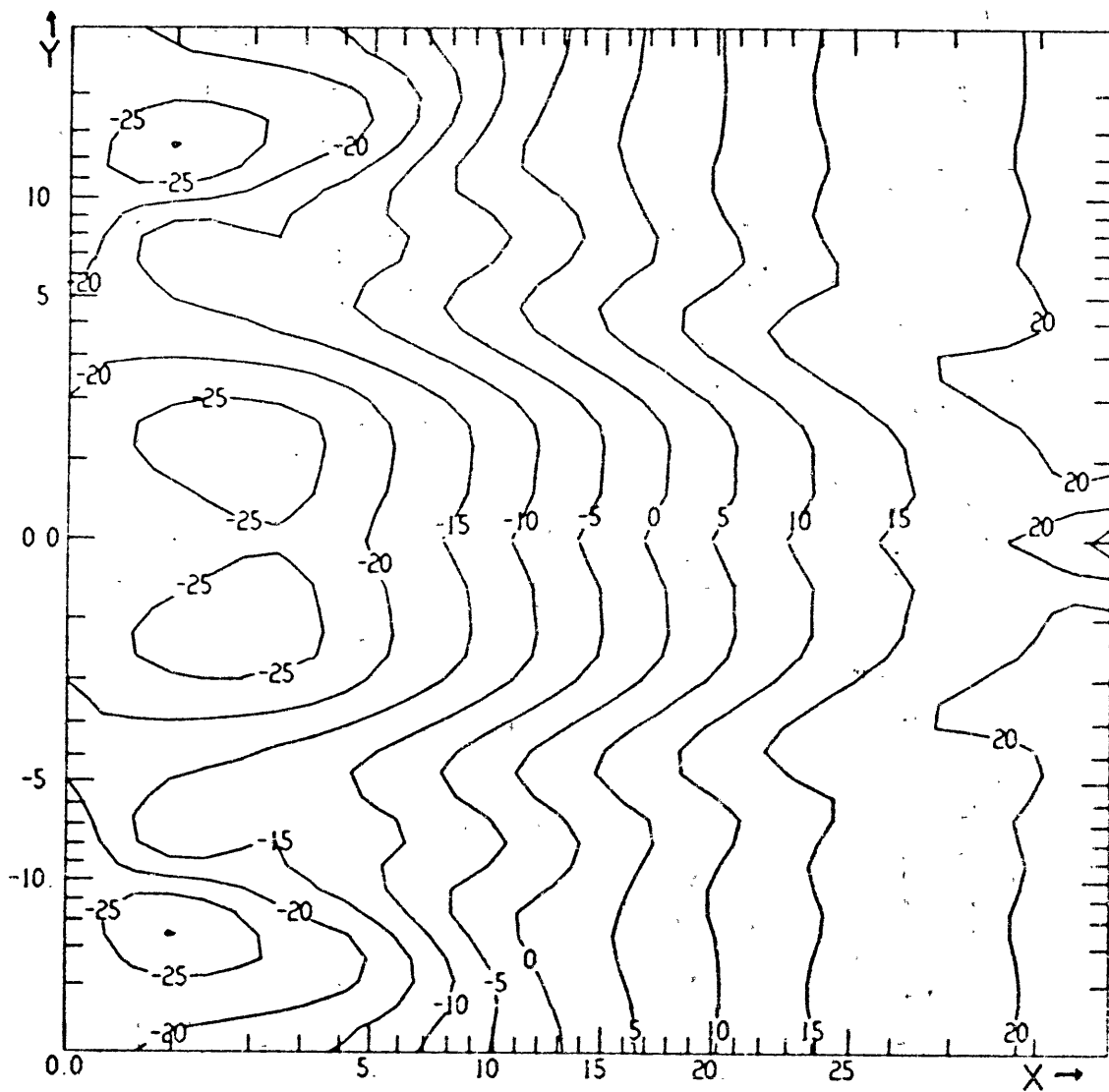
U LAYER S
 DAY 397 89 (T= 5000 00 MODEL STEP 10000) X= 0.0 TO 28.6 Y=-15.0 TO 15.0
 NZEIR N4CH3 30X44STR DELT= .5 E-1. E-8. BB-B1= .001 WIND=(5.0) EVERYWHERE 07/23/18

Fig. 5.59a u^S vectors at 398 days. Nonlinear. West wind.



DAY 397 89 (T= 5000 00 MODEL STEP 10000) X= 0 0 TO 28 6 Y=-15 0 TO 15 0
 NZEIR N4CH3 30X44STR DELT= 5 E-1 E=6.88-B1= 001 WIND=(5,0) EVERYWHERE 07/25/15 3

Fig. 5.59b u^1 vectors at 398 days. Nonlinear. West wind.

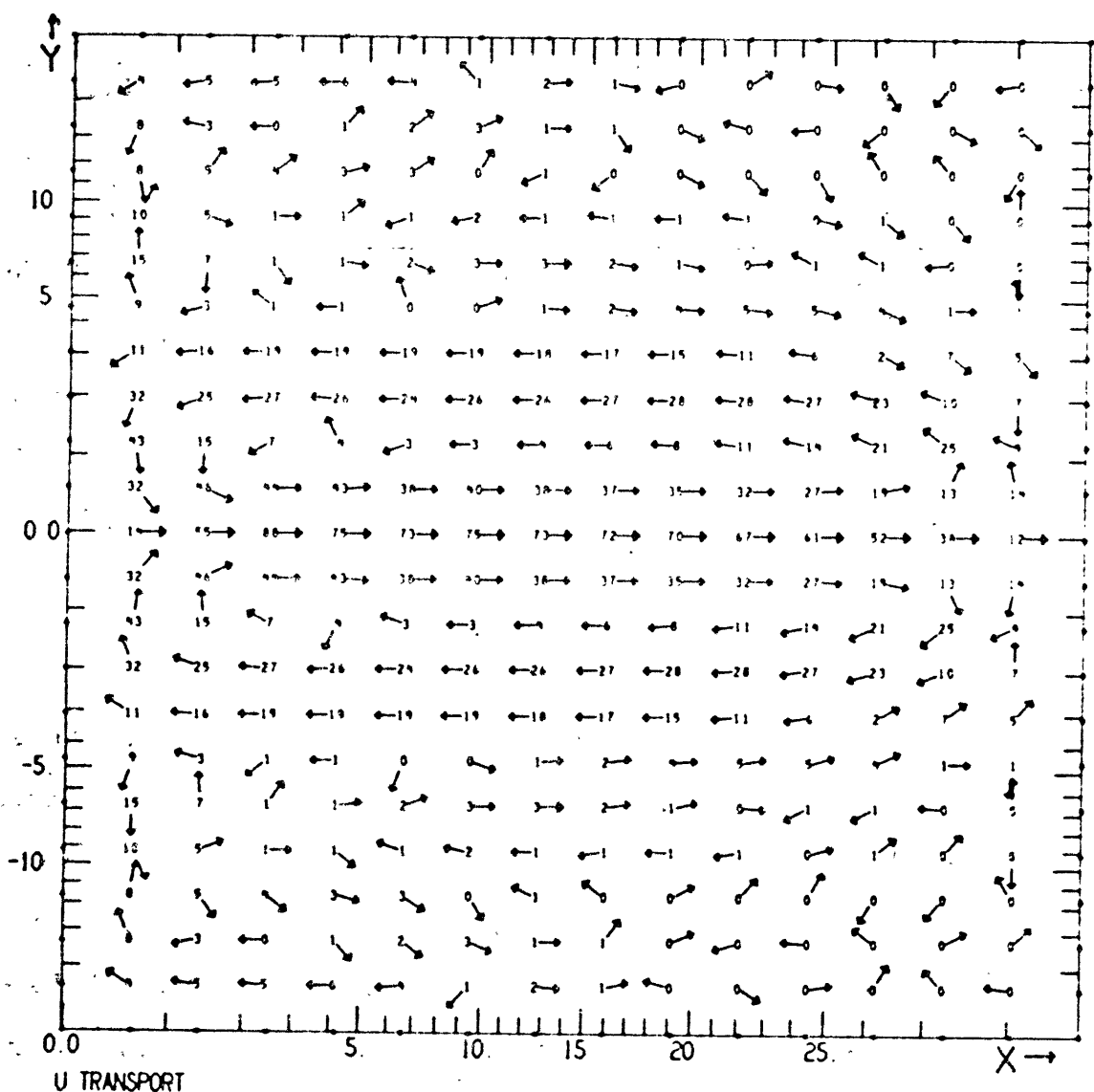


LAYER DEPTH LOW=-3.02E-01 HIGH= 2.87E-01 CI= 5.01E-02

DAY 397 89 IT= 5000 CO MODEL STEP 10000 X= 0.0 TO 28.6 Y=-15.0 TO 15.0
 N2E1R N4CH3 30X44STR DELT= 5.E-1.E-8.88.B1= 001 WIND=1 5.01 EVERYWHERE

07/23/18 !

Fig. 5.59c h contours at 398 days. Nonlinear. West wind.



DAY 397 89 (T= 5000 00 MODEL STEP 10000) X= 0.0 TO 28.6 Y=-15.0 TO 15.0
 NZEIR N4CH3 30X44STR DELT= 5 E=1.E-8,BB=81.001 WIND=(5.0) EVERYWHERE 07/23/18.

Fig. 5.59d \bar{u} vectors at 398 days. Nonlinear. West wind.

both layers reach a maximum at 2.5° from the western wall.

There is a secondary maximum 7° from the wall; east of this point the amplitude of the currents decreases monotonically.)

The arguments centered on Eq. (5.18) may be applied to the west wind case to deduce that the lower layer velocity will decrease from west to east and that the factor a in (5.17) will be positive; i.e., the zonal pressure gradient will be more negative than is required to balance the wind stress. A final noteworthy feature of the flow generated in response to a west wind is the absence of any instability during the course of its evolution.

5.7 Nonlinear Response to a Uniform Southeast Wind

In this case the initial state is taken to be the steady state circulation which came about in response to a uniform easterly wind. This state was described in Section 5.5. (To be precise the initial state is taken as the state which resulted after 384 days; equatorward of 10° it is indistinguishable from the one at day 398 depicted in Fig. 5.47.) At $t=0$ a southerly wind component is added to the prevailing easterly component so that each wind component is $.465 \text{ dynes cm}^{-2}$. This case is intended to be a very crude analogue of the southeast monsoon that occurs in the Atlantic in the late Spring. The linear response to a southeast wind is simply a superposition of the linear responses to a southwind and to an east wind. The nonlinear response is not related to the responses to a south and an east wind in such

a simple way, though resemblances are to be expected.

Figs. 5.60 and 5.61 show the energies. They suggest that even after 400 days the model ocean has not reached a truly steady state, even in the equatorial region. (Other model output indicates that the increase in PE and KE_1 at these later times is due to a strengthening of the current at 4.5°N . See Fig. 5.65.) After day 80 the potential and upper layer kinetic energy do not vary greatly. The lower layer kinetic energy takes about twice as long to become approximately constant. In the equatorial region only the upper layer kinetic energy is substantially different from its value at $t = 0$.

Fig. 5.62 is a plot of contours of u^1 at the equator with time as the ordinate. This plot is similar to Fig. 5.13, which showed a regular progression of phase for the wave-like instability that arose in that south wind case. In the present case, in the time period from about day 25 to about day 175 there is some apparent phase propagation to the west. However, none of the lines of constant amplitude cross the basin, and after day 175 all such east to west movement ceases. The pattern of evolution resembles the way in which the mixed mode in the linear south wind case (Section 5.2) contracts toward the western boundary with time (due to its Bessel function behavior; cf. (4.27)). We will return to this point after considering the early evolution of the flow.

The two most prominent developments in the first 40 days

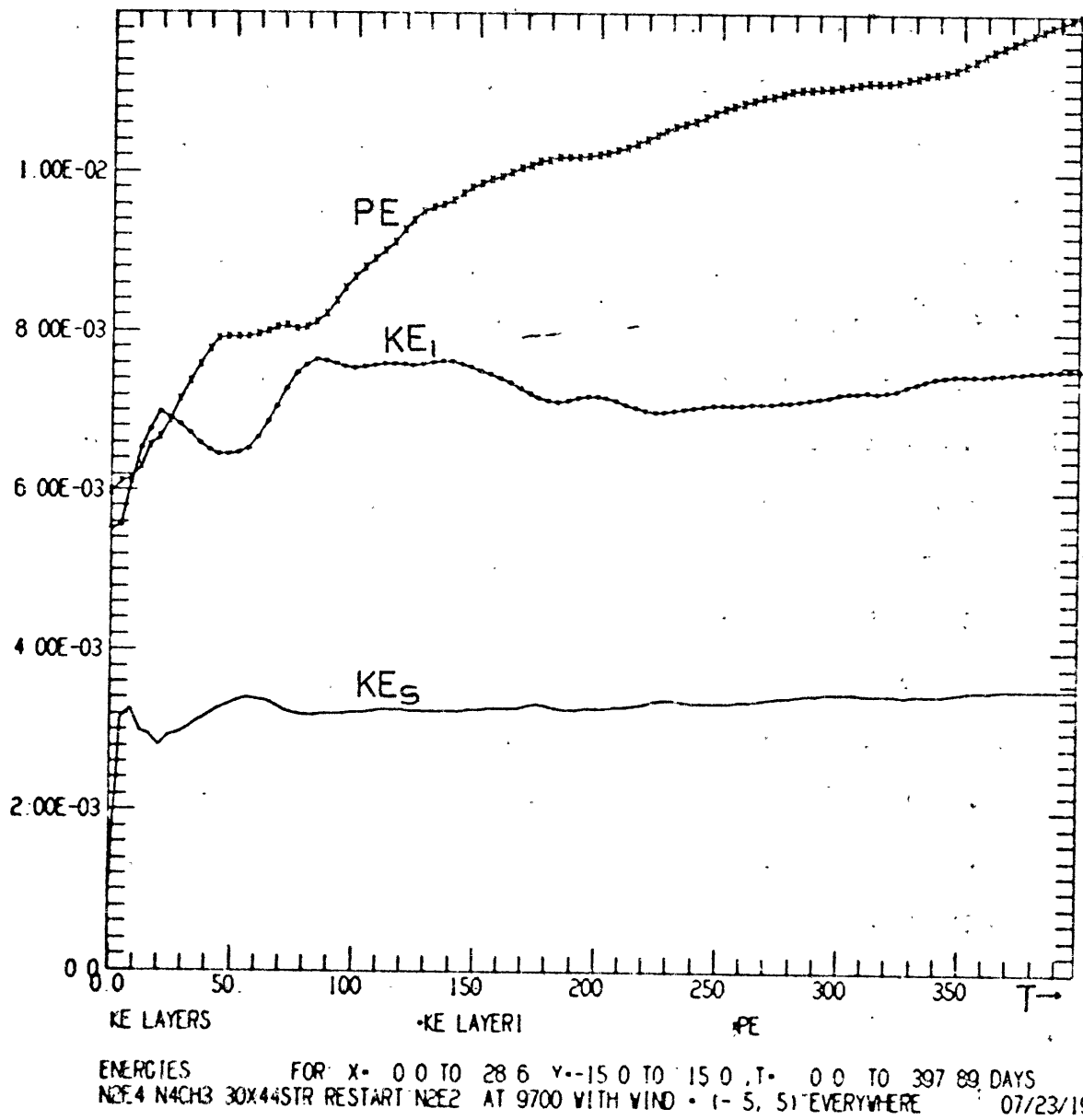
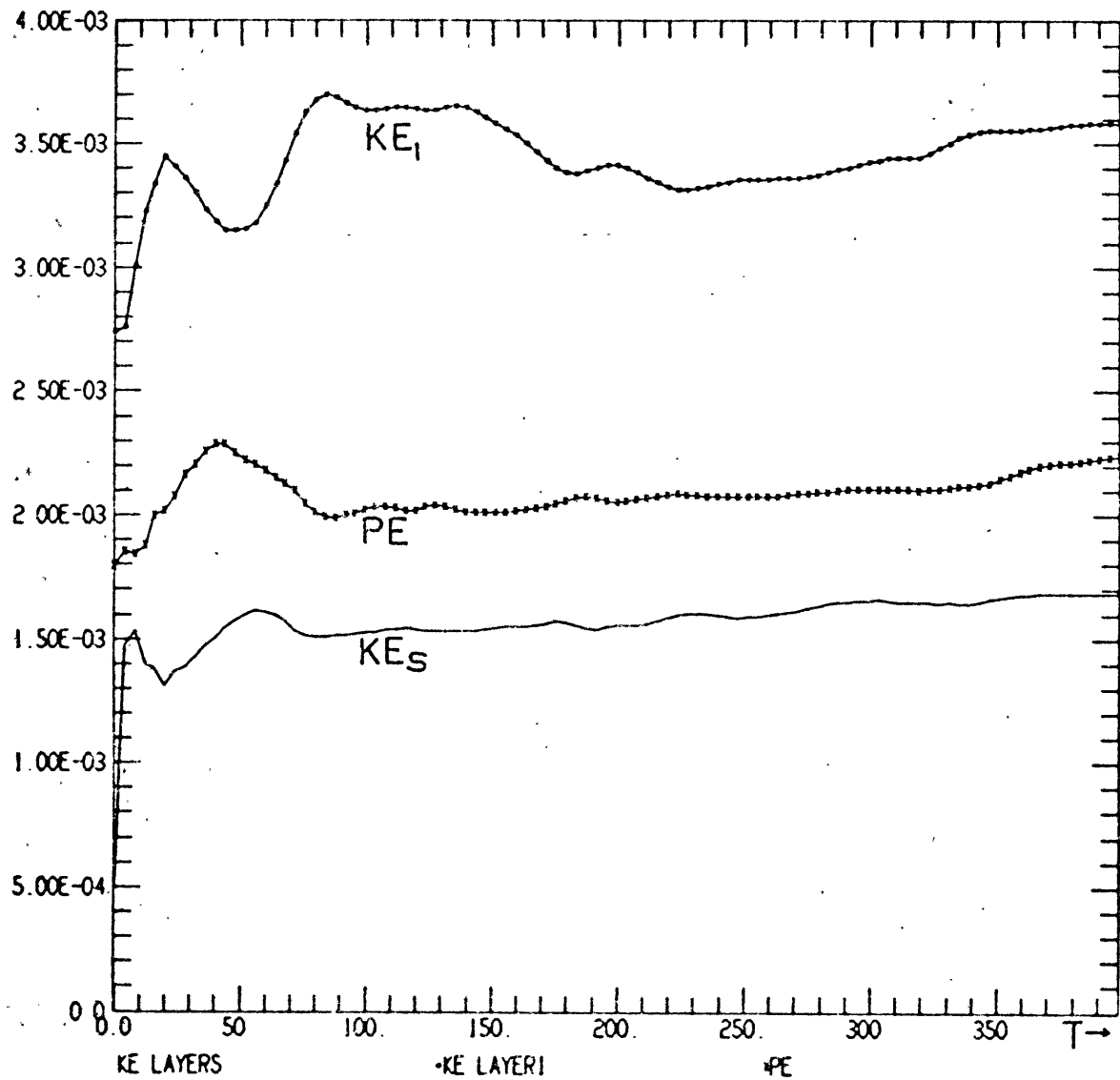
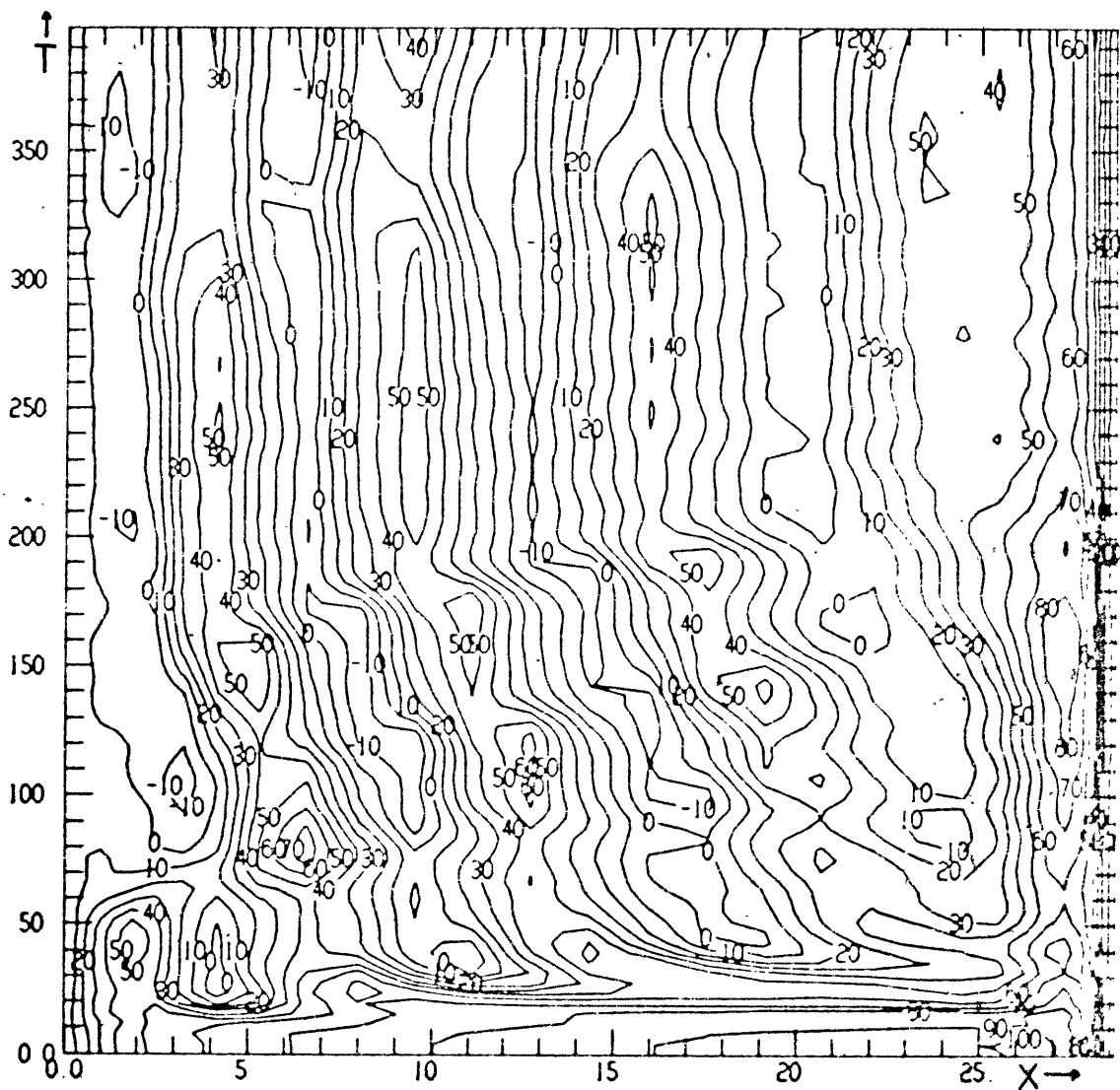


Fig. 5.60 Energies from 15°S to 15°N. Nonlinear. Southeast wind.



ENERGIES FOR X= 0.0 TO 28.6 Y= -5.6 TO 5.6 T= 0.0 TO 397.89 DAYS
 N2E4 N4CH3 30X44STR RESTART N2E2 AT 9700 WITH WIND = (-.5, .5) EVERYWHERE 07/23/19 1

Fig. 5.61. Energies from 5.6°S to 5.6°N. Nonlinear. Southeast wind.



U LAYER 1 LOW--1.93E-01 HIGH+ 1.02E 00 CI-10 • 1 E-02

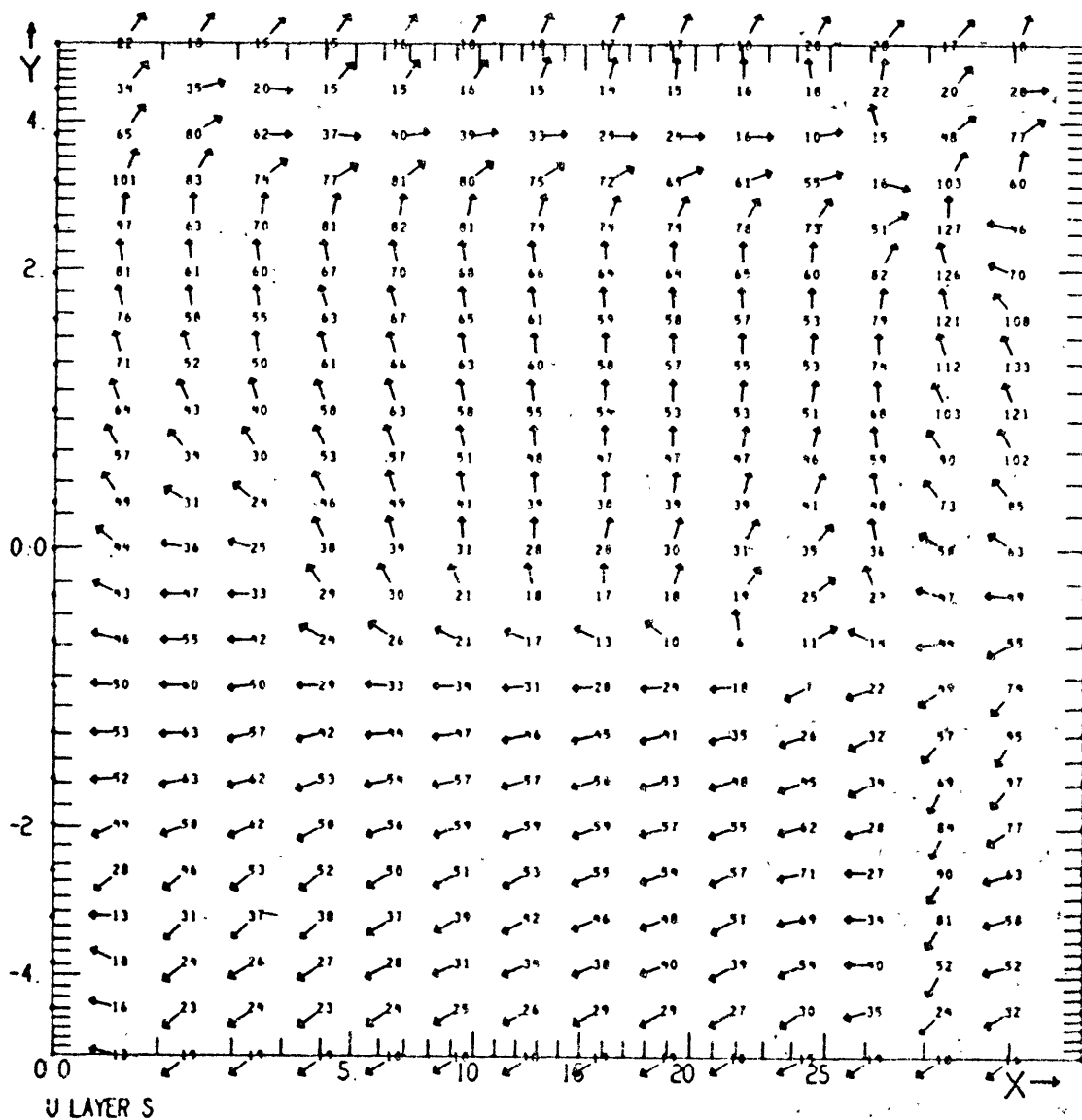
U LAYER 1 FOR Y- 0 0 X- 0 0 TO 28 6 .T- 0 0 TO 397 89 DAYS
 N2E4 N4CH3 30X44STR RESTART N2E2 AT 9700 WITH WIND : 1- 5, 51 EVERYWHERE

07/23/19 18

Fig. 5.62 u^1 contours at the equator to day 398. Nonlinear. Southeast wind.

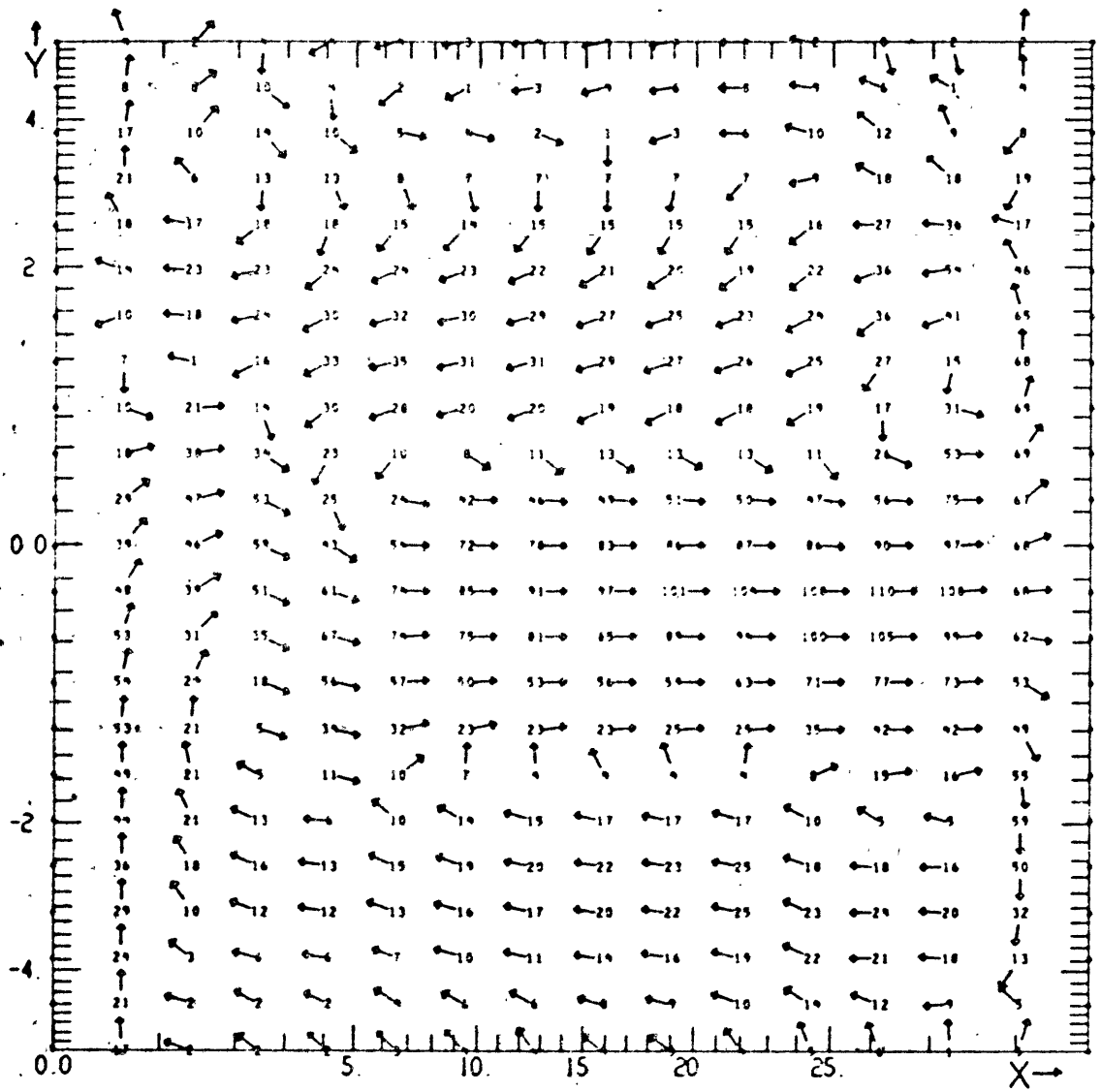
(Figs. 5.63 and 5.64) are the southward shift of the undercurrent and the development of an eastward current at between 3°N and 5°N . The southward shifting of the undercurrent is already evident at 8 days when the maximum zonal transport is at 0.3°S . At this time the surface winds near the equator are westward. This upwind shifting of the undercurrent in the presence of meridional winds has been found in earlier theoretical investigation (Robinson, 1966; Charney and Spiegel, 1971) and has been observed in the world's oceans (e.g., Taft and Knauss, 1967). An eastward flowing current centered at 3°N was the most prominent feature of the early response to a south wind, Section 5.3.

The surface flow at 16 days (Fig. 5.63a) strongly resembles that for the south wind case at 16 days (Fig. 5.16a). In the present case the eastward jet is a bit further northward (3.8°N instead of 3°N) and is weaker; the region of northward flow also starts further north (0.6°S instead of 2°S). The east wind influence shows most clearly in the poleward wind drift currents south of 1°S . The lower layer currents (Fig. 5.63b) show effects from both the south wind (cf., Fig. 5.16b) and the east wind (cf., Fig. 5.47b displaced south). The region of eastward flow centered at about $.5^{\circ}\text{S}$ is broader than is the case with either of the simpler wind systems. The flow at about 4° shows eastward currents induced by the southerly wind component appearing at the western side of the basin while the eastern side still shows the westward flow which returns the transport of the undercurrent



DAY 15 92 (T= 200.00 MODEL STEP 400) X= 0.0 TO 28.6 Y= -5.6 TO 5.6
 N2E4 N4CH3 30X44STR RESTART N2E2 AT 9700 WITH WIND = (- 5, 5) EVERYWHERE 07/23/19 1

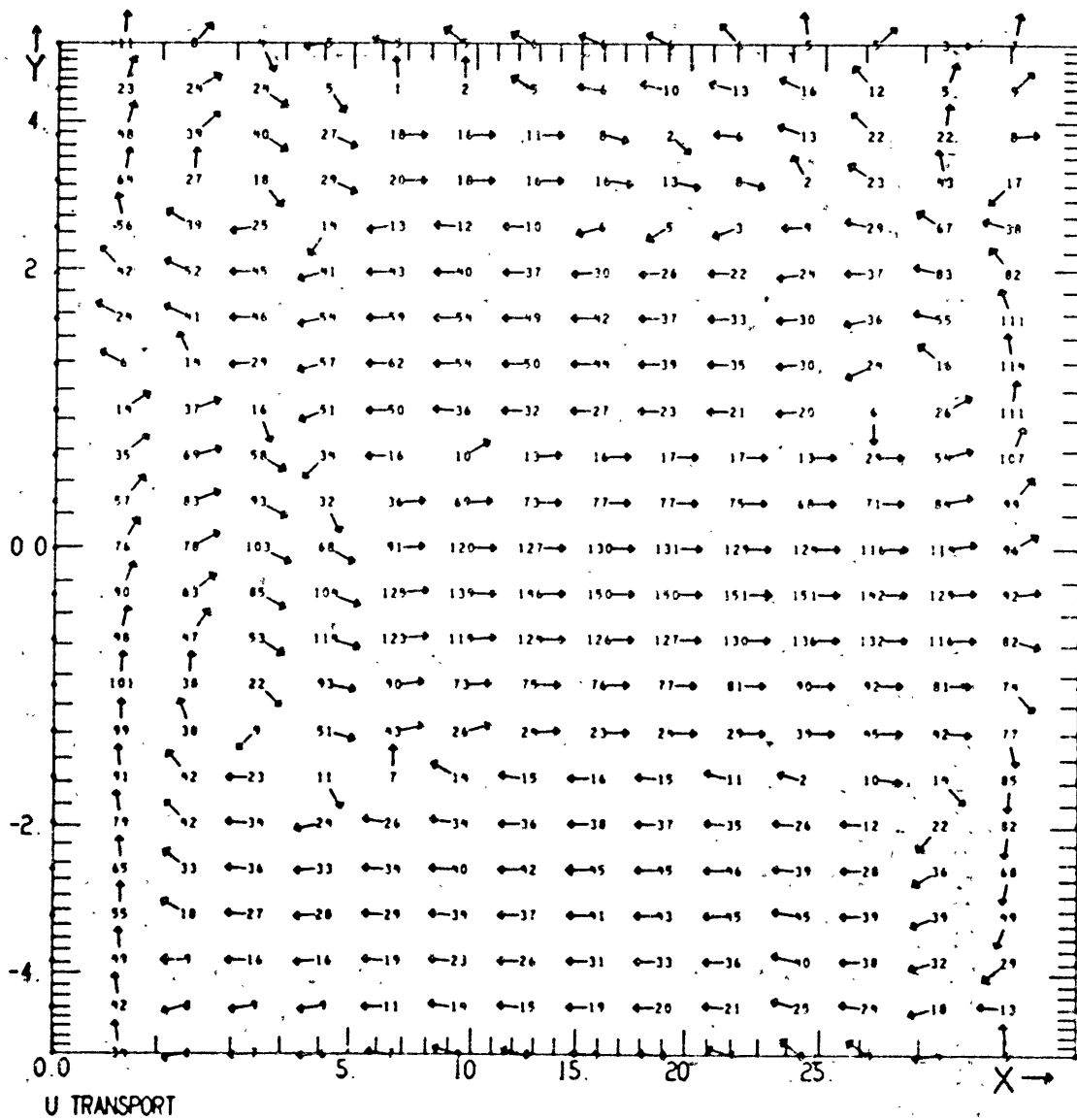
Fig. 5.63a u^S vectors at 16 days. Nonlinear. Southeast wind.



U LAYER 1

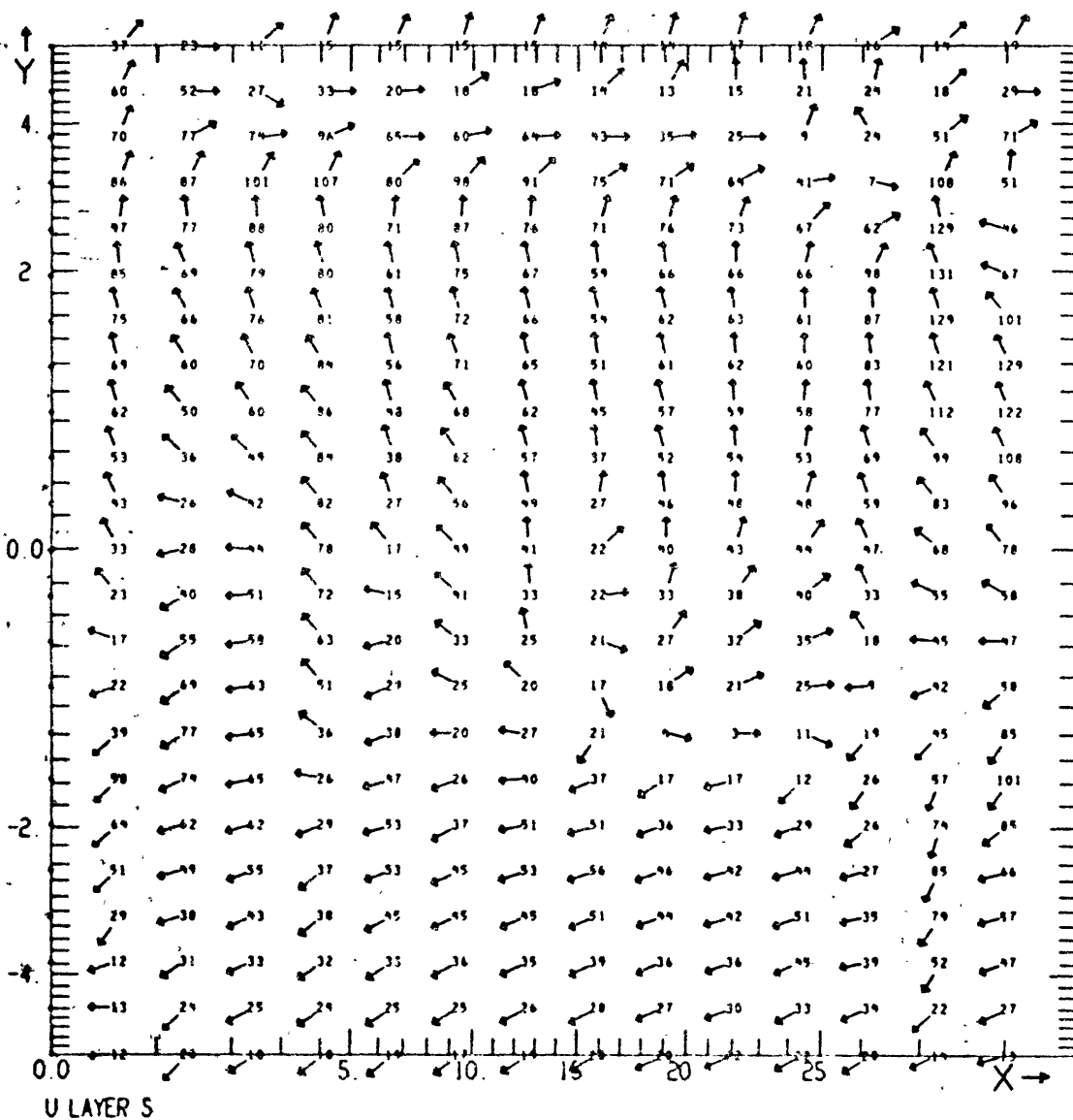
DAY 15.92 (T= 200.00 MODEL STEP 400) X= 0.0 TO 28.6 Y= -5.6 TO 5.6
 N2E4 N4CH3 30X44STR RESTART N2E2 AT 9700 WITH WIND = (- 5, 5) EVERYWHERE 07/23/19 18

Fig. 5.63b u^1 vectors at 16 days. Nonlinear. Southeast wind.



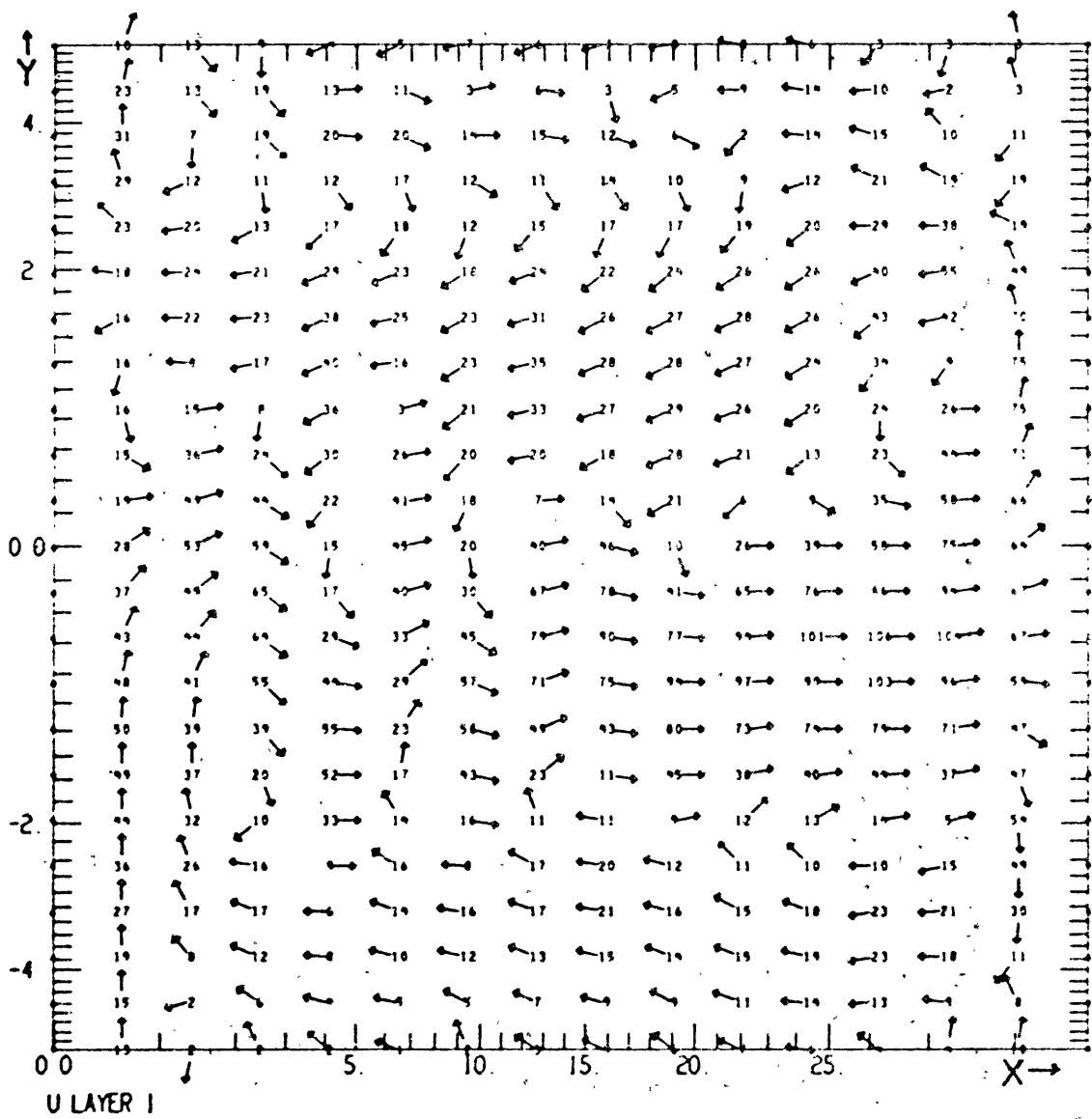
DAY 15 92 (T= 200.00 MODEL STEP 400) X= 0.0 TO 28.6 Y= -5.6 TO 5.6
 N2E4 N4CH3 30X44STR RESTART N2E2 AT 9700 WITH WIND = (-5, 5) EVERYWHERE 07/23/19

Fig. 5.63c \bar{u} vectors at 16 days. Nonlinear. Southeast wind.



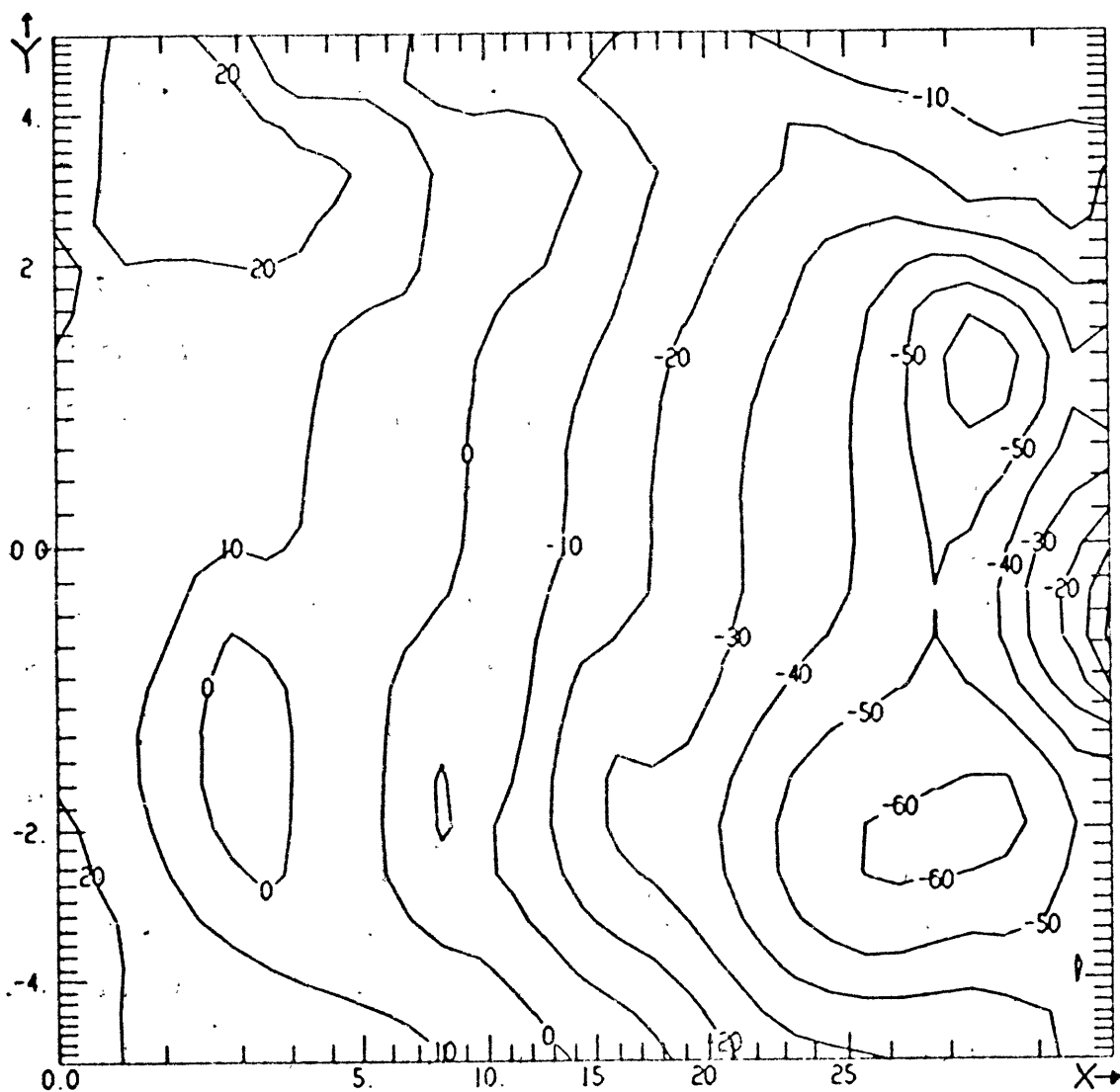
DAY 39.79 (T= 500.00 MODEL STEP 1000) X= 0.0 TO 28.6 Y= -5.6 TO 5.6
 N2E4 N4CH3 30X44STR RESTART N2E2 AT 9700 WITH WIND = (- 5, 5) EVERYWHERE 07/23/19 18

Fig. 5.64a u^s vectors at 40 days. Nonlinear. Southeast wind.



DAY 39.79 (T= 500 00 MODEL STEP 1000) X= 0 0 TO 28 6 Y= -5 6 TO 5 6
 N2E4 N4CH3 30X44STR RESTART N2E2 AT 9700 WITH WIND = (-5, 5) EVERYWHERE 07/23/19

Fig. 5.64b \vec{u}^1 vectors at 40 days. Nonlinear. Southeast wind.



LAYER DEPTH LOY=-6.59E-01 HIGH= 2.82E-01 CI=10.01E-02

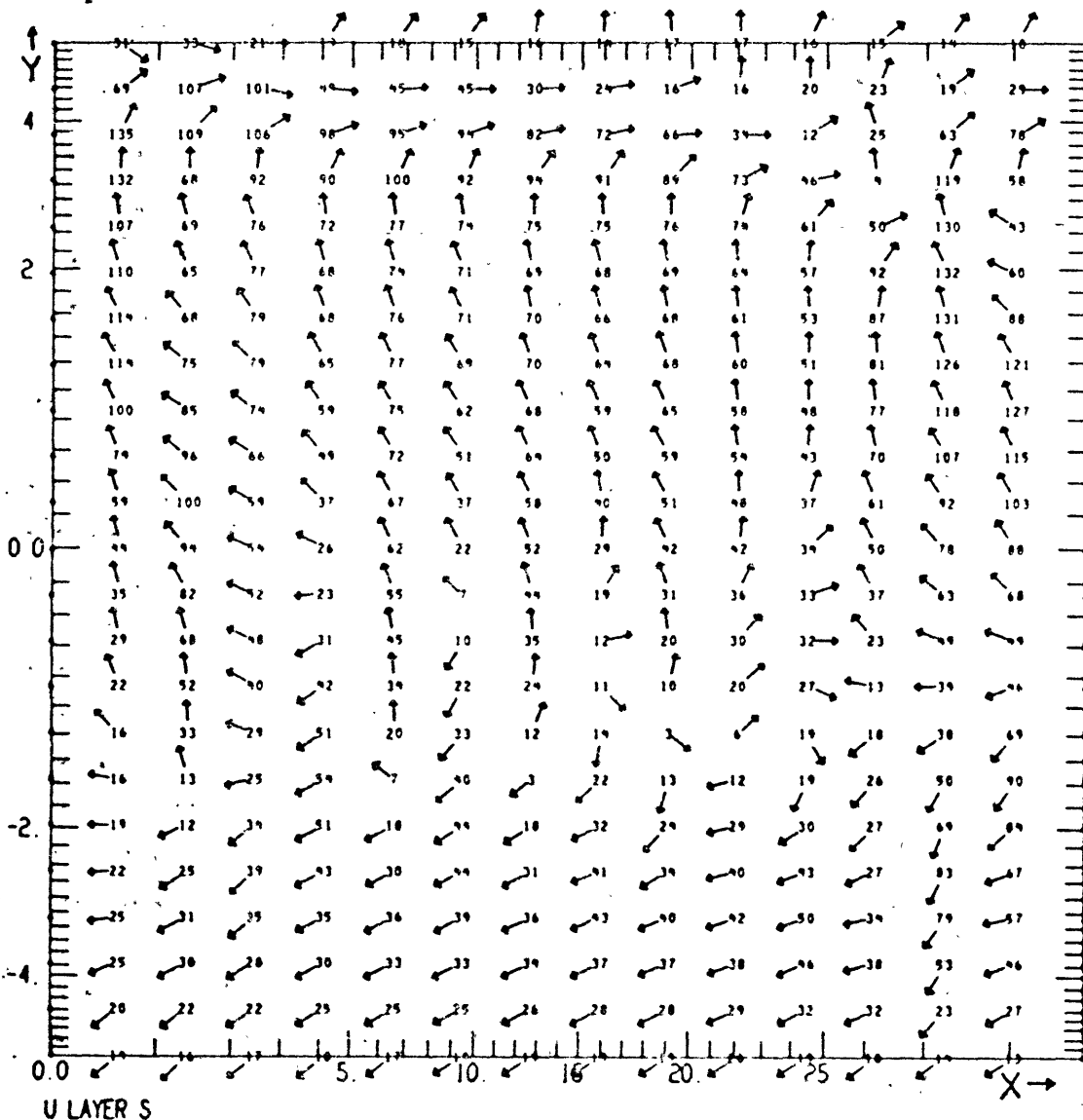
DAY= 39.79 (T= 500.00 MODEL STEP, 1000) X= 0.0 TO 28.6 Y= -5.6 TO 5.6
 N2E4 N4CH3 30X44STR RESTART N2E2 AT 9700 WITH WIND = (-5, 5) EVERYWHERE 07/28/24

Fig. 5.64c h contours at 40 days. Nonlinear. Southeast wind.

to the west. Comparison of Fig. 5.63c with Fig. 5.47d shows how the transports have been altered after 16 days.

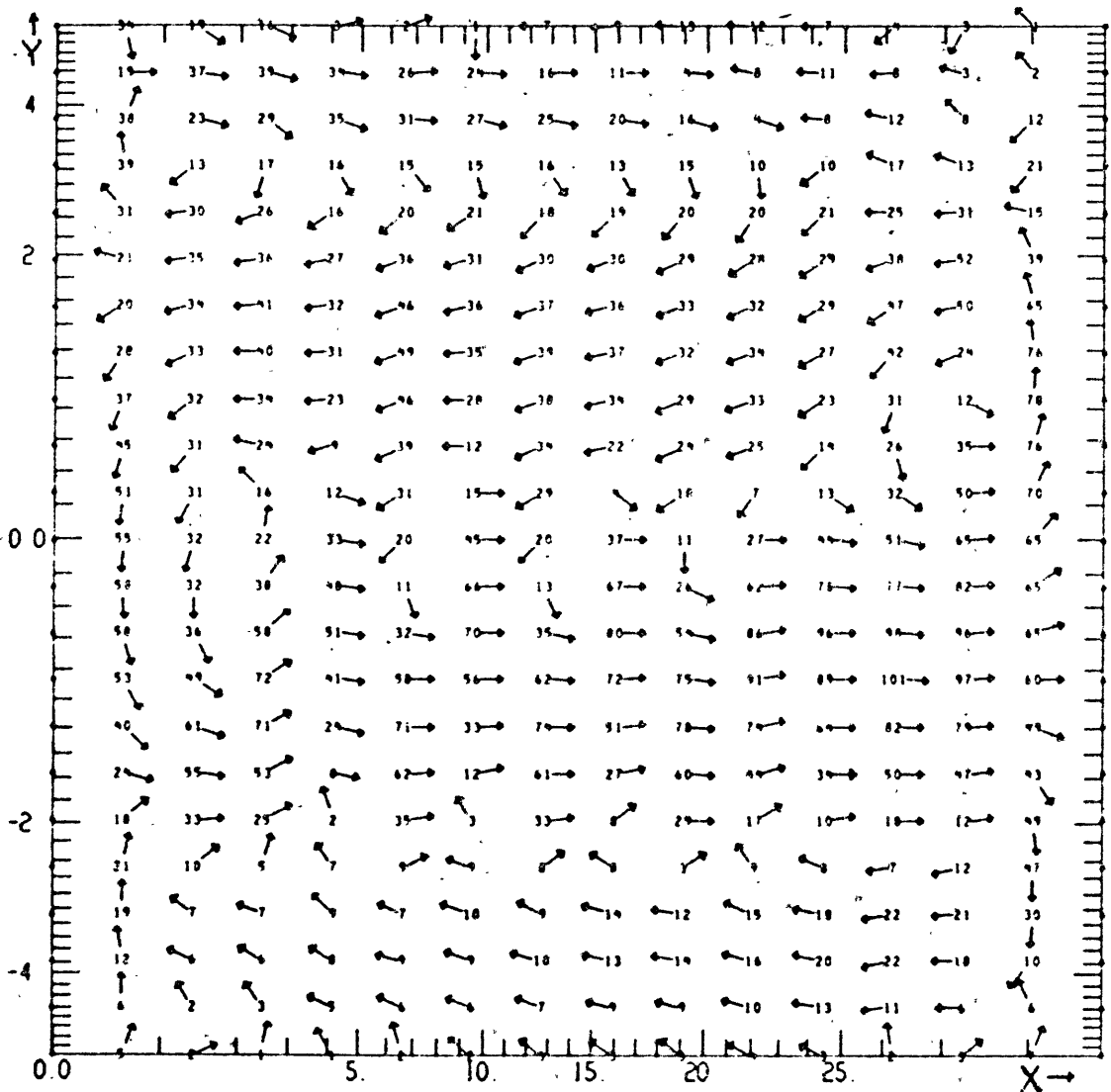
Fig. 5.64a shows that at day 40 the eastward jet in the surface layer, now at 4°N , is about twice as fast as it was at day 16. The other major change in the surface flow over this time period is the waviness from about 0° to 1°S . Note the area of eastward flow in the eastern side of the basin. The lower layer flow (Fig. 5.64b) shows greater changes. The eastward currents at 4°N are stronger and have greater longitudinal extent, so that the flow from 0° to 5°N resembles the south wind case (Fig. 5.18b) more closely. The layer depth still resembles its state at $t = 0$ (Fig. 5.47c) far more than the south wind response (Fig. 5.18c).

The most important feature to appear in the lower layer is the wavy pattern which causes the undercurrent to meander about its mean latitude of about 0.6°S . These meander persist thereafter; they are clearly evident at 398 days (Figs. 5.65, 5.66) though their form is somewhat different. A careful look at day 16 (Fig. 5.63b or 5.63c) shows that the waviness is already present at the western side of the basin. The disturbance propagates from west to east in the sense that it appears earlier at the western side. Fig. 5.62 showed that any phase propagation is westward, but to speak of phase propagation is misleading. That figure indicates that the meander pattern migrates westward over the first 175 days and then remains stationary. (This is



DAY 397.89 (T= 5000.00 MODEL STEP 10000) X= 0.0 TO 28.6 Y= -5.6 TO 5.6
 N2E4 N4CH3 30X44STR RESTART N2E2 AT 9700 WITH WIND = (-5, 5) EVERYWHERE 07/23/19

Fig. 5.65a u^s vectors at 398 days. Nonlinear. Southeast wind.



U LAYER 1

DAY 397 89 (T= 5000 00 MODEL STEP 10000) X= 0.0 TO 28.6 Y= -5.6 TO 5.6
 N2E4 N4C13 30X44STR RESTART N2E2 AT 9700 WITH WIND = (-5, 5) EVERYWHERE 07/23/19

Fig. 5.65b \vec{u}^1 vectors at 398 days. Nonlinear. Southeast wind.

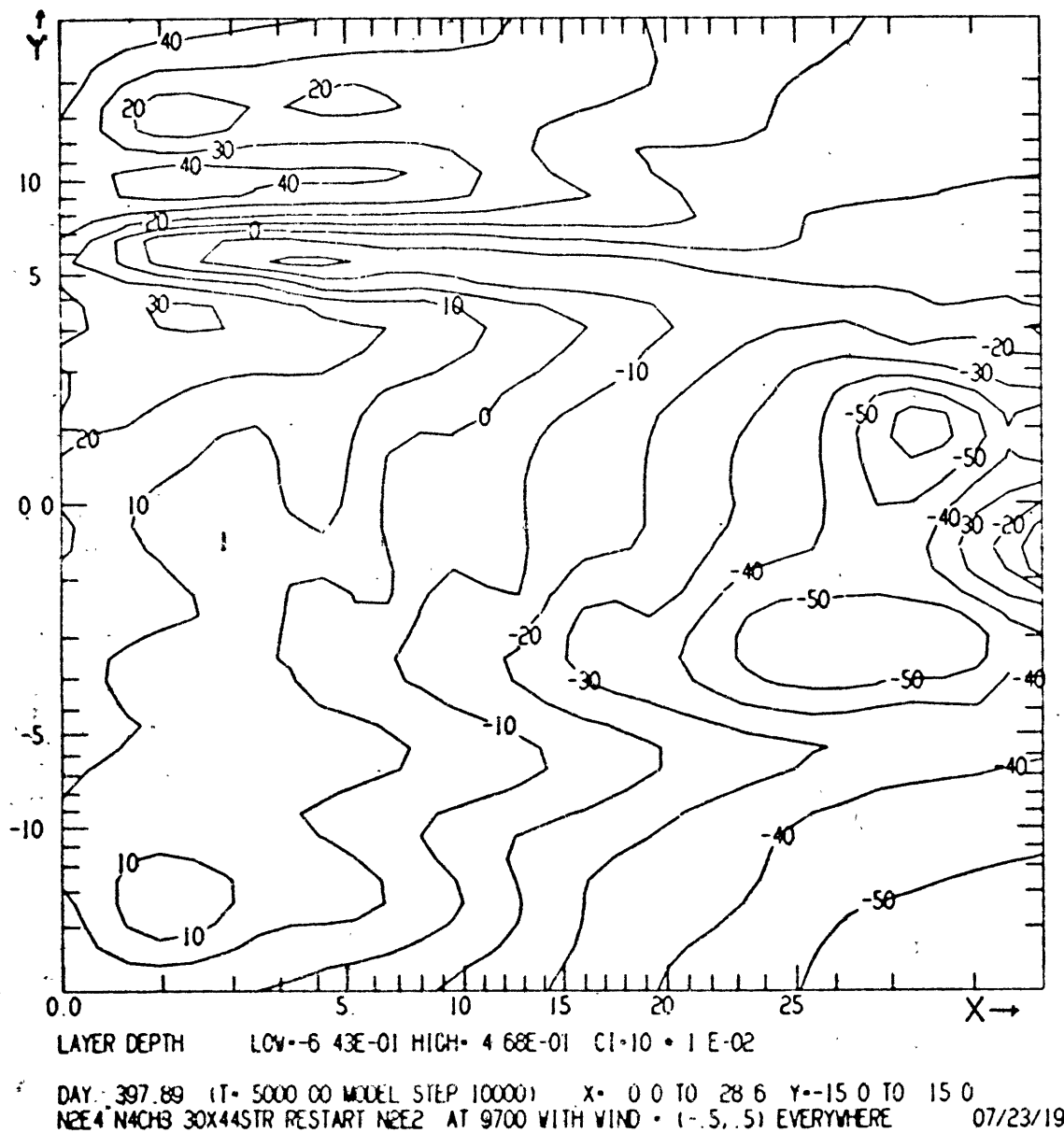


Fig. 5.65c h contours at 398 days. Nonlinear. Southeast wind.

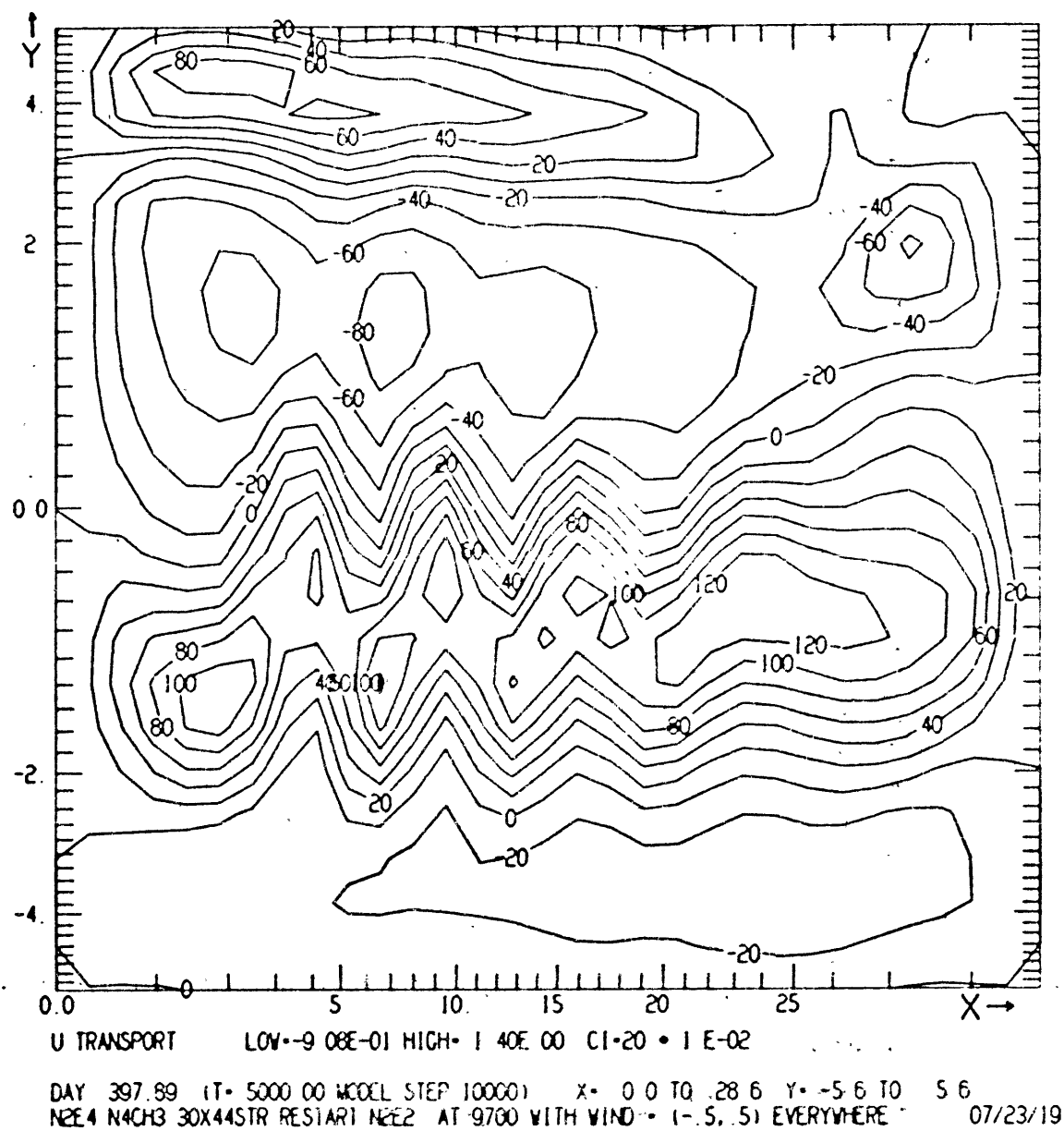


Fig. 5.66a \bar{u} contours at 398 days. Nonlinear. Southeast wind.

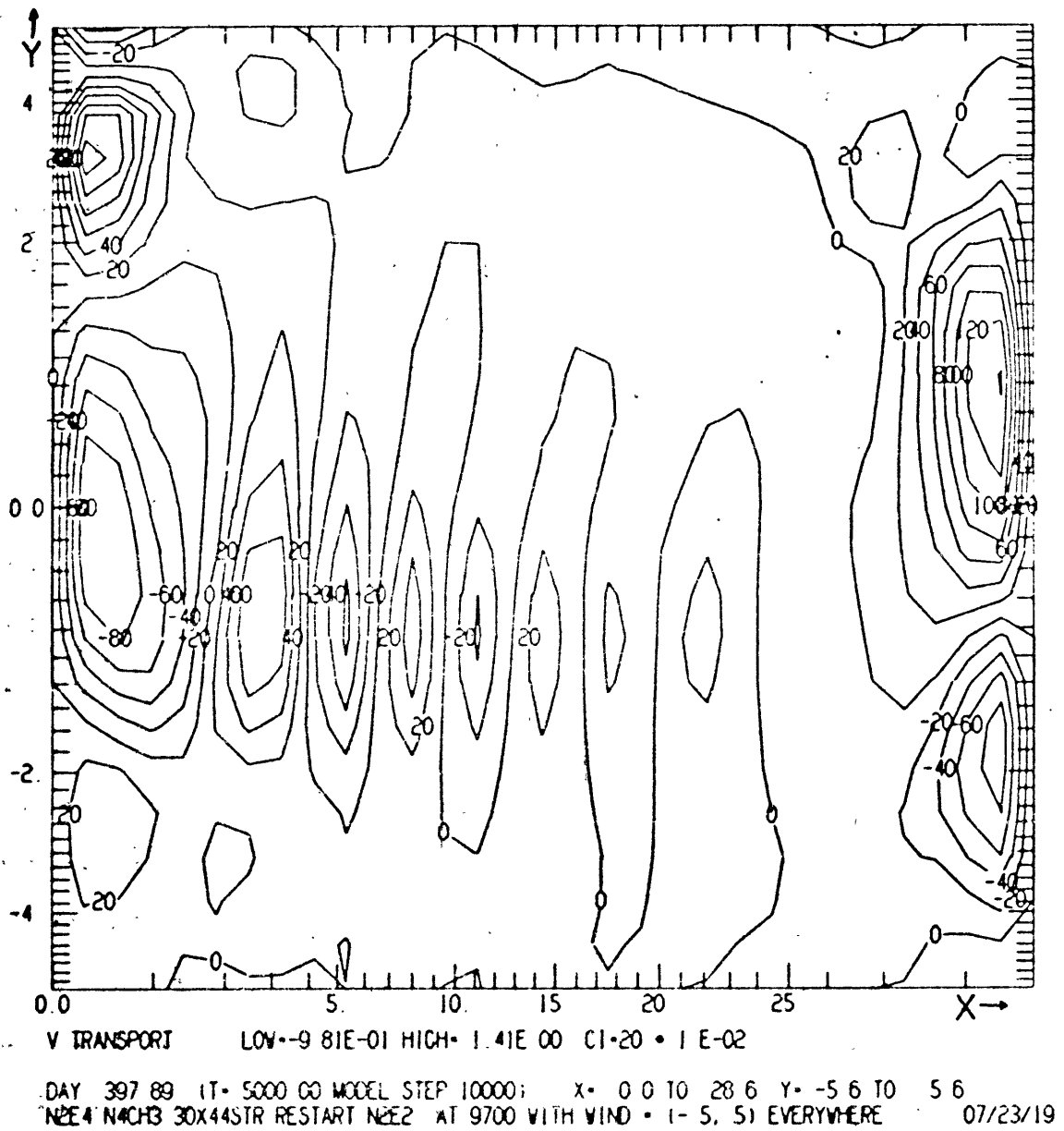


Fig. 5.66b \bar{v} contours at 398 days. Nonlinear. Southeast wind.

borne out by the more defined model results). The result might be described as a standing wave of zero frequency. The structure of these meanders is most clearly revealed by the contours of the zonal and meridional transports at day 398 shown in Figs. 5.66a and b. They have their largest amplitude between 0° and 2°S ; with the amplitude decreasing from west to east. The wavelength of the meanders is about 650 km and shows a slight increase from west to east. We offer the interpretation that these meanders are due to a mode generated at the western boundary in response to the south wind. Such a mode is the nonlinear analogue of the mixed mode that is generated when the initial state is a resting one. It plays the role of a barotropic instability in the sense of acting to reduce the horizontal shear of the zonal currents.

In addition to these meanders the other prominent features of the flow in the equatorial region at day 398 is the eastward jet in both layers centered at 4°N and the undercurrent with a mean position at about 0.7°S . Elsewhere between $\pm 5^\circ$ the lower layer currents are generally westward. Fig. 5.67 shows meridional sections of the zonal transport at the central longitude of the basin. Note that the equatorial flow quickly reaches its final value and that unlike the southwind case (Fig. 5.24) there is no oscillation in time. Except that the jet is slightly further north and its total transport less than in the south wind case, the mean flow between the equator and about 5°N

is very similar in the two cases. The arguments presented in Section 5.3 to explain the dynamics of the flow in that case will serve here as well. South of the equator the two cases are quite different due to the presence of the undercurrent at about 1°S and an additional region of westward transport to the south of it.

The flow pattern between 3°S and 3°N that we find at day 398 resembles the similar calculation made by Charney and Spiegel (1971). (See their Figs. 9 and 10; they only show the region from 3°S to 3°N .) Specifically, the zonal component of surface flow is westward everywhere, the undercurrent is found at about 0.5°S , and zonal flow at depth is westward elsewhere. Both the undercurrent maximum and the westward maximum in their calculation are smaller than ours. Of course, they cannot have the meanders since there is no zonal variation in their model. Flow in the meridional plane is similar in the two calculations, with the division between northward and southward surface flow occurring at the latitude of the undercurrent.

Fig. 5.65c shows contours of the layer depth at 398 days. The trough at 5°N is less pronounced than in the south wind case (Fig. 5.21c); on the whole the topography still has strong resemblances to the initial state; that is, the east wind response (Fig. 5.47c). Figs. 5.68a, b, c show the evolution of meridional sections of h at various longitudes; they should be compared with the corresponding sections for the south and east wind cases, Figs. 5.23 and 5.42, respectively. The final

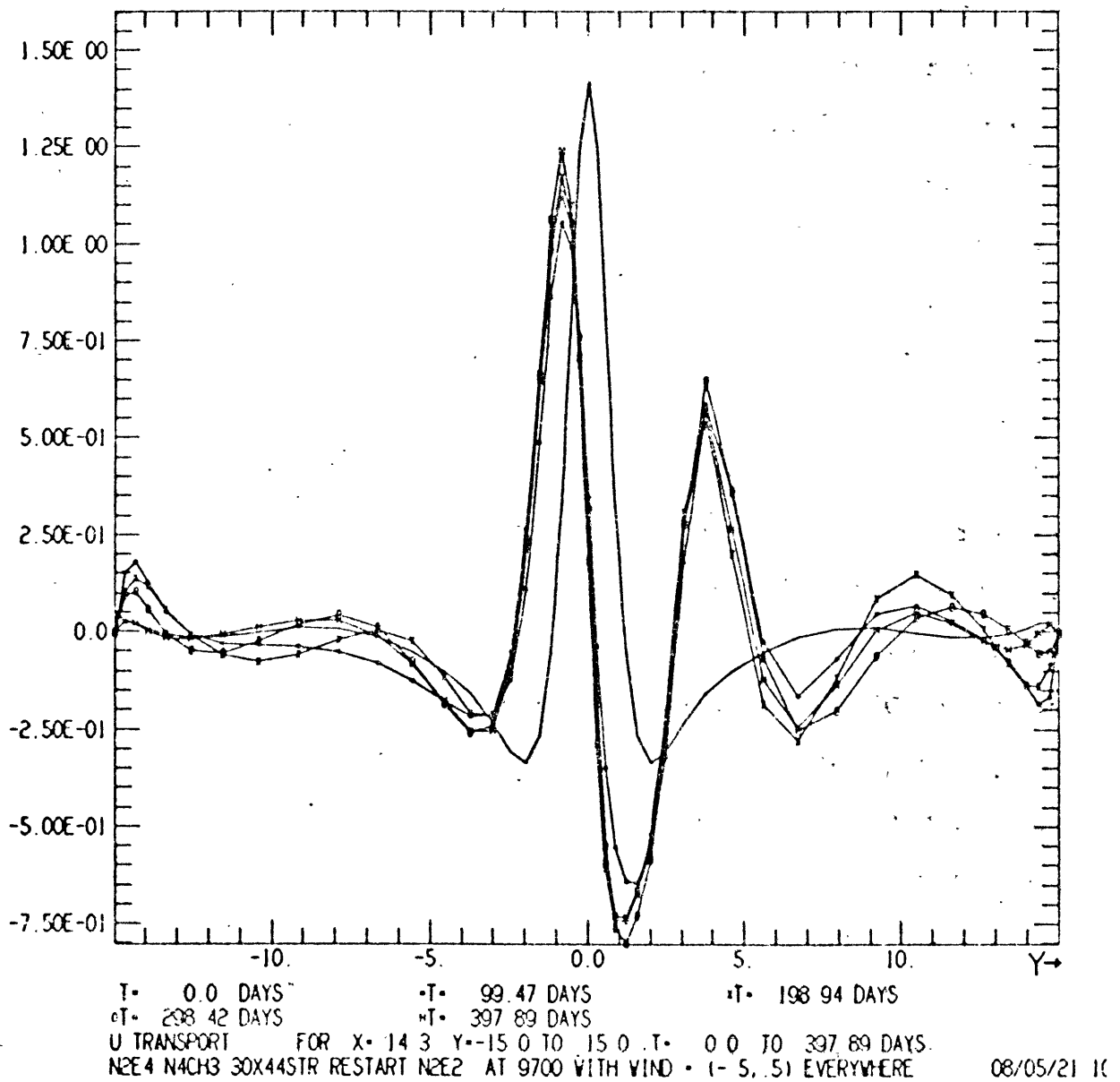


Fig. 5.67 Meridional sections of \bar{u} to day 398 at $x=14.3^\circ$.
Nonlinear. Southeast wind.

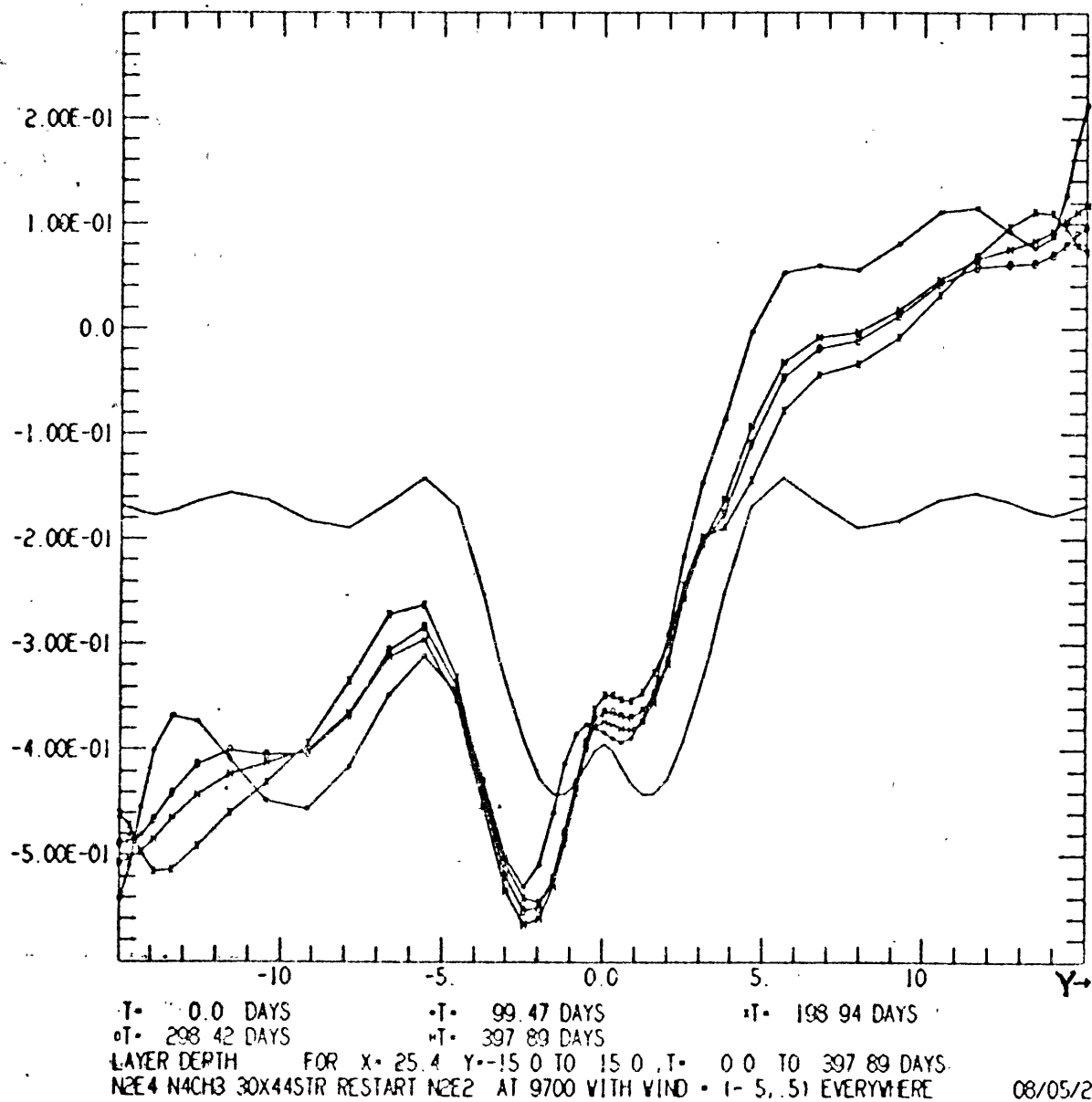
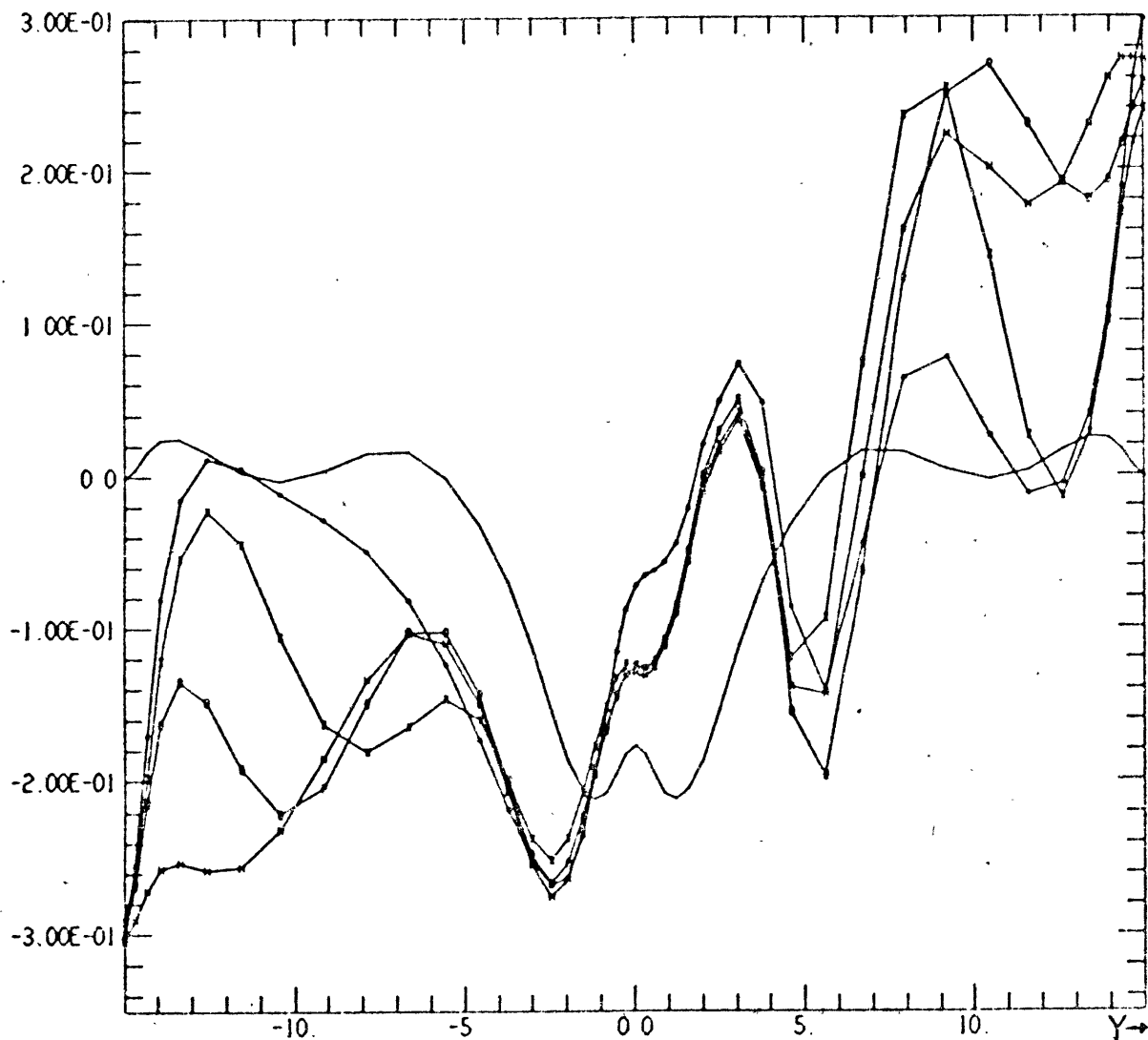


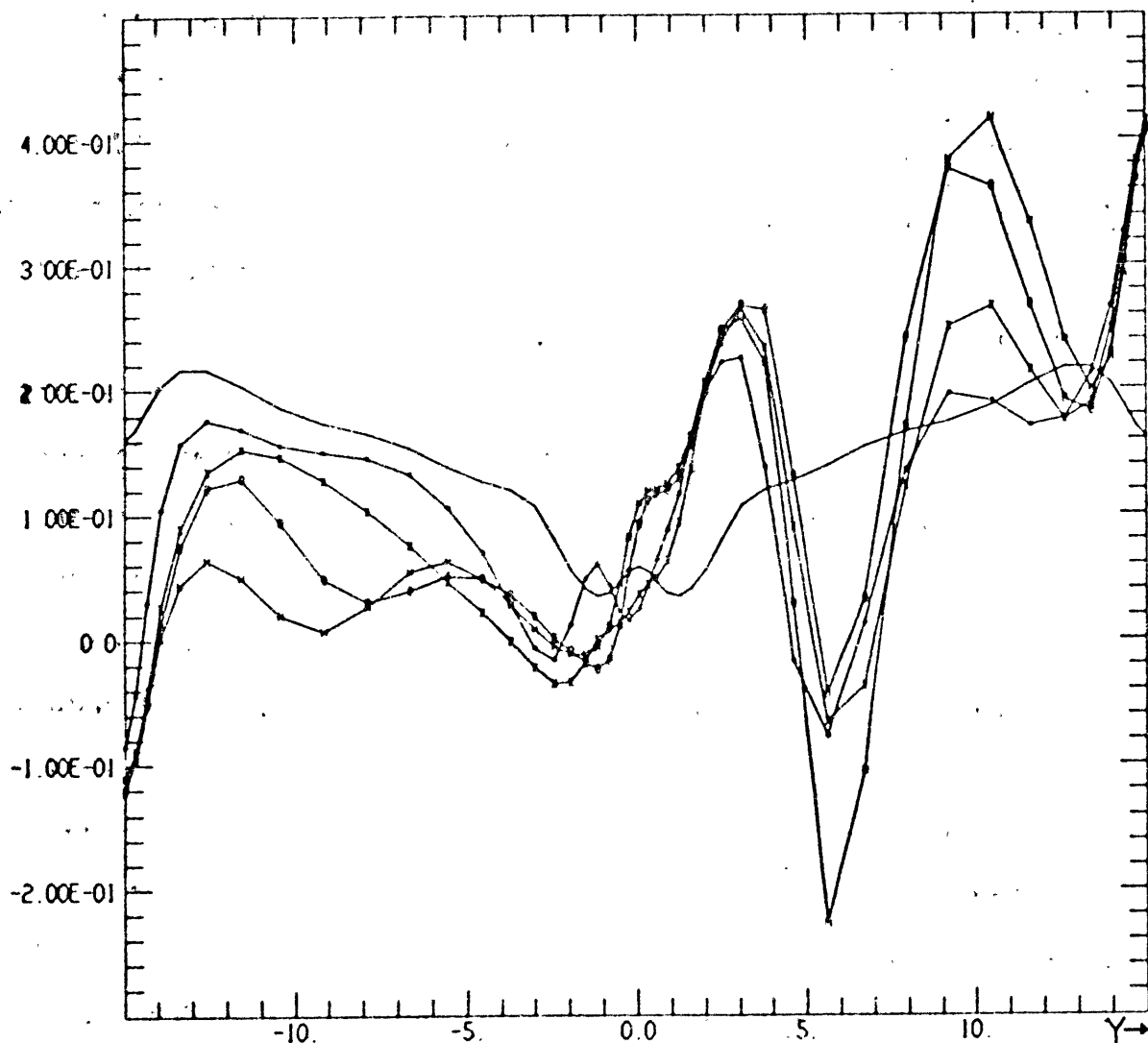
Fig. 5.68a Meridional sections of h to day 398 at $x=25.4^\circ$.
Nonlinear. Southeast wind.



T= 00 DAYS T= 99.47 DAYS T= 198.94 DAYS
 T= 298.42 DAYS T= 397.89 DAYS
 LAYER DEPTH FOR X= 14.3 Y=-15.0 TO 15.0 T= 0.0 TO 397.89 DAYS
 N2E4 N4CH3 30X44STR RESTART N2E2 AT 9700 WITH WIND = (1.5, .5) EVERYWHERE

08/05/21 10

Fig. 5.68b Meridional sections of h to day 398 at x=14.3°.
 Nonlinear. Southeast wind.



T= 0.0 DAYS T= 99.47 DAYS T= 193.94 DAYS
 T= 298.42 DAYS T= 397.89 DAYS
 LAYER DEPTH FOR X= 3.2 Y=-15.0 TO 15.0, I= 0.0 TO 397.89 DAYS
 N2E4 N4CH3 30X44STR RESTART N2E2 AT 9700 WITH WIND = (-5, .5) EVERYWHERE.

08/05/21 10

Fig. 5.68c. Meridional sections of h to day 398 at $x=3.2^\circ$.
 Nonlinear. Southeast wind.

meridional sections (especially at the center of the basin, Fig. 5.68b) clearly resemble the south wind sections more closely. The equatorial region adjusts more quickly than higher latitudes, reaching a final state within 200 days. Also, adjustment appears to occur most rapidly at the eastern side and proceed westward, though the evidence is less conclusive here than in the previous cases.

Our final remarks about this case concern its possible applicability to the undercurrent meanders observed in the Atlantic during GATE (Düing et. al. 1975). We don't wish to claim that the results presented here bear sufficient resemblance to the observations to be offered as an explanation, although together with those for the south wind they do leave open the possibility that a calculation with a more realistic wind stress distribution might do so. However, we wish to point out that a limited sampling of the model output, comparable in scope to the observations reported in Düing et. al., might lead one to misinterpret the initial stages of the evolution of the model circulation. Specifically, data like that shown in Fig. 5.62 might be interpreted as a westward propagating waves at the equator. For example, the variations at $x = 8^\circ$ over the first two months of the simulation could be interpreted as waves with periods of 19 days for the u^1 component and 11 days for the v^S component. Though we do feel that in view of the available data the most plausible explanation for the under-

current meanders is that they are a manifestation of an instability, the possibility that they are part of the adjustment to changes in the winds remains open. The argument of Düing et. al. (1975) that the winds were steady during GATE does not speak to the point that variations which occurred prior to GATE could be responsible. If such effects were felt via a reflection from, say, the coast of Brazil, the responsible wind shifts could have occurred four months or more earlier than the observed meanders.

6 Summary and Conclusions

Purpose. The purpose of this work was to study the response of a bounded equatorial ocean to an imposed wind stress. It is an extension of previous investigations (especially Charney and Spiegel 1971) to include zonal variation of the oceanic currents as well as time dependence. The intent is to experiment with a laboratory-like model to gain some insight into equatorial dynamics. We did not attempt to achieve a close mimicry of the real ocean. The linear dynamics were explored rather thoroughly by analytic methods and verified against numerical calculations. The fully nonlinear response was calculated numerically. Simple analytic models were invoked to explain some of the phenomena observed in the computations.

The Physical Model. The physical model was formulated in Chapter 2. The model is time dependent and treats fully variations in both the zonal and meridional directions. The ocean basin is rectangular, with a zonal extent of 28.6° of longitude and meridional extent from 15°S to 15°N . This size is sufficient to allow the equatorial dynamics to be independent of the effects of the zonal boundaries and to allow an interior circulation distinct from the effects of the meridional boundaries. The vertical structure consists of two layers above the thermocline with the same constant density (Fig. 2.2). The ocean below the thermocline is taken to be

of a higher constant density and to be approximately at rest. The upper of the two active layers is a constant depth surface layer which is acted upon directly by the wind stress. The lower active layer is not directly affected by the wind. Its depth is variable, with the variations being dynamically determined. The two layers communicate via the vertical velocity at their interface, as well as frictionally. Extra-equatorially, this structure is equivalent to a surface Ekman layer and an interior in which the currents are in geostrophic balance with the pressure. The pressure is proportional to the layer depth because of the assumption of hydrostaticity. To justify the assumption of a surface boundary layer near the equator, it is argued that inertial effects will prevent the surface Ekman layer from deepening without limit as the equator is approached from higher latitudes. The wind driving is sufficiently strong ($.5 \text{ dynes cm}^{-2}$) and the vertical and horizontal eddy viscosities sufficiently small ($15 \text{ cm}^2 \text{ sec}^{-1}$ and $6 \times 10^5 \text{ cm}^2 \text{ sec}^{-1}$, respectively) so that inertial effects are important in both layers in the vicinity of the equator.

The layer configuration described above allows for the vertical inhomogeneity that results from the wind stress being felt directly by the ocean at the surface but only indirectly below (e.g., via boundary layer pumping). If the wind stress has no curl, the more usual layered model with

each layer having a different density (e.g., Charney 1955) admits a steady state solution in which each interface tilts in such a way that there is no motion in any of the layers. The present model has the simplest vertical structure that permits a steady state undercurrent.

Numerical Methods. The methods used in the numerical solution of the model are explained in Appendix B. A variable size grid mesh is employed to allow increased resolution at the sidewalls and the equator. The finite difference scheme is second order in time and fourth order in space. A form which conserves first and second moments (e.g., energy) for a large class of finite difference approximations is derived. A new treatment of gravity wave terms is developed which prevents the contamination of the calculation by two-grid point noise. As a result, the fields of horizontal divergence (vertical velocity) are quite smooth. An analogue of this technique is developed to provide additional smoothing of small-scale noise without damping the larger scales appreciably or lowering the order of accuracy of the overall scheme. This permits long-time integrations to be carried out without introducing any explicit viscous dissipation.

Steady State Analytic Results. The presentation of the analytic results begins in Chapter 3. It is shown that the linear model is equivalent to one in which only the ver-

tically integrated transports and the surface boundary layer transports are calculated. These boundary layer transports may be identified as the Ekman transports extra-equatorially; at the equator they are in the direction of the wind stress. The linear steady state solution for the vertically integrated transport is shown to be the same as that of the Stommel (1948) model. If the bottom friction parameter (i.e., the stress at the bottom of the lower active layer) is nonzero, there is additional vertically integrated transport in a frictional boundary layer centered on the equator. This layer thickens from east to west. The interior transports are predominantly zonal; a boundary current is required at the western side to close the fluid circuit. For a wind stress which is independent of longitude at the equator and whose meridional variation is negligible on the boundary layer scale (0(30 km) for a vertical eddy viscosity of $15 \text{ cm}^2 \text{ sec}^{-1}$) we have the following results. A meridional wind stress produces a zonal transport which is zero at the equator and in the direction of the wind drift (e.g., to the right of the wind in the northern hemisphere) off the equator. This interior circulation is connected by a weak meridional flow across the equator directed opposite to the wind. A zonal wind stress produces a net transport in the direction of the wind at the equator. This result shows that the linear model cannot produce a vertically integrated transport in

the same direction as that for the observed undercurrent. A qualitative comparison is made with the linear model of Philander (1971) for a homogeneous ocean continuous in the vertical.

Time Dependent Analytic Methods and Results. The time dependent solution for the surface boundary layer velocity is readily obtained. This component of the model, which is just the Ekman layer transport away from the equator, spins up (i.e., reaches a value within e^{-1} of its steady state value) on the frictional timescale of γ_I^{-1} , where γ_I is a vertical Ekman number (Eq. 3.2) based on the coefficient of friction between the two active model layers. This time is about 20 days for a vertical eddy viscosity of $15 \text{ cm}^2 \text{ sec}^{-1}$. There is a second time-scale, referred to as the set-up time. This is essentially the time it takes for the sea surface to set up in response to the wind stress. It involves the evolution in time of the vertically integrated mass transports and the layer depth. For times less than one-half year, frictional effects are negligible in this process. Calculating this evolution is equivalent to finding the forced response of the inviscid shallow water equations in a bounded equatorial basin.

The solution of this latter problem is the content of Chapter 4 and constitutes the major analytic contribution of this thesis. Our solution makes it possible to calculate

the response to an arbitrary wind stress (and heat source). The method is similar to finding the Green's function for the shallow water equations on an equatorial beta plane with meridional boundaries. Meridional structure is expressed as an eigenfunction expansion and then the response of an unbounded ocean to a step function in time and the zonal direction is calculated. Boundary effects (e.g., reflections) are taken account of by finding the free modes which must be added to the unbounded response to satisfy the boundary conditions. Some general characteristics of the solution may be stated. Forcings with time scales much longer than two days tend to excite planetary (Rossby and Kelvin) modes rather than inertia-gravity waves. Consider now a wind stress which is a step function in time. The unbounded response to a zonal wind stress which is smooth in y will generally have zonal currents and layer depths which are equatorially confined and grow linearly in time. Extra-equatorially, the response consists primarily of a steady meridional current which approaches the wind drift current as the latitude increases. The non-inertia-gravity wave part of the unbounded response to an x -independent meridional wind stress consists of a steady zonal current and layer depth variation. At the equator, the pressure force due to the sea surface setup balances the wind stress; far from the equator, it is balanced by the vertical component of the Coriolis force due to the

zonal velocity.

The more equatorially confined a wave is, the larger its group velocity. Consequently, equatorial regions will evolve more rapidly than extra-equatorial ones. The response to an incident motion at the eastern boundary is less equatorially confined than the original motion. It asymptotes to a coastally-confined motion (e.g., a coastal Kelvin wave) at large latitudes. A western boundary response will have the same latitudinal extent as the incident motion with its amplitude tending to be greater near the equator. Most of the response is boundary trapped resulting in a strong western boundary current; this is similar to midlatitude oceans. However, part of the equatorial response is in the form of equatorial Kelvin waves which carry energy away from the boundary rapidly.

Results of Numerical Experiments. The numerical experiments are described in Chapter 5. These consisted of the linear and nonlinear responses to a uniform easterly wind and to a uniform southerly wind, and the nonlinear response to a uniform westerly wind. In all these cases the wind was turned on at $t=0$ and was steady thereafter. In the final experiment the nonlinear steady state response to an easterly wind was taken as the initial state. The wind was then changed to be from the southeast in a crude imitation of the monsoon over the Atlantic. The linear cases were also studied analytically.

ically by using the results of the preceding chapters.

There was close agreement between the numerical and analytic results. The results of these experiments may be summarized under the following headings:

(a) Spin up Times. All cases showed a frictional spin up time--the time for the transfer of wind energy to the upper layer to reach its final value--of about twenty days. In all cases the setup time (the time for the large-scale pressure gradients to become established) is shortest at the equator and on the order of one year at a latitude of 10° . The equatorial time varies greatly from case to case: it is about 100 days for the linear south wind case, 250 days for the linear east wind and nonlinear west wind, 140 days for the nonlinear east wind case. The nonlinear south wind case reaches an energy maximum at 150 days after which instabilities become prominent: an oscillating state with a steady mean is reached after 250 days. The southeast wind case attains its final state in approximately 200 days. Note that the inclusion of nonlinear effects may either lengthen or shorten the setup time, depending on the case. All of these times will vary (linearly) with the longitudinal extent of the basin. The setup times for the world's equatorial oceans are thus comparable to the time-scale of the major wind stress variations associated with the monsoons. This implies that steady state models are not entirely appro-

priate for studies of the equatorial ocean circulation.

(b) Early Nonlinearity. Using a (local) Rossby number as a measure, the currents in the surface layer near (or on) the equator are nonlinear within three or four days. Within two weeks, nonlinear distortions of the flow field in both layers are evident. Vertical velocities are large near the equator so that vertical advections become important within the frictional time of twenty days. While nonlinearity destroys the linear symmetry properties associated with meridional winds, these are preserved for zonal winds.

(c) Adjustment to a Final State. The south wind linear case adjusts monotonically to a steady state. The adjusted state "propagates" in from the eastern boundary while all the required transfer of mass between hemispheres occurs in the western boundary current. The east wind linear case does not adjust monotonically: the sea surface slope "overshoots" its final value. Both eastward propagating Kelvin waves generated at the western boundary and westward propagating Rossby waves generated at the eastern boundary participate actively in the spin up process. Extra-equatorially, however, the adjusted state is again attained at the eastern side first. The energy in the model ocean behaves like a damped oscillation, taking three 80-day cycles to closely approach a steady state. The nonlinear adjustments to zonal winds have many qualitative similarities to the linear case,

especially when the wind is from the west. For an easterly wind, the nonlinear terms restrain the tendency to overshoot the final steady state; the energy oscillations are effectively damped after one and a half cycles. The nonlinear cases have much more kinetic energy in the lower layer, a difference due primarily to vertical advection of momentum. Extra-equatorially, the evolution is approximately linear.

The nonlinear response to a south wind is also very much like its linear counterpart far from the equator. Near the equator it is entirely different. A current system with strong horizontal shears develops within two weeks, its most prominent feature being an eastward jet present in both layers at 2°N to 3°N (its position shifts to the north in time). Flow south of this is westward until about 1°S , where the lower layer flow becomes eastward. An instability which draws its energy primarily from the lower layer kinetic energy develops after about 100 days. It appears first near the western side of the basin and extends across the basin by 150 days. The southeast wind case also develops a jet-like "countercurrent" at about 4°N . In this case, a wavelike form is apparent across the length of the basin within one month after the southerly wind component is added (see next paragraph). This form appears near the western side first; it propagates (in the phase sense) slowly westward, reaching a steady (not oscillatory) state after 200 days.

(d) Stability. The zonal wind cases showed no evidence of instability (e.g., meanders of the undercurrent) whatsoever. This result is consistent with the stability analysis of Philander (1975). As already noted, the current system associated with a south wind is barotropically unstable. The instability has a regular wavelike form in the zonal direction with a wavelength of 950 km, a period of twenty-nine days and a westward phase speed of 32.5 km/day (38 cm/sec). The interpretation of the wavelike pattern which arises in the southeast wind case is less straightforward. The linear response to a southerly wind includes a wavelike mixed mode reflection from the western boundary extending far into the basin. A modified form of this mode is present in the nonlinear response to both the south and southeast winds. In the latter case, this mode first narrows its wavelength as it squeezes toward the western boundary (this is very much like the Bessel function behavior of the linear case, Section 5.2). It then reaches a steady state in which the wavelength of this feature varies from about 500 km near the western boundary to about 900 km in the eastern half of the basin. It appears that the mode initially generated at the western side is able to maintain its amplitude across the basin rather than only at the western side by absorbing energy from the mean flow (see below).

(e) Steady State Circulation Patterns. Except for the equatorial boundary layer due to bottom friction the linear cases have no vertically integrated mass transport. The upper layer flow is driven by the wind and limited by friction equatorially and Coriolis forces extra-equatorially. The lower layer flow provides the compensating mass flux in the opposite direction. In the east wind case, the meridional scale of the undercurrent is determined by the interfacial friction. For the most part, the fluid circuit which contains the undercurrent closes in the (x,z) plane: fluid upwells out of the undercurrent at the eastern side, travels westward in the surface layer and returns to the undercurrent in a western downwelling layer.

For the nonlinear response to an east wind the half-width of the undercurrent (100 km) is inertially determined. In the vicinity of the equator there is a net equatorward mass flux in the interior of the basin. As a consequence, the vertically integrated transport increases downstream, the pressure force due to the sea surface tilt overbalances the wind stress (by about one-third), and the poleward transports at the eastern end of the basin are larger than the equatorward transports at the western end. It was argued that some zonal variation in the interior was required. A scaling argument suggests that if inertial effects dominate and zonal variations are negligible, then at the equa-

tial wavelike zonal variations. Much of the flow pattern looks like a superposition of the south and east wind cases. The flow is essentially linear poleward of 5° . From just north of the equator to 5°N , the surface layer currents are predominantly northward; at 3.5 there is strong eastward flow in the surface layer (660 ms^{-1}); the flow in the lower layer is weakly to the east. This case, together with the south wind case, suggests that some of the transport of the North Equatorial Countercurrent may be attributable to the meridional winds rather than to the wind stress curl. The lower layer flow further south is like the south wind case, except for the undercurrent. The undercurrent meanders as it crosses the basin; the wavelength of the meanders increasing from west to east, as described above. Its latitude varies from about 0.3°S to about 0.9°S ; its mean position has been displaced upwind.

(f) Western Boundary Currents. Linear inviscid theory predicts that the western boundary current will be initially stronger for a south wind, but that the current will increase at a faster rate in the west wind case. This qualitative statement carries over to the nonlinear responses. These also exhibit a large eddy at their northern edge, similar to the "great whorl" observed in the Somali Current.

Further Theoretical and Observational Implications.

The result summarized in the last paragraph suggests that, with the onset of the Southwest Monsoon, it is the meridional wind along the coast of Africa that is initially responsible for the reversal of the Somali Current (M. Cox 1970). However, propagation from the interior of the Indian Ocean (the mechanism proposed by Lighthill 1969) is probably responsible for the maintenance of the current. The same conclusion has been reached by a number of recent studies (M. Cox, private communication). To go beyond this qualitative statement will require a much more elaborate investigation. One would need to consider how the current equilibrates as a function of nonlinear and (lateral and vertical) frictional effects, as well as of the longitudinal extent of the coastal winds. A much finer mesh than was employed in this work is required to adequately resolve the details of the coastal currents (this is predictable from the scale analysis in Chapter 4 and was confirmed by numerical experiment with a finer-grid model. This experiment also confirmed that the other features of the flow fields described in this work were adequately resolved.). The resolution required will be determined by the value of lateral viscosity used. Also, it has been suggested that the boundary conditions employed (no slip or free slip) strongly affect the results (M. Cox, private communication). We hope

tor the zonal surface stress and pressure gradient at depth would both be balanced by vertical advection of zonal momentum. Since the pressure and stress terms are of opposite sign and the vertical advection term is negative everywhere above the core of the undercurrent, this is not possible and additional terms must become important. For reasonable values of the coefficients of eddy viscosity and realistic basin sizes, zonal variations will enter before additional friction terms.

The transport needed to return the mass flux of the undercurrent to the west all takes place within 5° of the equator. Upwelling at the equator is strong enough to make the surface layer currents eastward in the interior of the basin. The maximum undercurrent speed is 1 msec^{-1} ; the surface maximum is $.3 \text{ msec}^{-1}$.

The response to a west wind has many parallels with the east wind case. In the vicinity of the equator there is a net poleward mass flux in the interior of the basin. As a consequence, the transport at the equator decreases downstream, the sea surface slope overbalances the wind stress (though only slightly) and the equatorward transports in the western boundary currents are larger than the poleward transports at the eastern end. The east to west return transport takes place within 5° of the equator; as with the east wind, it is primarily in the lower layer.

Currents in both layers are eastward at the equator. The maximum speeds are $.8 \text{ msec}^{-1}$ in the surface layer and $.5 \text{ msec}^{-1}$ in the lower layer. Both zonal wind cases become linear poleward of 5° .

The nonlinear response to a south wind behaves linearly south of about 2.5°S and north of 5°N . In between, the flow is unstable, as described above--it does not reach a steady state. The zonal mean in this region closely resembles the flow calculated by Charney and Spiegel (1971, Figs. 11 and 12). It may be characterized as follows. There is upwelling south of about 3°N , particularly south of the equator. The surface flow is northwestward at the southern edge of this region and turns clockwise, becoming due east in a jet-like flow at 3°N . There is a strong shear zone north of 3°N . There is a strong downwelling in the jet. As one moves south, the lower layer flow turns clockwise from due east at the jet; westward flow is strongest just north of the equator. Further south, the flow again becomes eastward. A simple argument based on conservation of vorticity and energy is offered to explain this flow pattern. The latitude of the jet scales like $\tau^{1/3}$ and the velocity in the jet like $\tau^{2/3}$ where τ is the magnitude of the wind stress (Eq. 5.8 ff.).

As noted in the previous subsection, the southeast wind case does reach a steady state, but one with substan-

to study some of these issues in the near future.

The model results have a number of other applications to the Indian Ocean. As pointed out by Charney and Spiegel (1971), the jet produced by the south wind has been observed in the Indian Ocean (Taft and Knauss 1967). The model calculation suggests that the current system is unstable. This instability may account for the absence of steady currents at the equator in the Indian Ocean during the Southwest Monsoon (Taft and Knauss 1967). The model calculation shows that eastward winds at the equator result in eastward flow at all depths above the thermocline, while meridional winds (north or south) produce westward flow. (These are nonlinear effects). The data collected by R. Knox at Gan in 1973 and 1974 (private communication) shows such a correlation between the winds and the currents.

The undercurrent simulation resembles the real undercurrent in many important respects, as well as sharing many features with the homogeneous ocean model of Charney and Spiegel (1971) (e.g., both models tend to form a cusp in the zonal velocity at the equator). Permitting zonal variations and not constraining the pressure force to balance the zonal wind stress, made for some important differences. The pressure gradient was larger in our model, making it more in line with observational evidence (Montgomery and Palmén 1940;

see Charney 1960, p. 305). The terms uu_x and vu_y are of comparable magnitude. Previous theoretical studies of the undercurrent in homogeneous oceans have neglected the former term by arguing that the zonal length scale is much greater than the meridional one. This argument also requires that u and v be scaled by the same magnitude. However, in the undercurrent $u \gg v$, causing this argument to break down. (Observational accounts of the momentum balance in the undercurrent (Knauss 1966; Taft, et al., 1974) has also neglected downstream advections, but this is due primarily to a lack of data.)

The model results show an increase in transport downstream while observations, while not conclusive, show that the undercurrent transports are less in the eastern half of the ocean than the western half for both the Pacific and the Atlantic. This suggests that a homogeneous model is inadequate to describe this feature. Philander (1973) simulated it by including the effects of the thermohaline circulation in his model. Observational evidence does not enable one to determine with certainty if the loss of fluid from the undercurrent occurs in the meridional plane or the vertical plane (via downwelling at the base of the undercurrent).

Our model results agree with the finding of Philander's (1975) stability study, that the undercurrent it-

self is stable but that the entire equatorial current-counter-current system may be unstable--in particular, because of the large shears between the westward flow near the equator and the eastward flow in the North Equatorial Counter-current. The southeast wind case had an undercurrent which meandered in space but was steady in time. In the course of reaching this steady state, the undercurrent exhibited time variations not unlike the GATE data (cf., Section 5.7). For example, the undercurrent velocity 8° from the western wall appears to oscillate with a nineteen-day period. It is thus possible that the meanders observed during GATE could be due to changes in the winds. We offer the general observational caution that, because of the relatively rapid propagation at the equator of fronts due to boundary reflections, one should be careful in interpreting observations as waves. Moreover, our calculations have shown that non-linear effects quickly become important at the equator, limiting the range of applicability of linear wave concepts.

REFERENCES

- Arakawa, A., 1966: Computational design for long-term numerical integration of the equations of fluid motion: Two-dimensional incompressible flow, Part I, J. Comput. Phys. 1, 119-143.
- Blandford, R. 1966: Mixed Gravity-Rossby waves in the ocean. Deep Sea Res., 13, 941-960.
- Cane, M., 1974: Forced motions in a baroclinic equatorial ocean. GFD Notes, Woods Hole Oceanogr. Inst., Ref. No. 74-63.
- Cane, M. and E. Sarachik; 1975: Forced response of an equatorial baroclinic ocean (to appear).
- Charney, J. G., 1955: The generation of ocean currents by wind. J. Mar. Res., 14, 477-498.
- Charney, J. G., 1960: Non-linear theory of a wind-driven homogeneous layer near the equator. Deep Sea Res., 6, 303-310.
- Charney, J. G. and S. Spiegel, 1971: Structure of wind driven equatorial currents in homogeneous oceans. J. Phys. Oceanogr., 1, 149-160.

- Düing, W., P. Hisard, E. Katz, J. Krauss, J. Meincke,
K. Moroshkin, G. Philander, A. Rybnikov, and K. Voigt, 1975:
Meanders and long waves in the Equatorial Atlantic.
(Submitted to Nature.)
- Fofonoff, N. P. and R. B. Montgomery, 1955: The equatorial
undercurrent in the light of the vorticity equation.
Tellus, 7, 518-521.
- Gill, A. E., 1971: The equatorial current in a homogeneous
ocean. Deep Sea Res., 18, 421-431.
- Gill, A. E., 1972: Models of Equatorial Currents. Proc.
Symp. on Numerical Models of Ocean Circulation, Nat. Acad.
Sci.
- Israeli, M. and D. Gottlieb, 1974: On the stability of the N
cycle scheme of Lorenz. Mon. Wea. Rev., 102, 254-256.
- Kálnay de Rivas, E., 1972: On the use of nonuniform grids in
finite-difference equations. J. Comput. Phys., 10, 202-
210.
- Kamekovich, V. M., 1967: On the coefficients of eddy diffusion
and eddy viscosity in large-scale oceanic and atmospheric
motions. Izv. Acad. Sci., USSR Atmos. Oceanic Phys. Eng.
Trans. 3, 1326-1333.

- Kirwan, A. D., 1969: Formulation of constitutive equations for large-scale turbulent mixing. J. Geo. Res., 74, 6953-6959.
- Knauss, J. A., 1966: Further measurements and observations on the Cromwell Current. J. Mar. Res., 24, 205-240.
- Kreiss, H. O. and J. Olinger, 1972: Comparison of accurate methods for the integration of hyperbolic equations. Tellus, 24, 199-215.
- Kreiss, H. O. and J. Olinger, 1973: Methods for the approximate solution of time dependent problems. Garp Publication Series No. 10, W.M.O.
- Leetmaa, A., 1973: The response of the Somali Current at 2°S to the southwest monsoon of 1971. Deep Sea Res., 20, 397-400.
- Lighthill, M. J., 1969: Dynamic response of the Indian Ocean to onset of the southwest monsoon. Phil. Trans. Roy. Soc., A 265, 45-92.
- Lilly, D., 1965: On the computational stability of numerical solutions of time dependent non-linear geophysical fluid dynamics problems, Mon. Wea. Rev. 93, 11-26.
- Lindzen, R., 1967: Planetary waves on beta-planes. Mon. Wea. Rev., 95, 441-451.

- Longuet-Higgins, M.S., 1968: The eigenfunctions of Laplace's Tidal Equation over a sphere. Phil. Trans. Roy. Soc., A 262, 511-607.
- Matsuno, T., 1966: Quasi geostrophic motions in the equatorial area. J. Met. Soc. Japan, 44, 25-43.
- McKee, W. D., 1973: The wind-driven equatorial circulation in a homogeneous ocean. Deep Sea Res., 20, 889-899.
- Mesinger, F., 1972: A method for construction of second-order accuracy difference schemes permitting no false two-grid interval wave in the height field. Tellus, XXV, 444-457.
- Montgomery, R. B. and Palmen, E., 1940: Contribution to the question of the Equatorial Counter Current. J. Mar. Res., 3, 112-133.
- Moore, D., 1968: Planetary-gravity waves in an equatorial ocean. Ph.D. Thesis, Harvard University.
- Moore, D., 1974: Free equatorial waves. GFD Notes, Woods Hole Oceanogr. Inst., Ref. No. 74-63.
- O'Brien, J. J. and H. E. Hurlbut, 1974: An equatorial jet in the Indian Ocean, Theory. Science, 184, 1075-1077.
- Orszag, S. and M. Israeli, 1974: Numerical simulation of viscous incompressible flows. in Annual Review of Fluid Mechanics, Vol. 6, Palo Alto, Annual Reviews.
- Pedlosky, J., 1965: A note on the western intensification of the oceanic circulation. J. Mar. Res., 23, 207-210.

Pedlosky, J., 1968: An overlooked aspect of the wind-driven ocean circulation. J. Fluid Mech., 32, 809-821.

Philander, S. G. H., 1971: The equatorial dynamics of a shallow homogeneous ocean. Geophys. Fluid Dyn., 2, 219-245.

Philander, S. G. H., 1973a: The equatorial thermocline. Deep Sea Res., 20, 69-86.

Philander, S. G. H., 1973b: Equatorial undercurrent: measurements and theories. Rev. Geophys., 11, 513-570.

Philander, S. G. H. 1975: Instabilities of equatorial currents. (To appear.)

Robinson, A. R., 1960: The general thermal circulation in the equatorial regions. Deep Sea Res., 6, 311-317.

Robinson, A. R., 1966: An investigation into the wind as the cause of the Equatorial Undercurrent. J. Mar. Res., 24, 179-204.

Stommel, H., 1948: The westward intensification of wind-driven currents. Trans. Amer. Geophys. Union, 29, 202-206.

Taft, B. A. and J. A. Knauss, 1967: The Equatorial Undercurrent of the Indian Ocean as observed by the Lusiad expedition. Bull. Scripps Inst. Oceanogr., 9.

- Taft, B., B. Hickey, C. Wunsch and D. Baker, 1974: The Cromwell Current at 150°W. Deep Sea Res., 21, 403-430.
- Veronis, G., 1963b: On the approximations involved in transforming the equations of motion from a spherical to the β -Plane, part I. Barotropic systems, J. Mar. Res., 21, 110-124.
- Veronis, G., 1963b: On the approximations involved in transforming the equations of motion from a spherical to the β -Plane, part II. Baroclinic systems, J. Mar. Res., 21, 199-204.
- Veronis, G. and H. Stommel, 1956: The action of variable wind stresses on a stratified ocean, J. Mar. Res., 15, 43-75.
- Williams, R. and C. Gibson, 1974: Direct measurement of turbulence in the Pacific Equatorial Undercurrent. J. Phys. Oceanogr., 4, 104-108.
- Wyrtki, K., 1973: An equatorial jet in the Indian Ocean, Science, 181, 262-264.
- Yoshida, K., 1959: A theory of the Cromwell current and of the equatorial upwelling, J. Oceanogr. Soc. Japan, 15, 154-170.

Appendix A Eddy Viscosity

We follow Kamenkovich (1967) and Kirwan (1969) in deriving a vector invariant form for the eddy viscosity for an anisotropic media. Let:

$$R_{ij} = \langle -u'_i u'_j \rangle - \rho \delta_{ij}$$

$$D_{ij} = \frac{1}{2} \left(\frac{\partial u_i}{\partial x_j} + \frac{\partial u_j}{\partial x_i} \right)$$

where R_{ij} is the Reynolds stress, u'_i is the turbulent fluctuation, and u_i the mean velocity and brackets denote averaging. We assume a linear relation between the Reynolds stress tensor and the strain tensor:

$$R_{ij} = K_{ijkl} D_{kl} \quad (A1)$$

In general K is a fourth order tensor with 81 components. Making use of the symmetry of R_{ij} and D_{kl} and of incompressibility and contracting R_{ij} reduces the number to 29; these 29 must satisfy 6 relations determined by (A1). Assuming isotropy in the surface defined by, say, the first two coordinates and using incompressibility reduces K_{ijkl} to a form which depends on three independent coefficients v_H , the horizontal eddy viscosity, v_V , the vertical eddy coefficient, and v_2 , a third coefficient for which there is no observational data. We will later take it to be zero. The requirement that the viscous terms always be dissipative yields the inequalities:

$$\nu_H \geq 0; \quad \nu_v \geq 0; \quad \nu_H \geq \frac{3}{4} \nu_2$$

Using the notation in the main body of the paper (cf. especially Eq. 2.7), we have:

$$R_{xx} = 2\nu_H \left[\frac{1}{m_x} \frac{\partial u}{\partial x} + \nu m_{xy} \right] + (\nu_H - \nu_2) \frac{\partial w}{\partial z}$$

$$R_{yy} = 2\nu_H \left[\frac{1}{m_y} \frac{\partial v}{\partial y} + u m_{yx} \right] + (\nu_H - \nu_2) \frac{\partial w}{\partial z}$$

$$R_{xy} = R_{yx} = \nu_H \left[\frac{1}{m_x} \frac{\partial v}{\partial x} + \frac{1}{m_y} \frac{\partial u}{\partial y} - u m_{xy} - \nu m_{yx} \right]$$

$$R_{xz} = R_{zx} = \nu_v \left[\frac{\partial u}{\partial z} + \frac{1}{m_x} \frac{\partial w}{\partial x} \right]$$

$$R_{yz} = R_{zy} = \nu_v \left[\frac{\partial v}{\partial z} + \frac{1}{m_y} \frac{\partial w}{\partial y} \right]$$

$$R_{zz} = 2\nu_2 \frac{\partial w}{\partial z}$$

The viscous forces which appear in the momentum equations are the divergences of the Reynolds stresses. They are:

$$F^{(x)} = \frac{\partial R_{xz}}{\partial z} + F_H^{(x)} \simeq \frac{\partial}{\partial z} (\nu_v \frac{\partial u}{\partial z}) + F_H^{(x)}$$

$$F^{(y)} = \frac{\partial R_{yz}}{\partial z} + F_H^{(y)} \simeq \frac{\partial}{\partial z} (\nu_v \frac{\partial v}{\partial z}) + F_H^{(y)}$$

$$F_H^{(x)} = \frac{1}{m_x} \frac{\partial}{\partial x} R_{xx} + \frac{1}{m_y} \frac{\partial}{\partial y} R_{xy} + m_{yx} (R_{xx} - R_{yy}) + 2 m_{xy} R_{xy} \quad (A2)$$

$$F_H^{(y)} = \frac{1}{m_y} \frac{\partial}{\partial y} R_{yy} + \frac{1}{m_x} \frac{\partial}{\partial x} R_{yx} + m_{xy} (R_{yy} - R_{xx}) + 2m_{yx} R_{yx} \quad (A3)$$

The model uses formulas (A2) and (A3) with $\frac{\partial w}{\partial z} = -\nabla \cdot \underline{u}$ and $v_2 = 0$ to compute F_H . Note that for Cartesian coordinates:

$$F_H^{(x)} = \nu_H \nabla^2 u + (\nu_H - \nu_2) \nabla \cdot \underline{u} \approx \nabla^2 u$$

$$F_H^{(y)} = \nu_H \nabla^2 v + (\nu_H - \nu_2) \nabla \cdot \underline{u} \approx \nabla^2 v$$

Appendix B Numerical Methods

Since no numerical method gives a perfect simulation, the scheme should be chosen with the particular problem in mind. In the present case, the chief requirements are: (i) to be able to run for long time periods (order of years) without numerical instability in order that the ocean may reach a steady state; (ii) to accurately simulate responses over short time periods (weeks or months) to varying winds; (iii) to resolve small scale features at the lateral boundaries and the equator without introducing excessive computational or viscous smoothing. Generally speaking, it is difficult to satisfy (i) on the one hand and (ii) and (iii) on the other.

B.1 Variable Grid

Many of the phenomena of interest in the equatorial ocean have spacial scales which are orders of magnitude less than the scale of the ocean basin. In order to be able to resolve these features we introduce a grid which is "stretched" so that there are more points per unit per length at the lateral boundaries and the equator. At the same time, we reserve the option of not resolving boundary layers when we are not interested in their structure and there is reason to believe that this will not increase the error in the interior. Following a suggestion of M. Israeli (private communication) we stretch with a function of the form:

$$\chi = b \left[c x^* + \sum_{i=1}^{N_I} \alpha_i f \left(\frac{x - x_i}{\beta_i} \right) + a \right] \equiv g(x^*) \quad (\text{B1})$$

on the interval $[x_0, x_N]$. Here x_i is the location of the i th internal or boundary layer, β_i is its thickness and α_i is a weighting factor. As before, x^* is the physical space coordinate and x is the grid coordinate; the points x_j^* are chosen to give equal intervals $\Delta x = g(x_j^*) - g(x_{j-1}^*)$.

The function $f(x)$ should be antisymmetric, non-decreasing and rapidly approach its asymptotic value $f(\infty)$; f is taken as arctangent in the present implementation. These properties guarantee that x is a monotonic function of x^* , that many grid points will lie near x_i and that internal layers will be symmetrically resolved. The formula (B1) while more complicated than those proposed by Kálnay de Rivas (1972), is more flexible; the parameters may be adjusted to an arbitrary physical situation.

B.2 Time Differencing

The leap frog scheme is not used because it is unstable with any damping term. While explicit dissipation can be handled by lagging the dissipation terms in time, correctly set boundary conditions will introduce some damping and hence a slow instability. Compensating for this requires extraordinarily complicated methods (cf., Kreiss and Olinger, 1973; Olinger, 1974). Instead, we choose methods that are not destabilized by dissipative terms. The Adams-Bashforth scheme

(Lilly 1965), which is also second order, has the opposite problem. It is slightly unstable for pure advection and we wish to make model run with a dissipation which is too small, as experience has shown, to stabilize the computation. We elect to use the N-cycle scheme of Lorenz (1971) with $N = 4$. This scheme has good stability properties for the parameter range of interest to us (see Appendix D) and is second order in time (fourth order for linear equations). It has the additional virtue of being particularly easy to apply on a computer --in fact, it is more readily described algorithmically than by an equation. For the equation $du/dt = f(u,t)$, where u and f may be vectors, the scheme may be described as follows:

Let the timestep be δt and let $\Delta t = N\delta t$. An auxiliary storage vector z the same size as u is required. The timesteps are counted by an index n which is initially zero and the vector u is set to its initial value. The steps of the scheme are

- (i) Let $K = n \bmod N$
- (ii) Let $a_n = -K/\Delta t$, $b_n = \Delta t/(N-K)$
- (iii) Let $z^n = b_n [a_n z^{n-1} + f(u^n, t^n)]$ (B2)
- (iv) Let $u^{n+1} = u^n + z^n$
- (v) Let $n = n + 1$

For a linear system of equations $du/dt = Au$, with A a constant matrix, the effect of this algorithm after N repetitions of these steps is to approximate $u(t_0 + \Delta t)$ by

$$\sum_{k=0}^N A^k u(t_0) (\Delta t)^k / k!$$

-- that is, by the first $N + 1$ terms of the Taylor series.

Also, at any intermediate point (K less than N) the linear term is correct; i.e.,

$$u(t_0 + k\delta t) = u(t_0) + Au(t_0)(k\delta t) + O(\delta t^2)$$

For non-linear systems the first of these properties is not maintained for N greater than 2; in addition to the Taylor series terms there are terms depending on second or higher derivatives of $f(u)$. For $N = 4$ the scheme is second order (cf., Lorenz 1971, Eq. 18).

In earlier runs, before some of the devices described in the next sections were introduced, it was necessary to use the Euler backward or Matsuno scheme (Lilly 1965) which strongly damps high frequency waves. This scheme is given by

$$\begin{aligned} u^* &= u^n + \Delta t f(u^n) \\ u^{n+1} &= u^n + \Delta t f(u^*) \end{aligned} \tag{B3}$$

It is first order in time and requires two computations of f per timestep.

B.3 Spatial Differencing: Finite Difference Approximations

The superiority of fourth order finite difference

schemes as compared with second order schemes is now firmly established (see the review by Orszag and Israeli (1974), the monograph by Kreiss and Olinger (1972)). For a given accuracy fourth-order schemes require sufficiently fewer points to offset their additional computational complexity. For example, to attain 5 percent accuracy in the solution of a linear-wave equation the fourth order scheme we use requires about ten points per wave while a centered second order scheme requires twenty. The computational labor is nowhere near twice as great.

Recall that the stretched coordinates were introduced via metric factors and that grid points are at equally spaced intervals in the "computational space" coordinate (Eqs. (2.7), (2.8) and (B1); i.e.,

$$\frac{\partial f}{\partial x^*} = \frac{1}{g'(x^*)} \frac{\partial f}{\partial x} \quad \text{and} \quad x_j = j \Delta x \quad j = 0, 1, \dots, N$$

Therefore it is sufficient to find a finite difference approximation $D_x f$ to $\partial f / \partial x$ when f is given at equally spaced points

$$f_j = f(x_j) \quad j = 0, 1, \dots, N$$

Define the operators

$$\begin{aligned} D_0(\Delta x) f_j &\equiv \frac{1}{2\Delta x} [f_{j+1} - f_{j-1}] \\ D_+ D_- (\Delta x) f_j &= \frac{1}{(\Delta x)^2} [f_{j+1} - 2f_j + f_{j-1}] \end{aligned} \quad (B4)$$

The fourth order centered difference approximation is used D_x :

$$\begin{aligned} D_x f_j &\equiv \left[\frac{4}{3} D_0(\Delta x) - \frac{1}{3} D_0(2\Delta x) \right] f_j \\ &= \frac{\partial f(x_j)}{\partial x} - \frac{\Delta x^4}{30} f^{(5)}(x_j) + O(\Delta x^6) \end{aligned} \quad (B5a)$$

for $j = 2, \dots, N-2$

This formula obviously cannot be used at the points on and immediately adjacent to the boundaries. There we use

$$\begin{aligned} D_x f_0 &\equiv \frac{1}{6\Delta x} \{-11f_0 + 18f_1 - 9f_2 + 2f_3\} \\ &= \frac{\partial f_0}{\partial x} + \frac{1}{4}\Delta x^3 f^{(4)}(x_0) + O(\Delta x^5) \end{aligned} \quad (B5b)$$

$$\begin{aligned} D_x f_1 &= \frac{1}{6\Delta x} \{-2f_0 - 3f_1 + 6f_2 - f_3\} \\ &= \frac{\partial f_1}{\partial x} - \frac{1}{12}\Delta x^3 f^{(4)}(x_1) + O(\Delta x^5) \end{aligned} \quad (B5c)$$

Similar formulas are used at the other end points $j = N - 1$ and $j = N$. These boundary approximations are third order. The fourth order finite difference formulas that we tried at the boundaries proved to be computationally unstable. Kreiss and Oliger (1973, Chapter 18) note that fourth order schemes are more likely than lower order schemes to be destabilized by the boundary conditions, especially in two dimensional geometries. They also indicate that one can often sacrifice an order of accuracy at the boundary without affecting the overall convergence estimates. Experiments indicate

that this is the case with our model. It is certainly plausible that these boundary approximations will not affect the accuracy of the interior solution when (as is our situation) the flow is either externally driven or the result of instabilities generated away from the boundaries.

The horizontal eddy viscosity terms and the treatment of gravity waves we use (Section B.5) both require that second derivatives be computed. For these we use the approximations:

$$\begin{aligned} D_{xx} f_j &\equiv \left\{ \frac{4}{3} D_+ D_- (\Delta x) - \frac{1}{3} D_+ D_- (2\Delta x) \right\} f_j \quad (\text{B6a}) \\ &= \frac{\partial^2 f_j}{\partial x^2} - \frac{1}{180} \Delta x^4 f^{(6)}(x^*) \quad j=2, \dots, N-2 \end{aligned}$$

$$\begin{aligned} D_{xx} f_0 &\equiv \frac{1}{12\Delta x^2} \left\{ 35f_0 - 104f_1 + 114f_2 - 56f_3 + 11f_4 \right\} \\ &= \frac{\partial^2 f_0}{\partial x^2} + \frac{5}{12} \Delta x^3 f^{(5)}(x^*) \quad (\text{B6b}) \end{aligned}$$

$$\begin{aligned} D_{xx} f_1 &\equiv \frac{1}{12\Delta x^2} \left\{ 11f_0 - 20f_1 + 6f_2 + 4f_3 - f_4 \right\} \quad (\text{B6c}) \\ &= \frac{\partial^2 f_1}{\partial x^2} - \frac{1}{24} \Delta x^3 f^{(5)}(x^*) \end{aligned}$$

B.4 Spatial Differencing: Conservation Form

A number of investigators (Orszag and Israeli 1974, Kreiss and Oliger 1972, 1973) have claimed that the greater accuracy of higher order finite difference schemes make it possible to avoid the so-called non-linear or aliasing insta-

bility while dispensing with the need for semi-conservative schemes (e.g., Arakawa 1966). The latter have the disadvantages of being computationally complex without being more accurate. The argument is that the aliasing instabilities will only appear in inadequately resolved simulations, leading to the conclusion that simulations using energy-conserving schemes with the same resolution become unstable.

Our experience, as well as that of others (E. Rivas, private communication; also see Crowley 1968) suggests that, in fact, calculations with energy-conserving schemes will continue to give good results in cases where non-conserving schemes become unstable. This difference may well arise from the kind of modelling assumptions which are usually made in simulating geophysical phenomena. Consider first the contrasting case of numerical simulation of some laboratory situation. All the physics of the real situation is included in the numerical model.

By "adequate resolution" one means that the grid spacing is small enough to resolve all scales of motion which are not strongly damped by (molecular) viscous forces; that is, the Reynolds number based on the grid scale is sufficiently small. In modelling geophysical phenomena, the physics of the real world is often drastically simplified (as is the case with our model). The resort to eddy viscosities is an admission that all of the physics has not been included--the effects of smaller scales of motion are being parameterized. It is not economically feasible to adequately resolve all scales

down to a size which will be damped by a small dissipation term. One is making the tacit assumption that the computation resolves all scales of interest--all scales which are important to the phenomena under study. The physics does not dictate a need for greater resolution and one wishes to avoid expending the extra computer time required by a fine grid merely to prevent the growth of spurious small-scale computational modes. As a practical matter then, it becomes more efficient to solve the problem of aliasing instability by using energy-conserving schemes, despite the extra computing time per point that they require.

The advantages of energy-conserving methods are more marked when a variable grid size is employed. If the dissipation term is the usual constant eddy viscosity coefficient multiplied by the Laplacian of the velocity component, then a value of the coefficient sufficient to damp the shortest waves where the mesh is fine may be insufficient where it is coarse. (Using a larger value would presumably introduce too much damping where the mesh is fine.) It is then necessary to resort to some means other than simple viscosity to prevent nonlinear instability. One possibility is to employ a more complicated form for the dissipation; for example, an eddy coefficient which varies with the velocity shear. We do not do this because large shears are associated with the undercurrent and such a form would introduce too much lateral friction there if it were large enough to control nonlinear instabilities elsewhere.

Instead, we prefer to stabilize the computation by using a form for the finite difference equations based on conservation notions. We proceed from the following analysis of the nature of nonlinear instabilities which derives from Kreiss and Oliger (1972).

The phenomenon called nonlinear instability can be demonstrated with a linear equation with non-constant coefficients. Consider the model advection equation

$$q_t + u(x) q_x = 0 \quad (B7)$$

with cyclic boundary conditions $q(1+x) = q(x)$, and $U(1+x) = u(x)$. Clearly, q is bounded for all time. Let variables be defined at the points

$$X_j = j \Delta x \quad j = 0, \dots, N; \quad \Delta x = \frac{1}{N} \quad (B8)$$

and approximate the spatial derivative in (B7) by the usual second order centered difference D_0 (B4):

$$\frac{\partial}{\partial t} q_j = -u_j D_0(\Delta x) q_j \quad j=0, \dots, N-1 \quad (B9)$$

Let $X_{-j} = X_{N-j}$, $X_{N+j} = X_j$ so that D_0 is defined everywhere.

Now suppose there is some point X_ν such that

$$u_{\nu+1} = u_{\nu+2} = 0; \quad u_{\nu+1} < 0 < u_\nu \quad (B10)$$

Then

$$\frac{\partial}{\partial t} q_\nu = -\frac{u_\nu}{2\Delta x} q_{\nu+1}; \quad \frac{\partial}{\partial t} q_{\nu+1} = \frac{u_{\nu+1}}{2\Delta x} q_\nu$$

so that q at both points will grow exponentially with a growth rate $|u_v u_{v+1}|^{1/2} / 2\Delta x$. On the other hand, if u is bounded away from zero, then it follows from (B9) that the weighted sum $\sum_{j=0}^{N-1} u_j^{-1} q_j^2$ does not change in time. (Use has been made of the identity

$$\sum_{j=0}^{N-1} D_0(K\Delta x) = \frac{1}{2K\Delta x} \sum_{l=-K}^{K-1} [f_{N+l} - f_l] = 0 \quad (\text{B11})$$

The last equality holding because of the cyclic boundary conditions.)

Now obtain the nonlinear case by letting $q \equiv u$ and taking (B10) as initial conditions. Then from (B9):

$$\frac{\partial}{\partial t} u_{v-1} = \frac{\partial}{\partial t} u_{v+2} = 0 \quad ; \quad \frac{\partial u_{v+1}}{\partial t} = -\frac{\partial}{\partial t} u_v = \frac{u_v u_{v+1}}{2\Delta x}$$

so that u_{v-1} and u_{v+2} will remain zero for all time while u_v and u_{v+1} will both grow in magnitude. If a situation approximately like (B10) should arise in the course of a numerical integration "non-linear instability" will result. As we have seen, the problem arises from the existence of a stagnation point in the flow field - a point where $u = 0$. It follows from the original differential equation (B7) that q is constant along characteristics $dx/dt = u(x)$. As time increases, more and more characteristics will crowd into the neighborhood of the point where $u = 0$ (and $u_x < 0$) so that a steep gradient of q will build up there. The finite difference approximation,

unable to resolve this gradient, allows q to flow into this neighborhood but not out of it. The same problem will arise with higher order schemes.

One way to help the flow pass this stagnation point is to add some dissipation to the right hand side of q ; e.g.,

$$\frac{\partial}{\partial t} g_j = -u_j D_0 g_j + A D_+ D_- g_j$$

As noted above, a value of A large enough to eliminate the "non-linear" instability will damp the solution too much elsewhere. Instead, we seek an approximation to the advective term which will prevent this artificial accumulation in the neighborhood of a zero in the flow field. If $\sum_{j=0}^{N-1} q_j$ cannot grow in time such an accumulation will be impossible.

To bring the model problem closer to the problem at hand, consider (B7) together with the shallow water equations

$$h_t + (hu)_x = 0 \quad (B12)$$

$$u_t + uu_x + h_x = 0 \quad (B13)$$

again with cyclic boundary conditions. The following conservation statements are true for the system (B7), (B12), (B13):

$$\frac{\partial}{\partial t} \int_0^1 h g^n dx = 0 \quad n = 1, 2, 3, \dots$$

$$\frac{\partial}{\partial t} \int_0^1 h dx = 0 \quad (B14)$$

$$\frac{\partial}{\partial t} \int \left[\frac{hu^2}{2} + \frac{h^2}{2} \right] dx = 0$$

We wish to find a finite difference approximation which preserves these relations at least for $n = 1$ and $n = 2$.

Now any centered difference approximation d_x to the derivative may be written

$$d_x f_j = \sum_{\ell=1}^K w_\ell D_\ell(\Delta x) f_j \quad (\text{B15})$$

For any f and g we have the relation

$$\begin{aligned} 2\Delta x \sum_{j=0}^{N-1} [f_j D_0(\Delta x) g_j + g_j D_0(\Delta x) f_j] & \quad (\text{B16}) \\ &= \sum_{j=0}^{N-1} \left\{ [f_{N+j-\ell} g_{N+j} - f_{j-\ell} g_j] + [g_{N+j-\ell} f_{N+j} - g_{j-\ell} f_j] \right\} \\ &= 0 \end{aligned}$$

the last equality following from the cyclic boundary conditions.

From (B11), (B15), and (B16) we have the identities

$$\sum_{j=0}^{N-1} d_x f_j = 0 \quad ; \quad \sum_{j=0}^{N-1} [g_j d_x f_j + f_j d_x g_j] = 0 \quad (\text{B17})$$

We proceed to use these identities to obtain the finite difference analogues of the conservation statements (B14) for any centered difference approximation. Write the original equations in the form

$$\frac{\partial}{\partial t} (h g) = -\frac{1}{2} \left\{ (h u g)_x + (h u) g_x + g (h u)_x \right\}$$

$$\frac{\partial}{\partial t} h = -(hu)_x$$

$$\frac{\partial}{\partial t} (hu) = -\frac{1}{2} \{ (huu)_x + (hu)u_x + u(hu)_x \} - hh_x$$

and then replace the derivatives by the finite difference operator:

$$\frac{\partial}{\partial t} (h_j g_j) = -\frac{1}{2} \{ d_x (h_j u_j g_j) + h_j u_j d_x g_j + g_j d_x (h_j u_j) \}$$

$$\frac{\partial}{\partial t} h_j = -d_x (h_j u_j) \quad (B18)$$

$$\frac{\partial}{\partial t} (h_j u_j) = -\frac{1}{2} \{ d_x (h_j u_j u_j) + h_j u_j d_x u_j + u_j d_x (h_j u_j) \} - h d_x h$$

It is easy to see that these forms overcome the stagnation problem: even with conditions (B10) and, say, h a constant, the points $v - 1$ and $v + 2$ remain coupled to points v and $v + 1$. This finite difference form advects q through the neighborhood of the point where $u = 0$.

By using (B17) one may readily verify that with the equations in the form (B18)

$$\frac{\partial}{\partial t} \sum h_j = 0 \quad ; \quad \frac{\partial}{\partial t} \sum g_j = 0$$

$$\frac{\partial}{\partial t} \sum h_j g_j^2 / 2 = \sum \{ g_j \frac{\partial}{\partial t} (h_j g_j) - \frac{g_j^2}{2} \frac{\partial}{\partial t} h_j \} = 0 \quad (B19)$$

$$\frac{\partial}{\partial t} \left\{ \frac{1}{2} \sum h_j u_j^2 + \frac{1}{2} \sum h_j^2 \right\} = -\frac{1}{2} \sum \{ h_j u_j d_x h_j + h_j d_x (h_j u_j) \} = 0$$

where all sums are from $j = 0$ to $j = N - 1$. Thus, Eqs. (B18) are in a form which will be free from non-linear instability for any operator d_x which satisfies the identities (B17). In fact, the difference operator D_x defined by (B5) does not satisfy these identities because we have non-cyclic boundary conditions so that the final equalities in Eqs. (B11) and (B16) do not hold. For any higher order scheme these analogues of

$$\int \frac{\partial f}{\partial x} dx \quad \text{and} \quad \int \left\{ g \frac{\partial f}{\partial x} + f \frac{\partial g}{\partial x} \right\} dx$$

will leave extra terms at the boundaries. In such a case, the finite difference forms on the right hand side of (B18) are merely "almost conservative". Experience indicates that this is sufficient to prevent nonlinear instabilities. These forms will still prevent a false accumulation at stagnation points and since the deviation from conservation is small, the scheme can be made dissipative by introducing a very small amount of (viscous) dissipation.

The generalization of these ideas to more dimensions is straightforward. It is evident from the finite difference form of the full model equations, which are given in Appendix C. The use of a stretched grid is a very minor complication. For example, if (B7) were replaced by one with a metric factor in the advective term, viz.,

$$\frac{\partial g}{\partial t} + \frac{u}{m_x} g_x = 0$$

then the appropriate sums in (B19) would be the "area" weighted

ones; e.g., $\Sigma_x q_j$ instead of Σq_j , so that the right hand sides of these equations would be as before.

B.5 Gravity Wave Terms

In practice, the use of conservation forms did succeed in eliminating the explosive growth due to "nonlinear" instability. The analysis given above does admit the possibility of short wavelength computational (i.e., non-physical) modes growing to noticeable size; this was observed to happen in our computation. These modes did not grow so large as to prevent the calculation from continuing, but their presence obviously meant that it was inaccurate. The use of conservation forms allowed an inaccurate calculation to continue (cf., the discussion at the beginning of the previous section).

The troublesome computational modes were traced to the gravity wave terms in the equations. Many numerical modelers have experienced a similar problem, particularly in the form of the so-called checkerboard instability (e.g., Mesinger 1972). There is an irony in the numerical gravity waves being the source of small-scale disturbances when in the physical system they are the mechanism that adjusts the flow to a more slowly varying (e.g., geostrophic) balance by propagating such disturbances rapidly away. Mesinger (1972) has pointed out that the usual numerical treatment of gravity waves fails to couple the grid points properly. This accounts for the disparity between their physical and numerical roles.

Consider the simplest system of linear equations

describing gravity waves:

$$u_t = -gh_x \quad ; \quad h_t = -Hu_x \quad (B20)$$

Put these equations in finite difference form by replacing x derivatives with the second order centered difference operator D_0 (B4) and calculating time derivatives with the Euler backward scheme (B3):

$$u_j^* = u_j^n - \Delta t g D_0 h_j^n \quad ; \quad h_j^* = h_j^n - \Delta t D_0 u_j^n$$

$$u_j^{n+1} = u_j^* - \Delta t g D_0 h_j^* \quad ; \quad h_j^{n+1} = h_j^* - \Delta t D_0 u_j^*$$

so that the equation

$$h_j^{n+1} = h_j^n - \Delta t H D_0 [u_j^n - \Delta t g D_0 h_j^n] = h_j^* + (\Delta t)^2 (gH) D_0^2 h_j^n \quad (B21)$$

relates values of h at successive timesteps. This is analogous to the wave equation

$$h_{tt} = gH h_{xx} \quad (B22)$$

Suppose that h^n has the form of a two grid point wave:

$$h^n(x) = \cos(\pi x / \Delta x) \quad \text{so} \quad h_j^n = \cos(\pi x_j / \Delta x) = (-1)^j$$

The right hand side of the continuous equation (B22) gives a local smoothing of order $(\Delta x)^{-2}$. More correctly, (B22) allows the wave to propagate the height extrema away with a speed $(gH)^{1/2}$. The finite difference equation (B21) becomes

$$\begin{aligned}
 h_j^{n+1} - h_j^n &= gH(\Delta t)^2 D_0^2 h_j^n = gH \frac{(\Delta t)^2}{(2\Delta x)^2} [h_{j+2}^n - 2h_j^n + h_{j-2}^n] \\
 &= gH \frac{(\Delta t)^2}{(2\Delta x)^2} [(-1)^{j+2} - 2(-1)^j + (-1)^{j-2}] = 0
 \end{aligned}$$

so that there is no smoothing at all. That is, the wave does not propagate and the disturbance remains. Presumably, whatever acted as the source of this disturbance will continue to pump energy into it--in phase since it is not propagating--and its amplitude will increase. The finite difference approximation has suppressed the ability of these gravity waves to adjust the flow. The approximation to the second derivative in (B22) connects only every other point because it has been made as two successive approximations to the first derivative. Any scheme which treats the equations in their original form (B20) will have essentially the same shortcoming; the particular scheme given here was chosen as the most straightforward illustration. For instance, the centered fourth-order scheme (B5a) will introduce a weak coupling between successive points--one which is an order of magnitude weaker than it should be, and, more importantly, has the wrong sign.

To remedy the difficulty, the finite difference scheme must capture the "smoothing" effect of the second derivative in the wave equation, (B22). For example, (B21) could be used with the D_0^2 operator replaced by D_+D_- , an approximation to the second derivative which uses three adjacent points, viz.

$$\text{or } h_j^{n+1} = h_j^* + (\Delta t)^2 g H D_+ D_- h_j^n$$

$$h_j^{n+1} = h_j^n - \Delta t H D_0 u_j^n + g H (\Delta t)^2 \{D_+ D_- - D_0^2\} h_j^n$$

The latter equation shows explicitly how the original finite difference equation has been altered. We have, in effect, added a smoothing operator $gH(\Delta t)^2\{D_+D_- - D_0^2\}$ to the equation. Since both D_+D_- and D_0^2 are second order approximations to the second derivative, their difference is $O(\Delta x^2)$, so that the change from the original equation is the same order as the error in that equation. Both the original and modified equations are formally the same order of accuracy in space and hence, from that point of view, equally correct. The latter is a better approximation because it alone preserves an important property of the original physical system.

It is not difficult to generalize this scheme. Consider the model equations

$$\begin{aligned} \frac{\partial}{\partial t} u &= f_1(u, h, x, t, \dots) - gh_x \\ \frac{\partial}{\partial t} h &= f_2(u, h, x, t, \dots) - Hu_x \end{aligned} \quad (\text{B23})$$

where H is a constant--for example, the mean value of h . We will time march with the N cycle scheme and approximate first and second derivatives by δ_x and δ_{xx} , respectively. Steps (iii) and (iv) of the N -cycle scheme (B2) are replaced by

$$(iii) \quad \begin{aligned} z_u^n &= b_n [a_n z_u^{n-1} + f_2^n - g \delta_x h^n + b_n^* g H(\delta_{xx} - \delta_x^2) u^{n-1}] \\ z_h^n &= b_n [a_n z_h^{n-1} + f_2^n - H \delta_x u^n + b_n^* g H(\delta_{xx} - \delta_x^2) h^{n-1}] \end{aligned}$$

$$(iv) \quad \begin{aligned} u^{n+1} &= u^n + z_u^n \\ h^{n+1} &= h^n + z_h^n \end{aligned} \quad (B24)$$

where

$$b_n^* = \begin{cases} 0 & \text{if } n \equiv 0 \pmod{N} \\ b_{n-1} & \text{otherwise} \end{cases}$$

The difference from the usual N cycle scheme is the term with the smoothing operator $\delta_{xx} - \delta_x^2$. If the operators δ_x and δ_{xx} are both accurate to order m then both δ_x^2 and δ_{xx} are m th order approximations to d^2/dx^2 and their difference is order m . Hence, the equations with the added term are formally of the same order as before.

In order to get a clearer picture of the effect of the smoothing operator, consider a function of the form $\exp(2\pi i x / K\Delta x)$, so that $K = 2, 3, 4, \dots$ corresponds to 2, 3, 4, ... grid point waves. For second order centered differences, $\delta_x = D_0$, $\delta_{xx} = D_+ D_-$

$$(\Delta x)^2 \{D_+ D_- - D_0^2\} \exp\left(\frac{2\pi i x}{K\Delta x}\right) = -4 \sin^4\left(\frac{\pi}{K}\right) \exp\left(\frac{2\pi i x}{K\Delta x}\right)$$

For fourth order centered differences (as are used in our model)

$$\delta_x \equiv D_x \quad ; \quad \delta_{xx} \equiv D_{xx}$$

$$(\Delta x)^2 [D_{xx} - D_x^2] \exp\left(\frac{2\pi i x}{k \Delta x}\right) = -\frac{16}{9} \sin^6\left(\frac{\pi}{k}\right) (2 + \sin^2\frac{\pi}{k}) \exp\left[\frac{2\pi i x}{k \Delta x}\right]$$

For convenience define

$$S_2(k) = 4 \sin^4 \frac{\pi}{k} \quad S_4(k) = \frac{16}{9} \sin^6\left(\frac{\pi}{k}\right) (2 + \sin^2 \frac{\pi}{k})$$

so that $S_2(k)$ and $S_4(k)$ are the smoothing factors for a k grid point wave for the second and fourth order schemes, respectively. Both are always positive and are a maximum for $k = 2$. To see their behavior for small k , we construct the following table; for comparison purposes we also include $1/4 D_+ D_- \exp(2\pi i x / k \Delta x)$; i.e., the usual approximation to the second derivative of the viscous term:

k=	2	3	4	5	6
$S_2(k)$	4.00	2.25	1.00	0.48	0.25
$S_4(k)$	5.33	2.06	0.55	0.17	0.06
$1/4 D_+ D_-$	1.00	0.75	0.50	0.34	0.25
$S_2(k)/S_2(2)$	1.00	0.56	0.25	0.12	0.06
$S_4(k)/S_4(2)$	1.00	0.39	0.10	0.03	0.01

The damping effect of the smoothing operators falls off extremely rapidly with increasing wavelength--much faster than the usual form of viscous dissipation. That of the higher order operator falls off the most rapidly--its effect on the four grid point wave is an order of magnitude smaller than on

the two grid point. For longer waves (larger k), S_4 falls off like k^{-6} and S_2 like k^{-4} while the second derivative approximation goes like k^{-2} . These smoothing operators--particularly the higher-order one that we use have the nice property of effecting only the very shortest scales, scales which are insufficiently resolved by the grid anyway.

Thus far, we have employed smoothing operators in a way which gives an improved approximation to certain terms in the equations and thereby retains an important property of the gravity waves in the physical system. However, the short wave selectivity of these operators suggests another use. Since the $\delta_{xx} - \delta_x^2$ is the same order as the error in the spatial finite differences, such a term may be added to any equation without changing its formal order of accuracy. Also, applying it at the previous timestep as in (B24) makes it an advective rather than a dissipative operator.

In a multi-dimensional problem there are velocity shears across the direction of flow (e.g., the latitudinal shear in the zonal velocity, U_y). Normally, very small-scale features --like two grid point waves--should be damped by viscosity. As previously noted, however, with a variable grid size the amount of viscous damping needed to suppress grid scale noise where the mesh is finest is insufficient where it is coarse. Rather than adopt the uneconomical option of making the grid size small everywhere, we prefer to add smoothing operators in the cross stream direction. For example, step (iii) of the N-cycle scheme (B24) would be changed to

$$(iii) \quad z_u^n = b_n \left(\dots + b_n^* g H (\delta_{yy} - \delta_y^2) u^{n-1} \right) \quad (B25)$$

A similar operator in the x direction would be added to the v momentum. (See Appendix C for the details of the full model equations.)

Unlike the previous procedure, this smoothing adds unphysical "momentum waves" to the equations--though only in a way which leaves the order of accuracy of the equations unaltered. (Every numerical procedure alters the physics of the original system somewhat. Usually it is difficult to describe the changes explicitly.) Since the operator is so wavelength selective, only the shortest waves are affected. Moreover, where the grid mesh is fine, the viscous damping is adequate to suppress small-scale noise so that these added operators have no effect in these regions--this was verified by experiment. It is not necessary to do this, but as a matter of taste we prefer to have the calculation controlled by the better understood dissipation mechanism in the regions of primary interest.

3.6 Summary

The model equations are marched forward in time using the 4-cycle scheme of Lorenz (Eqs. B2). The grid mesh is uniform in the computational space, but has variable size in physical space to give increased resolution at the equator and the sidewalls; the relation between the two coordinate systems is given by (B1) ff. The finite difference approximations to

spatial derivatives are fourth order in the interior and third order at the boundaries, Eqs. (B5), (B6). The equations are differenced in an "almost conservative" form (B18) to prevent "nonlinear" instability without introducing either excessive viscous damping or a number of grid points larger than would otherwise be required. In order to treat short waves in the height field more correctly, an improved approximation for the gravity wave terms is introduced (B24). A smoothing operator motivated by the gravity wave treatment is used to suppress two grid point waves in the velocity fields (B25). This has an effect only in areas of the grid where the spacing is too coarse for this suppression to be done by the viscous damping. The complete finite difference equations for a beta plane geometry are given in Appendix C.

In addition to allowing all of the parameters listed in Table 1 to be varied, the computer program allows the user to choose an f-plane, a beta plane or spherical geometry; to resolve or not resolve boundary layers at the walls and the equator; to locate the basin at any latitude and vary its size; to choose any of the boundary conditions (2.9a), (2.9b) or (2.9c); to have one active layer (2.4) or two active layers (2.8); and to use the nonlinear equations or to linearize about the basic state $u = v = 0$, $h = \bar{H}$; to apply the gravity wave correction (B24) to only the height field, or to the velocities in the downstream direction in addition, or to all fields in both horizontal directions.

Appendix C Finite Difference Equations on Beta Plane

This appendix derives the finite difference version of the model Eqs. (2.8). We do this only for the beta plane geometry described at the end of Section 2.1. The more general geometry complicates the equations without adding anything essential; moreover, all of the results presented in the body of this work are for the beta plane case.

We begin by putting the equations in a conservation form like (B18). For this purpose rewrite the model Eqs. (2.8) in the form

$$w = R_0 \eta \nabla \cdot \underline{u}^s \equiv R_0 \eta \left\{ \frac{1}{m_x} \frac{\partial u^s}{\partial x} + \frac{1}{m_y} \frac{\partial v^s}{\partial y} \right\} \quad (C1a)$$

$$\frac{\partial}{\partial t} q^s = -R_0 (\underline{u}^s \cdot \nabla) q^s - \frac{w}{2\eta} (q^s - q^1) + R_{qs} \quad (C1b,c)$$

$$\frac{\partial}{\partial t} q^1 = -R_0 (\underline{u}^1 \cdot \nabla) q^1 - \frac{w}{2\eta} (q^s - q^1) + R_{q1} \quad (C1d,e)$$

$$\frac{\partial}{\partial t} h = -R_0 \nabla \cdot (h \underline{u}^1) - w \quad (C1f)$$

Here q^s may be either u^s or v^s and q^1 either u^1 or v^1 . Multiply (C1b, c) by η and use (C1a) to rewrite $w/2 q^s$:

$$\begin{aligned} \frac{\partial}{\partial t} (\eta q^s) &= -R_0 \nabla \cdot (\eta q^s \underline{u}^s) + \frac{R_0}{2} \nabla \cdot (\eta \underline{u}^s) q^s + \frac{w}{2} q^1 + \eta R_{qs} \\ &= -\frac{R_0}{2} \left\{ \nabla \cdot (\eta q^s \underline{u}^s) + \eta (\underline{u}^s \cdot \nabla) q^s + q^s \nabla \cdot (\eta \underline{u}^s) \right\} \\ &\quad + R_0/2 q^s \nabla \cdot (\eta \underline{u}^s) + \frac{w}{2} q^1 + \eta R_{qs} \end{aligned}$$

$$\frac{\partial}{\partial t} (\eta q^s) = -\frac{R_0}{2} \left\{ \nabla \cdot (\eta q^s \underline{u}^s) + \eta (\underline{u}^s \cdot \nabla) q^s \right\} + \frac{w}{2} q^1 + \eta R_{qs} \quad (C2)$$

Equation (C2) is the desired analogue of (B18) for the upper level. For the lower level, multiply (C1d,e) by h and add q^1 x (C1f):

$$\begin{aligned} \frac{\partial}{\partial t}(h q^1) &= -R_0 \nabla \cdot (q^1 h \underline{u}^1) - \frac{W}{2} (q^s + q^1) + h R_{f1} \\ \frac{\partial}{\partial t}(h q^1) &= -\frac{R_0}{2} \left\{ \nabla \cdot (q^1 h \underline{u}^1) + h (\underline{u}^1 \cdot \nabla) q^1 + q^1 \nabla \cdot (h \underline{u}^1) \right\} \\ &\quad - \frac{W}{2} q^1 - \frac{W}{2} q^s + h R_{f1} \\ \frac{\partial}{\partial t}(h q^1) &= -\frac{1}{2} \left\{ R_0 \nabla \cdot (q^1 h \underline{u}^1) + R_0 h (\underline{u}^1 \cdot \nabla) q^1 \right. \\ &\quad \left. + q^1 \left(-\frac{\partial h}{\partial t} \right) \right\} - \frac{W}{2} q^s + h R_{f1} \quad (C3) \end{aligned}$$

Eq. (C3) is the required form for the lower level. As long as $\frac{\partial h}{\partial t}$ is calculated the same way in (C3) and (C1f) terms involving it will exactly cancel in the energy equation--as they should. However, if the finite difference formula for the lower level divergence $\nabla \cdot (h \underline{u}_1)$ is different from that used for the pressure gradient term, then the sum of the terms involving the conversions between potential and kinetic energy will not sum to zero identically. This is the case for our model equations (cf., Eqs. C6, below).

The basic finite difference operators are D_x and D_{xx} as given by (B5) and (B6) with similar operators D_y and D_{yy} in

y direction. It is convenient to define the following analogs of the differential operators:

$$\nabla \cdot \underline{u} \equiv \frac{1}{m_x} D_x u + \frac{1}{m_y} D_y v$$

$$(\underline{u} \cdot \nabla) \phi \equiv \frac{u}{m_x} D_x \phi + \frac{v}{m_y} D_y \phi \quad (C4)$$

$$\nabla^2 \phi = \frac{1}{m_x^2} D_{xx} \phi + \frac{1}{m_y^2} D_{yy} \phi - \frac{1}{m_x^2} \frac{\partial m_x}{\partial x} D_x \phi - \frac{1}{m_y^2} \frac{\partial m_y}{\partial y} D_y \phi$$

Also define smoothing operators

$$S_x \equiv \frac{1}{m_x^2} [D_{xx} - D_x^2] \quad S_y = \frac{1}{m_y^2} [D_{yy} - D_y^2]$$

All variables are defined at grid points $X_i = i\Delta x$, $i = 0, \dots, N_x$, $Y_j = y_s + j\Delta y$, $j = 0, \dots, N_y$ and times $t_n = n\delta t$. Where necessary, we write q_{ij}^n for $q(x_i, y_j, t_n)$ but we will suppress subscripts and superscripts where no confusion can arise. Specifying the finite difference equations requires that we specify steps (iii) and (iv) of the N-cycle scheme (B2) completely. We begin with the following definitions, based on (2.8), (C2), and (C3).

$$W = R_0 \eta \nabla \cdot \underline{u}^s$$

$$F_{us} = -\frac{R_0}{2} \left\{ \nabla \cdot (\eta \underline{u}^s u^s) + \eta (\underline{u}^s \cdot \nabla) u^s \right\} + \frac{W}{2} u^s \\ + F_{nd} \eta v^s - \eta E_r \frac{R_0}{m_x} D_x h + T \tau^{(x)} - B(u^s - u^t) + \eta E_n \nabla^2 u^s$$

$$F_{vs} = -\frac{R_0}{2} \left\{ \nabla \cdot (\eta \underline{u}^s v^s) + \eta (\underline{u}^s \cdot \nabla) v^s \right\} + \frac{W}{2} v^s \\ - F_{us} u^s \eta - \eta F_r^{-1} \frac{R_0}{m_y} D_y h + \overline{T} \tau^{(y)} - B(v^s - v^s) + \eta E_H \nabla^2 v^s$$

$$F_{u1} = -\frac{R_0}{2} \left\{ \nabla \cdot (\underline{u}^1 h u^1) + h (\underline{u}^1 \cdot \nabla) u^1 \right\} + \frac{U^1}{2} F_h - \frac{W}{2} u^s \\ + f_{us} h v^s - h F_r^{-1} \frac{R_0}{m_x} D_x h + B(u^s - u^1) - B_B u^1 + h E_H \nabla^2 u^1$$

$$F_{v1} = -\frac{R_0}{2} \left\{ \nabla \cdot (h \underline{u}^1 v^1) + h (\underline{u}^1 \cdot \nabla) v^1 \right\} + \frac{V^1}{2} F_h - \frac{W}{2} v^s \\ - F_{us} h u^1 - h F_r^{-1} \frac{R_0}{m_x} D_x h + B(v^s - v^1) - B_B v^1 + h E_H \nabla^2 v^1$$

$$F_h^n = -R_0 \nabla \cdot (h^n \underline{u}^{1n}) - w^n + b_n^{(1)} \{ S_x + S_y \} h^{n-1} \quad (C6)$$

(b⁽¹⁾) will be defined below.

Steps (iii) and (iv) of the N-cycle scheme are

(iii)

$$Z_{us}^n = b_n [a_n Z_{us}^{n-1} + F_{us}^n + (b_n^{(2)} S_x + b_n^{(3)} S_y) (u^s)^{n-1}] \\ Z_{vs}^n = b_n [a_n Z_{vs}^{n-1} + F_{vs}^n + (b_n^{(3)} S_x + b_n^{(2)} S_y) (v^s)^{n-1}] \\ Z_{u1}^n = b_n [a_n Z_{u1}^{n-1} + F_{u1}^n + (b_n^{(2)} S_x + b_n^{(3)} S_y) (u^1)^{n-1}] \\ Z_{v1}^n = b_n [a_n Z_{v1}^{n-1} + F_{v1}^n + (b_n^{(3)} S_x + b_n^{(2)} S_y) (v^1)^{n-1}] \\ Z_h^n = b_n [a_n Z_h^{n-1} + F_h^n] \quad (C7a)$$

(iv)

$$\begin{aligned}
 (nu^s)^{n+1} &= (nu^s)^n + Z_{us}^n \\
 (nv^s)^{n+1} &= (nv^s)^n + Z_{vs}^n \\
 (hu^1)^{n+1} &= (hu^1)^n + Z_{u1}^n \\
 (hv^1)^{n+1} &= (hv^1)^n + Z_{v1}^n \\
 h^{n+1} &= h^n + Z_h^n
 \end{aligned} \tag{C7b}$$

The $b^{(k)}$'s are defined by (cf., Eq. B24 ff):

$$b_n^{(k)} = \begin{cases} 0 & \text{if } n \equiv 0 \pmod{N} \text{ or } k > s \\ b_{n-1} T_r^{-1} R_0 \bar{H} & \text{otherwise} \end{cases} \tag{C8}$$

\bar{H} is the mean depth of two levels ($\bar{H} = \eta + H_1$), the a_n 's and b_n 's are the N-cycle coefficients given in (B2), and s is an input parameter which allows the smoothing to be applied selectively. Usually, $s = 3$ so that all the $b^{(k)}$'s are non-zero.

The finite difference equations for the one layer system are readily obtained from (C6) and (C7) by ignoring the upper layer equations, taking $w = B = 0$ and adding $T(x)$ and $T(g)$ to F_{u1} and F_{v1} , respectively. The two layer linear equations are obtained by linearizing the expressions in (C6) about the basic state $u_s = u_1 = 0$ and $h = H_1 = \text{constant}$. This amounts to taking $R_0 \equiv 0$ (except that $F_r^{-1} R_0$ remains finite) and $h = H_1$

when it appears multiplying another term--i.e., everywhere in the pressure gradient terms ($h\nabla h$ becomes $H_1\nabla h$). The one layer equations are linearized in the same manner.

Appendix D Computational Stability (Linear Analysis)

D.1 Time Differencing

We write our system of equations in the form

$$\frac{\partial \underline{u}}{\partial t} \approx \underline{A}(\underline{u}) \underline{u} \quad (D1)$$

Let $\lambda^j = i\lambda_A - \lambda_D$ be Δt , the timestep, times the j th eigenvalue of \underline{A} . The imaginary part, λ_A^j arises from the advective part of the operator \underline{A} and λ_D^j from the dissipative part; we assume the system is not growing in time so $\lambda_D^j \geq 0$. The eigenvalues with the largest values of λ_A or λ_D will set the stability criterion. Usually the largest magnitude of both λ_A or λ_D are associated with the same eigenfunction: the two grid point wave. Computational stability requires that all modes have a growth rate G^j such that $|G^j| \leq 1$.

For the Matsuno (Euler backward) time differencing scheme, the growth rate G of a mode with eigenvalue λ is

$$G = 1 + \lambda + \lambda^2 \quad (D2)$$

For computational stability:

(a) If $\lambda_A = 0$ then $\lambda_D \leq 1$

(b) If $\lambda_D = 0$ then $|\lambda_A| \leq 1$

As is well known, for a purely advective problem ($\lambda_D = 0$) the Matsuno scheme is always damping. This may be seen immediately by comparing (D2) with the Taylor series for the value of G given by the original equation, i.e., $G = \exp(\lambda)$.

For the N-cycle scheme

$$G = \sum_{n=0}^N \lambda^n / n! \quad (D3)$$

Computational stability requires, that, for the 4-cycle scheme

(a). If $\lambda_A = 0$ then $\lambda_D \leq 2.7$

(b). If $\lambda_D = 0$ then $|\lambda_A| \leq \sqrt{8} \approx 2.8$

For a purely advective problem we may obtain an estimate of the damping by noting that if $|\lambda_A| \ll 1$, then

$$G \approx e^{i\lambda_A} - (i\lambda_A)^{N+1} / (N+1)!$$

For N even

$$G \approx \cos \lambda_A + i [\sin \lambda_A - (-1)^{N/2} \lambda_A^{N+1} / (N+1)!]$$

and

$$|G|^2 \approx 1 - (-1)^{N/2} \frac{2}{(N+1)!} \lambda_A^{N+1} \sin \lambda_A \approx 1 - \frac{2(-1)^{N/2}}{(N+1)!} \lambda_A^{N+2}$$

Hence the scheme is damping if N is a multiple of 4.

For N = 4 $|G| \approx 1 - \lambda_A^6 / 5!$

For N = 8 $|G| \approx 1 - \lambda_A^{10} / 9!$

While for N = 6 $|G| \approx 1 + \lambda_A^8 / 7!$

For N = 4, the exact value is

$$|G|^2 = 1 - \lambda_A^6 / 72 + \lambda_A^8 / (24)^2$$

$$|G| \approx 1 - \lambda_A^6 / 144 = 1 - \frac{5}{6} \lambda_A^6 / 5!$$

D.2 Space Differencing

It remains to calculate the values of λ_A and λ_D appropriate to our finite difference equations. The prototypical advective term cu_x and dissipative term νu_{xx} are approximated by $cD_x u$ and $\nu D_{xx} u$ respectively. The maximum eigenvalues of D_x and D_{xx} will have the respective forms $\mu_1 / \Delta x$, $-\mu_2 / (\Delta x)^2$.

For the 4th order centered schemes we use $\mu_1 = 1.37$ and $\mu_2 = 5.33$. For an advective velocity $c = 2\text{m/sec}$ (i.e., the gravity wave phase speed) and Δt in units of $(2\Omega)^{-1}$ and Δx in degrees (=110 km)

$$\lambda_A = \frac{c\mu_1}{\Delta x_{dim}} \Delta t_{dim} = .17 \frac{\Delta t}{\Delta x} \approx \frac{\Delta t}{6\Delta x}$$

For $\nu_H = E^* 5.86 \times 10^5 \text{ cm}^2 \text{ sec}^{-1}$ (i.e., $E^* = 1$ corresponds to an Ekman number of 10^{-8})

$$\lambda_H = \frac{\nu\mu_2}{(\Delta x_{dim})^2} \Delta t_{dim} = 1.77 \times 10^{-4} \frac{E^* \Delta t}{(\Delta x)^2}$$

The vertical friction term gives a further dissipative contribution. In non-dimensional terms this is approximated by

$$\lambda_v \approx B^* B \Delta t / \eta = 10^{-3} \Delta t B^* / \eta$$

where the give value of B corresponds to $\nu_v = 15 \text{ cm}^2 \text{ sec}^{-1}$ and η is the boundary layer thickness in units of 100 m.

For the 4-cycle scheme with $\Delta t = 4\delta t$ we obtain the following restrictions on the timestep (remembering that the equations are 2-dimensional)

$$.42 \left[\frac{1}{\Delta x} + \frac{1}{\Delta y} \right]^{-1} \geq \delta t_A$$

$$3.8 \cdot 10^3 (E^*)^{-1} \left[\frac{1}{(\Delta x)^2} + \frac{1}{(\Delta y)^2} \right]^{-1} \geq \delta t_H$$

$$680 \eta / B^* \geq \delta t_V$$

For $B^* = E^* = 1$, $\Delta x = \Delta y = .3$ and $\eta = .25$

$$\delta t_A \leq .63 ; \delta t_H \leq 180 ; \delta t_V \leq 170$$

It is clear that the timestep is restricted by the advective terms; specifically, by the gravity wave terms. Since the system realizes current velocities of the order of 150 cm sec^{-1} treating the gravity wave terms implicitly would allow the timestep to be increased by only a factor of three or so. The additional computations required by such a semi-implicit method would appear to nullify the time saved by using a larger timestep.

APPENDIX E: COMPUTATIONAL FORMULAS FOR CHAPTER 4

E.1 Properties of the Hermite Functions

The Hermite functions $\psi_n(y)$ which appear in (4.7) ff. are defined by

$$\psi_n(y) = \pi^{-1/4} (2^n n!)^{-1/2} e^{-y^2/2} H_n(y) \quad (\text{E1})$$

where H_n is the n th Hermite polynomial

$$H_n(y) = (-1)^n e^{y^2} \frac{d^n}{dy^n} (e^{-y^2})$$

The Hermite functions vanish at infinity and are orthonormal; i.e.,

$$\int_{-\infty}^{+\infty} \psi_n(y) \psi_m(y) dy = \begin{cases} 0 & n \neq m \\ 1 & n = m \end{cases} \quad (\text{E2})$$

They satisfy the equation

$$(d^2/dy^2 - y^2) \psi_n = -(2n+1) \psi_n \quad (\text{E3})$$

The \underline{p}^n may be rewritten in terms of the ψ_n 's only by using

$$\begin{aligned} y \psi_n &= \left[\frac{n+1}{2} \right]^{1/2} \psi_{n+1} + \left[\frac{n}{2} \right]^{1/2} \psi_n \\ d\psi_n/dy &= -\left[\frac{n+1}{2} \right]^{1/2} \psi_{n+1} + \left[\frac{n}{2} \right]^{1/2} \psi_n \end{aligned} \quad (\text{E4})$$

E.2 The Projections of the Forcing Functions

That is, the calculation of $b_{n,j}$ such that

$$F = \sum b_{n,j} \phi_{n,j}$$

Let $u_\alpha(y) = (u_\alpha(y), v_\alpha(y), h_\alpha(y))$ For $\alpha = a$ or $\alpha = b$

and let $+$ denote complex conjugate. Define a scalar product by

$$(u_a, u_b)_v \equiv \int_{-\infty}^{\infty} \{u_a^+ u_b + v_a^+ v_b + h_a^+ h_b\} dy \quad (E5)$$

We may now normalize $\phi_{n,j}$ by defining the $N_{n,j}$ which appears in (5.8):

$$N_{n,j}^2(k) = (2n+1)(\omega_{n,j}^2 + k^2) + 2k\omega_{n,j} + (\omega_{n,j}^2 - k^2)^2 \quad (E6)$$

This leaves $\phi_{n,j}$ undefined for $k=0$ so define

$$\phi_{n,j}(0, y) = \lim_{k \rightarrow 0} \phi_{n,j}(k, y) \quad (E7)$$

Now

$$(\phi_{n,j}, \phi_{m,l})_v = \begin{cases} 1 & \text{if } n=m \text{ and } j=l \\ 0 & \text{otherwise} \end{cases}$$

and $b_{n,j} = (\phi_{n,j}, F)_v$

Let $F(k, y, t) = (F(k, y, t), G(k, y, t), Q(k, y, t))$

$$= \sum_{n=0}^{\infty} (f_n(k, t), g_n(k, t), \xi_n(k, t)) \psi_n(y)$$

where the ψ_n are the Hermite functions and

$$f_n = \int_{-\infty}^{+\infty} F \psi_n dy, \quad g_n = \int_{-\infty}^{+\infty} G \psi_n dy, \quad \xi_n = \int_{-\infty}^{+\infty} Q \psi_n dy$$

Define

$$\begin{aligned}
 d_n(k,t) &\equiv \int_{-\infty}^{+\infty} (yF + Q_y) \Psi_n dy \\
 &= \left(\frac{n+1}{2}\right)^{1/2} [f_{n+1} + g_{n+1}] + \left[\frac{n}{2}\right]^{1/2} [f_{n-1} - g_{n-1}] \\
 e_n(k,t) &\equiv \int_{-\infty}^{+\infty} (F_y + yQ) \Psi_n dy \\
 &= \left(\frac{n+1}{2}\right)^{1/2} [f_{n+1} + g_{n+1}] + \left(\frac{n}{2}\right)^{1/2} [g_{n-1} - f_{n-1}] \quad (E8)
 \end{aligned}$$

$$\begin{aligned}
 v_n(k,t) &\equiv [e_n - (2n+1)d_n] \left[\frac{2n+1}{4n(n+1)} \right] \\
 b_{-1}(k,t) = d_{-1}(k,t) &\equiv 2^{-1/2} \int_{-\infty}^{+\infty} (F+Q) \Psi_0 dy = 2^{-1/2} (f_0 + g_0)
 \end{aligned}$$

$$\text{Then } b_{n,j}(k,t) = N_{n,j}^{-1} \left\{ \omega_{n,j} d_n + K e_n + i(\omega_{n,j}^2 - k^2) g_n \right\} \quad (E9)$$

E.3 Boundary Response Terms

This part of the Appendix goes with Section 4.4.

We are concerned here with some aspects of the boundary response to the unbounded solution, Eqs. (4.15)-(4.17).

(a) Inertia gravity waves (4.15) at an eastern boundary. $x=X_E$

For example, let the incoming wave take the form (4.15) with $d_n=0$ (meridional wind stress only). Then,

$$\omega = (2n+1)^{1/2}, \quad K_{n,w}(\omega) = -\omega^{-1} = (2n+1)^{-1/2} \quad \text{and the outgoing}$$

propagating wave is

$$\underline{u}_w = \frac{g_n}{2n+2} \cos z_n \left[P_{-1}^n - (2n+1)^{-1} P_{-3}^n \right] - \frac{g_n}{(2n+1)^{1/2}} \sin z_n \left[\frac{n}{n+1} \right] P_{-2}^n \quad (E10)$$

with $Z_n = (2n+1)^{1/2} [t + (2n+1)^{-1} (x - X_E)]$
 for $X_E - x \leq t [2(2n+1) - \frac{1}{2n+1}]^{-1}$

The modes generated with $m > n$ are boundary trapped
 [see (4.30)],

$$K_{m,w} = -\frac{1}{2} (2n+1)^{-1/2} - i \left[2(m-n) - \frac{1}{4(2n+1)} \right]^{1/2} \quad (E11)$$

(b) Reflection of Kelvin mode (4.17) at an eastern boundary
 $x = X_E$:

Define the symbol α_m^n by

$$\alpha_m^n = \begin{cases} 0 & \text{if } m > n \text{ or } m \not\equiv n \pmod{2} \\ 1 & \text{if } m = n \\ \left[\frac{n}{n-1} \cdot \frac{n-2}{n-3} \cdots \frac{m+2}{m+1} \right]^{1/2} & \text{otherwise} \end{cases} \quad (E12)$$

Let the incoming Kelvin mode be $t d_1 \phi_{-1}$. The
 response $\underline{u}_{K,e}$ may be found from the algorithm (4.39)

$$\underline{u}_{K,e} = d_1 \sum_{n=1}^{\infty} \alpha_1^n S(Z_n) \left\{ Z_n \left[\frac{2n+1}{2n(n+1)} \right] \underline{P}_R^n + 2 \underline{P}_2^n \right\} \quad (E13)$$

with $Z_n = t + (2n+1)(x - X_E)$ and S is the Heaviside
 step function. Note that $(0, 0, 1) = \pi^{1/4} \left\{ \phi_{-1} - \sum \frac{2n+1}{2n(n+1)} \alpha_1^n \underline{P}_R^n \right\}$

and that $y = 2\pi^{1/4} \sum \alpha_1^n \Psi_n$ so that $t d_1 \phi_{-1} + \underline{u}_{K,e}$

tends toward $d_{-1} \pi^{-1/4} (0, y, t)$ at the boundary.

(c) Reflection of a Rossby mode of the form $v_J t P_R^J$ (4.16) at a western boundary $x=0$.

The response is calculated by the algorithm (4.37). The small ω approximation (4.33) is made so $K_{n,e} \approx -(2n+1)\omega$ and $K_{n,w} \approx -\omega^{-1}$. The asymptotics of Section 4.4 apply.

$$v_J t P_R^J = v_J t P_3^J - \frac{v_J t P_1^J}{2J+1}$$

$$\text{Let } a_{J,J} = -v_J \left[1 - \frac{1}{2J+1} \right] = -v_J \frac{2J}{2J+1} \quad (\text{E14})$$

$$a_{J,n} = v_J \frac{2}{2J+1} \alpha_n^J \quad 0 \leq n < J$$

$$a_{J,1} = a_{J,1}$$

$$\begin{aligned} \text{The response } u_{R,w} = & \sum_{n=1}^J a_{J,n} S(t - 8(2n+1)x) \left\{ \left[\frac{z_n}{x} \right]^{1/2} J_1(2\sqrt{xz_n}) P_3^n \right. \\ & + \frac{z_n}{x} J_2(2\sqrt{xz_n}) P_2^n \left. \right\} + a_{J,-1} S(t-x) (t-x) \phi_{-1} \\ & + a_{J,0} S(t-x) \left\{ \left[\frac{z_0}{x} \right]^{1/2} J_1(2\sqrt{xz_0}) P_3^0 + \frac{z_0}{x} J_2(2\sqrt{xz_0}) P_2^0 \right\} \quad (\text{E15}) \end{aligned}$$

$$\text{with } z_n = t - (2n+1)x$$

The amplitude of the Kelvin mode in response to all modes of the form (4.16) is

$$A_{-1} = \sum_{J=1}^{\infty} a_{J,-1} = 2 \sum_{J=1}^{\infty} \frac{r_J}{2J+1} \alpha_1^J$$

The amplitude of the nth Rossby mode in response to all of the modes of the form (4.16) is

$$A_n = \sum_{J=n+2}^{\infty} \frac{2 r_J}{2J+1} \alpha_n^J - \frac{2n}{2n+1} r_n$$

For the case $\underline{F} = (1, 0, 0)$:

$$d_{-1} = \pi^{1/4}, \quad e_J = 0, \quad d_J = 2\pi^{1/4} \alpha_1^J, \quad r_J = -\pi^{1/4} \frac{\alpha_1^J}{2J(J+1)} \quad (\text{E16})$$

So

$$A_{-1} = -\pi^{1/4} \sum_{J=1}^{\infty} \frac{(\alpha_1^J)^2}{J(J+1)(2J+1)} \approx -0.26 \approx -\frac{\pi^{1/4}}{5} \quad (\text{E17})$$

$$A_n = \pi^{1/4} \left\{ \frac{\alpha_1^n}{(n+1)(2n+1)} - \sum_{J=n+2}^{\infty} \frac{\alpha_1^J \alpha_n^J}{J(J+1)(2J+1)} \right\} \quad (\text{E18})$$

APPENDIX F: ORTHOGONALITY AND COMPLETENESS OF THE EIGENFUNCTIONS
FOR THE SHALLOW WATER EQUATIONS

(a) Orthogonality

From the orthogonality of the Hermite functions ψ_n , it follows that

$$\left(\phi_{n,j}(k,y), \phi_{m,l}(k,y) \right)_V = 0 \quad \text{if } n \neq m$$

It remains to show that

$$A_{j\ell}^n = N_{n,j} N_{n,\ell} \left(\phi_{n,j}, \phi_{n,\ell} \right)_V = 0 \quad \text{if } j \neq \ell.$$

From the definition of the scalar product (E5):

(i) $A_{j\ell}^0 = 1 + \frac{1}{\omega_{01}\omega_{02}}$ for $j \neq \ell$; since ω_{01}, ω_{02} satisfy

$$\omega^2 - K\omega - 1 = 0$$

their product is -1 and

$$A_{j\ell}^0 = 0 \quad \text{for } j \neq \ell$$

(ii) For $n > 0$ $A_{j\ell}^n = \omega_j \omega_\ell [2n+1 + \omega_j \omega_\ell]$

$$+ K(\omega_\ell + \omega_j) + K^2 [2n+1 + K^2(\omega_\ell + \omega_j)^2 + 2\omega_\ell \omega_j]$$

(where we have written ω_j for $\omega_{nj}(k)$, etc.). Now ω_j and ω_ℓ satisfy the dispersion relation (4.4); let the third root be ω_* . Making use of the relations $\omega_j + \omega_\ell + \omega_* = 0$ and

$$\omega_\ell \omega_j \omega_* = K \quad \text{we obtain}$$

$$\begin{aligned}
 A_{j\lambda}^n &= \frac{K}{\omega_*} \left[2n+1 + \frac{K}{\omega_*} \right] - K\omega_* + K^2 \left[2n+1 + K^2\omega_*^2 + \frac{2K}{\omega_*} \right] \\
 &= \frac{K}{\omega_*} \left[2n+1 + \frac{K}{\omega_*} - \omega_*^2 \right] + K^2 \left[\frac{K}{\omega_*} \right] = 0
 \end{aligned}$$

since ω_* satisfies (4.4).

(b) Completeness

We wish to show that if all the components of the vector

$\underline{F} = (F, G, Q)$ have expansions of the form

$$\sum_{n=0}^{\infty} a_n(K, t) \Psi_n(\gamma)$$

then F has an expansion of the form $\sum b_{n,j} \phi_{n,j}$

It is sufficient to show that, for all n , $(1, 0, 1) \Psi_n$, $(0, 1, 0) \Psi_n$ and $(1, 0, -1) \Psi_n$ have such expansions. From (5.7), (5.8) and (E4) it follows that for $n \geq 1$, the vectors $(1, 0, 1) \Psi_{n+1}$, $(0, 1, 0) \Psi_n$, $(1, 0, -1) \Psi_{n-1}$ have expansions of the form $b_{n,1} \phi_{n,1} + b_{n,2} \phi_{n,2} + b_{n,3} \phi_{n,3}$

if the matrix

$$\begin{bmatrix} \left[\frac{n+1}{2}\right]^{1/2} (\omega_1 + K) & \omega_1^2 - K^2 & \left[\frac{n}{2}\right]^{1/2} (\omega_1 - K) \\ \left[\frac{n+1}{2}\right]^{1/2} (\omega_2 + K) & \omega_2^2 - K^2 & \left[\frac{n}{2}\right]^{1/2} (\omega_2 - K) \\ \left[\frac{n+1}{2}\right]^{1/2} (\omega_3 + K) & \omega_3^2 - K^2 & \left[\frac{n}{2}\right]^{1/2} (\omega_3 - K) \end{bmatrix}$$

is non-singular. After some manipulation it may be seen that this is true if

$$\begin{bmatrix} 1 & \omega_1 & \omega_1^2 \\ 1 & \omega_2 & \omega_2^2 \\ 1 & \omega_3 & \omega_3^2 \end{bmatrix}$$

is non-singular, or if $(\omega_1 - \omega_2)(\omega_1 - \omega_3)(\omega_2 - \omega_3) \neq 0$. This is equivalent to the statement that the three roots of the dispersion relation (4.4) are distinct, which may be readily demonstrated by a reductio ad absurdum argument. By making use of the fact that $\omega_{01} \neq \omega_{02}$, the remaining vectors needed, i.e., $\Psi_0(1,0,1)$, $\Psi_1(1,0,1)$ and $\Psi_0(0,1,0)$, may be expanded in the vectors ϕ_{-1} , ϕ_{01} , ϕ_{02} .

BIOGRAPHICAL NOTE

I was born in 1944 in Brooklyn, New York. After graduating from Midwood High School, I entered Harvard College, graduating magna cum laude, Phi Beta Kappa in Applied Mathematics in 1965. I spent the following summer as a civil rights worker in the South. This was a great learning experience, at least if such things may be measured by the number of illusions dispelled. That fall, I entered graduate school at Harvard in Applied Mathematics (Computer Science), but after a year I decided I needed a respite from being a student. I returned to New York City and found employment at the Goddard Institute for Space Studies as a programmer and mathematical analyst. My participation in research on the Hadley Circulation and on the problem of utilizing satellite data in numerical weather prediction kindled an interest in meteorology and oceanography.

In 1968, I married Barbara Haak, and in 1970, our daughter, Laura, was born. Shortly thereafter, we left New York for rural New Hampshire, where I taught mathematics at New England College. After two pleasant years, it was clear that I am hopelessly married as well as addicted to doing research. So I entered graduate school in meteorology at MIT in the fall of 1972. The following year, Jacob joined his sister as a source of delight to his parents.